THERMOMECHANICAL FATIGUE CRACK FORMATION IN NICKEL-BASE SUPERALLOYS AT NOTCHES

A Thesis
Presented to
The Academic Faculty

by

Patxi Fernandez-Zelaia

In Partial Fulfillment
of the Requirements for the Degree
Master of Science in the
George W. Woodruff School of Mechanical Engineering

Georgia Institute of Technology
August 2012

THERMOMECHANICAL FATIGUE CRACK FORMATION IN NICKEL-BASE SUPERALLOYS AT NOTCHES

Approved by:

Dr. Richard W. Neu, Advisor
George W. Woodruff School of
Mechanical Engineering
Georgia Institute of Technology

Dr. Stephen. D. Antolovich
School of Materials Science and Engineering
Georgia Institute of Technology

Dr. David L. McDowell
George W. Woodruff School of
Mechanical Engineering
Georgia Institute of Technology

Date Approved: 15 May 2012

ACKNOWLEDGEMENTS

The work presented in this thesis was made possible by a number of individuals that provided support and guidance during the course of my work. The support I received greatly influenced the quality of this work and contributed to both my personal and academic maturity. I would like to express my thanks to those involved in aiding me over the course of this project.

I would like to thank my advisor, Dr. Richard W. Neu, for his support, guidance, criticism and encouragement throughout this work. His aid was critical in completion of this thesis and it was a pleasure to work with him during my time at Georgia Tech. I'd also like to thank my committee members, Dr. David McDowell and Dr. Stephen Antolovich, for their effort and time in reviewing the material presented in this thesis and the detailed feedback they provided.

I'd like to thank several graduate students for their friendship and aid; Robert Amaro, Mike Hirsch, Mike Kirka, Matt Siopis, Ben Adair and Siddharth Avachat. I'd also like to thank research engineer J.D. Huggins for the time, effort and enthusiasm in aiding with the experimental portion of my work.

The support of my family, both during my undergraduate studies and graduate studies, has been incredibly influential in motivating my academic endeavors. Their emphasis on the value of education and maintaining a strong work ethic has been is essential to my personal development.

Lastly I would like to thank my corporate sponsors. Without the financial support of Pratt & Whitney and Siemens Power Generation, this research would not have been possible.

TABLE OF CONTENTS

LIST OF TABLES

LIST OF FIGURES

SUMMARY

Hot section components in the high pressure turbine section of gas turbine engines undergo complex thermomechanical loads which complicates component life prediction. Components such as blades and disks contain stress elevating features that can have a detrimental effect on component endurance. This work characterizes the behavior of a directionally solidified blade material, CM247LC DS, and a fine-grained polycrystalline disk material, PM IN100, in circumferentially notched specimens This study consists of an experimental phase as well as a numerical modeling phase. The experimental phase consists of conducting high temperature thermomechanical fatigue experiments on smooth and circumferentially notched specimens. The numerical modeling phase consists of predicting local response variables in the tested notched specimens utilizing appropriate material constitutive models within a finite element framework.

The role of stress concentration severity on notch specimen crack initiation under thermomechanical fatigue loadings is investigated for CM247LC DS. The TMF fatigue life of notched specimens loaded in the longitudinal orientation are compared to analogous experiments on uniaxial specimens. Results show that blunt notches ($k_t = 1.3$) show little or no detrimental effect on fatigue life under $500°C \leftrightarrow 950°C$ and $500°C \leftrightarrow 750°C$ temperature ranges. Notch geometry corresponding to $k_t = 1.7$ falls in between the life trend produced by blunt notches and sharp notches for both temperature ranges. The blunt notches ($k_t = 1.3$) also show little or no detrimental effect on fatigue life under $500°C \leftrightarrow 950°C$ IP TMF. The von Mises and inelastic cyclic strain from simulated results correctly capture qualitative initiation location trends.

Material around stress concentrations in components are subjected to localized inelastic deformation. To correctly understand and predict initiation in these 'hot spots' requires that experiments are performed under representative boundary conditions in a laboratory setting. The influence of remotely applied boundary conditions is studied in both alloys under thermomechanical fatigue conditions by performing experiments under remote displacement and force control. For IN100 under TMF conditions the effects of boundary conditions had a significant effect on crack propagation under both IP and OP loading. Never the less, under OP TMF both force and displacement control conditions produce similar life trends within experimental error. Under IP TMF displacement control results indicate that there is a significant decrease in crack propagation driving force that caused crack arrest prior to detection. CM247LC DS under OP TMF conditions produced similar life trends for both force and displacement control conditions under $500°C \leftrightarrow 950°C$ and $500°C \leftrightarrow 750°C$ temperature ranges. Damage mechanisms were observed to be the same under both control modes.

Cyclic response parameters were used to decouple simulated inelastic strains in notch models into cyclic and ratchet strains. A Smith-Watson-Topper parameter utilizing the cyclic inelastic strain and von Mises stress was utilized in a nonlocal area method approach to predict $500°C \leftrightarrow 950°C$ OP TMF life trends. Life prediction values were within a factor of two of the experimentally determined lives.

CHAPTER 1 INTRODUCTION

1.1 Motivation

Gas turbines are often utilized as a significant source of power generation. Land-based turbines draw in atmospheric air into a multi-stage compression section. Each stage is designed to increase the air pressure until a desirable pressure is achieved for fuel mixing and combustion. Once ignited, the hot gas flow is directed into a multi-stage turbine section. Each stage utilizes the escaping gas to drive a rotor between 3000 and 3600 revolutions per minute. The turbine rotors then drive the compressor stages ahead of the combustor and also drive a downstream generator that feeds to the transmission grid. The operating conditions, or duty cycle, vary between units depending on the generator capacity and seasonal shifts in grid demand.

Due to the extreme temperatures experienced in the hot section, blades are internally cooled by gases from the upstream compressor. These cooling holes serve as local stress elevators. Turbine disks experience lower maximum temperatures, as the disk itself is further from the gas path, yet still also undergo thermomechanical fatigue. Turbine blades are attach to disks at the fir-tree which acts as a local stress raiser in the disk. The surrounding material around these stress elevators undergo localized plasticity and hence are a potential site of fatigue crack nucleation [1-2]. These cracks can lead to premature retirement of components or worst, component failure.

During start up and shutdown components experience transient conditions that contribute to non-uniform temperature distributions. These conditions contribute to low-cycle thermomechanical fatigue due to thermal mismatches superimposed onto centrifugal loads. During steady-state operation, radial loads and high temperature contribute to creep-fatigue

damage interactions. During both transient and steady-state loadings components are exposed to corrosive combustion species at high temperature. These conditions promote oxidation and degradation of surface materials.

Traditional methods for prediction of component endurances typically focus on simplifying the problem to isothermal low-cycle fatigue analysis. Quantifying damage under thermomechanical conditions using low-cycle fatigue has been done with varying success [3-4]. Isothermal low-cycle fatigue component analysis are favored as it greatly simplifies model complexity and simple experimental results are more prevalent.

1.2 Research Objectives

Gas turbine engines undergo transient start-ups and shut-downs as well as high temperature dwells during steady-state operation. Components are inevitably designed with stress elevators which are a source of localized inelastic deformation and crack initiation. As a majority of component life is spent in the crack initiation phase of life, this research will focus on the crack initiation of directionally solidified CM247LC DS and fine-grained polycrystalline IN100 notched specimens under thermomechanical fatigue loading. The specific goals are:

1. **Study the effect of notch severity on TMF crack initiation life of CM247LC DS.** Perform experiments on circumferentially notched specimens to simulate stress elevators in turbine blades. Specimens corresponding to elastic stress concentrations of $k_t = 1.3$, $k_t = 1.7$, $k_t = 2.0$ and $k_t = 3.0$ will be loaded longitudinally under TMF conditions. Results from this study will be coupled with $k_t = 2.0$ and $k_t = 3.0$ results from Kupkovits to address the role of notch severity on TMF crack initiation life.

2. **Study the effects of applied boundary conditions on TMF crack initiation life of CM247LC DS and IN100.** Perform experiments on both CM247LC DS and IN100 utilizing displacement boundary conditions and compare to force controlled experiments. Traditionally the inelastically deforming material around notched features is assumed to be under displacement control due to constraints imposed by the surrounding elastic medium and multiaxiality. In reality some plastic/creep ratcheting occurs at the notch root and as such a mixed-mode boundary condition is more realistic. Displacement controlled experiments will be complimented by post failure specimen inspection to identify damage mechanisms present.
3. **Determine the local notch response in both CM247LC DS and IN100 using finite element analysis under TMF conditions.** As the local notch response cannot be determined directly from experiments numerical analysis must be used. A transversely isotropic viscoplastic model is used in a parametric study to determine the local response across all CM247LC DS notch geometries. A unified creep-plasticity model is developed and calibrated for IN100 to determine the notch response in $k_t = 2.0$. In both analyses inelastic strains are decoupled into ratchet and cyclic strains to understand the material response at elevated temperature.
4. **Determine the role of thermomechanical fatigue loading parameters on crack initiation and deformation of notched IN100.** The influence of loading waveform (IP & OP) and the cyclic temperature range is to be studied on $k_t = 2.0$ specimens. The experimental response will provide insight into dominant

deformation and damage mechanisms. Fatigue lives and post failure specimen inspection will address the role of loading parameters on damage mechanisms.

5. **Investigate life prediction methods for notched specimens.** Utilize the local notch response from numerical simulations to determine experimentally observed initiation lives. Interpret results and compare the effectiveness of different methods. The goal is to provide insight into life modeling on the component scale under complex loadings for future comprehensive life prediction modeling.

1.3 Thesis Overview

This work is organized such that each chapter can be a standalone document. The writing is organized such that work presented is in a developmental order, spanning from a brief background, methods, results and then a summary. Chapter 2 is an overview based on previous works on nickel-base superalloys, thermomechanical fatigue and notch component fatigue. Chapter 3 contains microstructural descriptions and mechanical property behaviors for the alloys utilized in this study; CM247LC DS and IN100. Chapter 4 contains the experimental procedure for thermomechanical fatigue testing and post failure microscopy. A review of the constitutive models utilized in this study are found in Chapter 5 along with details on the finite element analysis procedure. Chapter 6 focuses on the influence of applied boundary conditions on CM247LC DS and IN100 notch crack initiation lives. The influence of notch severity on TMF crack initiation life of CM247LC DS is found in Chapter 7. The effects of thermomechanical loading parameters on notched IN100 are in Chapter 8. Chapter 9 consists of a summary and conclusion of this work and Chapter 10 contains recommendations for future work.

CHAPTER 2 BACKGROUND

To understand the failure of notched Ni-base superalloy service components under thermomechanical fatigue a fundamental understanding of the deformation mechanisms and damage mechanisms under TMF is needed. Included in this chapter is an overview of TMF behavior of Ni-base superalloys based on both experimental and service observations. An overview of some methods for quantifying notch damage is included. Fatigue and thermomechanical fatigue of notched component behavior is included to address the role of notched features on fatigue life.

2.1 Microstructure and Ni-base Superalloy Properties

Nickel-based superalloys are used in the hot sections of gas turbine engines due their high strength at elevated temperatures, excellent creep resistance and oxidation resistance. To improve engine efficiencies and output thrust designers strive to increase maximum engine operating temperatures and rotational velocities. This increases the need to design materials that can withstand higher temperatures and applied loads as well as improve the predictability of material degradation.

Complex component geometries and the high strength of Ni-base superalloys make machining difficult so components are typically manufactured by investment casting. Dependent on the mechanical loads and temperatures a particular component is exposed to, three different grain patterns are utilized within gas turbine engines: equiaxed polycrystalline, directionally solidified (DS) and single crystal alloys (SC or SX). Polycrystalline materials can be cast to produce a sufficiently homogeneous grain distribution which can be treated as isotropic relative

to the representative volume element (RVE). Directional solidification results from casting of several columnar grains where the primary orientation (longitudinal) is prescribed by a seed crystal oriented for growth in the [001] direction. Single crystal casting is the most difficult and as such a most expensive method. A turbine blade cast to produce the three different grain patterns is shown in Fig. 2-1.

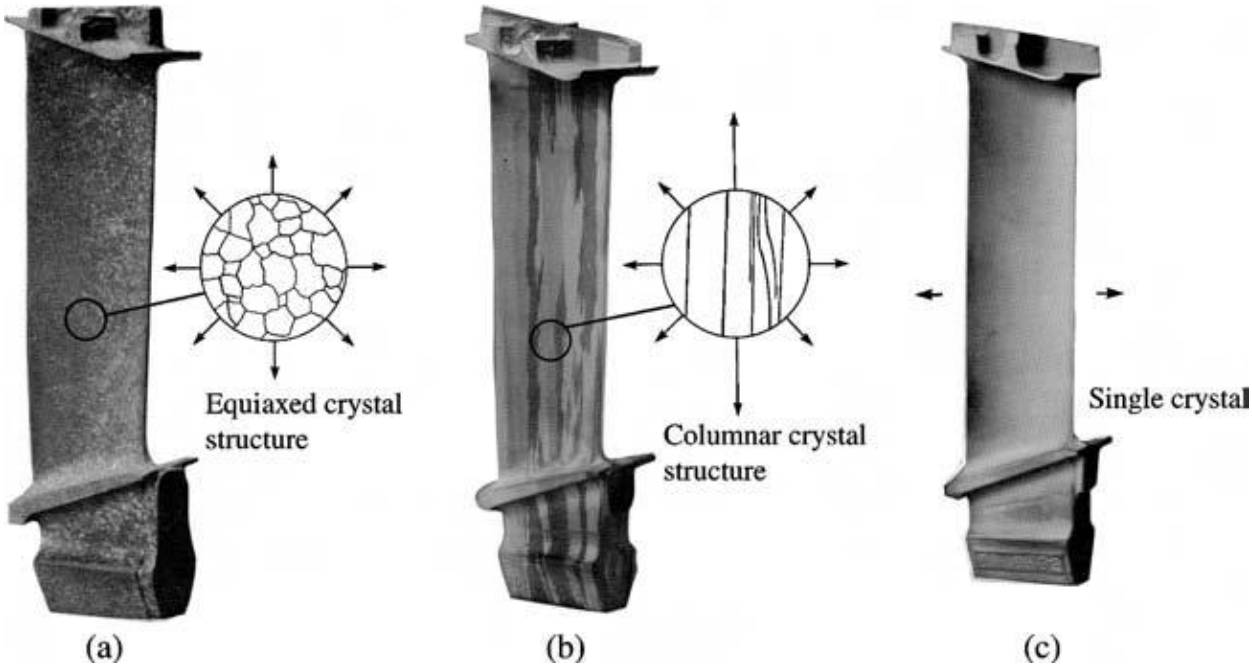

Figure 2-1. Turbine blade cast as (a) polycrystalline equiaxed, (b) directionally-solidified and (c) single crystal [5].

Primary dendritic arms in superalloy grains grow along the [001] direction. Secondary and tertiary dendrite arms grow orthogonally to the primary arms along the [100] and [010] directions, see Fig. 2-2.

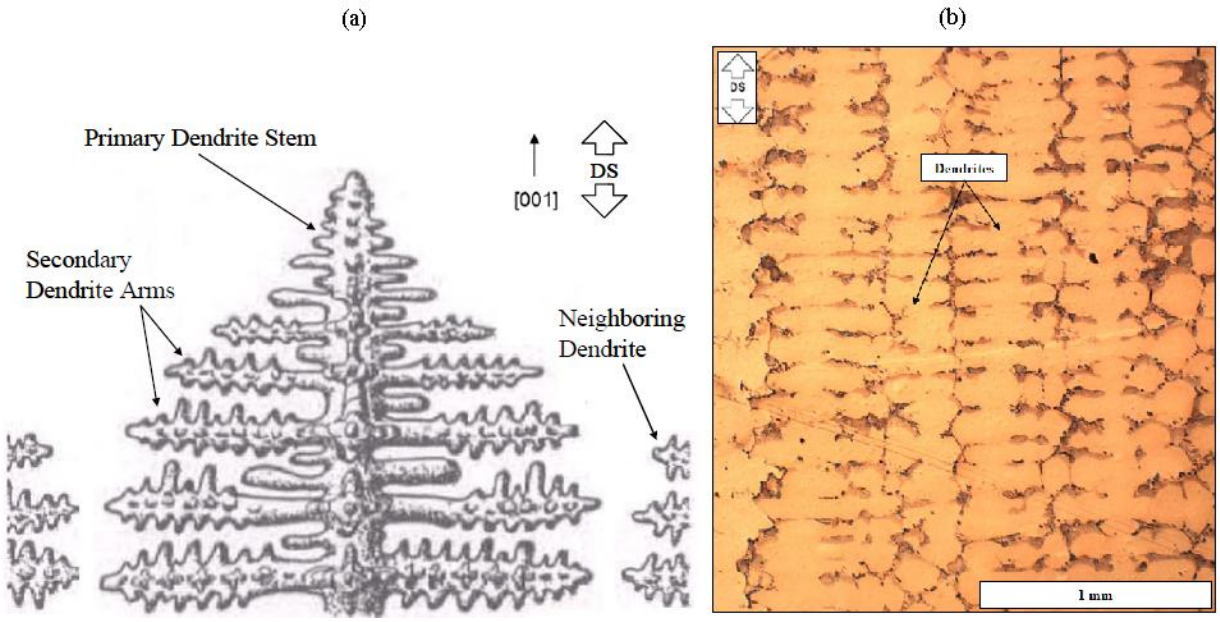

Figure 2-2. (a) Schematic of primary dendrite arm growth and secondary arms [2] (b) Primary, secondary and tertiary dendrites in CM247LC DS microstructure [6].

Microstructural discontinuities such as carbides, inclusions, undissolved eutectic pools, oxides, micropores and freckle defects are often concentrated in the interdendritic regions [4-5, 7]. These inhomogeneities are a leading contributor to fatigue crack initiation at elevated temperatures. Carbides or borides can form during heat treatment if sufficient quantities of carbon and boron are present which combine with reactive species such as titanium, tantalum and hafnium to form MC carbides. These carbides typically form along grain boundaries and can be sources of fatigue crack initiation. Mazur et al. [1] found that preferred crack initiation occurred at carbide γ-grain boundaries that caused local decreases in ductility and toughness in IN738LC turbine blades.

The microstructure of typical superalloys consists of several phases. The gamma phase (γ) is an FCC austenitic Ni solid solution with strengthening elements. Gamma-prime precipitates (γ') are a cuboidal or spherical ordered FCC super-lattice of Ni_3Al that reside coherently within the matrix and are provide strengthening characteristics. Secondary gamma-precipitates (γ'') can form upon cooling in superalloys that are rich in niobium. The γ' precipitates contribute to the anomalous yielding behavior exhibited by nickel-based superalloys, as shown in Fig. 2-3. Here the volume fraction of γ' was varied to study the precipitates effect on yielding behavior. This phase is typically rich in aluminum, chromium, titanium and tantalum.

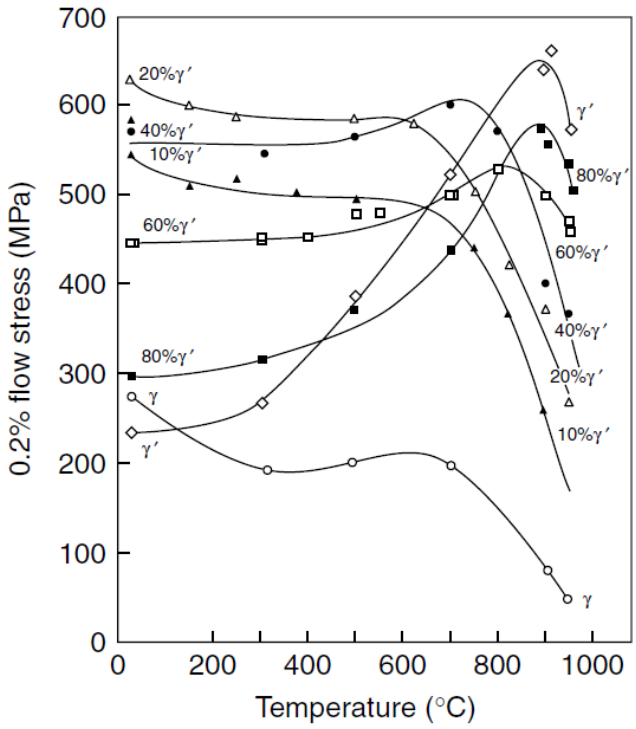

Figure 2-3. Yield stress variation for a Ni-Cr-Al alloy with varying volume fraction of γ' precipitates [5].

The anomalous increase in yield stress with temperature in γ' alloys around 700°C is attributed to a strengthening mechanism provided by the γ' precipitates. Cross slip occurs from the preferred

octahedral slip systems to the cube planes which cause the formation of Kear-Wilsdorf locks that provide additional resistance to flow stress [5].

Fatigue damage results from irreversible shear slip accumulation along crystallographic glide planes during cyclic straining generating slip fields. Under cyclic straining cracks tend to initiate in locations where these slip fields impinge upon the material free surface [8]. Slip fields present on the surface of a notched SX sample is shown in Fig. 2-4.

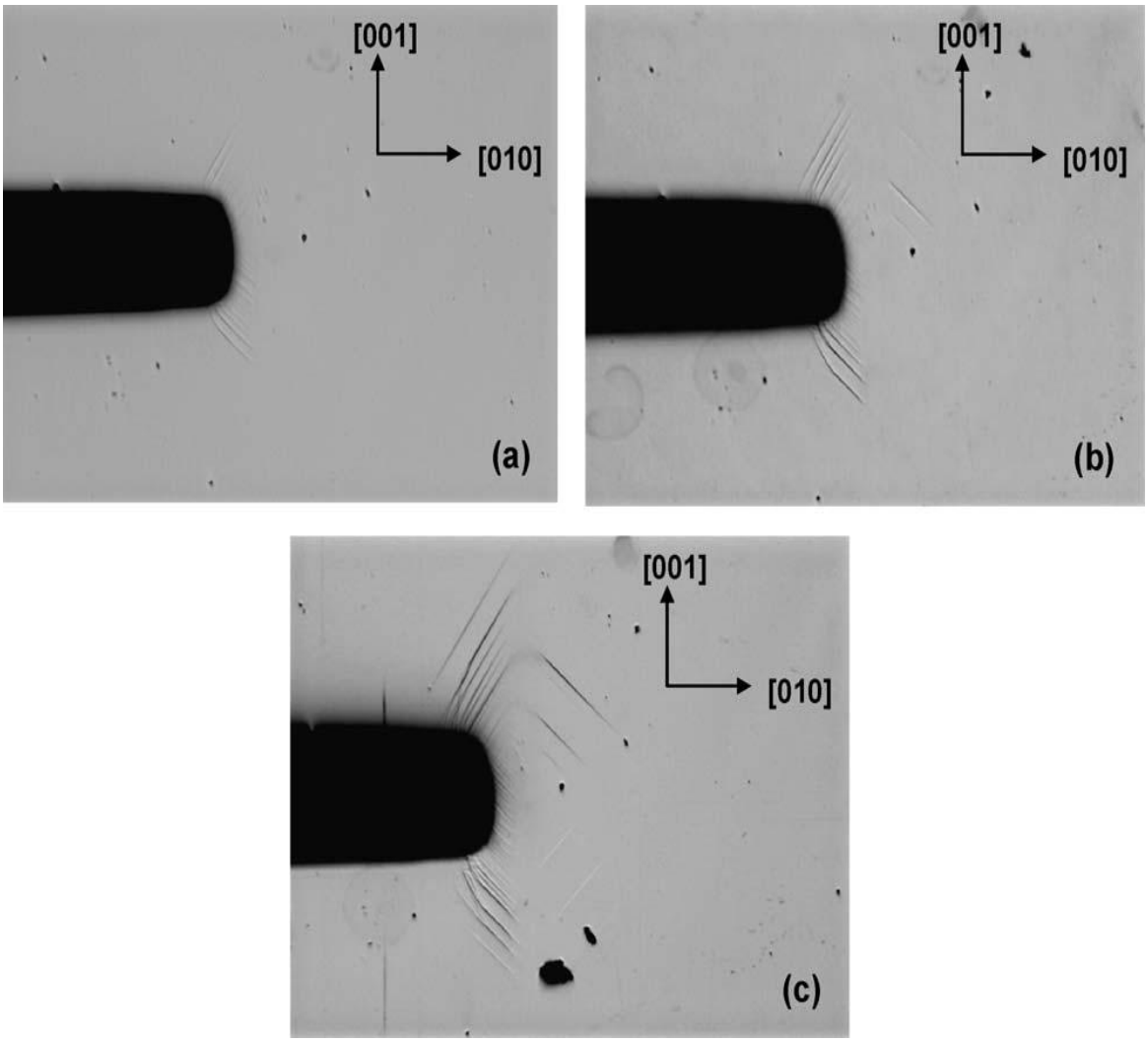

Figure 2-4. SX Ni-base superalloy slip field formation in notched geometry under increasing load (a-c) [9].

Extrusions of these slip fields at the material surface, slip steps, behaves as a local stress raiser which promotes additional slip and eventual crack initiation. Extrusions from slip bands in copper at the free surface are shown in Fig. 2-5. Amaro [10] developed a extrusion based crack initiation model for SX superalloy PWA1484 under environmental-fatigue interactions.

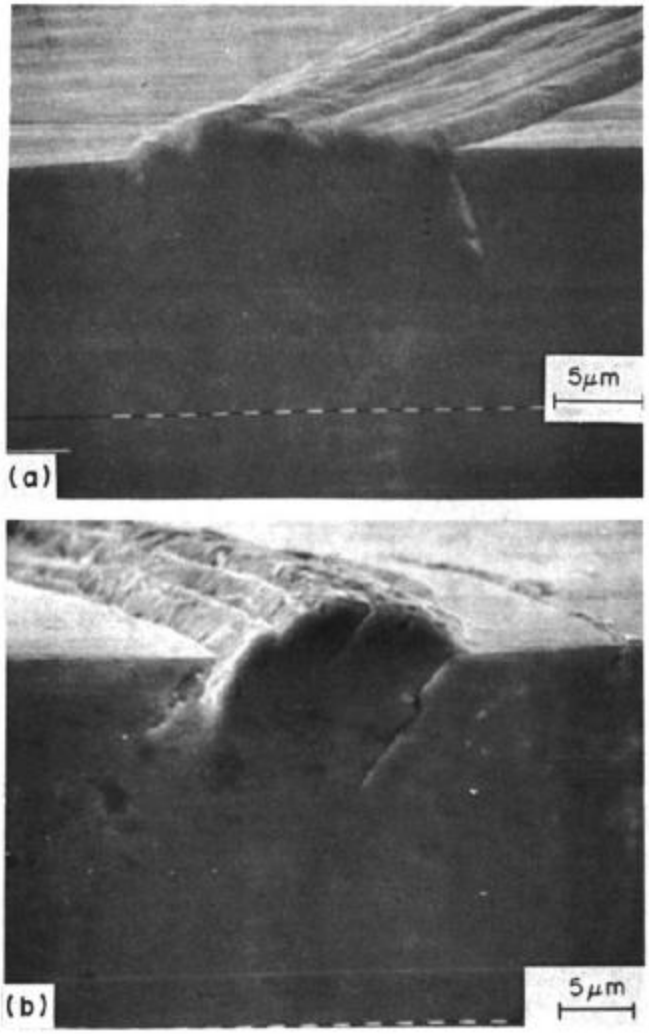

Figure 2-5. Fatigue crack initiation at a persistent slip band surface intersection in Cu [11].

The precipitates in superalloys also enhance creep strengthening. Provided the applied stresses during creep deformation are not large enough to shear precipitates, the precipitates

restrict mobile dislocations to γ-channels effectively decreasing the dislocations mobility [12], see Fig. 2-6. Here CMSX-3 was subjected to 552 *MPa* static stress at 850°C.

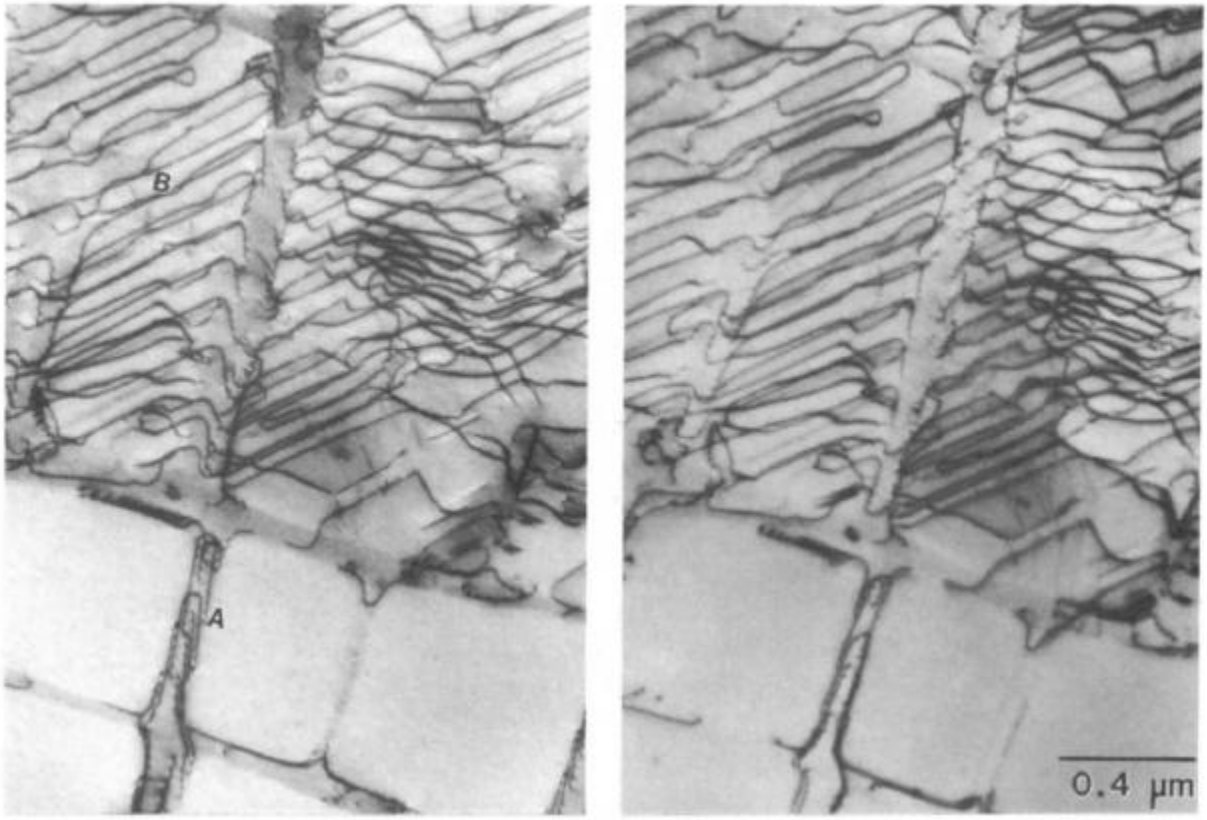

Figure 2-6. Stereo pair of dislocation structure during primary creep of CMSX-3 under an applied 552 *MPa* static stress at 850°C. At location A the dislocations are constrained to a γ-channel oriented vertical to the TEM foil. At location B the dislocations are restricted to a γ-channel in the plane of the TEM foil [12].

The degree of creep strengthening is directly dependent on the precipitate volume fraction, as seen in Fig. 2-7. The γ' fraction in a coarse and fine grain superalloy was varied to study the resulting minimum creep rate. Both microstructures exhibited a reduction in creep rate with increasing γ' fraction.

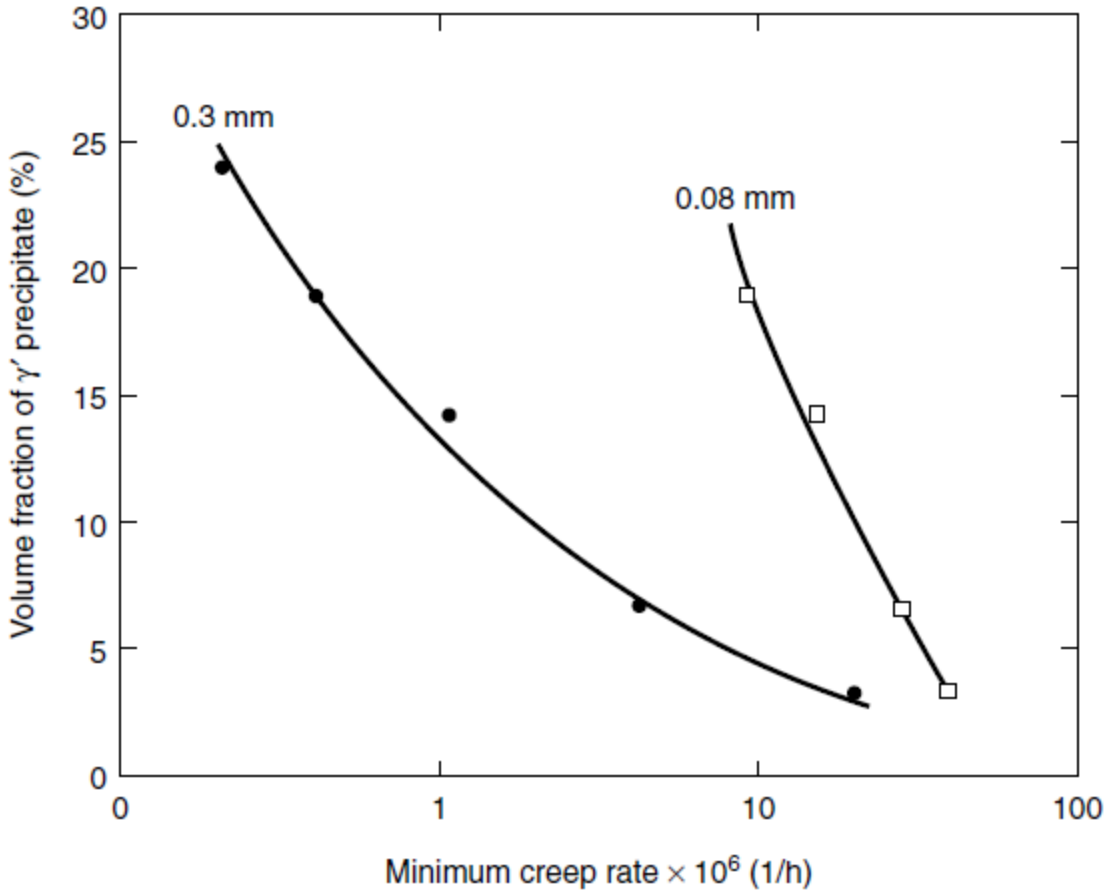

Figure 2-7. Minimum creep rate of coarse and fine grained superalloys with varying volume fraction of precipitate at 800°C and 150MPa [5].

2.1.1 Directionally Solidified Superalloys

Directionally solidified cast blades are typically oriented to the principle axis of the blade in the [001] crystallographic direction as this direction has the lowest modulus of elasticity which reduces thermal stresses that are generated during operation [13]. The elastic modulus of CM247LC DS at 850°C as a function of orientation relative to the longitudinal axis is shown in Fig. 2-8.

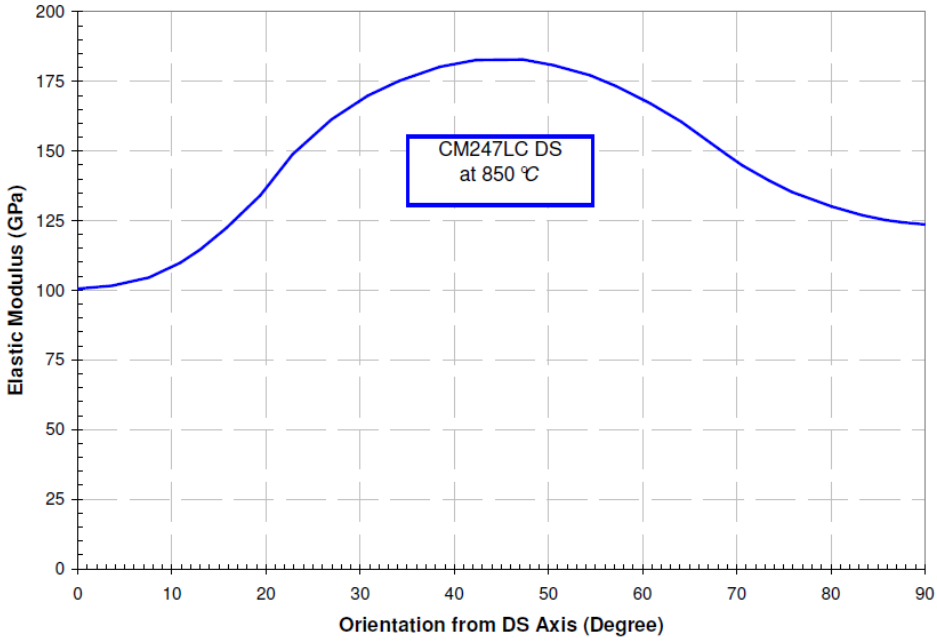

Figure 2-8. Elastic modulus of CM247 LC DS at 850°C as a function of orientation [14].

Temperature dependent yield stress for longitudinal and transverse oriented CM247LC DS are shown in Fig. 2-9. The transverse oriented corresponds to a 90° rotation from the longitudinal direction.

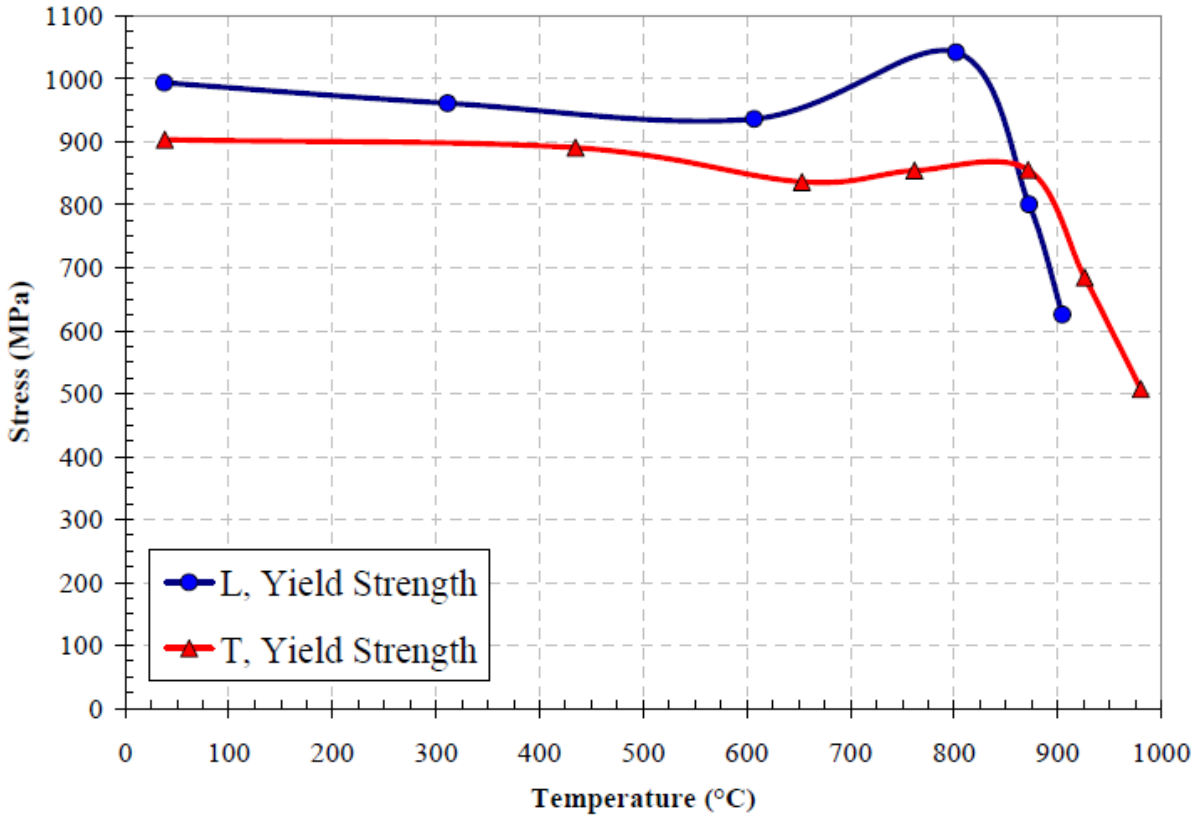

Figure 2-9. Temperature dependent yield strength of CM247LC DS oriented in the longitudinal (L) and transverse (T) direction [14].

Investment casting of turbine blades to produce DS or SX blades greatly increases the creep resistance of components by reducing the grain boundary volume. Grain boundaries provide energetically favorable pathways for diffusion which enhances creep processes and decreases creep resistance at elevated temperatures and loads. Results from an early study by Kear and Piearcey [15] on Mar-M200 are shown in Fig. 2-10. They found that the creep rates decreased between conventional cast, DS and SX castings. Additionally the DS and SX material were able to sustain creep strains an order of magnitude larger than the polycrystalline alloy.

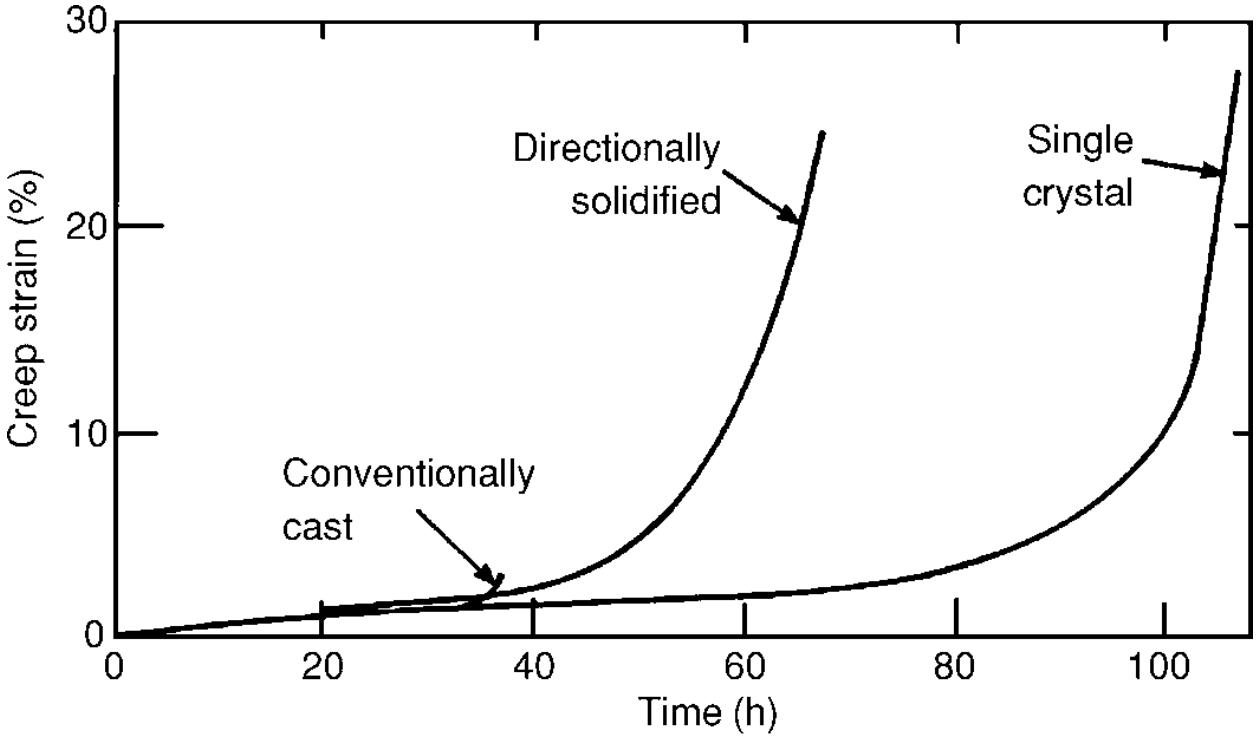

Figure 2-10. Creep strain evolution under a static stress of 206MPa at 982°C in Mar-M200 in polycrystalline, DS and SX states [15].

The creep rupture properties for CMSX-4 at 850°C in the presence of one grain boundary are shown in Fig. 2-11.

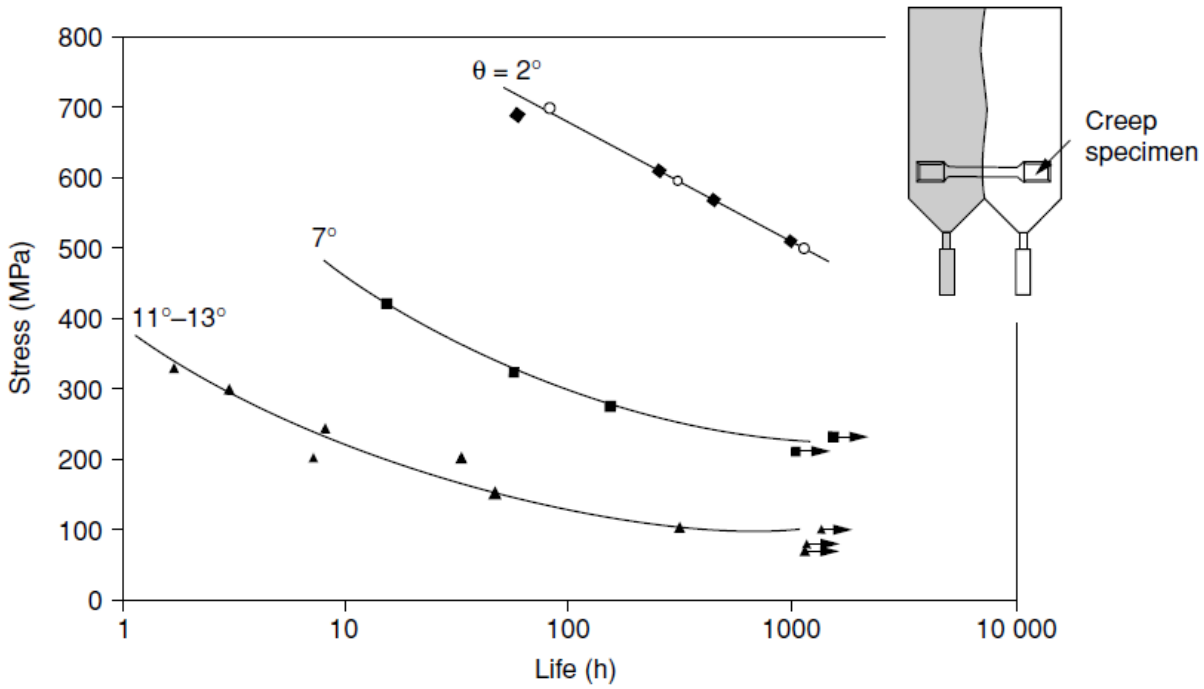

Figure 2-11. Creep rupture performance or CMSX-4 at 850°C for bi-crystal specimens machined to achieve a desired misorientation angle θ [5].

Here investment casting of two single crystals was performed simultaneously to generate a single grain boundary at the bi-crystal interface. Specimens were machined to achieve a desired misorientation angle and creep rupture properties were determined based on this angle. The results indicate that the grain boundary is detrimental towards creep strength and the misorientation angle quantities the degree of strength decrease.

Small amounts of carbide and boride formations in single crystals have been shown to be beneficial for creep performance. Liu et al. [16] performed a study comparing the creep resistance of on two SX Ni-base superalloys; one with no carbon and the other with 0.015 wt.% carbon. The introduction of elemental carbon promoted the precipitation of coherent carbides which increased creep performance as shown in Fig. 2-12.

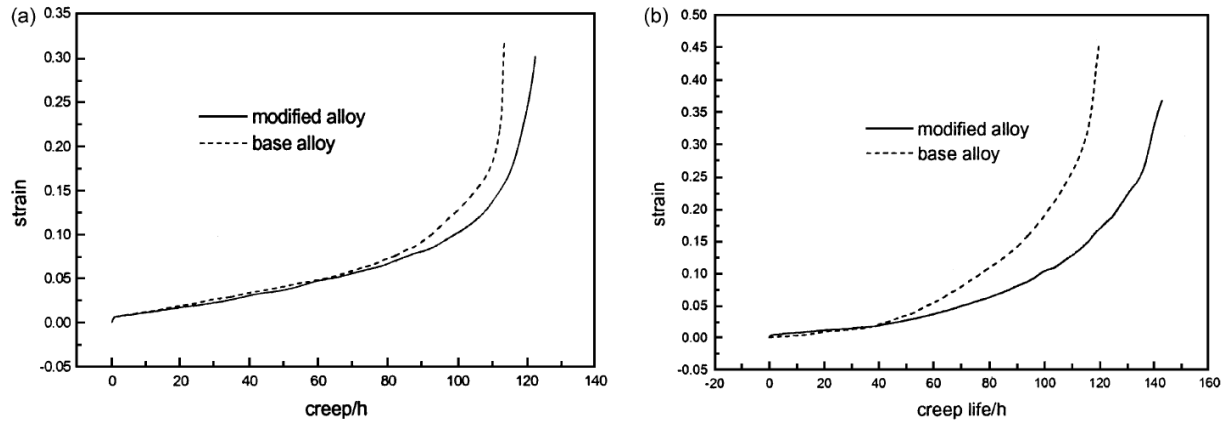

Figure 2-12. Beneficial creep effects from carbide formation in a SX Ni-base superalloy at (a) 871°C/552 *MPa* and (b) 1038°C/172 *MPa*. Base material contains 0 wt.% carbon, modified alloy 0.015 wt.% carbon [16].

2.1.2 Behavior of Polycrystalline Ni-base Superalloys

Polycrystalline superalloys are typically used in components experiencing lower applied mechanical loads and temperatures. This includes stationary stator vanes and turbine disks. Stator vanes are typically manufactured utilizing the investment casting method but disks are typically fabricated by the machining of superalloy forgings. The preparation of billets prior to forging can be produced using a cast-and-wrought method or powder metallurgy. Alloys such as Waspaloy and IN718 are typically cast-and-wrought products whereas IN100 Rene 95 and RR1000 are produced utilizing powder metallurgy [5]. The deciding factors in selecting a fabrication method is cost (powder is more costly) and the degree of alloying; high levels of alloying can cause cracking during thermomechanical working in the cast-and-wrought method.

Fatigue damage in polycrystalline metals also occurs due to irreversible slip along crystallographic planes. In the case of polycrystalline alloys, impingement of PSBs of grain boundaries can cause crack initiation as shown in Fig. 2-13.

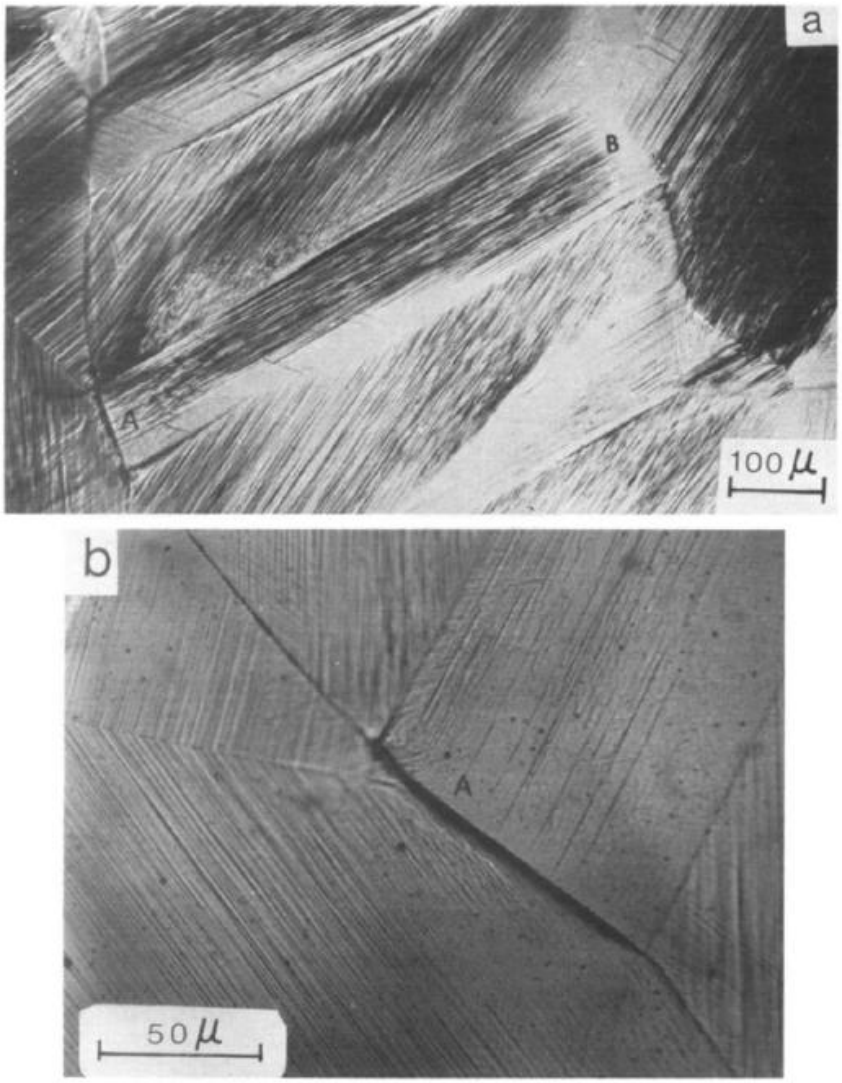

Figure 2-13. Fatigue crack initiation along a grain boundary in Cu [17].

Kim & Liard showed that fatigue cracks in Cu could nucleate at grain boundaries if the angle of misorientation was sufficiently high, the active slip system in a grain was directed at the intersection of a grain boundary and free surface, or if traces of high grain boundaries made a large angle with the direction of applied tensile stress [17].

Polycrystalline superalloy strength is very sensitive to the fraction of strengthening precipitates (γ' and γ") present in the material. Variation of yield stress at 650°C for many

common turbine disk alloys are shown in Fig. 2-14. Similar to DS and SX alloys, the Kear-Wilsdorf locking mechanism is responsible for precipitate strengthening in polycrystalline superalloys.

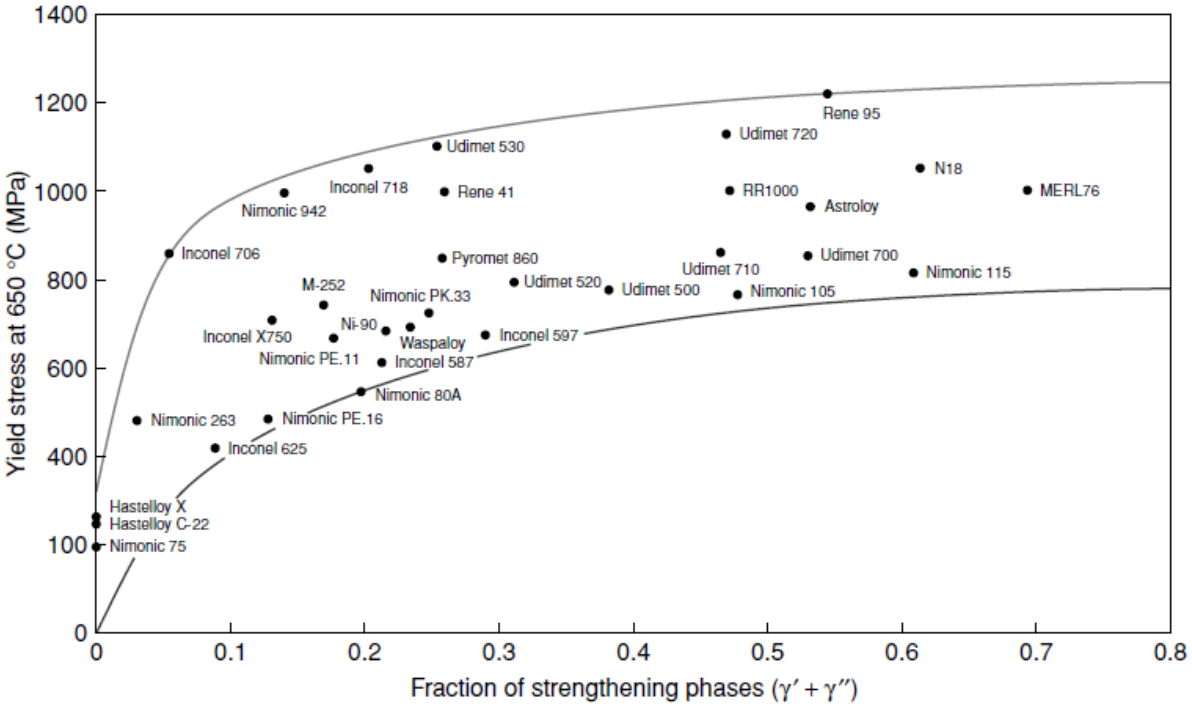

Figure 2-14. Yield stress dependence on fraction of strengthening precipitates in several common turbine disk superalloys at 650°C [5].

Creep performance in equiaxed superalloys is also improved due to precipitate strengthening. 1000 hr creep rupture stress at 700°C is shown as a function of precipitate volume in Fig. 2-15.

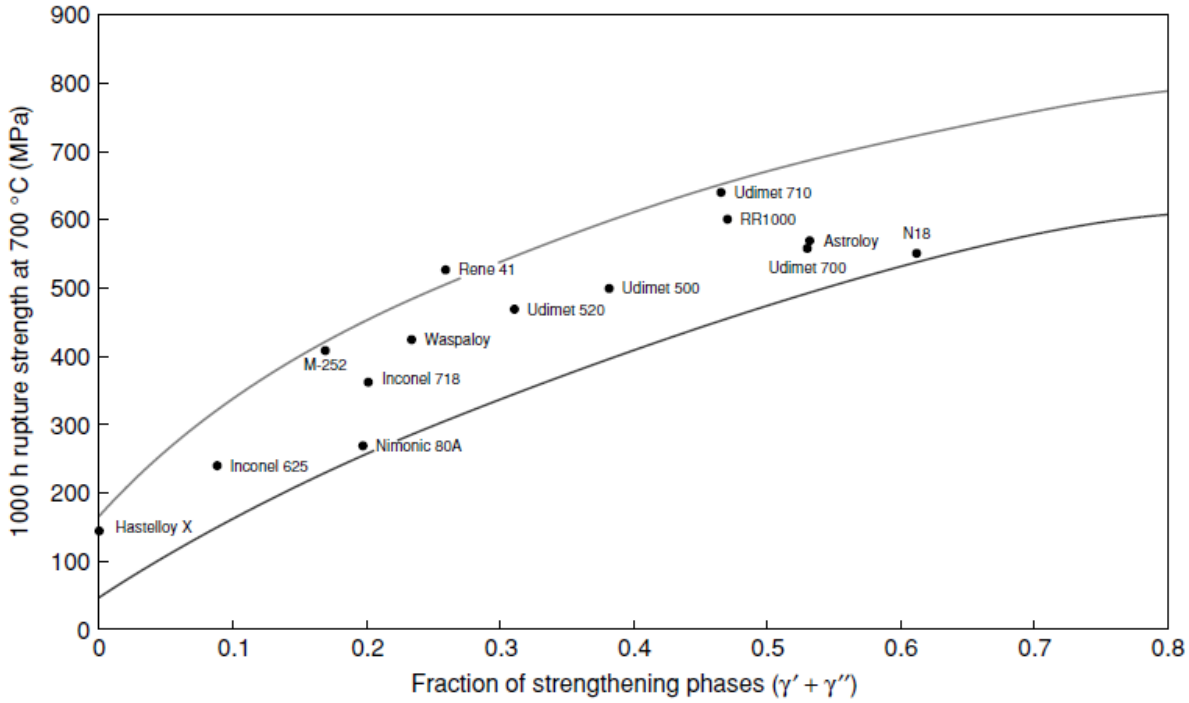

Figure 2-15. 1000 hr rupture strength at 700°C as a function of precipitate fraction for several turbine disk superalloys [5].

Both the creep and yield strength of turbine disk alloys are heavily dependent on the fraction of precipitates found in the material. The applied heat treatment following forging dictates both the grain size distribution and volume fraction of precipitate phases. In sub-solvus heat treatments the undissolved γ' precipitates, located at grain boundaries, remain and provide a pinning mechanism which limits grain growth and produces finer grains in the microstructure. In super-solvus heat treatments the primary γ' precipitates dissolve into the matrix, reducing the total fraction of strengthening precipitates and increasing the average grain size.

The introduction of grain boundaries is detrimental to both the creep and oxidation resistance of Ni-base superalloys. Grain boundaries provide a pathway for short circuit diffusion whereas lattice diffusion (bulk diffusion) represents a larger energetic barrier. The diffusion

coefficient along grain boundaries is several orders of magnitude larger than for lattice diffusion [18]. Many researchers have found that at elevated temperatures grain boundary oxidation in superalloys results in embrittlement of the grain boundary which results in crack initiation along surface connected grain boundaries [4, 19-23].

Polycrystalline exposure to elevated temperatures introduces creep damage in the form of cavitation along grain boundaries and grain boundary sliding. At sufficiently low stresses, most metals and alloys can experience creep deformation by grain boundary cavitation at temperatures between one-third and two-thirds the melting temperature. Cavitation can occur at nominal stresses well below 100 MPa [8]. Creep cavitation in polycrystalline Ni-base superalloy C263 is shown in Fig. 2-16. Many have observed that polycrystalline superalloys can fail at high temperatures due to intergranular cracking nucleated by grain boundary cavitation and sliding [21-22, 24].

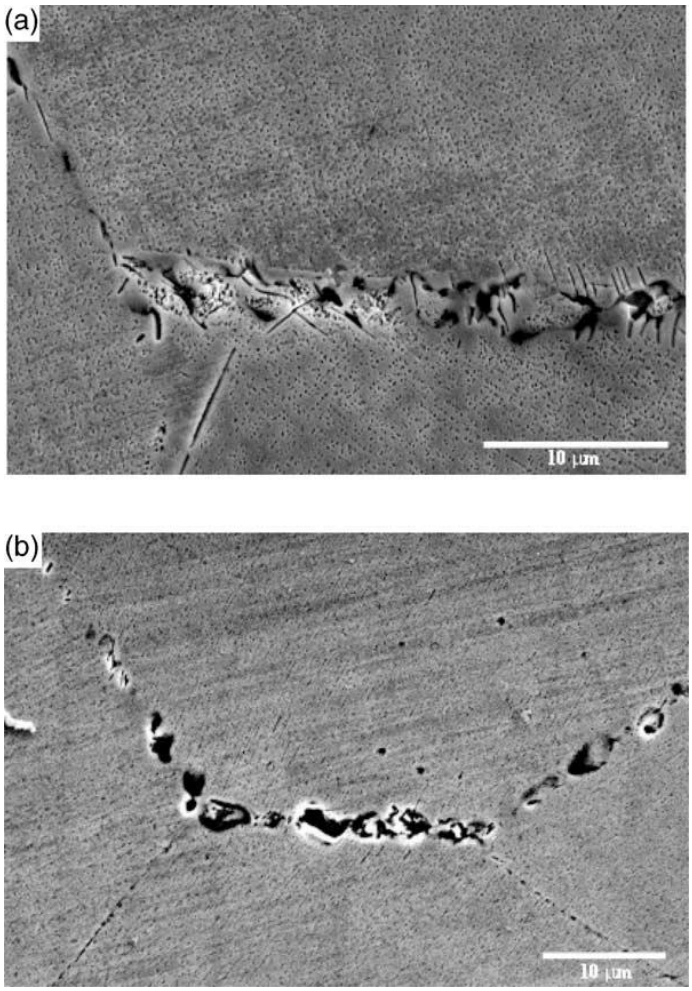

Figure 2-16. Creep cavitation at 800°C applied static stress 160 MPa for Ni-based superalloy C263 (a) without a pre-strain and (b) with a 5.1% pre-strain at room temperature [25].

Creep performance is improved in polycrystalline alloys by the addition of boron and carbon which prefer to form a long grain boundaries [5]. Formation of small, coherent and closely spaced carbides that precipitate on grain boundaries constrain the grain boundary sliding mechanism and yield beneficial creep performance for polycrystalline alloys. As such these elements are referred to as grain boundary strengtheners.

The influence of material inhomogeneities is even more pronounced in polycrystalline materials due to the high grain boundary density. Carbides, borides, inclusions, pores and other

defects behave as localized stress elevators due to mismatches in behavior with the surrounding material. These defects are commonly found along grain boundaries and as such promote decohesion and eventual cracking. In the presence of high temperature mechanisms such as creep or environmental damage the effect of defects is even more pronounced.

2.2 Effects of Stress Elevators on Fatigue

Notch severity in structural analysis is typically quantified utilizing the theoretical elastic stress concentration factor,

$$k_t = \frac{\sigma}{S} \tag{2.1}$$

where σ is the local stress and S is the nominal stress. The nominal stress can be taken as the far-field stress or the stress at the net cross-sectional area. Here all reported stress concentrations are defined utilizing the net cross-sectional area.

For studying the fatigue of metals in the presence of stress elevators, the stress concentration factor is overly conservative for predicting the detrimental effects of fatigue life. For quantifying the effects of notches on fatigue like, the fatigue notch factor is utilized [8, 26].

$$k_f(N) = \frac{\sigma_{ar}(N)}{S_{ar}(N)} \tag{2.2}$$

This expression relates the fully reversed stresses for a smooth specimen, S_{ar}, to the stresses in a notched specimen, σ_{ar}, at a prescribed fatigue life, N. The fatigue notch factor approaches the stress concentration factor for large notch root radii (blunt notches). At lower radii however the stress concentration factor is significantly larger than the fatigue notch factor. A comparison

between fatigue notch factor and theoretical elastic stress concentration factor for mild steel is shown in Fig. 2-17.

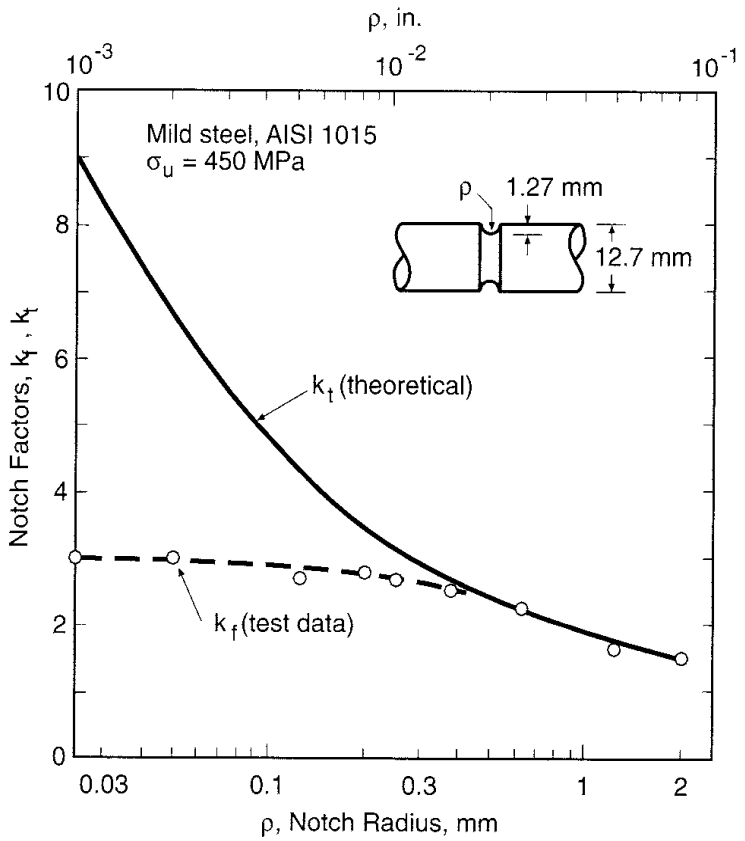

Figure 2-17. Fatigue notch factor and theoretical elastic stress concentration as functions of the notch radius for mild steel [26].

This observation can be explained by understanding the role of relevant spatial gradients present in the material. Rather than fatigue being dominated by the peak response at a point, fatigue is controlled by the response over a small, but finite, volume. In the case of sharp notches with small notch root radii, the stress gradients are very large and stresses drop-off fairly quickly away from the peak location, as shown in Fig. 2-18 (a) . The size of this drop-off region statistically controls the likelihood that a microstructural defect may coincide in the highly stressed volume. Also, it is possible that cracks may initiate very early in sharp notches but the

propagation rate quickly diminishes due to large stress gradients. The theoretical elastic stress concentration factor may over predict for sharp notches in some cases because of local yielding at the notch which reduces stresses predicted by elasticity as shown in Fig. 2-18 (b).

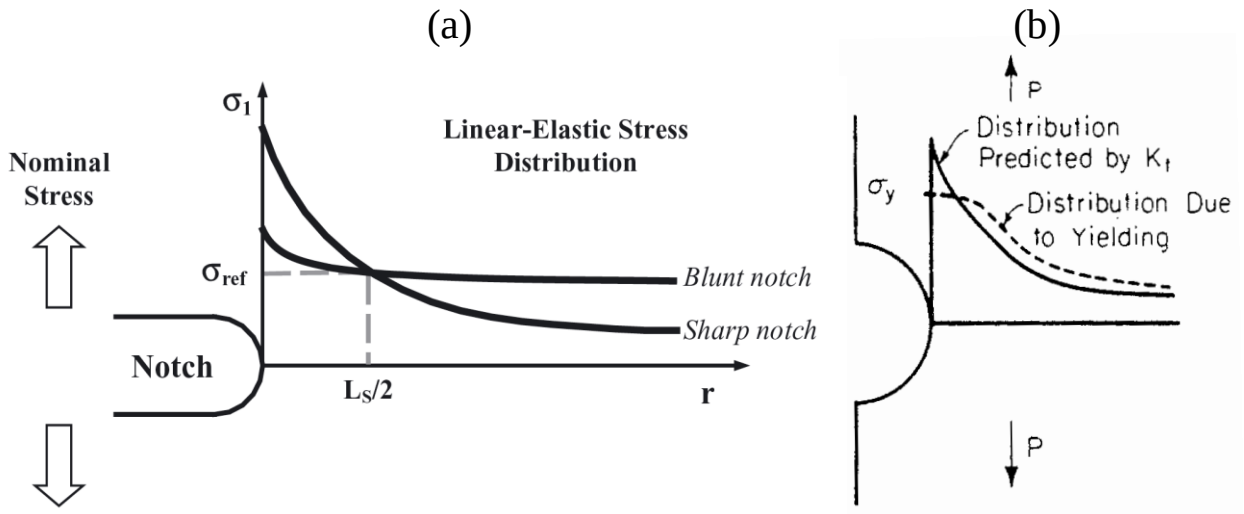

Figure 2-18. (a) Stress gradient response in a blunt and sharp notch [27]. (b) Notch blunting due to localized yielding [28].

Several methods have been proposed for relating the theoretical elastic stress concentration factor to the fatigue notch factor [29-30]. These expressions are highly empirical and define a relationship between the stress concentration factor and fatigue notch factor based on material properties and the geometric specimen features such as the notch root radius. The relationships only hold for simple geometries and are highly dependent on the applied loading conditions.

Neuber [31] first introduced the theory of utilizing non-local measures for determining the fatigue of notched components in the high cycle fatigue regime (HCF). He argued that the averaged stresses over some finite volume near the notch should be the controlling metric for

quantifying fatigue life. A generalization of the theory of critical distances is described by Taylor [32]. Four non-local quantities are presented for quantifying the notch life effect; Point Method (PM), Line Method (LM), Area Method (AM) and Volume Method (VM). Point method utilizes response variables at a point some critical distance away from the maximum stress. LM, AM and VM all utilize an averaging scheme over a critical line, area and volume, respectively. The point method and various averaging methods implicitly take into account the response gradients present in the notch root. Each method utilize a length scale, *L*, which is used in conjunction with the averaging method for defining the necessary integration domain. One commonly used length scale depends on the crack propagation threshold and fatigue limit for the appropriate load ratio,

$$L = \frac{1}{\pi}\left(\frac{K_{th}}{\sigma_0}\right)^2 \tag{2.3}$$

where K_{th} is the crack propagation threshold and σ_0 is the smooth specimen fatigue limit. This quantity implicitly is related to the length of a non-propagating crack in an un-notched specimen.

The critical length itself may be a function of the number of cycles to failure particularly in the medium cycle fatigue (MCF) regime [27]. In this methodology an iterative method is needed to predict lives to crack initiation. Two methods are utilized for developing a relationship between the critical length and the cycles to failure. The first method utilizes static failure and fatigue limit data for determining a relationship. The second method calibrates the critical length to the two extremes of smooth fatigue results and notched fatigue results.

Low cycle fatigue (LCF) and MCF fatigue lives in a low-carbon steel and aluminum notched specimens was studying by Susmel and Taylor [33]. Elastic-plastic analysis was utilized to determine the local response around several different notched geometries and make life

predictions. As the local R-ratio around the notch root deviates from the fully reversed case, leading to the development of mean stresses, a Smith-Watson-Topper (SWT) damage metric was utilized in conjunction with a point method and line method nonlocal approach. Alternatively other damage parameters can be used in nonlocal analysis . The critical length for PM and LM is determined directly from experimental results, see Fig. 2-19.

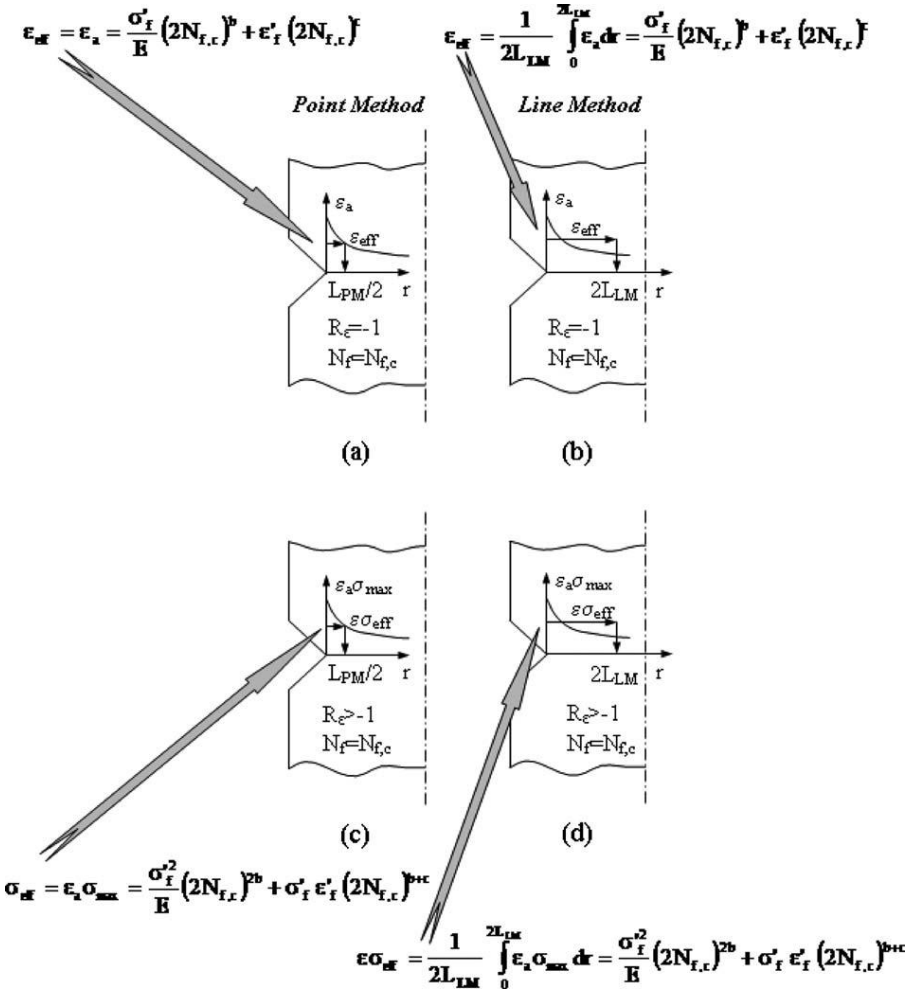

Figure 2-19. Procedure for determination of critical distance values in PM and LM critical distance methods [33].

Using a point method, Fig. 2-19 (a) and (c), the response is taken from a location some distance L_{PM} in the r-direction. In the line method, Fig. 2-19 (b) and (d), integration of the response is

done over a domain along the notch root from the notch surface inward a distance L_{LM} in the r-direction. Given a calibrated SWT expression from uniaxial fatigue lives, the critical distances are determined such that they will produce the experimental notched fatigue results using the SWT relationship. Susmel and Taylor suggest using the most severely notched fatigue results for calibration. In this fashion the life prediction methodology spans over the two extremes; the smooth fatigue results and the most severely notched fatigue results. It is assumed that these critical lengths are only dependent on the material and are not a function of specimen geometry or the applied loading. Life results for both alloys were mostly within a factor of two spanning across both the LCF and MCF regimes regardless of the method employed (PM or LM) as seen in Fig. 2-20.

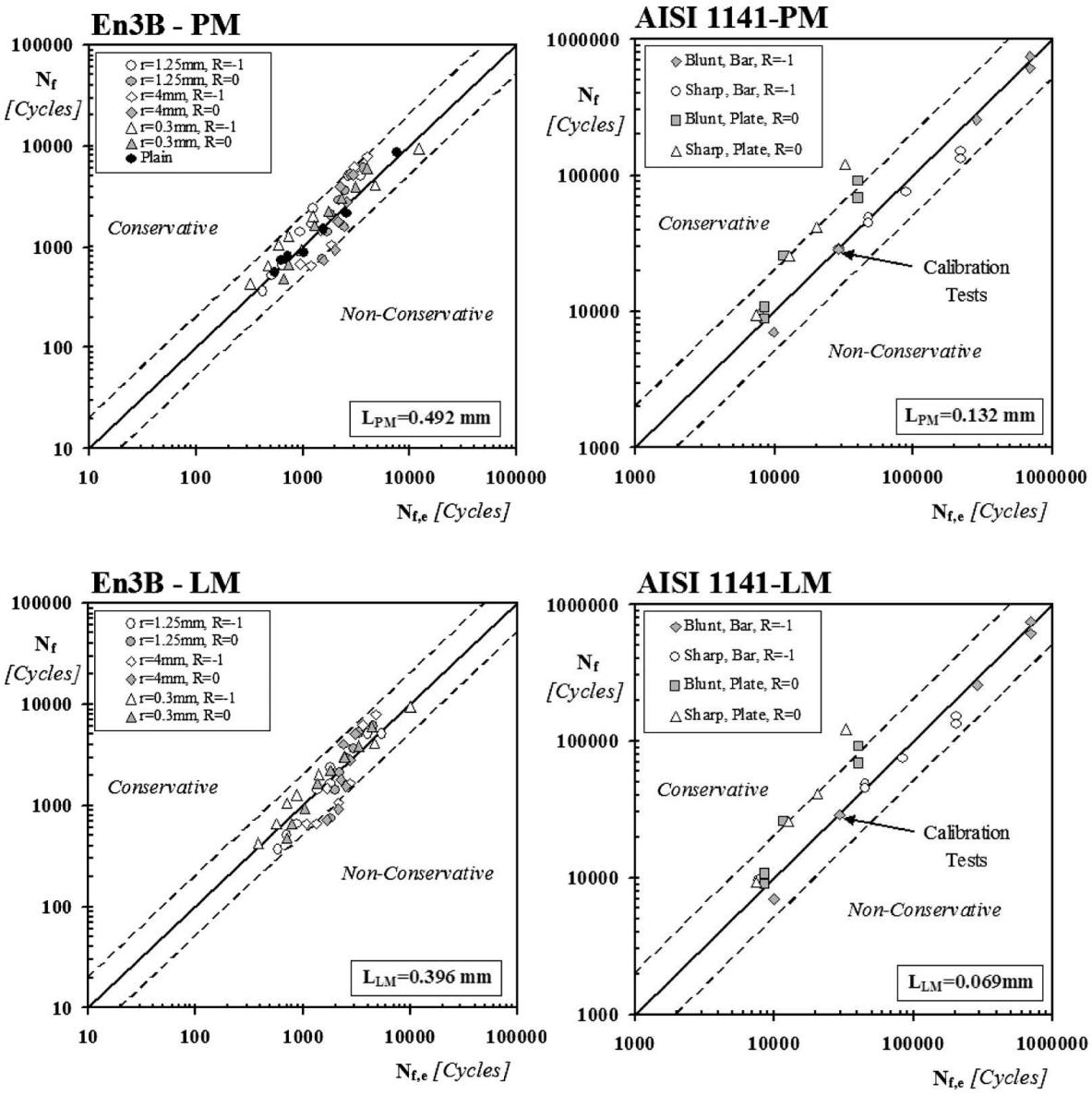

Figure 2-20. Notch fatigue results for En3B aluminum and AISI 1141 low-carbon steel [33].

Mücke and Kiewel [34] performed a study utilizing nonlocal approaches for sharp notch prediction of 1.5CrNiMo rotor steel at room temperature, 300°C and 400°C. Local effects were considered by utilizing life results from uniaxial experiments where the response is spatially uniform. Nonlocal considerations were implemented by considering the strain amplitude gradient responses around the notch. A Coffin-Manson type relationship was used for relating notch life

to smooth life utilizing local strain amplitudes. The coefficients for the Coffin-Manson relationship were found to be directly dependent on strain gradients present near the notch root. A linear trend was found to explicitly capture the Coffin-Manson premultiplier as a function of strain gradients. A quadratic relationship was necessary for relating the exponent to strain gradients. The method developed for the rotor steel was then validated to work on Ni-base superalloy Mar-M247 CC. For Mar-M247 CC the same methodology was applied but life results were improved if presented in terms of stress amplitude rather than strain amplitude.

For the study of localized high temperature plasticity around notched features it is helpful to introduce quantities that decouple ratcheting strains from cyclic plasticity. Abrico and Begley introduce cyclic response parameters that decouple total accumulated inelastic strain over a cycle into two components; cyclic inelastic strain range and ratcheting inelastic strain increment [35].

$$\Delta\varepsilon_{ij}^{rat} = \varepsilon_{ij}^{in}(t_f) - \varepsilon_{ij}^{in}(t_1) \tag{2.4}$$

$$\Delta\varepsilon_{cyc,ij}^{in} = \max_{t_1 \le t \le t_f}\left(\Delta\varepsilon_{ij}^{in}\right) - \Delta\varepsilon_{ij}^{rat} \tag{2.5}$$

The ratcheting inelastic strain increment is the difference in strain at the beginning (t_1) and end of a cycle (t_f). The cyclic inelastic strain range is the largest inelastic strain range over a cycle with the contribution from ratcheting removed.

The critical plane approach is often used in fatigue analysis of components undergoing multiaxial loadings [36-38]. The approach follows two steps: (1) determination of the orientation of a plane within the material within which the driving force for damage accumulation is greatest based on some criterion and (2) correlating the critical damage metric on the critical plane to fatigue life. Moore [39] utilized a multiaxial Neuber-based constitutive model to predict local

notch responses coupled with a critical plane SWT approach to predict LCF lives of notched CM247LC DS components at elevated temperatures.

HCF lives in notched specimens of Ti-6Al-4V were determined using a combination of critical plane parameters and nonlocal methods [40]. A variation of the Findley parameter [41] was utilized to quantify crack initiation,

$$FIN(\theta) = \tau_a + k\sigma_{\max} \tag{2.6}$$

where τ_a is the shear stress amplitude on a critical plane defined by a rotation in the x-y plane of θ, k is a material dependent parameter and $\sigma_{\max}$ is the maximum normal stress on the critical plane. The multiaxiality is taken into account by using a modified Findley parameter in the vicinity of the notch root,

$$FIN = \max_{\theta}\left(\max_{cycle}\left\{FIN1, FIN2\right\}\right) \tag{2.7}$$

$$FIN1 = \tau_a + k\sigma_{x,\max} \qquad FIN2 = \tau_a + k\sigma_{y,\max} \tag{2.8}$$

Where $\sigma_{x,\max}$ and $\sigma_{y,\max}$ are the maximum x-direction and y-direction normal stresses relative to the rotation plane. The modified Findley parameter was then integrated over a line domain at the notch root to determine the average value,

$$G_r(a_c, N) = \frac{1}{a_c}\int_0^{a_c} FIN(x, N)dx \tag{2.9}$$

This line-averaged parameter is a function of the integration upper bound, a_c, and is assumed to be a function of the number of cycles to failure, *N*. The relationship to crack initiation life is made by assuming that crack initiation occurs when the line-averaged Findley parameter is equal to some scalar multiple of the smooth Findley-life function,

$$G_r(a_c, N) = \frac{1}{a_c}\int_0^{a_c} FIN(x, N)dx = G_F \cdot FIN_{smooth}(N) \tag{2.10}$$

This can be seen schematically in Fig. 2-21. G_F is a parameter called the Findley gradient factor. The smooth Findley parameter functional form is known from uniaxial testing on smooth specimens. In this study lives ranged from 10^4 to10^8 cycles and as such a Basquin and Manson-Coffin double power-law expression was used to fit life results across several decades. The constants a_c and G_F are then determined for each notched experiment to match experimentally determined lives.

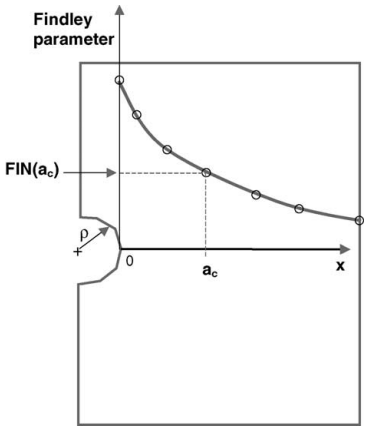

Figure 2-21. Determination of the integration domain utilizing the Findley parameter distribution along the notch root [40].

2.3 Thermomechanical Fatigue

Failure of turbine blades in industrial gas turbines occurs due to the superposition of applied loads and thermal transients across components during operation. Isothermal testing

conditions cannot always capture the complex temperature-load interactions occurring during service of components. Although the loadings experienced by components do have complex and nonlinear temperature-load phasing, experiments are typically simplified to comparable linear waveforms. Example waveforms for out-of-phase (OP) and in-phase (IP) waveforms are shown in Fig. 2-22.

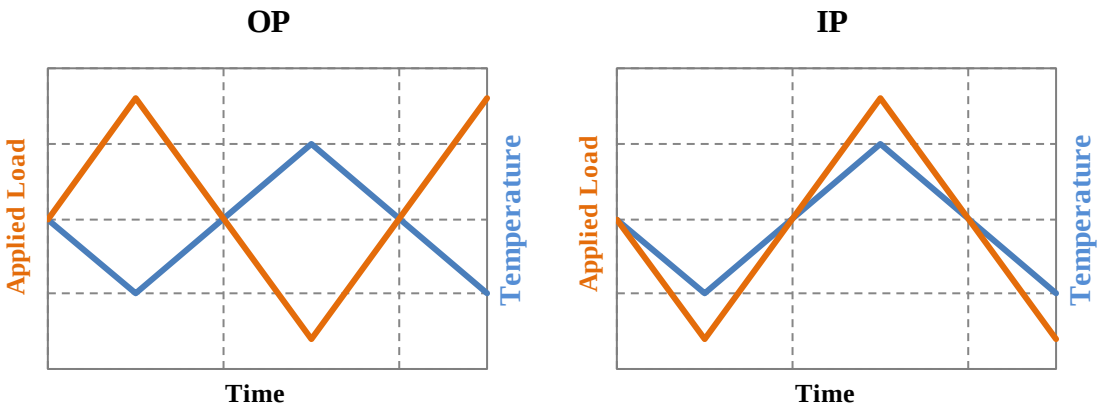

Figure 2-22. Out-of-phase (OP) and In-phase (IP) thermomechanical fatigue waveforms.

Under OP loading the temperature and loading waveforms are 180° out of phase, under IP loading the waveforms are in phase (0°). Another popular variation is the diamond waveform where the phase angle is between 0° and 180°. Loading can refer to applied force, axial strain, diametric strain, displacement, etc.. The prescribed phasing angle has a great deal of influence on crack initiation as the interactions between temperature and mechanical loads dictate the resulting damage mechanisms.

2.4 Thermomechanical Fatigue Damage Mechanisms in Ni-based Superalloys

Ni-base superalloys under high temperature thermomechanical fatigue loadings typically are influenced by three damaging mechanisms; fatigue, environmental interactions and creep [2,

10, 21]. These three damaging mechanisms can also be coupled simultaneously. The influence and interactions between these three mechanisms under TMF loading is dependent on the applied loads, temperatures and load-temperature phasing.

In pure metals the microscopic origin of fatigue damage results from irreversible shear slip accumulation along crystallographic glide planes during cyclic straining. Fatigue damage is typically observed at relatively low metal temperatures at high applied strain rates where inelastic deformation is typically time-independent and the influence of environmental and creep damage is negligible [8].

Environmental interactions occurs at elevated temperatures under conditions where the metal is exposed to a reactive ambient atmosphere [21]. Elevated metal temperatures provide sufficient thermally applied energy such that the metal constituents can undergo oxidation-reduction reactions with environmental species. These interactions result in degrading material close to the surface and development of a brittle oxide layer. In the case of superalloys, there are often ten or more elemental constituents and multiple phases present in the alloy which increase the likelihood of promoting a sustainable reaction and can result in complex oxide formation [42].

Creep damage is a result of time dependent diffusional processes occurring at sufficiently high elevated temperatures and applied stresses [43]. The physical manifestation of creep damage is found in the formation of microvoids. Coalescence of these microvoids can facilitate crack initiation and can enhance small crack propagation.

These fundamental damage mechanisms often interact in a complex fashion during high temperature TMF loadings. The degree of damage contribution from each damage mechanism is

dependent on the applied load, temperature and waveform phasing. The most typical interactions are pure-fatigue, environmental-fatigue and creep-fatigue.

2.4.1 Pure-Fatigue Damage

Under pure-fatigue conditions the effects from environmental interactions and creep damage are negligible. Damage is caused by reversed cyclic straining, which at sufficiently high strains, promotes dislocation slip along glide planes. These shear displacements are irreversible and as such accumulate with cycling. At the material surface these slip bands can be observed as 'roughening' the material surface. Slip bands at the material surface eventually form intrusions and extrusions, which serve as local stress concentrations, increasing the level of inelastic deformation. These intrusions and extrusions of persistent slip bands at the material surface often are locations of crack initiation [5, 8, 10]. In polycrystalline materials slip bands also occur internally but do not result in surface topology flaws unless at the surface. In Ni-base superalloys pure-fatigue only occurs at low homologous temperatures typically less than 500°C ↔ 600°C [5, 21, 24].

Irreversible inelastic deformation along glide planes can be enhanced by the introduction of material inhomogeneities such as pores, carbides and inclusions often found in commercial alloys [8]. Fatigue strength can be significantly decreased due to introduction of these defects. The degree to which fatigue life is decreased is dependent on several factors including slip characteristics of the base material, relative strengths of the two and strength of the material-defect interface.

For pure fatigue the simplest relation for LCF is the Coffin-Manson relation [21],

$$N_i^{fat} = C(\Delta\varepsilon_{in})^d \qquad .(2.11)$$

Other relationships utilizing mechanical strain and mean stress can be utilized if the inelastic strain range is small or difficult to capture. One such functional relationship is the Smith-Watson-Topper (SWT) expression [44],

$$\varepsilon_a \sigma_{\max} = \frac{\sigma_f^{'2}}{E}\left(2N_i^{fat}\right)^{2b} + \sigma_f^{'}\varepsilon_f^{'}\left(2N_i^{fat}\right)^{b+c} \tag{2.12}$$

where $\sigma_f^{'}$, $\varepsilon_f^{'}$, b and c are experimentally determined constants and E is the elastic modulus. Expressions that account for mean stresses may be necessary for Ni-base superalloys as their transition life from LCF to HCF is between $10^4 \leftrightarrow 10^5$ [5].

2.4.2 Environmental-Fatigue Damage

The coupling of environmental degradation and fatigue damage occurs under sufficiently high homologous temperatures (at least between 400°C and 650°C for polycrystalline Ni-based superalloys [24]) and cyclic applied inelastic strain. It has been observed that high temperature LCF crack initiation lives under vacuum benefit greatly when compared to ambient environment conditions [45]. Antolovich et al. [23] found that the effect of stress free pre-exposure of Rene 80 at 982°C prior to LCF testing at room temperature was detrimental towards life. Machining away of the oxide layer restored fatigue strength back to the original as-heat treaded condition, illustrating the detrimental effects of an oxide-layer under environmental-fatigue interactions.

Aside from bulk diffusion, equiaxed and DS alloys can exhibit short circuit diffusion as it is energetically preferred under which diffusion occurs along grain boundaries [22, 46-47]. A study on Rene 80 by Romanoski et al. [19] found that fatigue life was determined by grain boundary decohesion along environmentally degraded grain boundaries. For the same alloy Antolovich et al. [23] found that cracks initiated along environmentally degraded grain

boundaries at the material surface. Micrographs of oxidized MarM-247 and intergranular crack initiation under out-of-phase TMF are shown in Fig. 2-23.

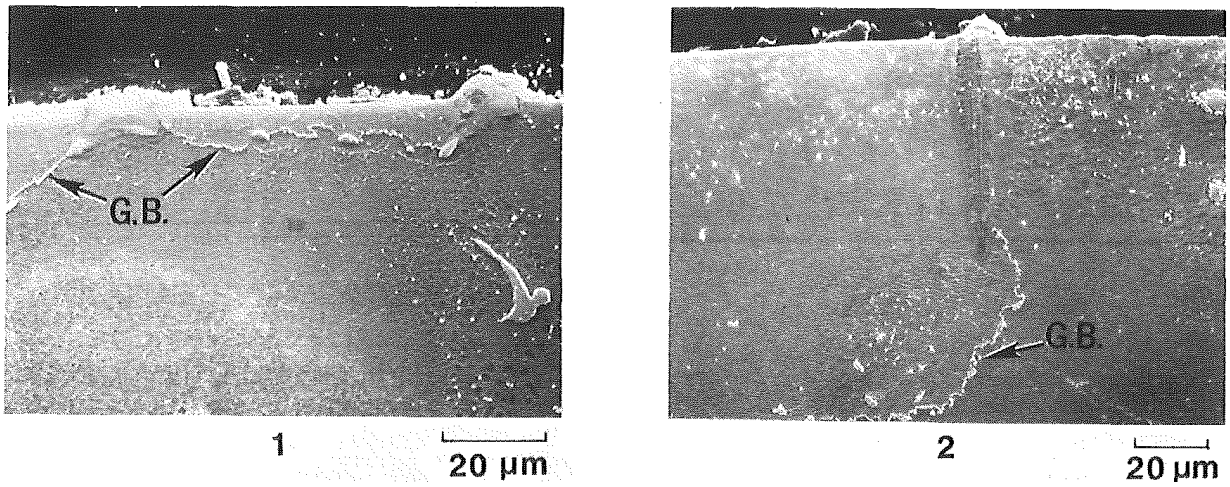

Figure 2-23. Preferred grain boundary oxidation and crack initiation for MarM-247 under 500°C-871°C OP TMF [22].

The effects of process defects (carbides, pores, inclusions) on crack initiation are magnified in the presence of environmental interactions. Remy and Malpertu [4] observed that under TMF loading of polycrystalline IN100 microcracks formed at environmentally degraded MC carbides interfaces in interdentritic areas. In a coupled crystal plasticity-diffusion computational study of a single crystal Ni-base alloy, Zhao et al. [48] found that oxidation effects increase stresses and inelastic strains locally around near-notch meso-scale voids.

Oxidation of the exposed surface material results in the development of separate oxide scales forming on free surfaces. Giggins and Pettit [49] performed a comprehensive parametric study of oxide formation in Ni-Cr-Al alloys by varying elemental contents and exposure temperature. It was observed that after a transient period of oxidation, lasting no longer than one hour, steady-state conditions resulted in formation of continuous oxide layers which grow

according to parabolic kinetics. Schematics of three distinctly formed oxide types are shown in Fig. 2-24: (1) a continuous NiO layer above a subscale of Al_2O_3 or Cr_2O_3 (2) Cr_2O_3 layer with internally oxidized Al_2O_3 particles (3) a continuous layer of Al_2O_3.

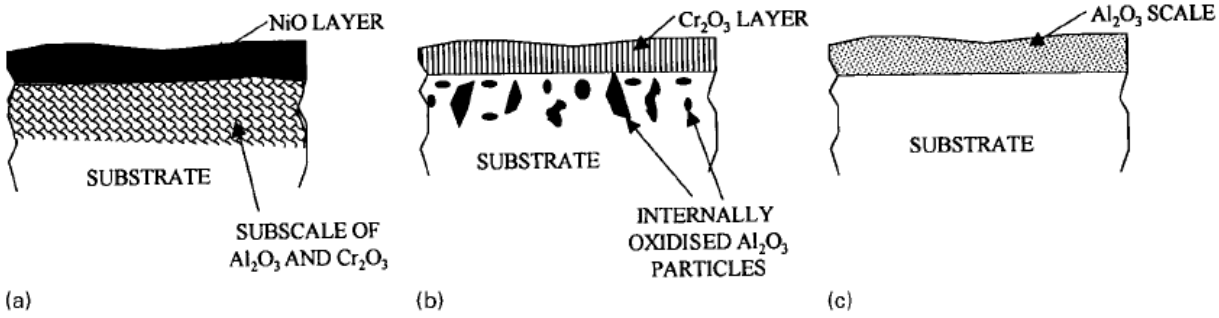

Figure 2-24. Schematic diagram of oxides formed in Ni-Al-Cr ternary alloy [49].

The study found that it is the alloy composition that has greatest effect on determining which particular oxide will form following the initiation transient period; in particular the volume fraction of Cr_2O_3 and Al_2O_3.

A high temperature (1000°C-1200°C) oxidation study of CM247 LC DS by Das et al. [42] found that the transient period for this superalloy was fairly long, up to 20 hours at 1100°C. An exterior scale of spinel ($NiAl_2O$) or a mixture of spinel and NiO was always found to form above a alumina (Al_2O_3) scale. Chromium (III) oxide or alumina oxides are considered to be protective as diffusion of chemical species through these oxides is slower than in the base material, particularly alumina [47, 50-51]. The diffusion of elemental aluminum and chromium from aluminum/chromium rich γ' precipitates to the surface creates a layer of γ' depleted zone where only the gamma matrix is left, see Fig. 2-25. This zone of matrix that lacks precipitate strengthening is a potential source for crack initiation [21-22].

Under applied tensile loads the mismatch in elastic modulus at the oxide-metal interface induces stresses higher than the fracture strength of the oxide scale [52]. Fracture of the oxide scale and subsequent oxidation and fracture of subsurface material results in formation of oxide spikes into the material, as shown in Fig 2-25(a). Under OP TMF conditions there is also a superimposed mismatch in thermal expansion coefficient between the oxide scale and base material which accelerates the spiking mechanism. This brittle fracture can be particularly damaging as it can lead to crack propagation into the substrate. Under compressive loadings oxide scales can buckle or wedge [52-53] as shown in Fig 2-25(b). This is the case under IP TMF where the effect of thermal mismatch accelerates the process.

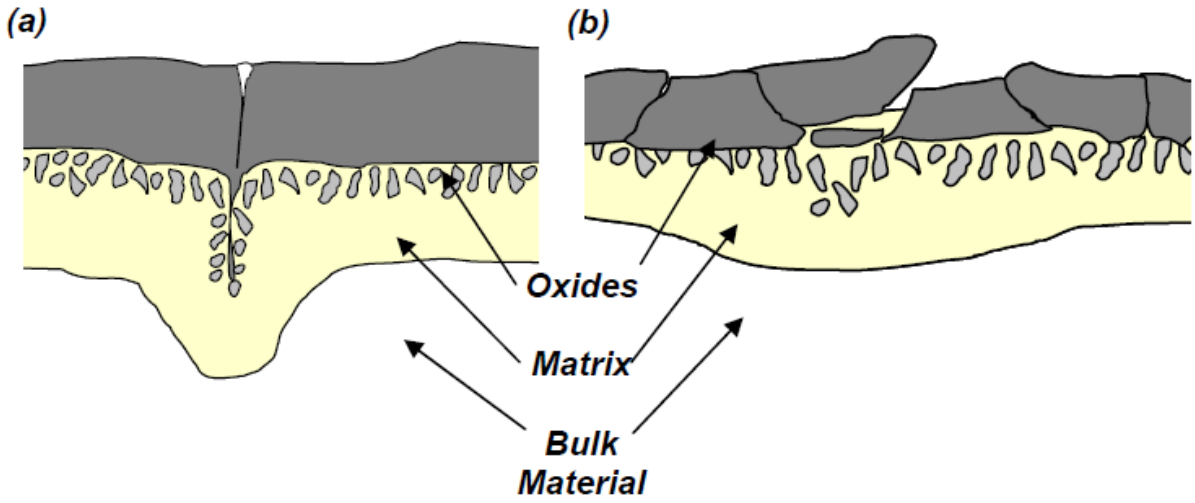

Figure 2-25. Surface oxidation and mechanical interaction illustrating (a) oxide spiking and (b) oxide spallation schematic [2].

Oxide layer rupture can also occur due to applied strains from (1) the applied load (2) thermal expansion mismatch between the oxide and base material (3) volume mismatch (4) strain from geometry effects (5) strain from relative creeping and (6) dilatational strain due to diffusion of oxygen inwards [21]. An oxide spike from a study on TMF of CM247LC DS [54] is shown in Fig. 2-26.

Figure 2-26. Oxide spike formation under 500°C-950°C OP TMF conditions in CM247 LC DS [54].

Although creep deformation does occur in compression in OP TMF loading, damage accumulation under compression is typically negligible as compressive stresses will not contribute to microvoid growth and coalescence [21].

2.4.3 Creep-Fatigue Damage

Diffusion of atoms occurs at sufficiently high temperatures due additional input thermal energy. This input energy can be mitigated by input mechanical work. Ni-base superalloys subjected to high temperatures and applied loads undergo diffusion of elemental species where the rate controlling mechanisms is vacancy diffusion or self-diffusion. This time-dependent diffusion mechanism under cyclic-fatigue loadings introduces creep-fatigue damage interactions [21-22, 55-57]. These interactions include: (1) intergranular void coalescence ahead of a crack (2) magnified crack tip plasticity due to superposition of void plastic zones ahead of a crack tip (3) grain boundary sliding leading to wedge-type crack initiation at grain boundaries and at second-phase particles on grain boundaries (4) flow localization and crack growth along weakened grain boundaries and (5) relaxation of stress/strain fields ahead of crack tips lacking cavities [21]. Grain boundary embrittlement due to creep has been observed to facilitate

intergranular fatigue cracking in IP TMF tests on the superalloy Mar-M247 [21] as seen in Fig. 2-27.

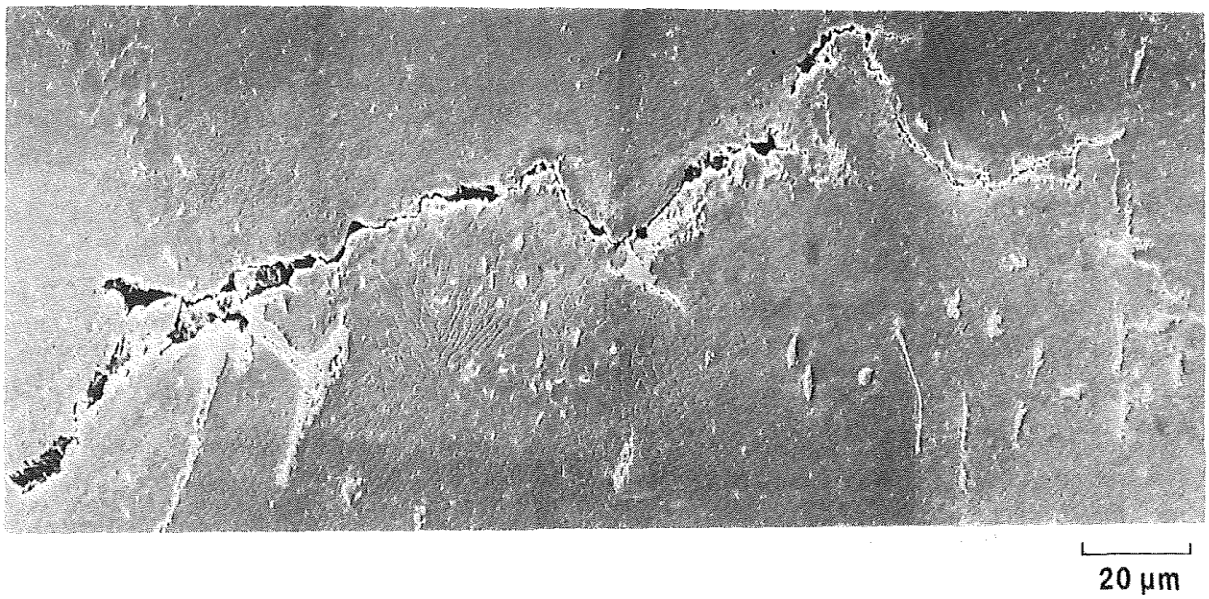

Figure 2-27. Intergranular crack growth from creep-fatigue interactions in Mar-M247 IP TMF $500°C \leftrightarrow 871°C$ [21].

Mazur et al. found evidence of microvoids around cooling holds of an in-service turbine blade made of IN738LC [1]. Small creep voids were found along intergranular facets at the crack tip indicative of a creep-fatigue interaction mechanism. Internal crack initiation in a smooth CM247 LC DS specimen under IP TMF is shown in Fig. 2-28(a). Microvoid coalescence and growth in a notched specimen under the same conditions is shown in 2-28(b).

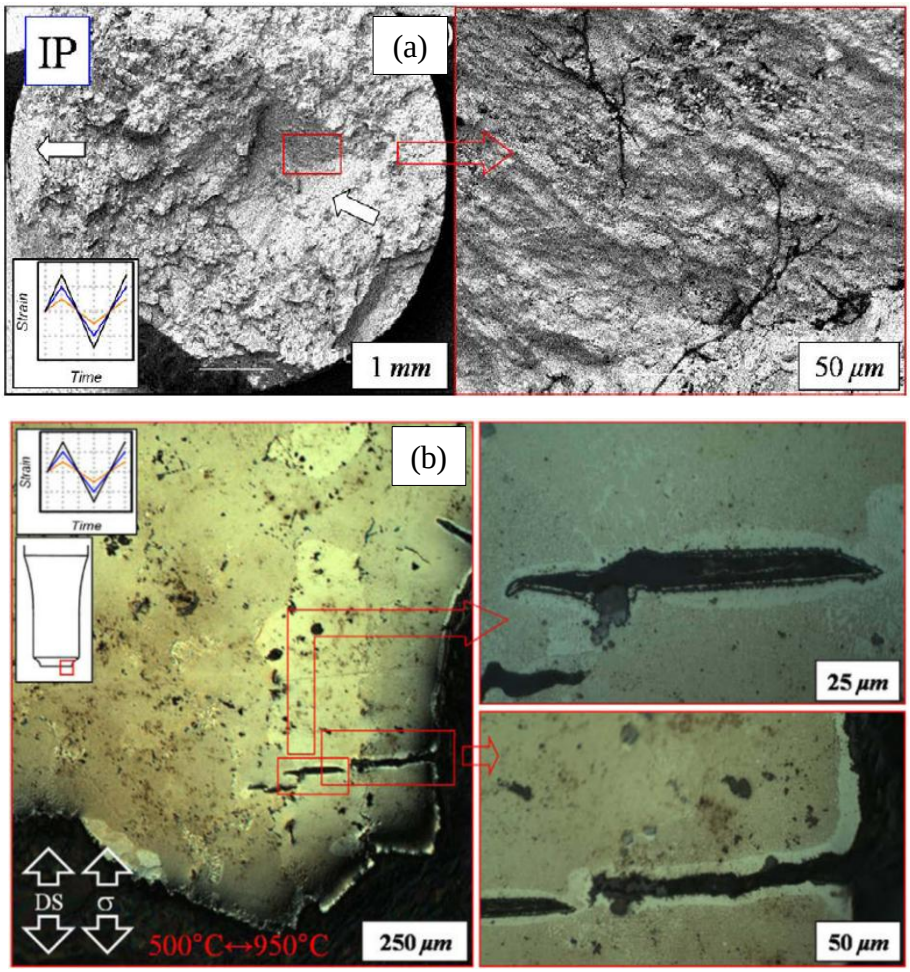

Figure 2-28. IP TMF 500°C↔950°C (a) Internal crack initiation from microvoids in a smooth specimen (b) Microvoid coalescence and growth contributing to crack initiation in a notch specimen [54].

2.5 Thermomechanical Fatigue of Notched Components

Kupkovits and Neu [54] performed a study on the TMF of notched components of CM247LC DS. Specimen geometries corresponding to theoretical elastic stress concentration factors of $k_t = 2.0$ and $k_t = 3.0$ where used. Under $500°C \leftrightarrow 950°C$ OP TMF conditions, specimens loaded in the longitudinal (L) orientation were observed to follow the same crack initiation life trend as shown in Fig 2-29. The same observation was made for $500°C \leftrightarrow 750°C$ OP TMF.

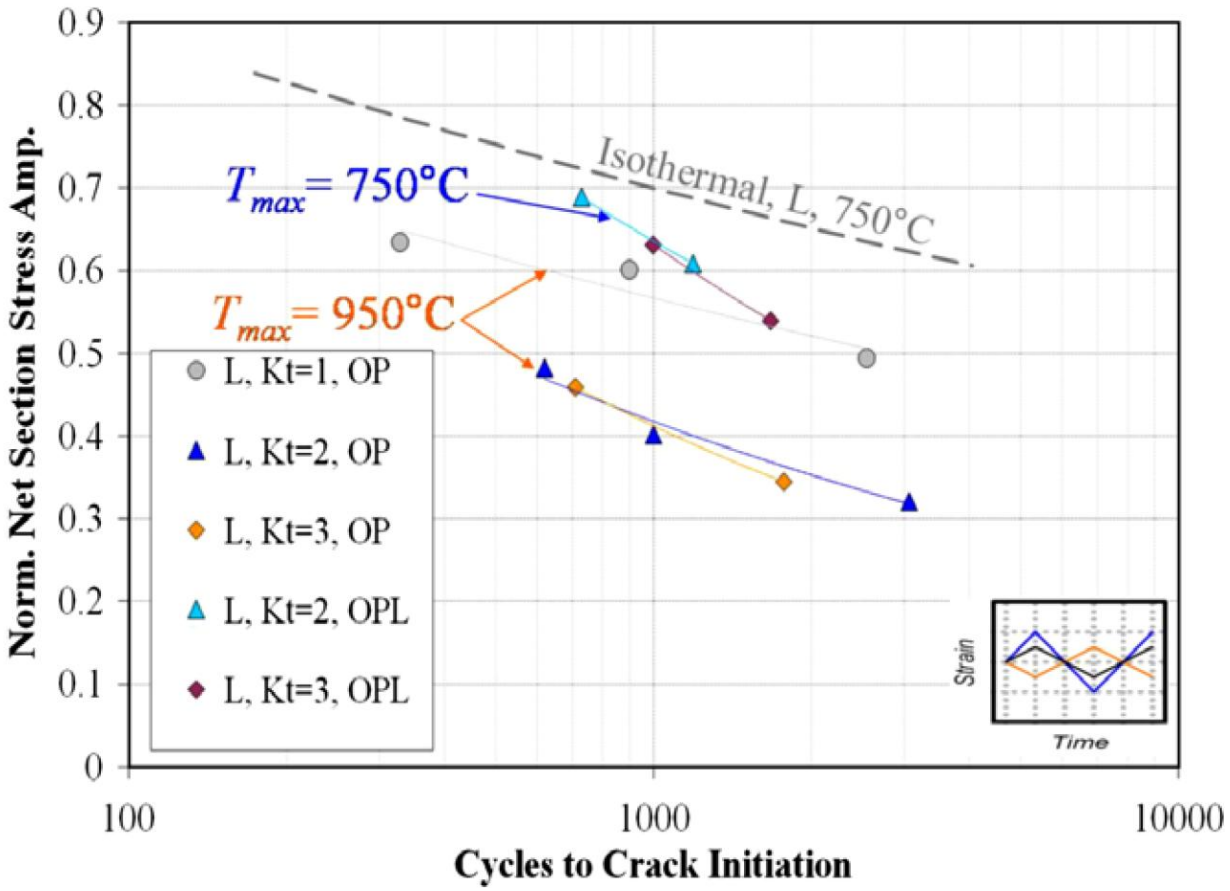

Figure 2-29. Stress based life results for CM247LC DS under OP TMF $500°C \leftrightarrow 950°C$ and $500°C \leftrightarrow 750°C$ [54].

The fatigue notch factor for transversely loaded specimens was less severe relative to longitudinally loaded specimens. This was due to additional material inhomogeneities introduced by grain boundaries which contribute non-negligibly to the crack initiation mechanism and were not present for longitudinally oriented specimens.

Fatigue-environmental damage mechanisms were observed in both notched and smooth OP TMF $500°C \leftrightarrow 950°C$ tests. Under IP TMF $500°C \leftrightarrow 950°C$ creep-fatigue damage mechanisms were observed in both smooth and notched components. All notched specimen

experiments resulted in crack initiation in the location of maximum Hills' or Von Mises equivalent stress as shown in Fig. 2-30.

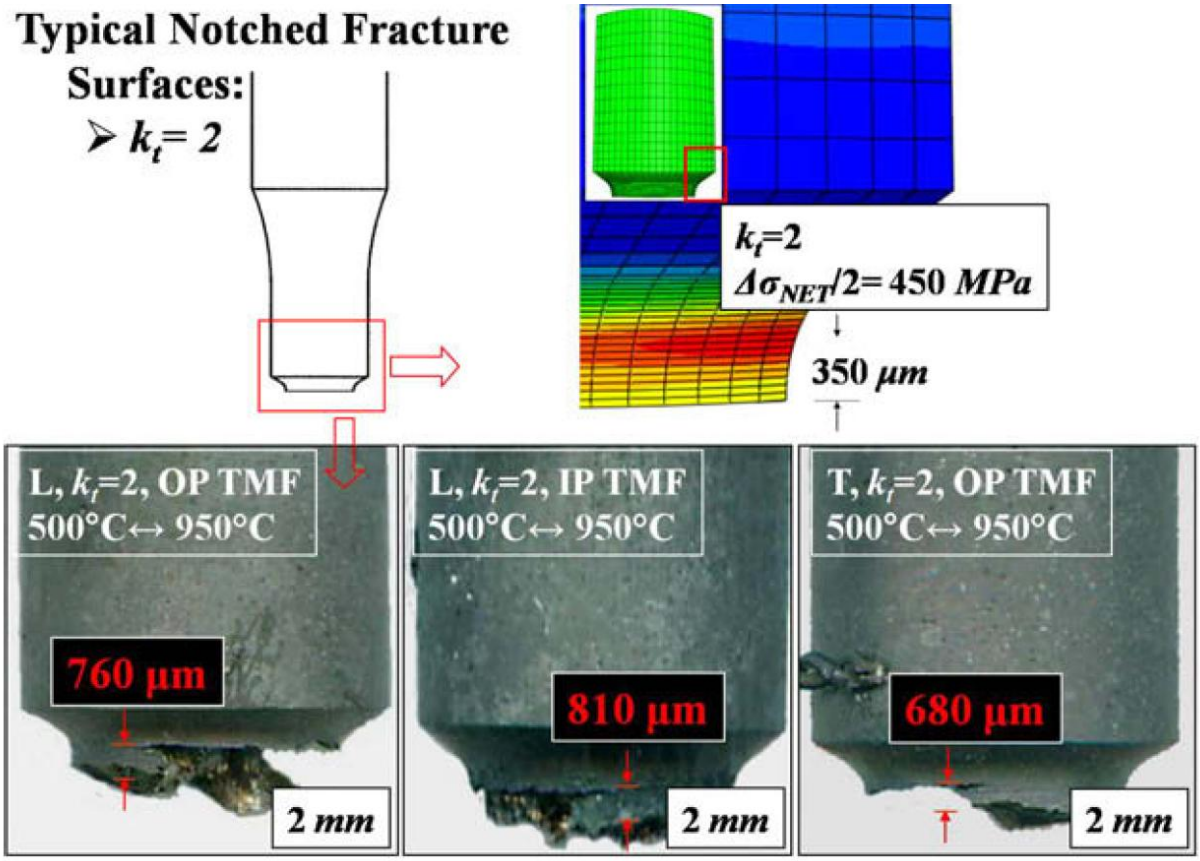

Figure 2-30. Crack initiation location in $k_t = 2.0$ notched specimens under $500°C \leftrightarrow 950°C$ IP and OP TMF loadings. The location of maximum Von Mises stress captures initiation location well.

Mazza et al. [3] performed both LCF and TMF experiments on 1CrMoV circumferentially notch round bar specimens. TMF cycles did not follow OP or IP phasing, but rather service-life TMF cycles were utilized ranging in temperature from 300°C to 565°C, see Fig. 2-31.

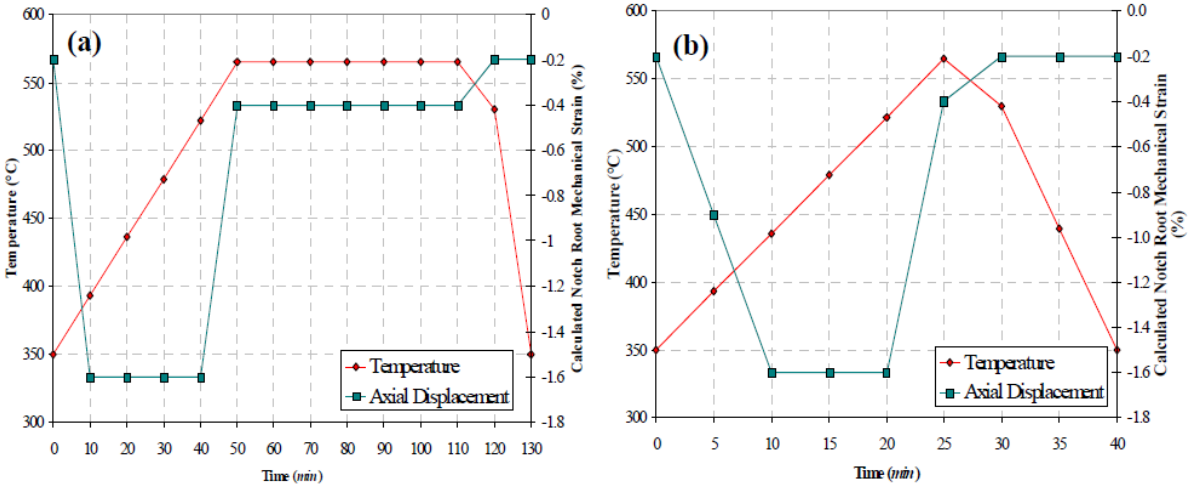

Figure 2-31. Service like TMF cycles (a) with 1 *hr* holds and (b) continuous cycling [3].

Remote boundary conditions were applied so that service like TMF conditions resulted at the notch root. This was done by performing finite element analysis with a calibrated constitutive model and determining the relationship between the local notch response and remote boundary conditions. A PD voltage drop method was used to measure crack initiation at a very small scale. Continuously cycled notched TMF crack initiation lives correlated well with both uniaxial TMF results and LCF results with 1 *hr* superimposed holds. Lives were comparable as conditions in the notch root were prescribed to match analogous un-notched experiments and initiation could be measured very accurately (0.1 *mm*). Notched LCF lives best matched LCF and TMF lives with no holds. Life results are shown in Fig. 2-32.

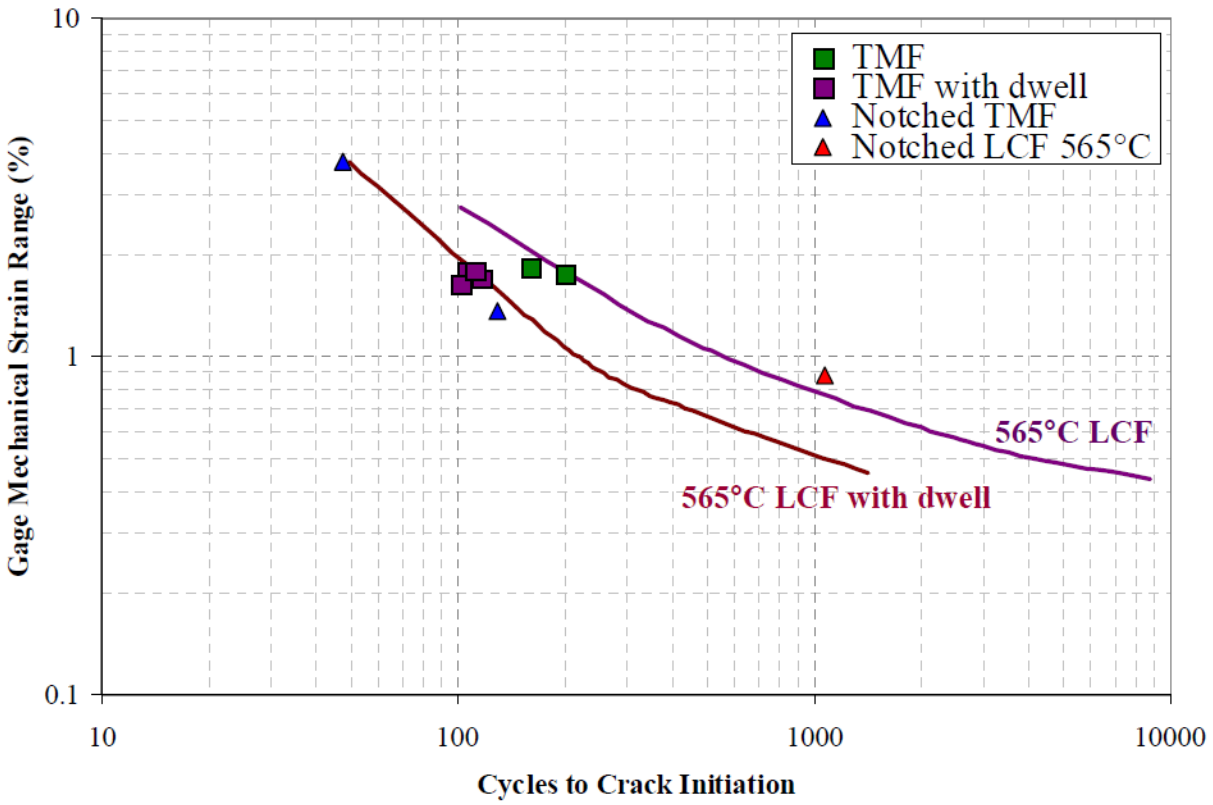

Figure 2-32. Crack initiation lives for notched and smooth 1CrMoV rotor steel under applied LCF and TMF conditions [3].

Microscopy found that cracks initiated in notched specimens were fully circumferential unlike smooth specimens. Additionally it was observed from potential drop methods that crack growth in notches were much slower than analogous smooth specimen experiments. This was attributed to the highly localized response around the notch root. Stress gradients quickly decreased below uniform values in the analogous smooth specimens. Hence the driving force for creep damage and fatigue crack growth was significantly smaller away from the notch root in notched specimens than in corresponding smooth specimens. For identical crack initiation criteria, this effect could potentially increase the measured endurance as the slower crack growth rate in notched specimens may influence detection.

2.6 Influence of Boundary Conditions on Fatigue Crack Initiation

In a study on the effects of control mode on isothermally loaded metal matrix composites, Lerch and Halford found that under fully-reversed conditions fatigue lives as a function of applied stress were insensitive to the applied control mode [58]. Three control modes were utilized; force, strain and a hybrid strain control model. The hybrid mode maintains the prescribed minimum strain but adjusts the maximum strain so as to not surpass a prescribed maximum force. The authors conclude that the fatigue lives insensitivity to control mode was due to similar material responses between the two testing conditions; there was little load drop or strain ratcheting observed during testing. In a study on a titanium matrix composites Sanders and Mall [59] made also found that fatigue lives as a function of applied strain range were insensitive to the applied control mode. They attributed the results to maintaining the same damage and deformation mechanisms across the two control modes.

TMF crack initiation in circumferentially notched 1CrMoV specimens were found to correlate well with uniaxial fatigue lives because the response locally in the notch root were prescribed to match conditions from separate uniaxial experiments [3]. Also the PD voltage drop method was capable of detecting initiation fairly early (0.1 *mm*).

Sonsino [60] performed a study on ferritic-pearlitical fine grained steel FeE under combined axial-torsion loading to simulate the multiaxiality experienced in notched components. For notched components below the structural or global yield point, only displacement controlled smooth life results can be used. Force or torque conditions applied on un-notched specimens resulted in unconstrained ratcheting which is only present in notched components subjected to global yielding.

CHAPTER 3 MATERIAL MICROSTRUCTURE AND MECHANICAL BEHAVIOR

This section provides an overview of the microstructure, composition, mechanical properties and manufacturing of IN100 and CM247LC DS used in this study. The metallography procedure is presented followed by microstructural material characterization of the virgin material. Mechanical properties relevant to high temperature damage and deformation in both alloys are presented for a better understanding of TMF. Together this information will be utilized to understand the fatigue response and failure of notched components.

3.1 Materials

Material was received from the sponsors in the form of ten powder metallurgy IN100 semi-cylindrical billets and two slabs of longitudinally cast CM247LC DS. The composition of these alloys are given in Table 3-1 and Table 3-3. A subsolvus heat treatment was applied to the IN100 by the sponsor to yield a microstructure representative of a turbine disk microstructure. A proprietary heat treatment was applied by the sponsor on CM247LC DS to produce a microstructure representative of an in-service blade material. Both a light optical microscope (LOM) and scanning electron microscope (SEM) were used for imaging.

3.2 Material Characterization

3.2.1 PM IN100

The material had a microstructure similar to that shown in Figure 3-1, which identifies the key features of the microstructure. Average grain size was 5 μm. Primary γ' precipitates were 1 μm in diameter and only present along the grain boundaries. The

strengthening precipitates are the secondary γ' which are present within the grains and are of 100 *nm* average diameter. Tertiary γ' precipitates could not be resolved in the SEM.

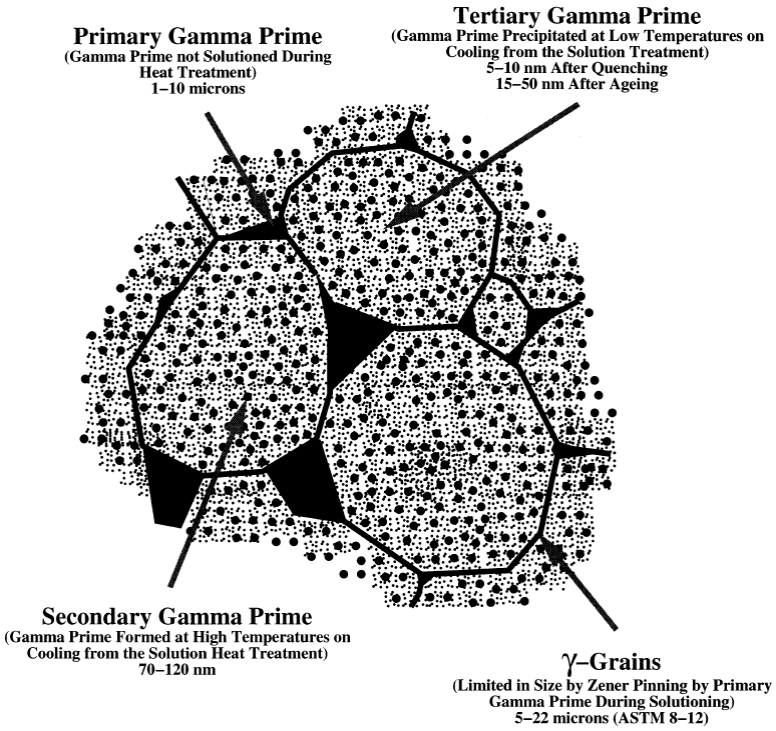

Figure 3-1. Microstructure of UDIMET 720Li, a turbine disk alloy [61].

As-received IN100 microstructure images are shown in Figure 3-2.

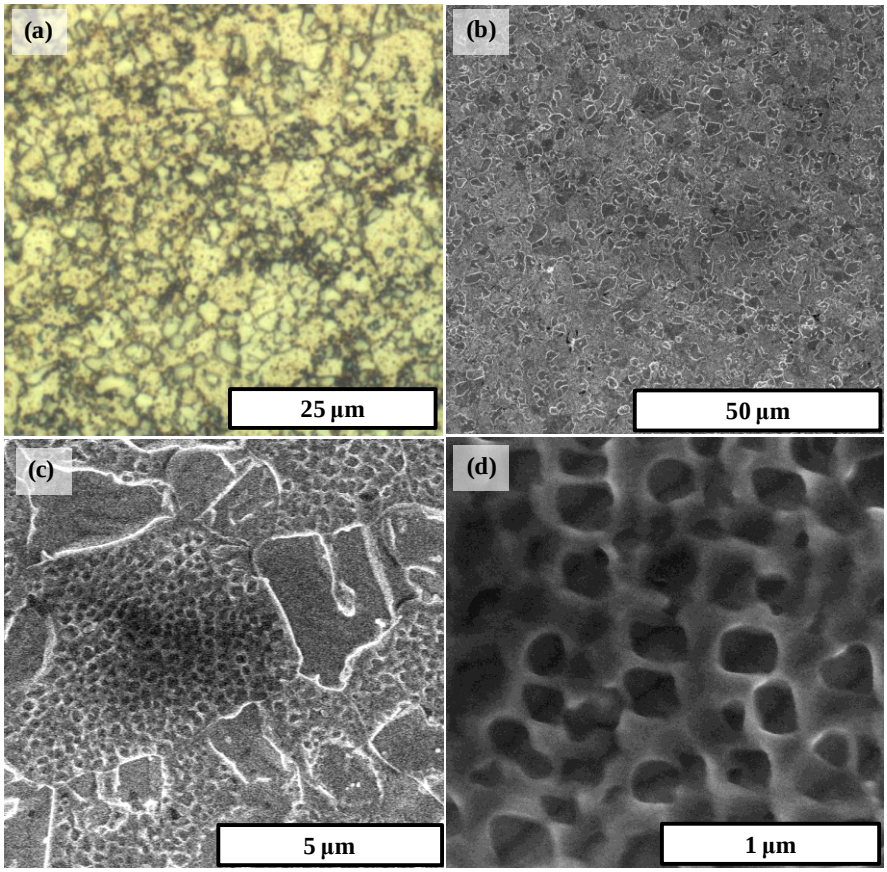

Figure 3-2. Microstructure of PM IN100. (a) Optical light microscope image showing grain size and distribution (b) SEM image showing γ'distribution (c) SEM image showing grains, primary $\gamma'$and secondary γ' (d) SEM image showing secondary γ'.

Table 3-1: Nominal IN100 composition by wt.% [5]

Ni	Cr	Co	Mo	Al	Ti	C	B	Zr
Bal	10.0	15.0	3.0	5.5	4.7	0.180	0.014	0.060

The volume fractions of γ' determined by digital image analysis is given in Table 3-2. Thirteen images were taken and analyzed using Image-Pro Plus v5.1.1.38 to produce a sufficiently large sample of data. An example image is shown in Figure 3-3 and the statistical results generated from analyzing a sample of 19 images is presented in Table 3-2.

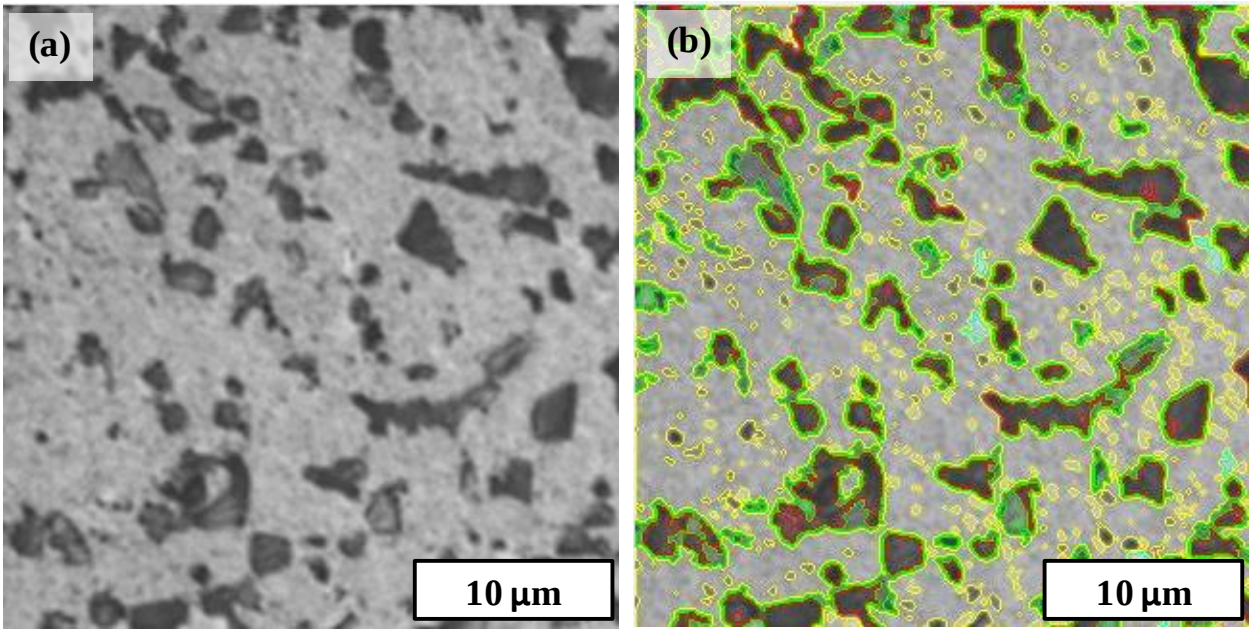

Figure 3-3. Optical microscope micrographs of IN100 (a) Digitally unprocessed micrograph (b) Digitally processed micrograph assigning green and red shades to the γ' phase, the remainder being the γ matrix.

Table 3-2: Volume fraction γ' statistical results

Statistical Distribution					
	N	Mean	Max	Min	Standard Deviation
γ	19	66.2	75.5	51.5	5.6
γ'	19	33.8	48.5	24.5	5.6

3.2.2 CM247LC DS

Images of the virgin samples in the longitudinal direction are shown in Figure 3-4. The as-received material had longitudinal oriented columnar grains with grain diameter varying from 200 *µm* to 1 *mm* with an average grain diameter of 0.5 *mm*. Images of the precipitates are shown in Figure 3-5. Cuboidal γ' precipitates are the primary strengthening precipitates and have an average side length of 500 *nm* with an average volume fraction within the microstructure of 60%.

Secondary γ' precipitates are present in γ matrix and have an average diameter of 75 *nm*.

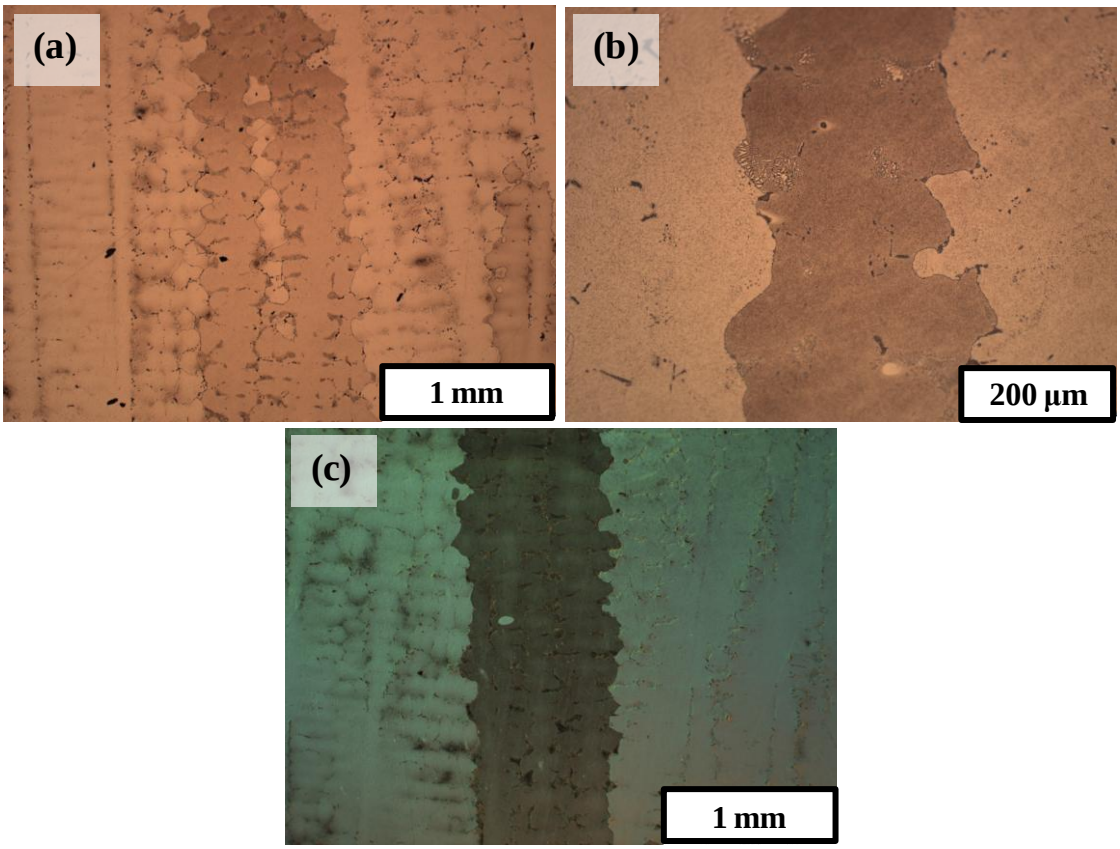

Figure 3-4. Light optical microscope images of polished and etched (Kalling's #2) CM247LC DS. (a) and (b) images using a polarizing filter to identify grains and (c) using dark field lighting.

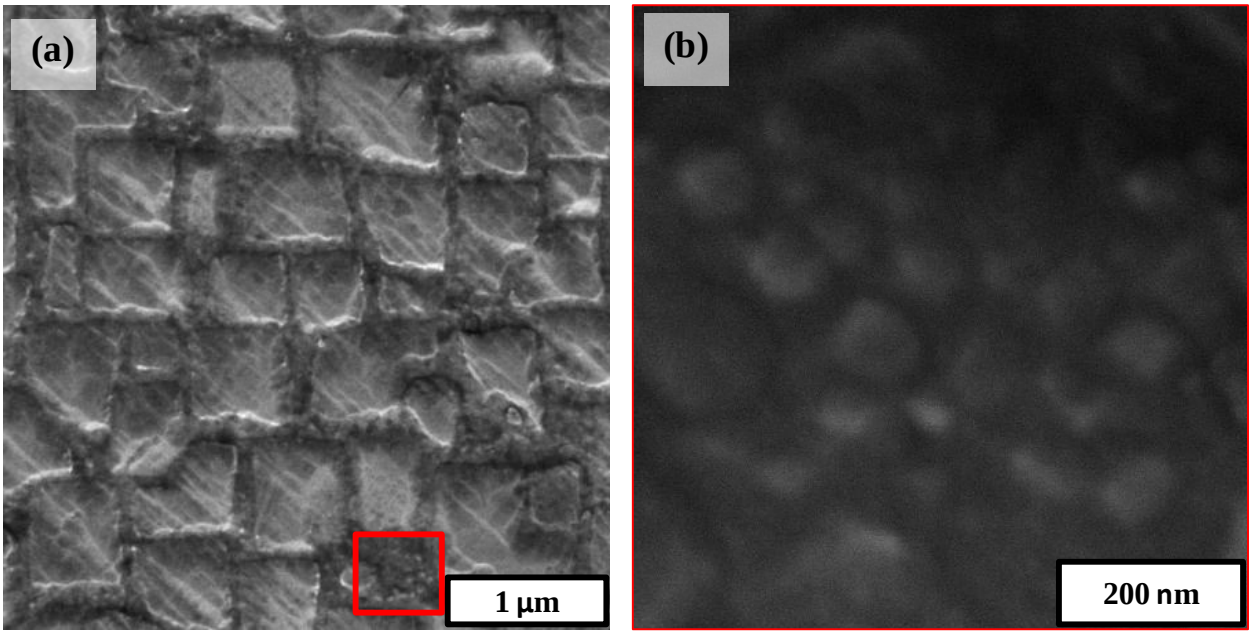

Figure 3-5. SEM images of CM247LC DS microstructure (a) cuboidal primary γ' structure (b) secondary γ' particulates.

Nominal alloy composition for CM247LC and the parent alloy Mar-M247 are shown in Table 3-3 [5]. Directional solidification of Mar-M247 resulted in a great deal of grain boundary cracking during casting due to a lack of ductility. CM247LC DS was developed as a response to the cracking. A study of alloy composition and its effects on cracking during casting showed that a reduction in C decreased carbide formation during casting and significantly decreased grain boundary cracking [14].

Table 3-3: Nominal CM247LC DS composition by wt.% [5]

	Ni	Cr	Co	Mo	W	Al	Ti	Ta	Hf	C	B	Zr
CM247LC	Bal.	8.0	9.3	0.5	9.5	5.6	0.7	3.2	1.4	0.07	0.015	0.01
MarM247	Bal.	8.0	10.0	0.6	10.0	5.5	1.0	3.0	1.5	0.15	0.015	0.03

Images of the dendrite structure are shown in Figure 3-6. Dendritic structures form within columnar grains during the solidification process. The primary dendrite stems grow parallel to the [001] solidification direction. Secondary branches grow in the c and [010] directions. The dendrite structures serve as a fracture toughening feature that hinder crack propagation or prevent crack coalescence [43].

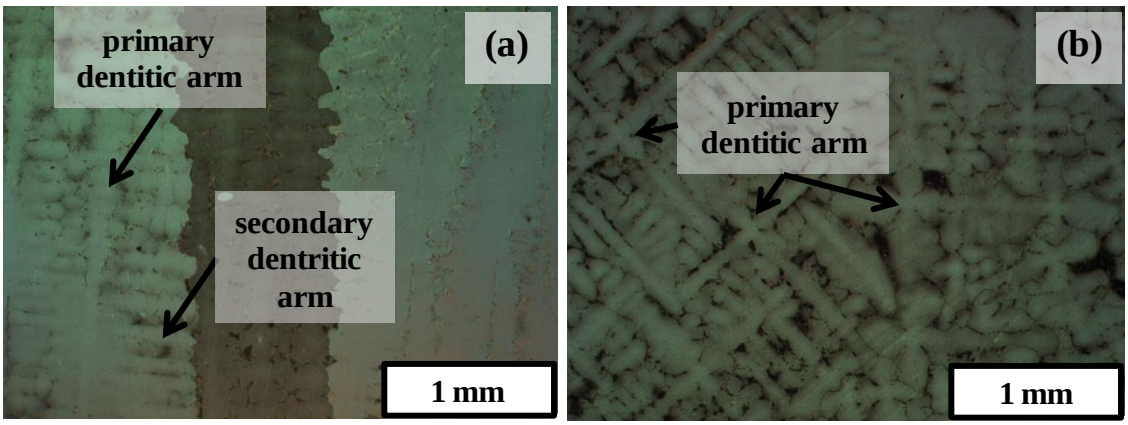

Figure 3-6. Optical images of dendritic structure (a) in a longitudinal section and (b) transverse section.

Figure 3-7 shows carbides forming along the grain boundary in CM247LC DS. During alloying C can react with reactive alloying elements such as Ti, Ta and Hf to form MC carbides. During solidification and subsequent heat treatments the MC carbides can decompose into $M_{23}C_6$ or M_6C species. Boron has the tendency to combine with elements such as Cr or Mo to form borides which also prefer to form along γ-grain boundary interfaces [5]. The relative content of these species can affect fatigue properties as they are susceptible to oxidation along interdentritic boundaries and were shown to be a source of crack nucleation under both LCF and TMF loadings [4]. Additionally carbides and borides are very stiff, nearly rigid compared to the ductile matrix, and act as local stress concentrators within the material.

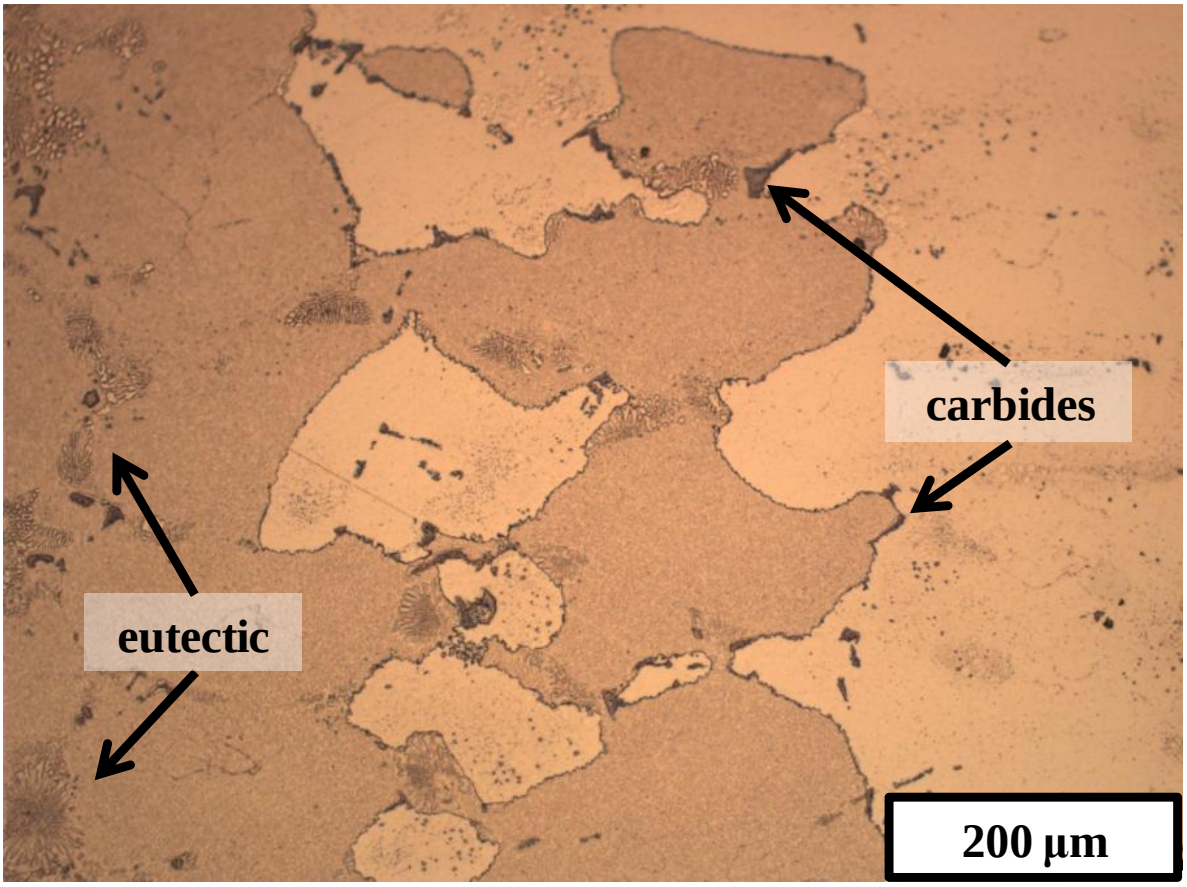

Figure 3-7. Eutectic pools and MC carbides along grain boundaries.

Figure 3-7 also shows eutectic nodules of $\gamma - \gamma'$ which commonly form at grain boundaries and interdentritic regions. The eutectics form due to the casting process and are the last constituents to solidify [62]. Similar to the carbides and borides, eutectic nodules act as local stress concentrators when the material is under load [2].

3.3 Mechanical Properties

3.3.1. IN100

The length scale associated with test specimens (10 *mm*) is significantly larger than fine equiaxed grains that are randomly oriented. As such the IN100 is assumed to be sufficiently

homogenized based on representative volume element (RVE) theory and exhibits a isotropic material response.

Temperature dependence of the elastic modulus, yield strength and coefficient of thermal expansion are given in Table 3-4. Modulus and yield strength are plotted in Fig. 3-8. Modulus was determined from the linear-elastic material response using a linear least squares fit. Yield strength was calculated using a tight 0.02% offset method. Each point represents a different specimen.

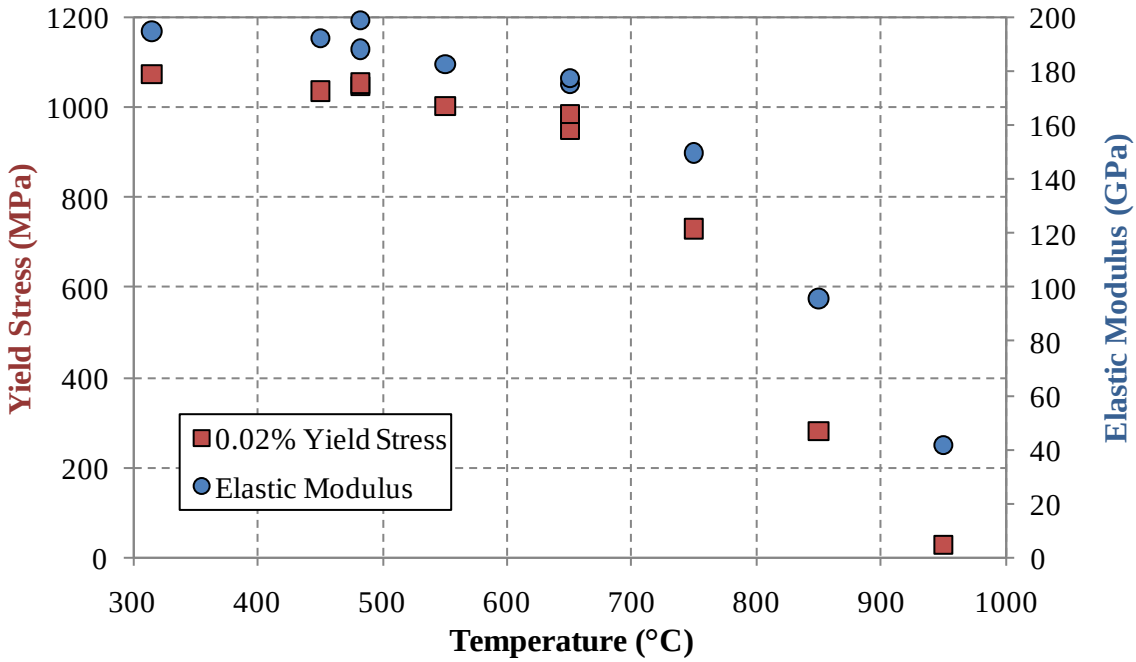

Figure 3-8. Elastic modulus and yield stress versus temperature for IN100.

Table 3-4: IN100 monotonic test conditions and results

Monotonic Mechanical Testing Results				
T (°C)	Strain Rate (s^{-1})	Elastic Modulus (GPa)	Yield Stress (MPa)	CTE α ($°C^{-1}$)
315	2.50E-05	195.1	1075.6	1.41E-05
450	2.44E-04	192.6	1037.1	1.54E-05
482	2.50E-05	188.3	1048.0	1.49E-05
482	2.50E-03	198.9	1054.9	1.42E-05
550	2.67E-04	182.7	1002.8	1.51E-05
650	2.50E-05	175.2	951.5	1.49E-05
650	2.67E-04	177.4	985.0	1.51E-05
750	2.22E-04	149.9	730.3	1.53E-05
850	1.67E-04	95.9	281.1	1.59E-05
950	1.11E-04	41.4	28.3	1.62E-05

The coefficient of thermal expansion is shown in Fig. 3-9. The relationship between thermal strain and temperature is given using a secant relationship,

$$\varepsilon_\theta = \alpha\left(T - T_{ref}\right) \tag{3.1}$$

where ε_θ is this thermal strain, α the secant coefficient of thermal expansion, T the temperature and T_{ref} a reference temperature. The reference temperature was room temperature (20°C) for all tests. The thermal strain was recorded at each temperature after sufficient stabilization and maintaining zero force.

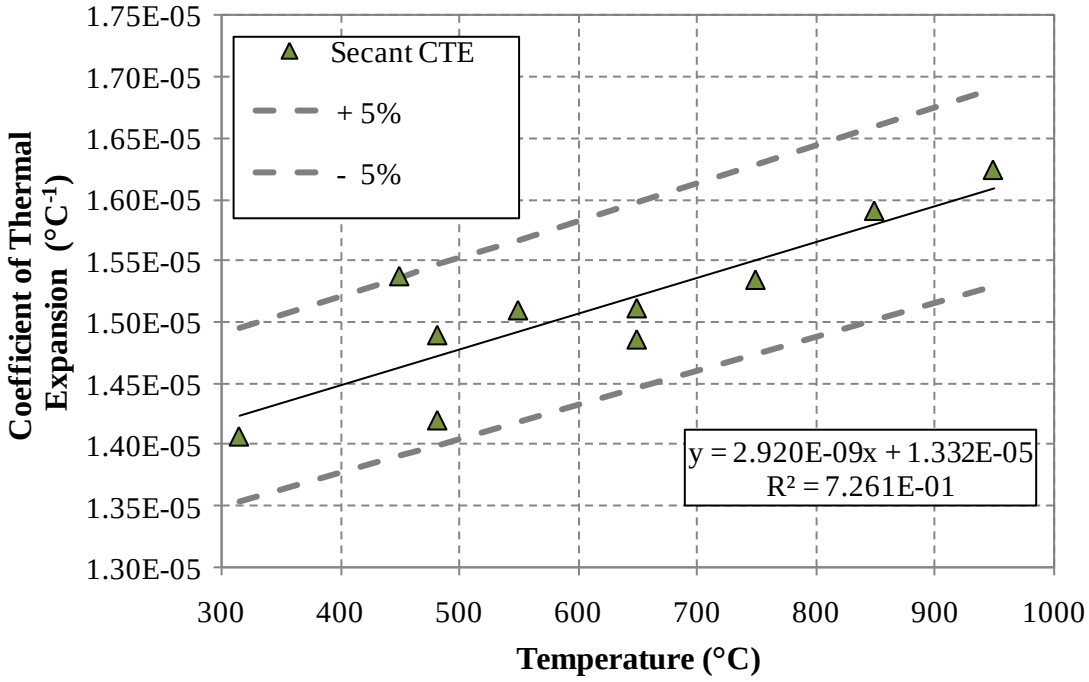

Figure 3-9. Secant coefficient of thermal expansion in IN100 with $T_{ref} = 20°C$.

Isothermal experiments were performed with imposed strain holds at 450°C, 550°C, 650°C, 750°C and 850°C. Strain holds occurred at both peak tensile and compressive strains, detailed experimental conditions are in Table 3-5.

Table 3-5: IN100 experimental stress relaxation conditions

T (°C)	Strain Hold (%)	Hold Time (s)
450	1.10	165.0
	-1.10	165.0
550	1.20	180.0
	-1.20	180.0
650	1.20	180.0
	-1.20	180.0
750	-1.00	180.0
850	-0.75	180.0

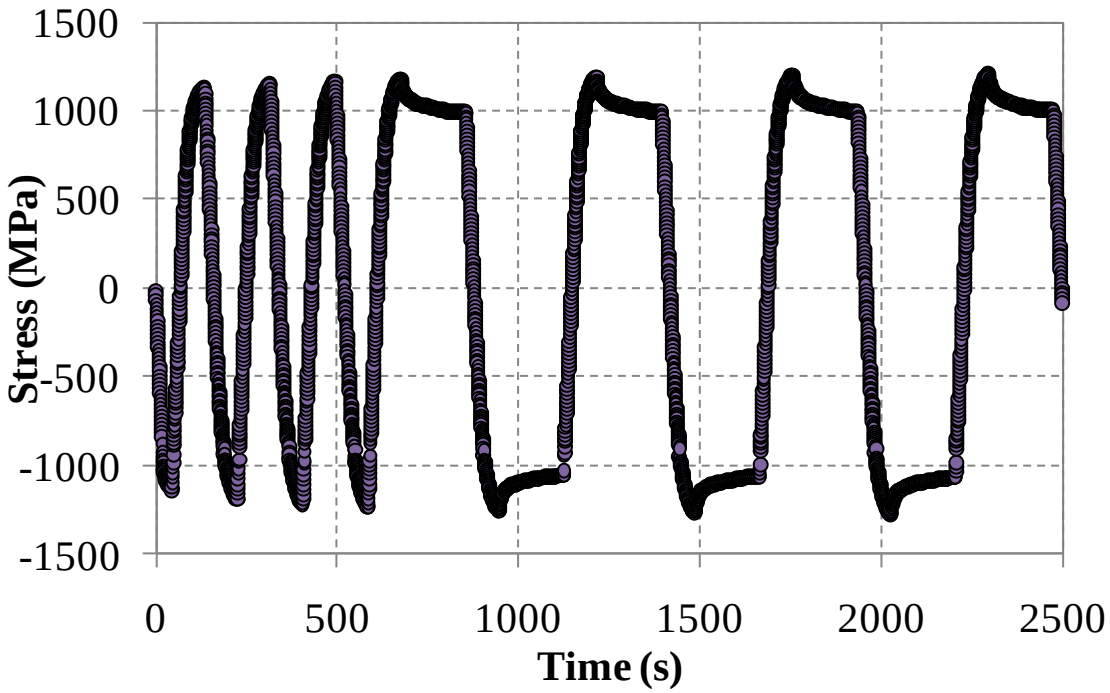

Figure 3-10. Stress response for $R = -1,\ \Delta\varepsilon^{tot} = 2.4\%$ at 750°C with 180s strain holds at $\pm 1.2\%$.

Relaxation results at 450°C, 550°C, 650°C, 750°C and 850°C are shown for compressively applied strain holds over 165 *s* in Fig. 3-11. Stresses are normalized with respect to the initial stress so that the temperature dependency of relaxation can be seen.

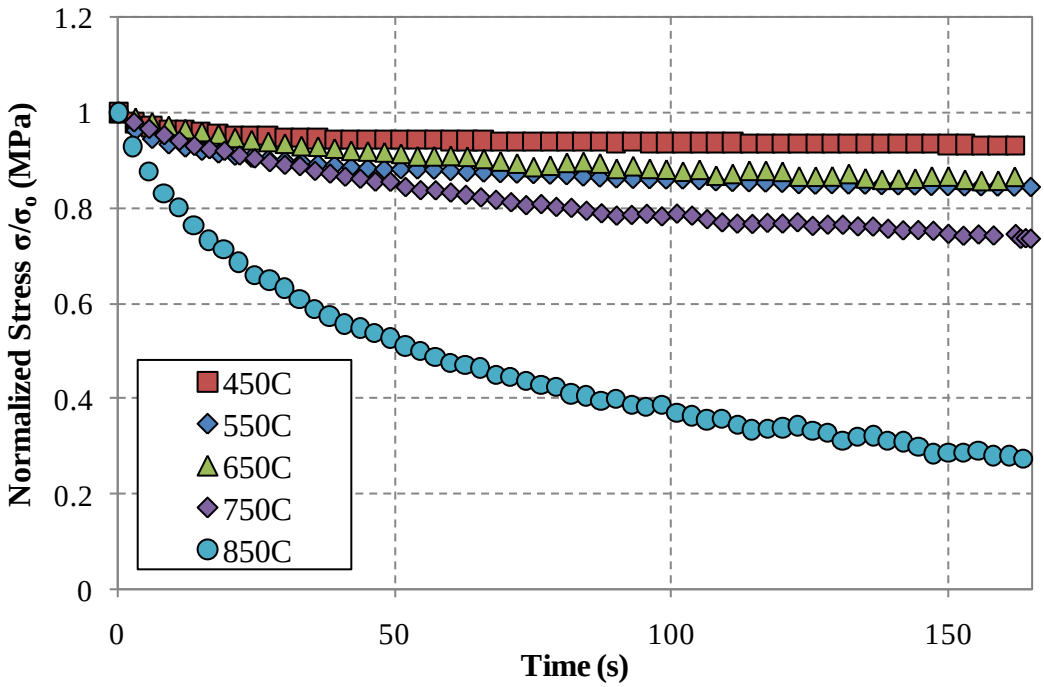

Figure 3-11. Tensile stress relaxation curves. Curves are normalized by the respective initial stress.

Even at relatively low temperature (450°C) relaxation is non negligible. There is a substantial increase in stress relaxation at 850°C.

CHAPTER 4 THERMOMECHANICAL FATIGUE – EXPERIMENTAL METHODS

4.1 Specimen Preparation

Raw materials were provided by the industry sponsors in cast slabs and powder metallurgy (PM) billets, see Fig 4-1 and Fig. 4-2. CM247LC-DS was provided as two heat treated slabs from which individual notched specimens were produced. Ten PM IN100 semi-cylindrical billets were provided in subsolvus heat treated form from which smooth and notched specimens were produced.

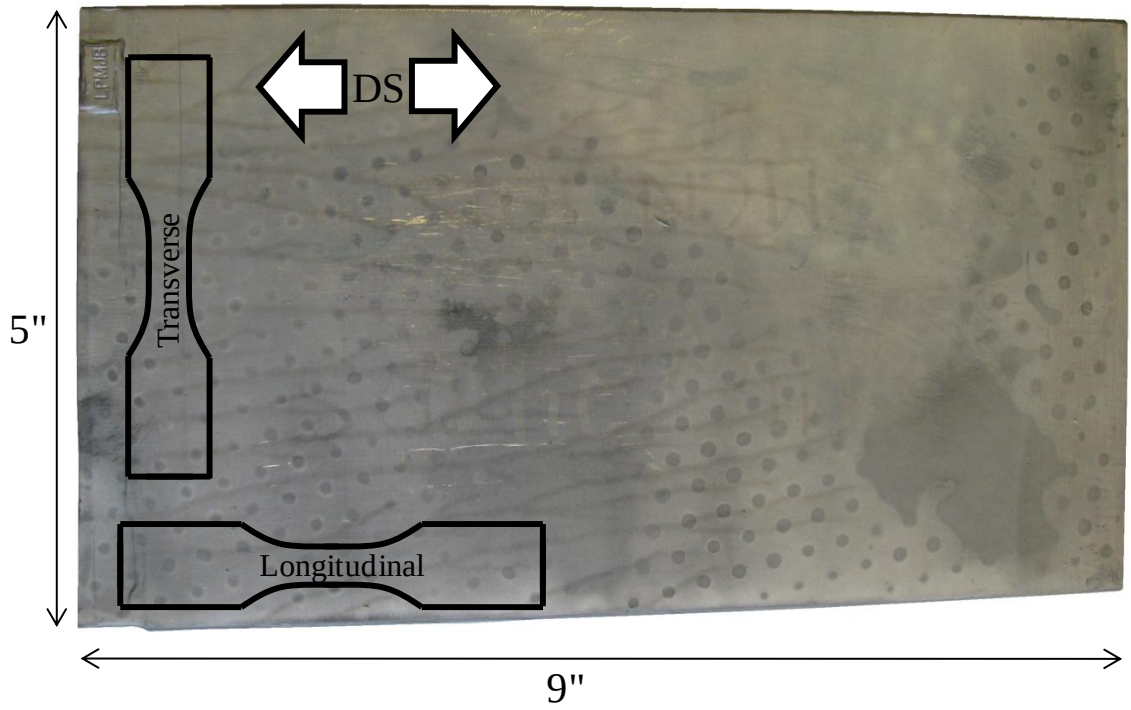

Figure 4-1. CM247LC-DS cast slab showing dimensions, specimen layout and direction of solidification (DS) indicated by grains.

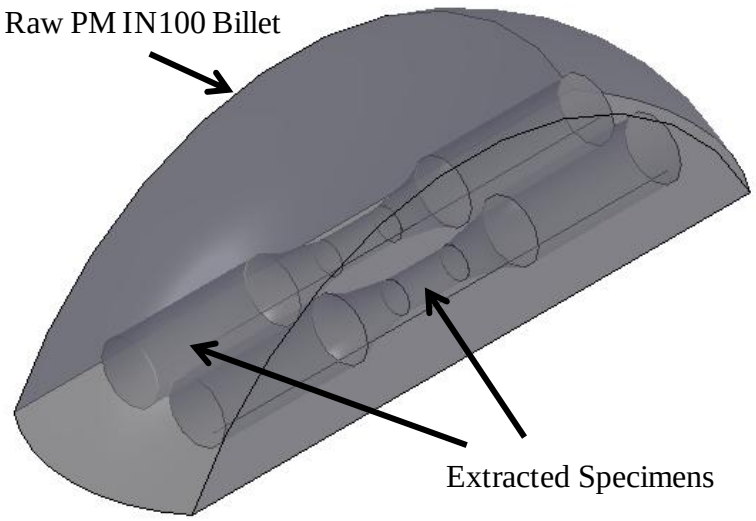

Figure 4-2. 3D model of billet 6 of the IN100 raw material showing the two fatigue specimens that can be produced from billet 6.

The manufacturing of test specimens from raw material was done by Cincinnati Testing Laboratories, Inc. (Cincinnati, Ohio). To reduce the effects of machining marks and residual stresses on fatigue testing a low stress grinding process was used on all specimens. Machining instructions included the grinding wheel size (7.5" DIA A-120-S5-BA2), speed (1260RPM) and required surface finish (P600-P1000 circumferential). These instructions were also provided to vendors in previous studies on CM247LC-DS at Georgia Tech.

The smooth cylindrical specimen geometry corresponding with no stress concentration , $k_t = 1$, is shown in Fig. 4-3. This geometry was the same one used in previous studies on CM247LC-DS at Georgia Tech. The design meets recommended dimensions of both ASTM Standard Practice for Strain-Controlled Fatigue Testing (ASTM E606-04) and ASTM Standard Practice for Strain-Controlled Thermomechanical Fatigue Testing (ASTM E2368-04).

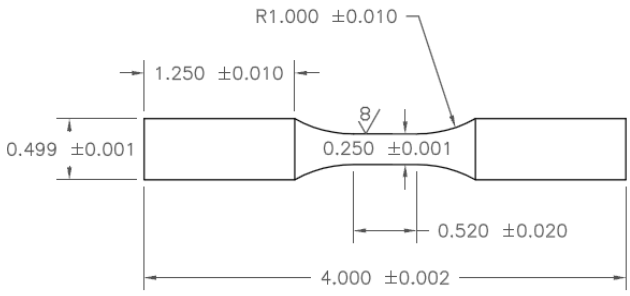

Figure 4-3. Smooth Specimen Geometry, $k_t=1$. Dimensions are in inches.

Notch specimen geometries are shown in Figure 4-4. Each of the individual notch geometries utilized adhere to the machining requirements provided by ASTM Standard Test Method for Sharp-Notch Tension Testing with Cylindrical Specimens (ASTM E602-03). The specimen geometry with an elastic stress concentration factor $k_t=2$ is identical to a previously used geometry in a study on CM247LC-DS at Georgia Tech. The $k_t=1.7$ and $k_t=1.3$ specimens were designed utilizing linear-elastic FEA analysis to have the desired elastic stress concentration factors of 1.7 and 1.3, respectively. All notch geometries were designed with the constraint that they have a notch root cross section diameter of 6.35 *mm* (0.250 *in*). The $k_t=1.7$ specimen was designed by imposing a 60° v-notch and then varying the notch radius until the desired elastic stress concentration was reached. The milder $k_t=1.3$ notch could not be achieved using a v-notch and as such only an arc extrusion was necessary. The notch radius of the $k_t=2.0$ specimen was found to be 0.9271 *mm* (0.036 *in*), 1.3462 *mm* (0.053 *in*) for the $k_t=1.7$ specimen and a notch radius of 3.5560 *mm* (0.140 *in*) for the $k_t=1.3$ specimen.

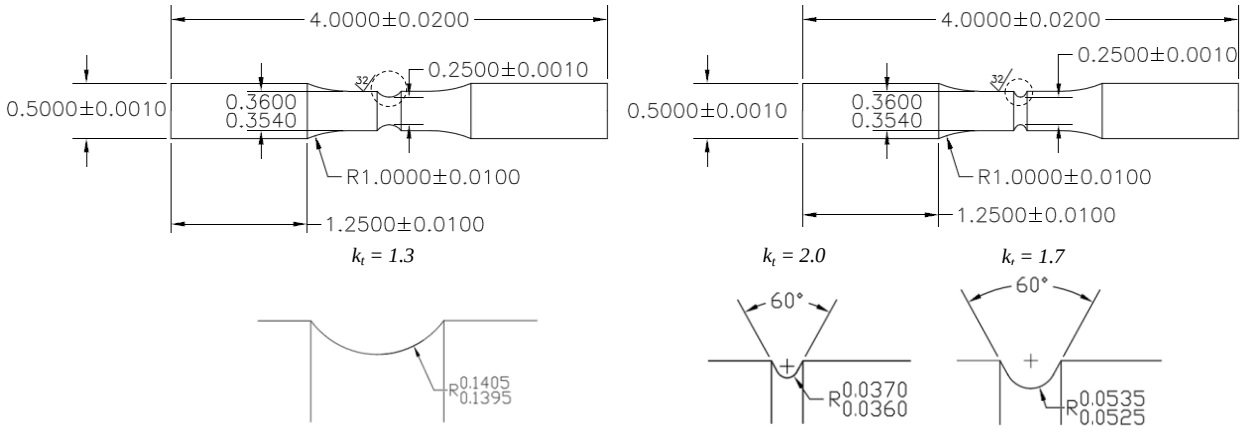

Figure 4-4. Notch specimen geometries. Dimensions are in inches (not to scale).

All specimens were visually inspected for surface markings upon being received. Prior to each test the specimen notch root was measured using a Starrett® Sigma HB400 optical comparator. Before every test specimens were also cleaned and degreased using acetone and then rinsed with ethanol. Ethanol was utilized in the final cleaning stage as it leaves no residual film on the surface.

4.2 Thermomechanical Fatigue Experimental Setup

A 44.5 *kN* (10 *kip*) MTS® axial servo-hydraulic testing machine with load cell resolution of ±100 *lbf* was utilized for all testing. Water cooled MTS® model 646 grips were utilized to grip circumferential bog bone specimens and provide conductive cooling for TMF testing. A dual-channel digital controller was utilized for most tests with TestStar software (Testware SX® 4.0D). The digital controller was upgraded to FlexTest40 and the Testware software was replaced by MTS TestSuite® Multipurpose Elite Software. An analogue temperature command signal was output by the digital controller to the Watlow 945A-2FK5-A000 PID temperature controller. The input analogue signal to the temperature controller served as a remote set point

necessary to determine the error signal for PID control. An analogue current output was provided by the Watlow temperature controller to an Ameritherm 2kW induction heater which induced the desired temperatures in each specimen. Temperature feedback was provided by a K-type thermocouple (Omega® model GG-K-26_SLE). Nominal hydraulic pressure applied to grip the specimens was 29 *MPa* (4200 *psi*).

Axial displacement within the gage section was measured using a high temperature extensometer (MTS® model 632.52E-14), as shown in Fig. 4-5. Ceramic rods extended from the extensometer, passed between induction coil turns and pressed against the gage section of the specimen. The 5.0 *mm* diameter alumina rods had v-wedge ends which were held against the specimen by a spring mechanism mounted in the support brackets. The nominal gage length for both smooth and notched specimens (position of zero displacement) between extensometer tips was 12.7 mm (0.5 in).

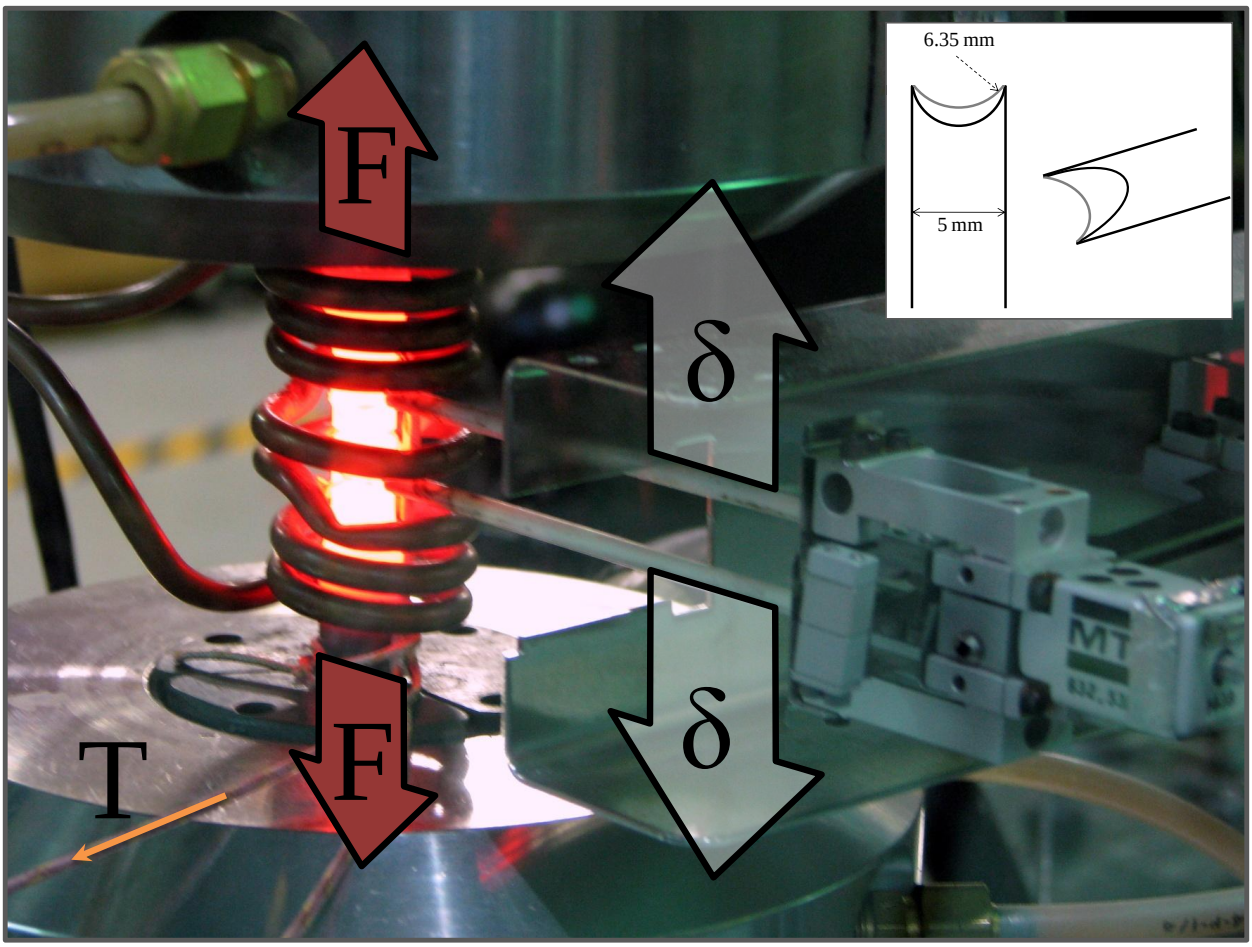

Figure 4-5. Experimental setup displaying temperature (T) measurement, controlled or measured force (F) and the controlled or measured displacement (δ).

Each test had two thermocouples (TCs) spot welded onto opposite sides of the gage section as shown in Fig. 4-6. One was utilized as the control TC and the other a backup. For smooth specimen testing the thermocouples were placed slightly outside of the extensometer rod seating location as to not introduce any flaws into the gage section. For notch testing the thermocouples were located away from the notch but within extensometer rod seat locations to provide a temperature reading closer to the notch. When spot welding thermocouples to the notch specimen, a piece of Kimwipe® was wrapped around the notch root to protect it from any spot welding splatter. The two thermocouples provided a rough method for ensuring sufficient

temperature uniformity in each test per ASTM E2368-04. A detailed validation of temperature uniformity was performed for each new coil or specimen geometry utilized.

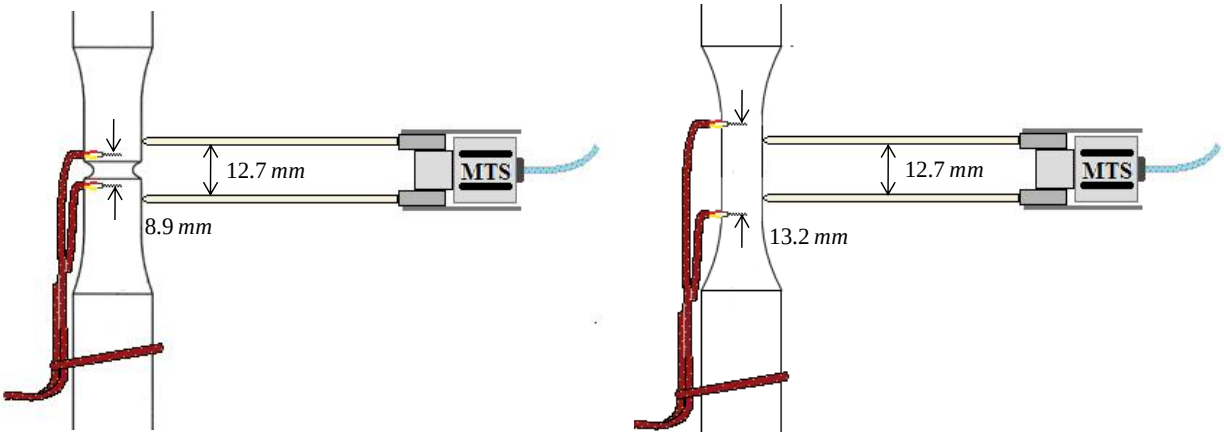

Figure 4-6. Thermocouple positioning on notched specimens and smooth specimens.

The induction coil used in conjunction with the Ameritherm® heater was made from copper tubing having 4.7 *mm* (0.1875 *in*) outer diameter. The number of turns and diameter of each turn has a direct influence on the magnetic flux density produced in the specimen. Induction coils are inherently material, specimen geometry and test specific. For both materials and each specimen used in this study one coil design was sufficient. A total of seven turns were utilized in the coil including a middle turn between the extensometer rods. The middle turn had a inner diameter of 28 *mm* (1.1 *in*) and all others 23 *mm* (0.9 *in*).

4.3 Thermal Expansion Compensation

To determine the mechanical strain during TMF testing it is necessary to decouple the deformation associated with thermal expansion from deformation associated with elastic or inelastic behavior. For specimens with smooth gage sections it is assumed that the deformation

in the gage section is uniform. The total strain ε, measured by the extensometer, is the sum of the mechanical strain and thermal strain,

$$\varepsilon = \varepsilon_{\theta} + \varepsilon_{mech} \tag{4.1}$$

The total strain is the engineering strain based on the extensometer displacement measurement at the specimen surface and a 0.5 *in* gage section. Thermal strain can be calculated as a function of temperature or loading time. Errors in the thermal strain can be caused by thermal gradients (radial or axial) in the test specimen, error in thermocouple reading and small test to test variations in the coil placement.

In the case of notched specimens, the displacement across the extensometer rods cannot be used to determine the engineering strain because the material response is highly localized and multiaxial at the notch. Rather the displacement measured by the extensometer is an aggregate result of local deformation over the entire notch geometry between the rods. This is shown schematically in figure 4-7.

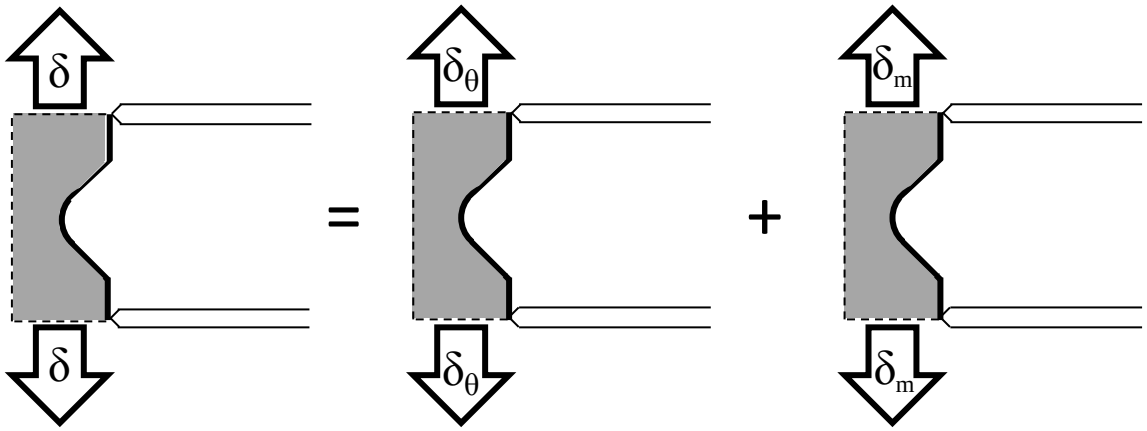

Figure 4-7. Deformation measured by the extensometer across the notch root. The total displacement at the rod tips is a result of thermal and mechanical deformation of material between the rod tips.

The Testware SX control software allows for the definition of *Calculated variables* which can be utilized in data acquisition or as a mode of control. *Calculated variables* are signals that are defined as functions of other test signals; in this case temperature and extensometer displacement. The thermal displacement is defined by the user as a function of temperature and the mechanical displacement is the difference between the calculated thermal displacement and measured total displacement,

$$\delta_{mech} = \delta - \delta_{\theta} \tag{4.2}$$

For calculating the thermal expansion from a secant method, a linear relationship is assumed between thermal expansion and temperature,

$$\varepsilon_{\theta} = \alpha(T - T_o) \tag{4.3}$$

where α is the coefficient of thermal expansion and T_o is a reference temperature. The relationship can be made nonlinear by introducing a temperature dependent thermal expansion coefficient or by introducing greater order temperature terms.

$$\varepsilon_{\theta} = \alpha(T)(T - T_o) \tag{4.4}$$

$$\varepsilon_{\theta} = \sum_{i=0}^{N} \alpha_i T^i \tag{4.5}$$

The nonlinearity of thermal expansion can be attributed to nonlinear expansion typical at high temperatures in Ni-base superalloys. In the case of extensometer displacement measured from thermal expansion in the notches (δ_{θ} rather than ε_{θ}), geometric constraints during free expansion also contribute to the nonlinearity of the aggregate response.

Defining the thermal strain or thermal displacement as a function of temperature corresponds to temperature-based thermal strain compensation as described in ASTM E2368-04. This compensation can be implemented in Testware SX or Multipurpose Elite by fitting a polynomial to free expansion data. The free expansion response can vary between tests with identical temperature ranges based on variations in extensometer seating, specimen gripped section and coil positioning. As such, prior to each TMF test a free expansion test was performed. The free expansion tests prescribe force to 0 N and cycle temperature at a mean value, range and cycle time identical to the TMF test. Figure 4-8 displays the results from a free expansion test on a IP TMF test with $k_t = 1.3$, $\Delta T = 500°C \leftrightarrow 950°C$ and a 180 s cycle time. A third order polynomial was sufficient for capturing the nonlinear expansion.

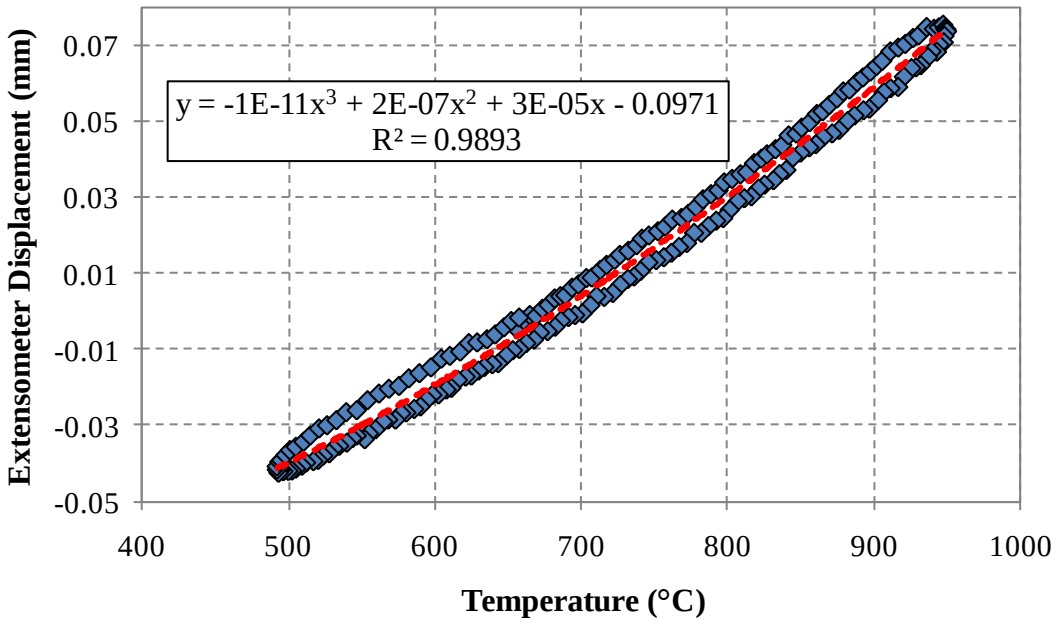

Figure 4-8. Extensometer displacement against temperature in a free expansion test in a notched specimen.

The expansion response exhibits some hysteresis that is dependent on whether the material is being cooled or heated which is found in some metals. The ASTM standard E2368-04 provides limits on the error between measured and calculated thermal expansion. To adhere to this standard utilizing temperature-based compensation, temperature controller PID values were varied by the user during thermal cycling to reduce the maximum hysteresis width to within 5% of the expansion range.

Time-based compensation is another method suggested by ASTM E2368-04. Noting that the applied temperature is a periodic function in time, the thermal expansion can also be expressed as a function of time,

$$\varepsilon_\theta = f(T(t)) = g(t) \tag{4.6}$$

$$\delta_\theta = f(T(t)) = g(t) \tag{4.7}$$

A good candidate for replicating periodic functions in time is a truncated Fourier series,

$$g(t) = \frac{1}{2}a_0 + \sum_{n=1}^{N}\left(a_n \cos(nt) + b_n \sin(nt)\right) \tag{4.8}$$

where the coefficients can be calculated numerically provided periodic free-expansion data. The parameterization of both thermal expansion and temperature in time allows for the thermal hysteresis to be accounted for almost exactly. This method is also advantageous as the thermal expansion can be expressed as a smooth function. Methods that utilize two separate temperature-based expressions for heating and cooling can introduce discontinuities at the maximum and minimum temperatures, especially in the presence of noise associated with the measured temperature signal. Discontinuities can be extremely detrimental if utilized as a control signal.

Figure 4-9 shows the measured experimental data and corresponding fit for a IP TMF temperature waveform with $k_t = 2.0$, $\Delta T = 450°C \leftrightarrow 750°C$ and a 180 *s* cycle time.

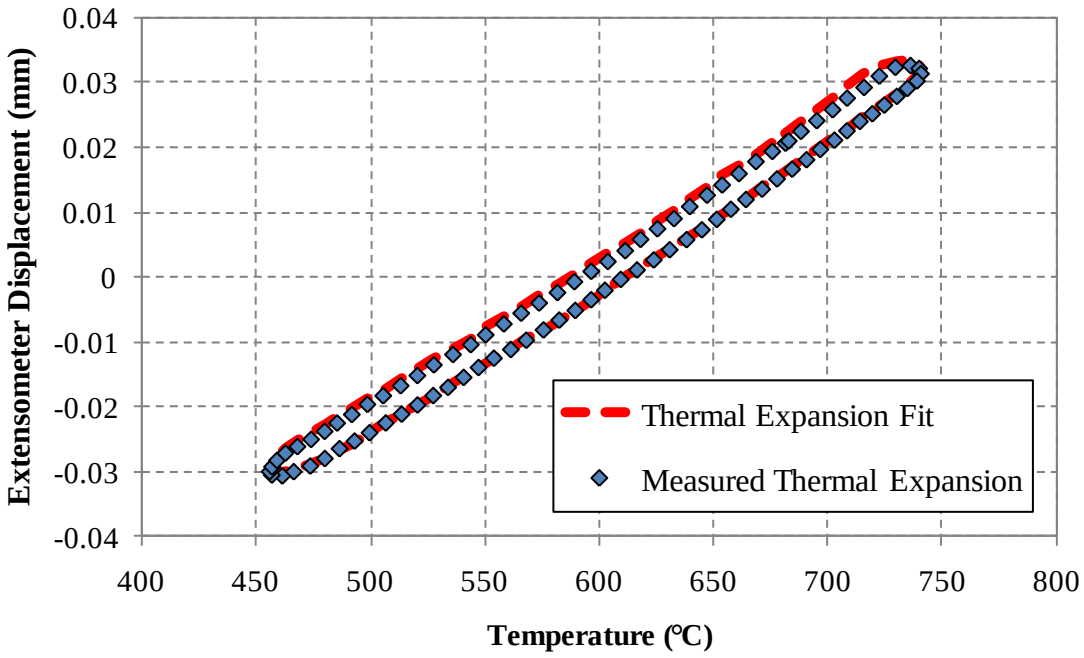

Figure 4-9. Measured extensometer displacement in a free expansion test and the corresponding thermal expansion Fourier series fit.

4.4 Thermomechanical Test Control In Notched Specimens

Notched specimen TMF tests were performed in both force and mechanical extensometer displacement control. Force control tests were performed utilizing a full reversed ($R_{\sigma_{nom}} = -1$) triangular waveform with constant amplitude. For each force controlled experiment the extensometer displacement was measured across the notch root the entire duration of the test.

Displacement control tests were developed based on the displacement response of force control tests. From the steady state or half-life displacement response during a force control test,

an analogous displacement control test was developed. Figure 4-10 (a) shows the stabilized response in IN100 following a period of ratcheting along with stabilized displacement values at the saturation cycle, N_{sat}. Figure 4-10 (b) displays heavy ratcheting in a CM247LC DS test where there is no clear stabilized response and N_{sat} is taken at the half life.

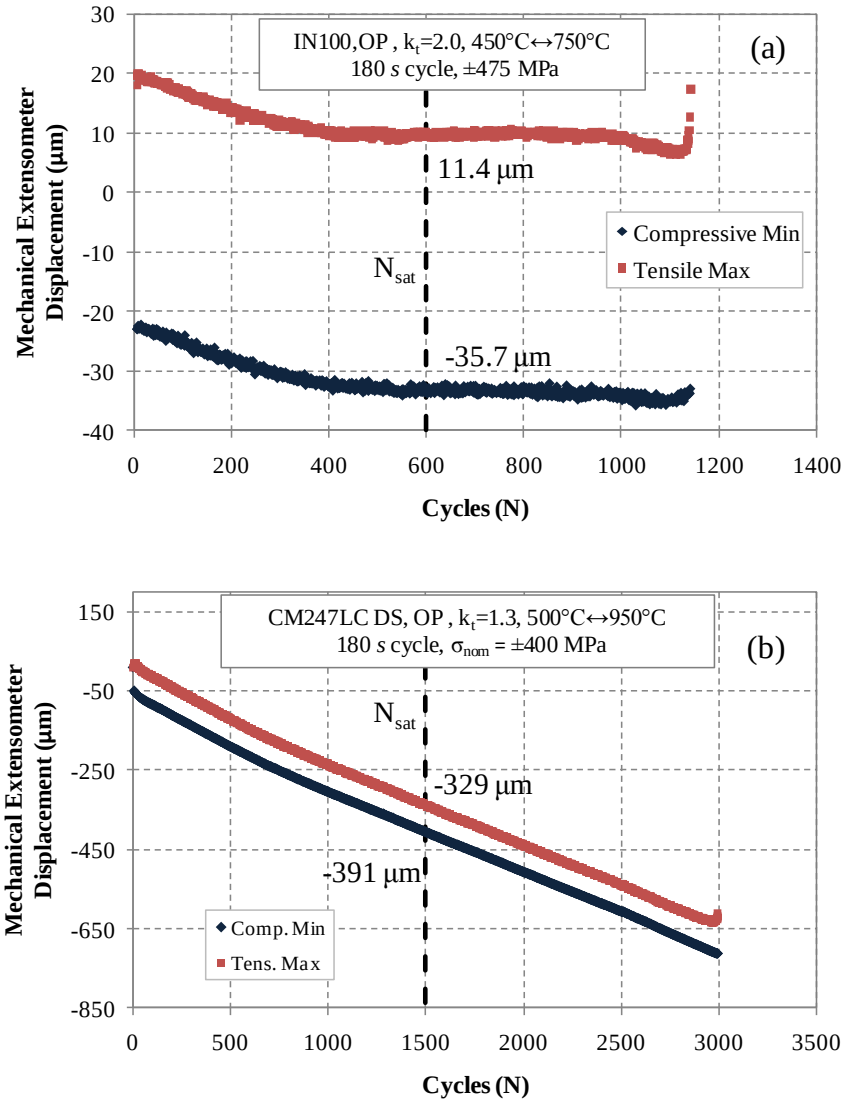

Figure 4-10. (a) Mechanical extensometer displacement and stabilized response following plastic ratcheting. (b) Mechanical extensometer displacement displaying heavy ratcheting. Displacement values taken at half-life.

Additional displacement control tests were performed utilizing the displacement amplitudes obtained from force control tests, but varying the mean displacement and thus varying the displacement R-ratio, R_δ.

The phasing relationship between the applied mechanical boundary condition (force or extensometer displacement) and applied temperature is critical in influencing the damage processes that lead to crack initiation and failure of each specimen. The applied boundary conditions and temperature both follow a triangular waveform with the same cycle time. The phasing between the two waveforms directly influences the relative quantities of high temperature damage processes. The difference between the peak temperature and peak applied mechanical boundary condition is defined as the phase shift angle and by convention has units of degrees. The range is set to $[-180°, 180°]$, where a positive value corresponds to the temperature profile leading the applied mechanical boundary condition. The most common waveforms are linear in-phase (IP) and linear out-of-phase (OP) TMF tests. These represent the life-limiting conditions in turbine blades and hence are of most value to study. Examples of IP and OP waveforms can be seen in Fig. 4-11.

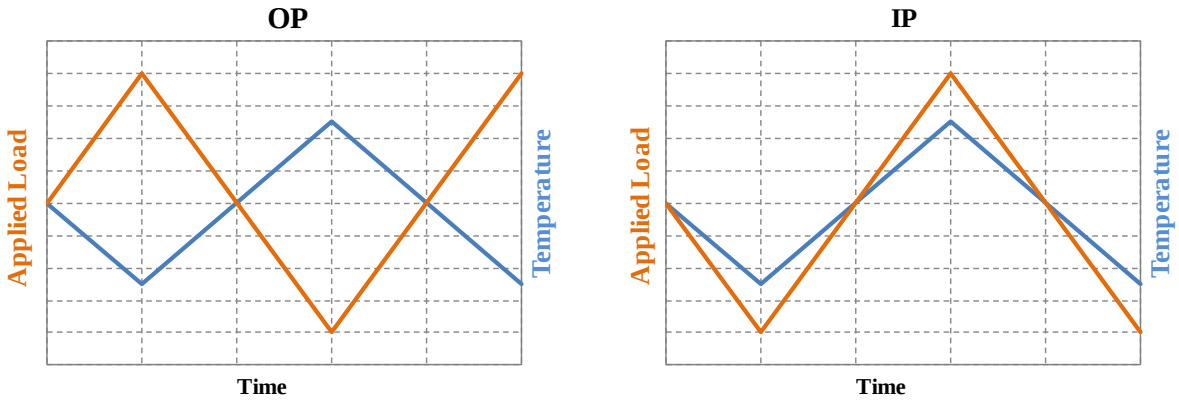

Figure 4-11. Examples of linear out-of-phase (OP) and linear in-phase (IP) waveforms. Applied load can refer to uniaxial applied force or applied displacement at the extensometer rod tips.

4.5 Testing Methodology

All TMF tests were performed while adhering to ASTM E2368-04 (*Standard Practice for Strain Controlled Thermomechanical Fatigue Testing)* and ASTM E466-07 (*Standard Practice for Conducting Force Controlled Constant Amplitude Axial Fatigue Tests of Metallic Materials*) when applicable. ASTM E2368-04 applies for strain controlled tests in smooth specimens, which is not applicable towards notched specimens, but does provide standards related to the applied temperature profile:

1. The maximum allowed temperature differential over the length of the gage section at any time during cycling shall not be greater than ±1% of T_{max} in °K or ±3°K, whichever is greatest.
2. During free expansion cycling the thermal hysteresis shall be no more than 5% of the total thermal strain range (in this case the equivalent extensometer displacement).
3. In mechanical strain control tests the response may not deviate from the control signal by no more than 2% of the range. This analogous for extensometer displacement controlled tests. In force controlled tests the force amplitude is to be within 2% of the desired value for all time.
4. The phase shift shall not deviate more than 5° of the desired value for all time.

The first criterion is dependent on the design of the induction coil. A newly fabricated induction coil must be first be thoroughly tested for temperature differentials prior to any TMF testing. The coils used in this study were validated to produce a sufficiently uniform temperature distribution by welding 10 thermocouples to a smooth specimen and testing at discrete

isothermal temperatures within the TMF range (550°C, 850°C, 950°C, 1050°C). Six thermocouples measured temperature differentials in the axial direction and four in a radial fashion at the center of the gage section. Induction coils were modified or remade until the temperature distribution was sufficiently uniform.

To minimize the thermal hysteresis produced in thermal cycling tests, the temperature control parameters (PID values) were varied during cycling until the hysteresis width was sufficiently small. Prior to tuning the control parameters, roughly 10-20 thermal cycles were applied to allow the response to stabilize and remove any transient material behavior that is not representative of long term behavior. On the upgraded control systems with MTS® Multipurpose Elite, the time-based Fourier series thermal expansion compensation was utilized to capture steady-state thermal expansion behavior. The time based compensation captures thermal expansion hysteresis and as such this criteria was automatically satisfied.

To satisfy the criterion on phase shift the time lag between temperature command and thermocouple feedback was quantified and incorporated so that phasing in the control program offset the time lag associated with temperature control error. Prior to each test a few elastic TMF cycles (force control or mechanical strain control) were performed to ensure that phasing compensation adhered to the standards, and if not, the phase lag was modified until ASTM standards were satisfied. For all tests the necessary phase lag needed to adhere to ASTM standards varied between -20° and -24°.

4.6 Crack Initiation Criteria

A suitable crack initiation criteria is needed to differentiate macroscopically large crack initiation from crack propagation, which can be a significant portion of life. A crack of 0.5 to 1

mm is typically used to define a macroscopically large crack in Ni-base superalloys. As both force and extensometer displacement control tests were utilized, two unique crack initiation criterion were used.

4.6.1 Mechanical Extensometer Displacement Controlled Tests

Tests on notched specimens under prescribed mechanical extensometer displacement (δ_m) utilized a force-drop method for determining the life to crack initiation. For a specimen with a macroscopically large crack present, a smaller tensile force is necessary to achieve the prescribed displacement. As such, a decrease in tensile force is expected as a crack initiates and grows. It is important to note that the force time history may also change as a result of cyclic hardening or softening, cyclic shakedown and any microstructural changes due to elevated temperatures. As such a 10% *tensile load deviation* criteria was utilized that measures the force drop against the stabilized force response trend. Figure 4-12 (a) shows the peak-valley data corresponding to the net section stress measured during a extensometer displacement controlled notch test. Figure 4-12 (b) displays only the tensile data which exhibits analogous tensile behavior around 1100 cycles.

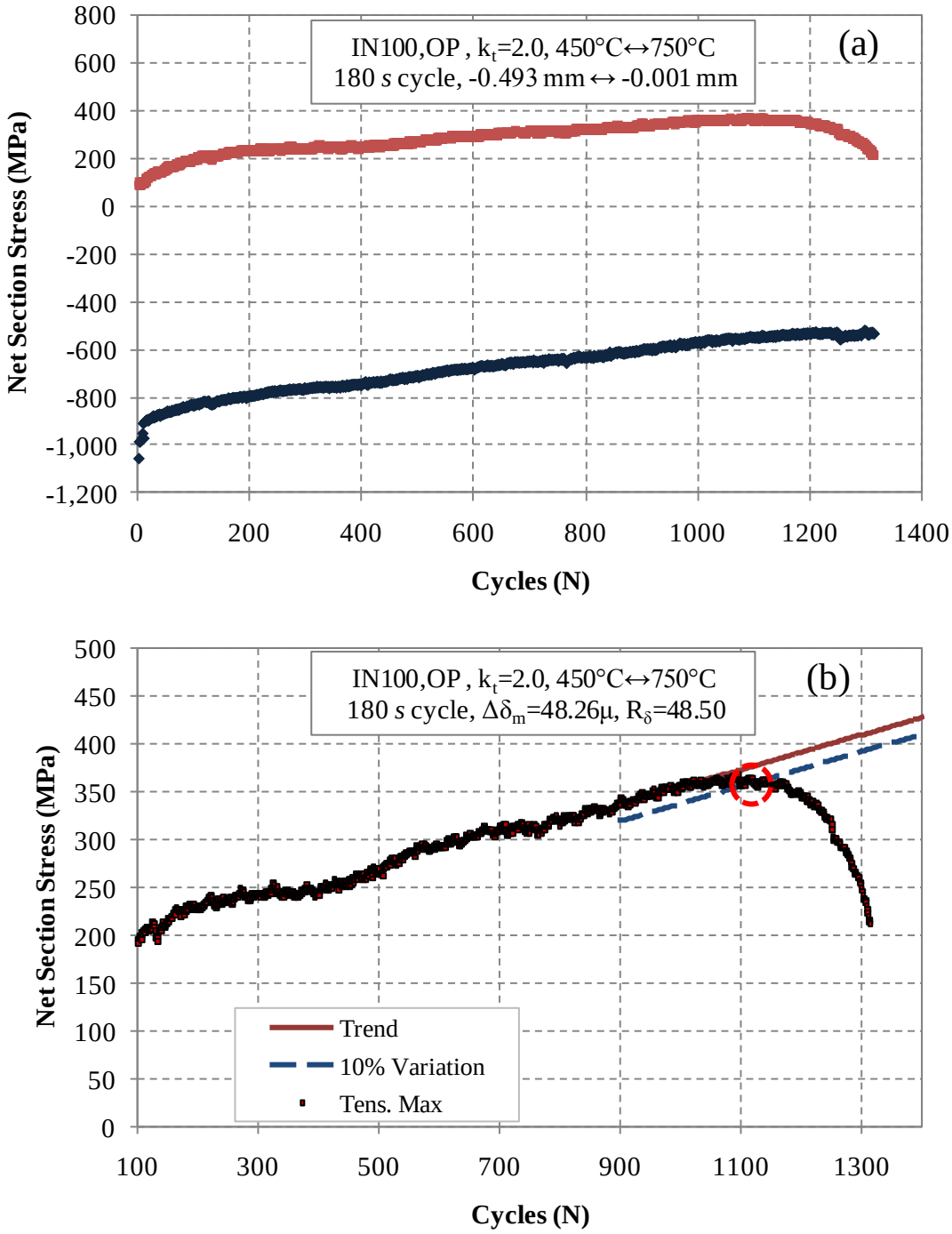

Figure 4-12. (a) Cyclic peak-valley data displaying shakedown towards zero mean net section stress. (b) Tensile peak data displaying a near-linear trend in increasing net section stress. Included is the linear trend fit and the crack initiation criterion corresponding to a 10% force drop.

4.6.2 Force Controlled Tests

Crack initiation under prescribed force conditions can be predicted utilizing a stiffness drop method where a deviation in linear-elastic tensile stiffness response indicates an initiated crack. The stiffness is calculated using a linear regression of the first *n* points during specimen unloading between the force and mechanical extensometer displacement.

$$S \cdot \delta_m(t_i) = F(t_i) \tag{4.9}$$

The number of points to use is dependent on the sampling rate and test. For 180 *s* cycles with a 1 *Hz* sampling frequency *n* was typically 30-40 points.

The stiffness history for a IN100 notched specimen under TMF loading is shown in figure 4-13 (a). Figure 4-13 (b) displays the hysteresis loop for the 1000th cycle along with points utilized to calculate the stiffness. The associated noise is because the stiffness accrues error from both the displacement and force signals. As the force is prescribed, a better method is to directly utilize an extensometer displacement to determine initiation.

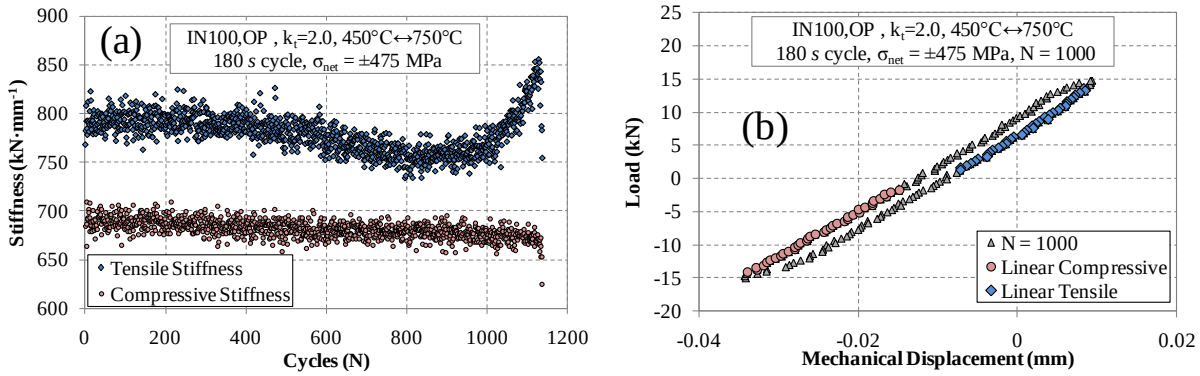

Figure 4-13. (a) Stiffness history for a notched specimen. (b) Data utilized for the elastic unloading regime for $N = 1000\,cycles$.

Notched specimens with prescribed force boundary conditions utilized a mechanical extensometer displacement based crack initiation criteria. Analogous to force-history evolution in extensometer displacement controlled tests, the extensometer displacement history can vary in force control tests due to cyclic softening and hardening, plastic and creep ratcheting or material microstructure evolution. Hence a 10% *tensile mechanical extensometer displacement deviation* criteria was used to determine crack initiation.

Peak-valley displacement data associated with the same test from Fig. 4-13 is shown in Fig. 4-14. Initially the displacement in both compression and tension decrease with cycling indicating ratcheting caused by a combination of plasticity and high temperature creep. The material stabilizes between cycles 400 and 1000 in both tension and compression. Around cycle 1000 the tensile trend exhibits anomalous behavior different from the compressive trend which is indicative of macroscopic crack initiation.

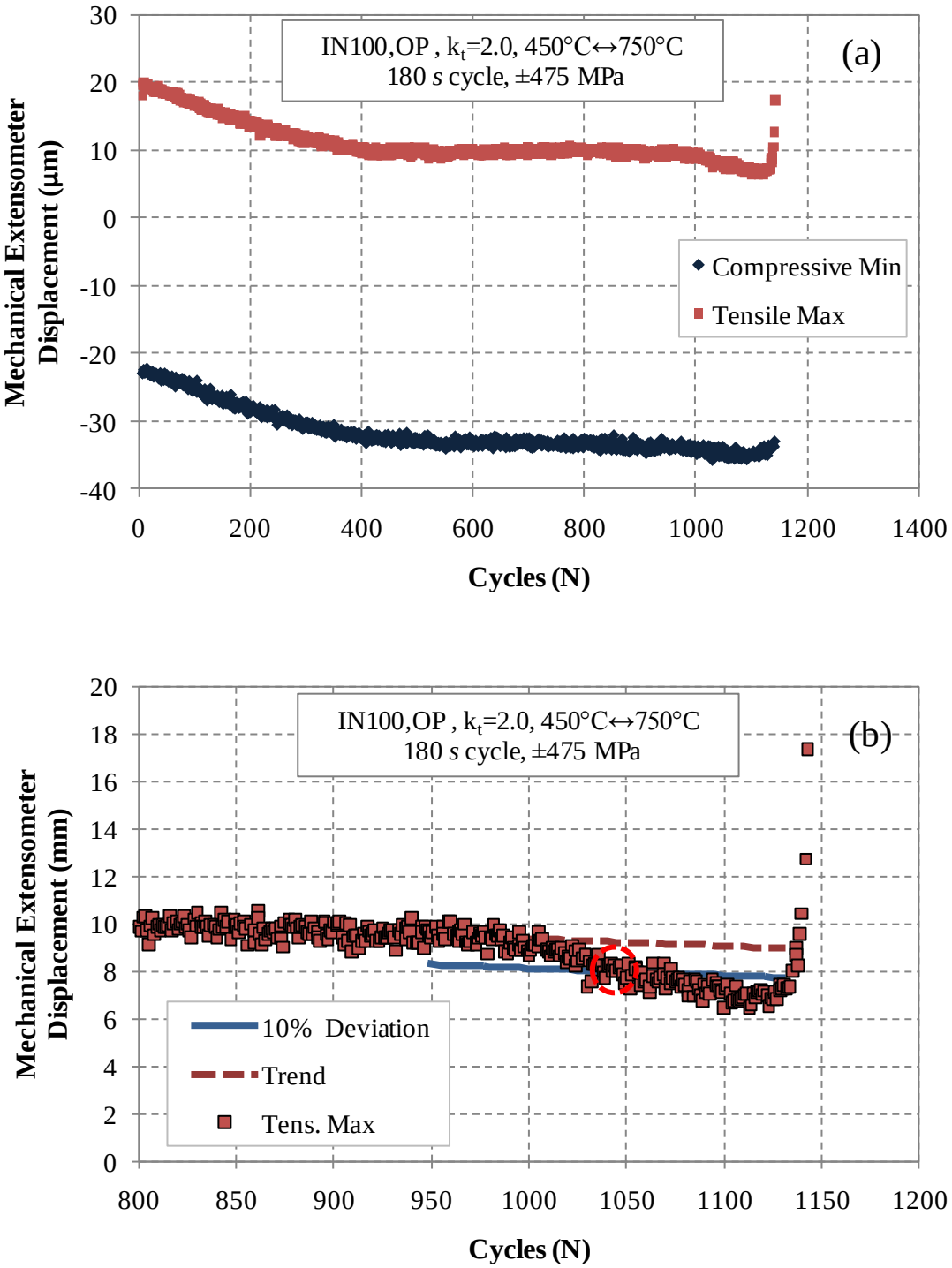

Figure 4-14. (a) Peak-valley mechanical extensometer displacement history (b) Tensile portion of displacement history near final fracture of the specimen. Linear trend and 10% variation used to determine crack initiation are shown.

4.7 Metallography Preparation

Metallography was necessary for studying material microstructure as well as imaging damage in post-failure specimens. Not including fracture surfaces, samples were first sectioned to achieve the desired viewing plane. Following the sectioning came cold-mounting samples in Struers ® Epofix resine, HQ. Resin was mixed with Struers ® Epofix hardener, HQ. The mount was cured for 24 *hrs* followed by grinding and polishing given by the procedure given in Table 4-1.

Table 4-1: Grinding and polishing steps

Step	Procedure	Polishing Disk	Applied Force (N)	Speed (RPM)	Suspension	Lubricant	Duration (min)
1	Coarse Grind	320 grit	15	100	None	Water	10
2	Medium Grind	800 grit	20	120	None	Water	10
3	Fine Grind	1200 grit	25	140	None	Water	8
4	Course Polish	4000 grit	25	150	None	Water	8
5	Medium Polish	MD Mol (Woven wool)	20	150	DiaPro Mol	None	8
6	Fine Polish	MD Chem (Porous synthetic)	15	150	OP-S Suspension	None	2

Kalling's 2, etchant #94 in ASTM standard E407-99, was used to reveal grain boundaries and the $\gamma - \gamma'$ interfaces in each alloy. Polished cold mounts were submerged in the etchant for 35-45 *s* and then immediately rinsed with ethanol.

CHAPTER 5 CONSTITUTIVE MODELING OF NI-BASE SUPERALLOYS UNDER TMF LOADINGS AT STRESS ELEVATORS

The local response is critical for understanding the coupling between damaging physical processes and component geometries. To examine and study key localized quantities at a notch such as stresses, inelastic strains and relevant spatial gradients, finite element analysis (FEA) models with material specific constitutive models were utilized. The constitutive models need to capture rate dependency and creep behavior as materials are exposed to elevated temperatures and local deformation rates can vary near stress elevating features.

An accurate macroscopic unified creep-plasticity internal state variable model [63-65] was implemented for IN100 as a User-Defined Material Subroutine (UMAT) within the commercial finite element package Abaqus [66]. Kinematic hardening was included to capture yielding dependence on directionality (Bauschinger Effect). Isothermal calibration of model parameters was performed in a systematic fashion over the TMF temperature range of interest. Linear interpolation of model parameters was utilized to predict TMF behavior.

For predicting the local notch response in CM247LC DS a transversely isotropic continuum viscoplasticity model developed by Shenoy et al. [67-68] for a similar DS superalloy, GTD-111, was utilized. Shenoy et al. calibrated the constitutive model isothermally and verified response predictions for OP and IP TMF over the temperature range 427°C ↔ 1038°C. The constitutive model was implemented as a UMAT within Abaqus.

Finite element models for each notch geometry utilized axisymetric and planar boundary conditions to reduce the complexity of the mesh. Each mesh was refined at locations of high

stresses and verified to be sufficiently convergent for anisotropic elastic analysis. Appropriate uniform pressure conditions were applied remotely to achieve prescribed net section stresses.

5.1 IN100

5.1.1 Unified Creep-Plasticity Constitutive Model

The inelastic strain rate can be defined using a viscoplastic potential [69]

$$\dot{\varepsilon}_{ij}^{in} = \dot{p} n_{ij} \tag{5.1}$$

where $\dot{p}$ is defined as

$$\dot{p} = f\left(\sqrt{\frac{3}{2}}\left\|\sigma_{ij}^{'} - \alpha_{ij}\right\|\right) \tag{5.2}$$

where he function f is the viscoplastic potential, $\sigma_{ij}^{'}$ is the deviatoric stress, α_{ij} is the deviatoric backstress and n_{ij} defines the direction of inelastic deformation in deviatoric stress space.

$$n_{ij} = \frac{\sigma_{ij}^{'} - \alpha_{ij}}{\left\|\sigma_{ij}^{'} - \alpha_{ij}\right\|} \tag{5.3}$$

The flow potential was chosen to follow a power law relationship,

$$\dot{p} = A_v \sqrt{\frac{3}{2}} \left\langle \frac{\sqrt{\frac{3}{2}}\left\|\sigma_{ij}^{'} - \alpha_{ij}\right\| - \kappa}{D} \right\rangle^{n} \tag{5.4}$$

A yield surface model is utilized to represent the viscous overstress similar to Chaboche's theory [63]. The size of the yield surface is then is captured by the threshold stress, κ. Directional

hardening is captured by the backstress, α_{ij}. The drag stress, D, is a measure of the material's resistance to inelastic flow. The exponent n represents the power-law deformation observed for inelastic deformation. The pre-multiplier A_v is a material dependent property that scales the flow potential term. It follows an Arrhenius type relationship to provide the flow potential with temperature dependency.

$$A_v = A \cdot \exp\left(-\frac{Q}{RT}\right) \tag{5.5}$$

To capture history effects in the material, the backstress, α_{ij} , behaves as an internal state variable (ISV) that evolves with time. The backstress evolves according to [70]

$$\dot{\alpha}_{ij} = \left(\frac{2}{3}A_1 n_{ij} - \sqrt{\frac{2}{3}}B_1\alpha_{ij}\right)\dot{p} \tag{5.6}$$

The quantity B_1 is a material property equivalent to $A_1/\alpha_{\lim}$ where $\alpha_{\lim}$ represents the uniaxial equivalent saturation limit for the backstress.

Stress values are updated by forward integration of the rate form of elasticity defined in deviatoric terms,

$$\dot{\sigma}'_{ij} = 2G\dot{\varepsilon}'^{el}_{ij} = 2G(\dot{\varepsilon}'^{tot}_{ij} - \dot{\varepsilon}^{in}_{ij}) \tag{5.7}$$

where $\dot{\sigma}'_{ij}$ is the deviatoric stress rate, G is the shear modulus, $\dot{\varepsilon}'^{el}_{ij}$ is the deviatoric elastic strain rate, $\dot{\varepsilon}'^{tot}_{ij}$ is the deviatoric total strain rate and $\dot{\varepsilon}^{in}_{ij}$ is the inelastic strain rate. Thermal expansion contributes only to the hydrostatic stress rate, $\dot{\sigma}_{kk}$.

$$\dot{\sigma}_{kk} = 3K\left(\frac{1}{3}\dot{\varepsilon}_{kk}^{tot} - \alpha\dot{T}\right) \tag{5.8}$$

Where K is the bulk modulus, $\dot{\varepsilon}_{kk}$ is the total hydrostatic strain rate, α is the coefficient of thermal expansion and $\dot{T}$ is the temperature rate.

The constitutive model was programmed in FORTRAN as a UMAT for use in ABAQUS v6.9 [66]. The model is implemented utilizing fully implicit integration scheme to improve convergence, decrease error and allow for larger time steps without compromising accuracy. A Newton-Rhapson scheme with linear line search is incorporated into the program to solve for the viscoplastic potential step $\dot{p}$ [71-72].

5.1.2 Constitutive Model Calibration Methodology

Temperature dependence of the material constants is necessary to have TMF predictive capability. The temperature range of interest corresponds to $450°C \leftrightarrow 750°C$. The high-level approach is to calibrate to isothermal experimental results and then develop an interpolation scheme between temperatures to predict TMF responses. Calibration experiments were conducted that included strain rates varying across one decade (10^{-3} s^{-1} to 10^{-4} s^{-1}) and strain holds on the order of 3 *minutes* to capture stress relaxation behavior.

Strain-controlled cyclic isothermal experiments were performed to generate uniaxial responses for calibration. Applied conditions for all tests are shown in Table 5-1. Applied strain ranges were sufficiently large to induce significant inelastic deformation necessary for constitutive model calibration. Strain holds were included into slow rate calibration tests to capture stress relaxation behavior. An example of an applied waveform for slow strain rate tests is shown in Fig. 5-1.

Table 5-1. Isothermal constitutive model calibration test conditions

Temperature (°C)	R_ε	$\Delta\varepsilon$	No. Cycles without Hold	Strain Rate (s^{-1})	ε_{min} Hold (s)	ε_{max} Hold (s)	No. Cycles With Hold
450	-1	0.0220	3	2.66E-04	165	165	4
550	-1	0.0240	3	2.66E-04	180	180	4
650	-1	0.0244	3	2.70E-04	180	180	3
750	-1	0.0200	3	2.22E-04	180	-	4
450	-1	0.0200	3.5	2.00E-03	-	-	-
550	-1	0.0200	3.5	2.00E-03	-	-	-
650	-1	0.0190	5	1.90E-03	-	-	-
750	-1	0.0195	4.5	1.95E-03	-	-	-

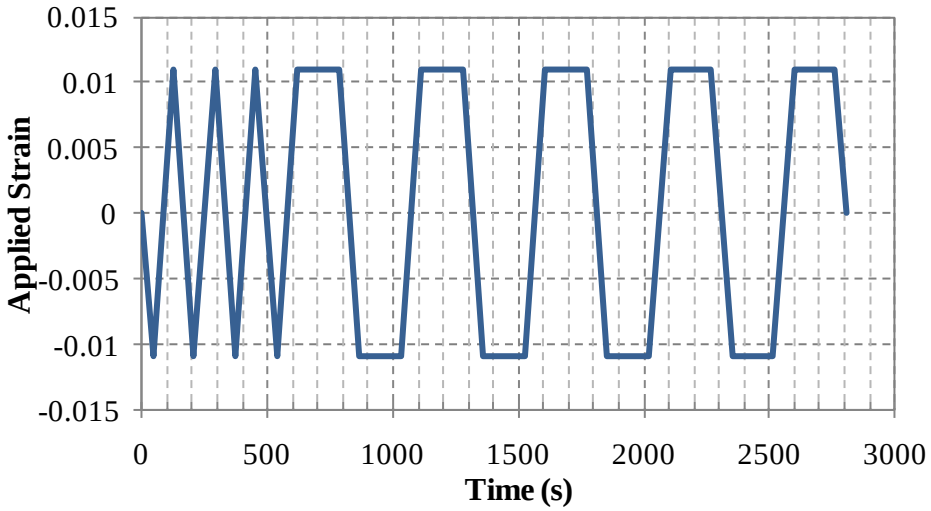

Figure 5-1. Strain waveform applied during isothermal 450°C 10^{-4} s^{-1} experiments.

Four temperatures were utilized (450°C, 550°C , 650°C and 750°C) to span the TMF range of interest, $450°C \leftrightarrow 750°C$. Holds were performed both in compression and tension with the exception of the 750°C test that only had prescribed compressive holds. Experiments with applied strain rates of 10^{-3} s^{-1} were run until failure and the stabilized response was utilized for calibration. Slow rate experimental responses from time $t = 0$ were utilized to capture ISV evolution.

The model parameters corresponding to this material were determined in a systematic fashion. The elastic modulus was determined directly from the linear response in cyclic tests. The coefficient of thermal expansion was determined from free-expansion experiments. The uniaxial equivalent saturation limit for the backstress was determined directly from relaxation responses. For determining all other inelastic parameters an iterative procedure was utilized to systematically iterate parameters to match the simulated response to experimental data. Optimization scripts were developed in the Matlab environment for determining flow potential and ISV evolution parameters. To reduce calibration time a 1D uniaxial reduction of the model was developed within Matlab. This model was utilized to produce the simulated response needed during optimization.

For optimization a scalar value objective function was utilized to quantify the difference between the simulated results produced from the constitutive model and measured experimental results. Weighting scalars were applied to the inelastic portions of the response to place greater emphasis on fitting the inelastic response. The objective function follows a mean squared error functional form to ensure positive-definiteness necessary for convergence.

$$Error = \sum_{t=0}^{t=t^*} W(t)\left(\sigma_{\exp}(t) - \sigma_{sim}(t)\right)^2 \tag{5.9}$$

Where $W(t)$ is a weighting function, $\sigma_{\exp}(t)$ the experimental response, $\sigma_{sim}(t)$ the simulated uniaxial response and t^* the duration of the test. In this study a weighting function of 1 was used for time during purely elastic deformation and 5 during inelastic deformation (plasticity and relaxation). The built-in Matlab function *fmincon.m* was utilized for constrained optimization.

To ensure that rate dependency was accurately captured by the flow potential both fast strain rate (~10^{-3} s^{-1}) and slow strain rate (~10^{-4} s^{-1}) results were fit simultaneously for each temperature. The updated objective function contains two terms corresponding two separate tests performed at the same temperature but under two different applied strain rates; fast (f) and slow (s).

$$Error = \sum_{t=0}^{t=t^*} \left[W_f(t)\left(\sigma_{f,\exp}(t) - \sigma_{f,sim}(t)\right)^2 + W_s(t)\left(\sigma_{s,\exp}(t) - \sigma_{s,sim}(t)\right)^2 \right] \tag{5.10}$$

Relaxation results were utilized to directly calculate the uniaxial backstress limit, $\alpha_{\lim}$. During a sufficiently long strain hold, the stress response approaches this equilibrium stress. Holds performed during calibration experiments were not sufficiently long to measure the equilibrium stress directly, but the quantity could be calculated indirectly from the response.

Analytically the relaxation during a strain hold may be captured utilizing a power-law expression. It is assumed that a equilibrium stress exists above which creep occurs. For tensile deformation the expression is

$$\dot{\varepsilon}_{cr} = \left\langle \frac{\sigma - \sigma_s}{A} \right\rangle^n \tag{5.11}$$

where $\dot{\varepsilon}_{cr}$ is the creep strain rate, σ the uniaxial stress, σ_s the equilibrium stress, A a material constant and n the Norton creep exponent. It is assumed that inelastic strains are dominated by creep processes during a strain hold. It follows that the uniaxial constitutive relation during a strain hold is captured by expressing the total strain rate as a sum of elastic strain and power-law creep strain rates.

$$\dot{\varepsilon}_{tot} = \frac{\dot{\sigma}}{E} + \left(\frac{\sigma - \sigma_s}{A} \right)^n \tag{5.12}$$

$\dot{\varepsilon}_{tot}$ is the total strain rate and E is the elastic modulus. As the total strain is held constant, the total strain rate is prescribed to be zero. This yields a first-order differential equation for σ which can be solved by direct integration,

$$\sigma(t) = \sigma_s + (\sigma_o - \sigma_s)\left[1 + (n-1)\frac{E}{A}\left(\frac{\sigma_o}{A} \right)^{n-1} (t - t_o) \right]^{\frac{1}{1-n}} \tag{5.13}$$

where σ_o is the initial stress at the time when the strain hold begins, t_o. This expression was fit using Matlab nonlinear least squares optimization routine *lsqcurvefit.m* to both tensile and compressive relaxation data at 450°C, 550°C, 650°C, 750°C and 850°C. The assumption is made that this equilibrium stress does not evolve with time, which is not necessarily true as hardening or softening can affect the equilibrium stress. All relaxation data was used to fit an average equilibrium stress. Fitted responses are shown in Fig. 5-2. Fitted values for the equilibrium stress and test conditions are shown in Table 5-2.

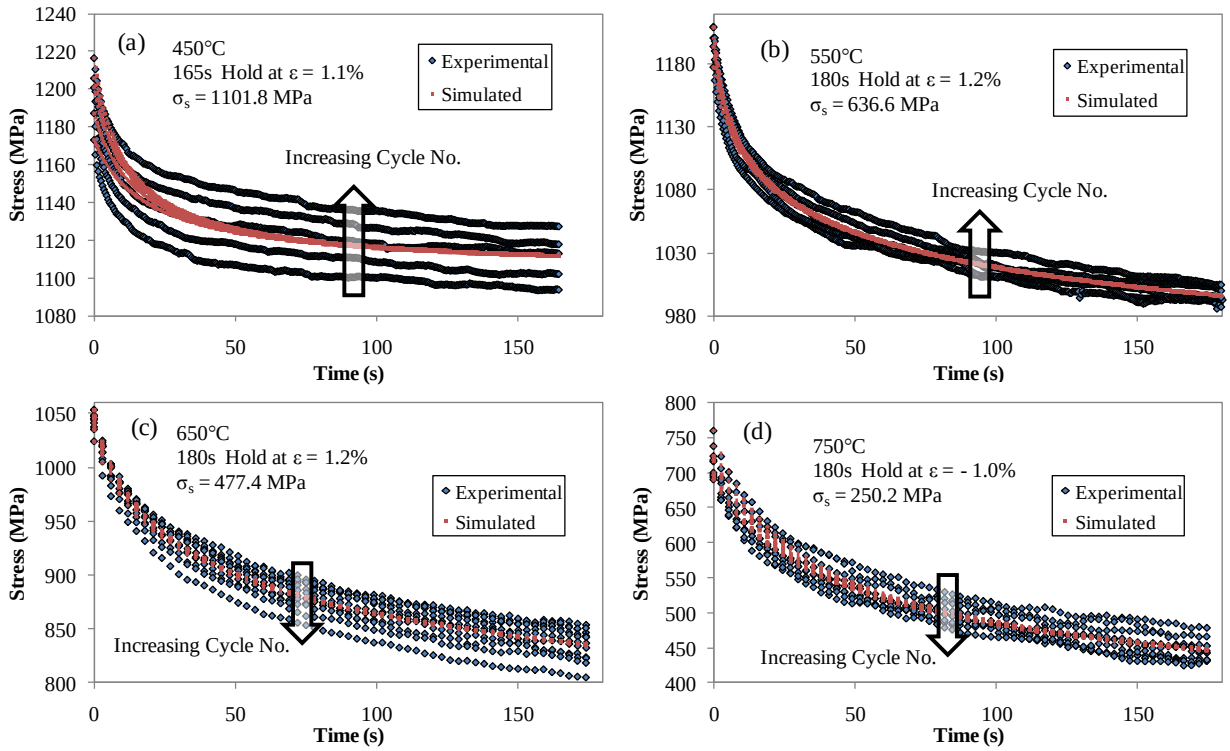

Figure 5-2. Strain holds comparing the calculated fit and experimental results. (a-c) display tensile strain holds and (d) displays utilizes compressive strain holds.

Table 5-2: IN100 stress relaxation conditions and analytical equilibrium stress

Stress Relaxation Fitting Results				
Temperature (°C)	Strain at Hold (%)	Hold Time (s)	Axiality	σ_s (MPa)
450	-1.10	165	C	1163.1
450	1.10	165	T	1101.8
550	-1.20	180	C	960.4
550	1.20	180	T	636.6
650	-1.20	180	C	376.8
650	1.20	180	T	477.4
750	-1.00	180	C	250.2
850	-0.75	180	C	0.0

The increasing or decreasing trends of relaxation curves with respect to cycle number are indicative of the hardening or softening mechanisms present in the material. At 550°C and below the equilibrium stress increases with cycling. At 650°C and above the equilibrium stress

decreases with applied loading. Average equilibrium stress values are shown against temperature in Fig. 5-3.

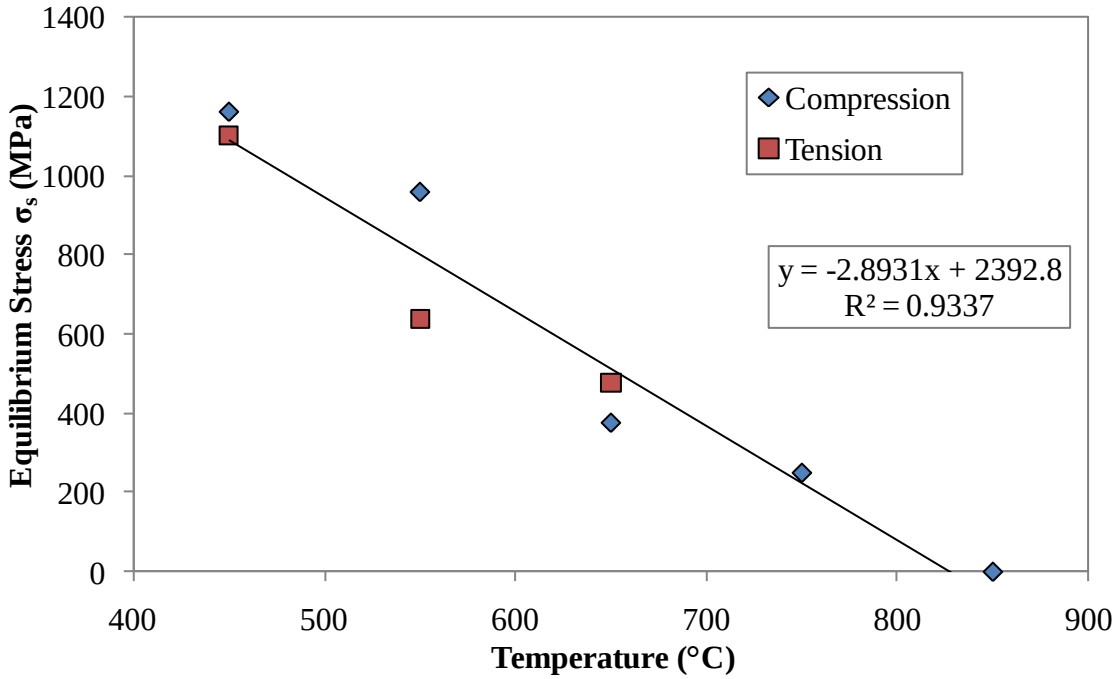

Figure 5-3. Temperature dependence of numerically determined equilibrium stress from experimental relaxation tests.

Stress relaxation is a manifestation of thermally activated diffusional processes and as such is expected to increase with increasing temperature. At sufficiently high homologous temperatures it is expected that the stress would relax completely due to diffusion being the dominant deformation mechanism. The fitting results capture a decreasing equilibrium stress trend with increasing temperature eventually resulting in complete stress relaxation above 800°C after sufficient time. Tension compression asymmetry was observed, as seen in Fig. 5-3 and Fig. 5-5 to Fig. 5-7, however this effect was neglected. It is important to note that the equilibrium stress values are measured stresses, whereas the backstress is a deviatoric quantity. As such the backstress uniaxial limit, $\alpha_{\lim}$, is 2/3 of the determined equilibrium stress.

Capturing the uniaxial backstress saturation value reduces the number of unknowns during optimization by one which decreases calibration time and decreases the likelihood of determining non-unique material parameters. Optimization was additionally simplified as it was determined that isotropic hardening could be neglected for constitutive modeling. The isotropic hardening saturated very quickly upon loading across most temperatures. Hardening behavior at 450°C and an illustration of a yield surface are shown in Fig. 5-4. For a J_2-based flow rule, the yield surface in the plane $\sigma_1 - \sigma_2$ is an ellipse with semi-major axis along the $\sigma_1 = \sigma_2$ direction, but here the schematic is made circular for conceptual simplicity. *R* represents the isotropic hardening that expands the size of the yield surface. Each cycle the equilibrium stress (taken as the stress measured at the end of each hold) and peak stress can be directly measured. The virgin yield stress is known from the first cycle.

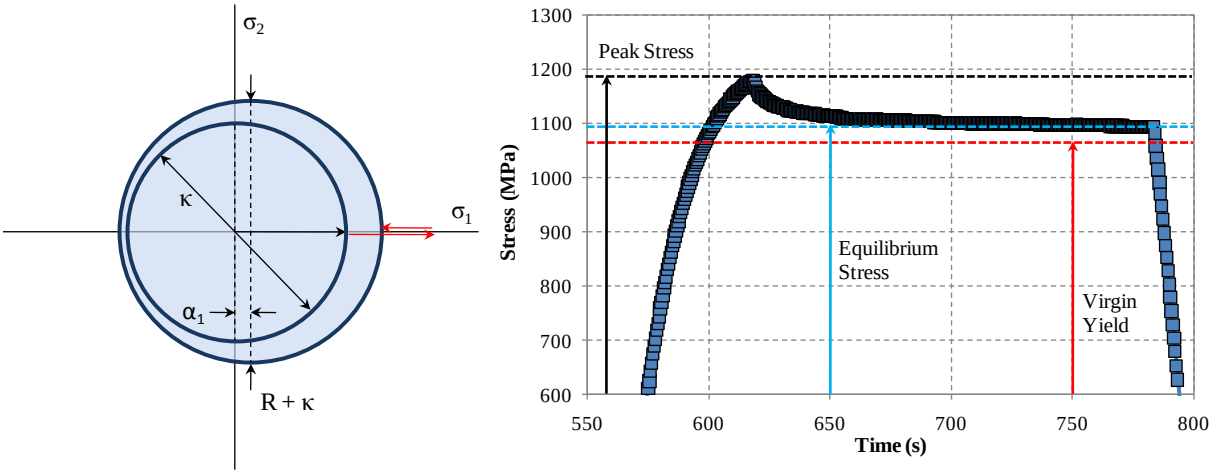

Figure 5-4. (a) Illustration of yield stress hardening, translation and viscous overstress (b) Experimental results indicating hardening and relaxation behavior.

At 450°C, 550°C and 650°C the final relaxation stress in both tension and compression are known. At 750°C only compressive strain holds were applied. It is important to note that as strain holds were relatively short (165 *s* to 180 *s*) and the final stress at the end of a strain hold

does not exactly represent the equilibrium stress. Never the less this value is assumed sufficiently close to the equilibrium stress and can aid in determining the significance of ISVs. Given an approximation of the equilibrium stress value in both tension and compression, the expansion of the initiation yield surface (isotropic hardening) and be estimated. Experimental responses capturing backstress and isotropic hardening evolution between 450°C and are 750°C are shown in Fig. 5-5 through Fig. 5-8.

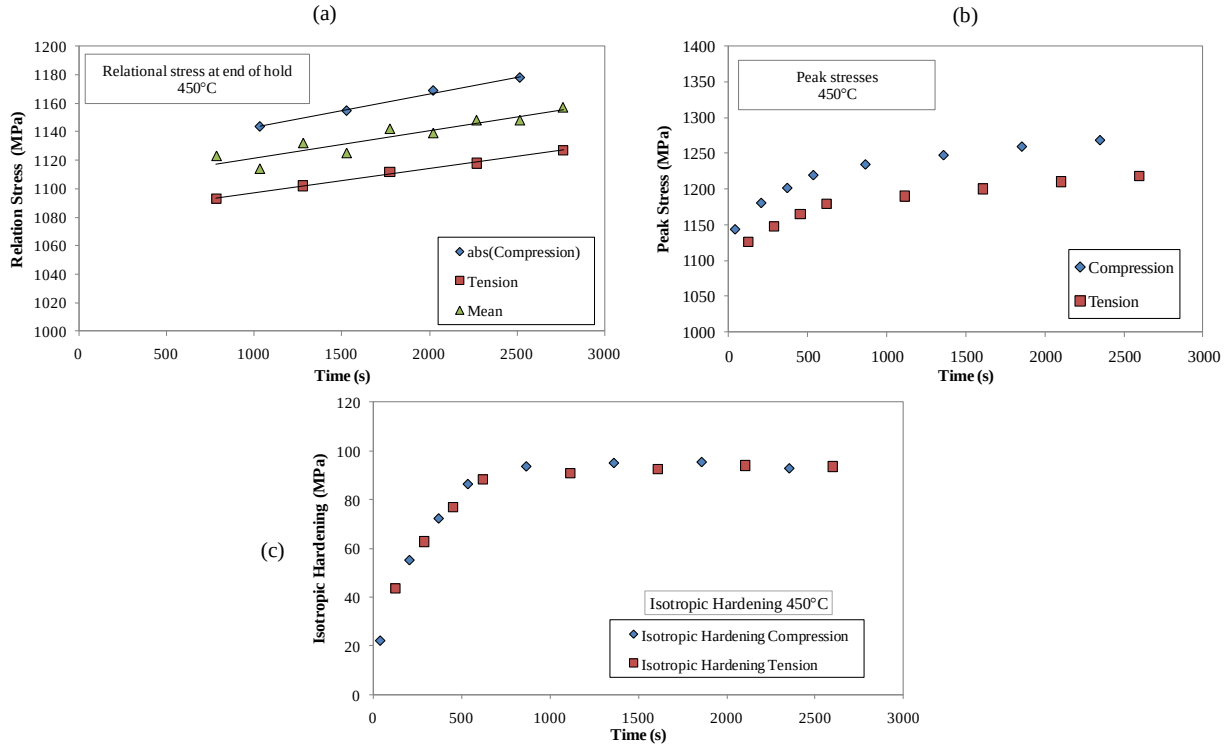

Figure 5-5. Constitutive experiment stress response results corresponding to slow rate with superimposed holds at 450°C. Shown is (a) relaxation stress at the end of each hold (b) peak stresses (c) calculated isotropic hardening.

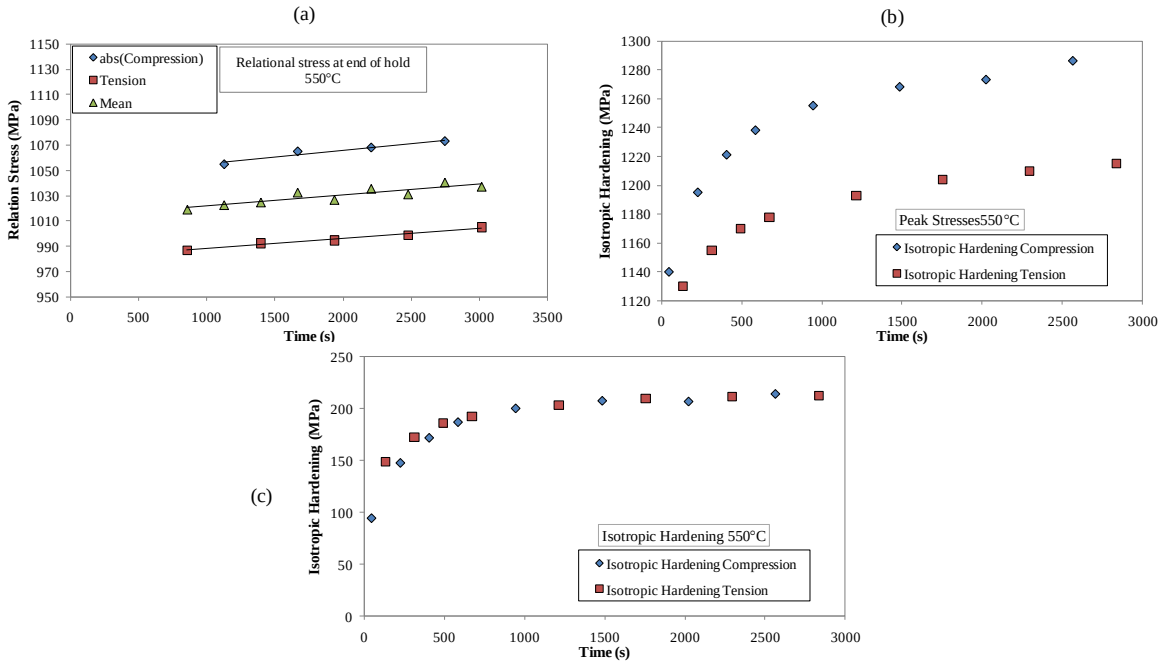

Figure 5-6. Constitutive experiment stress response results corresponding to slow rate with superimposed holds at 550°C. Shown is (a) relaxation stress at the end of each hold (b) peak stresses (c) calculated isotropic hardening.

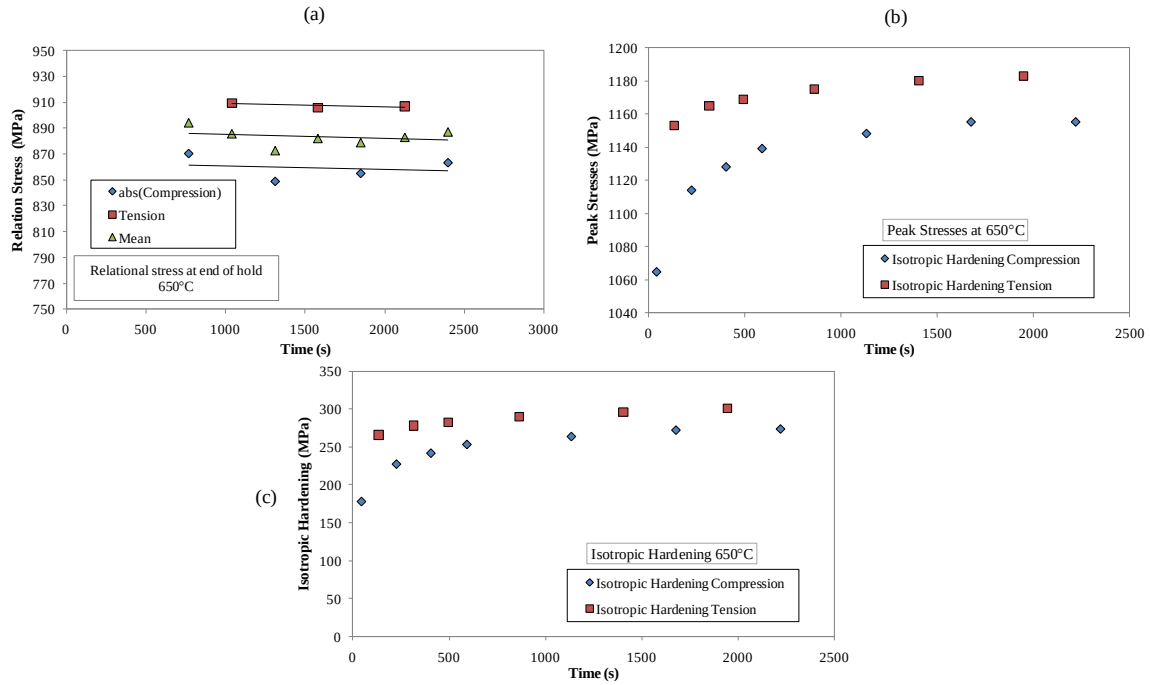

Figure 5-7. Constitutive experiment stress response results corresponding to slow rate with superimposed holds at 650°C. Shown is (a) relaxation stress at the end of each hold (b) peak stresses (c) calculated isotropic hardening.

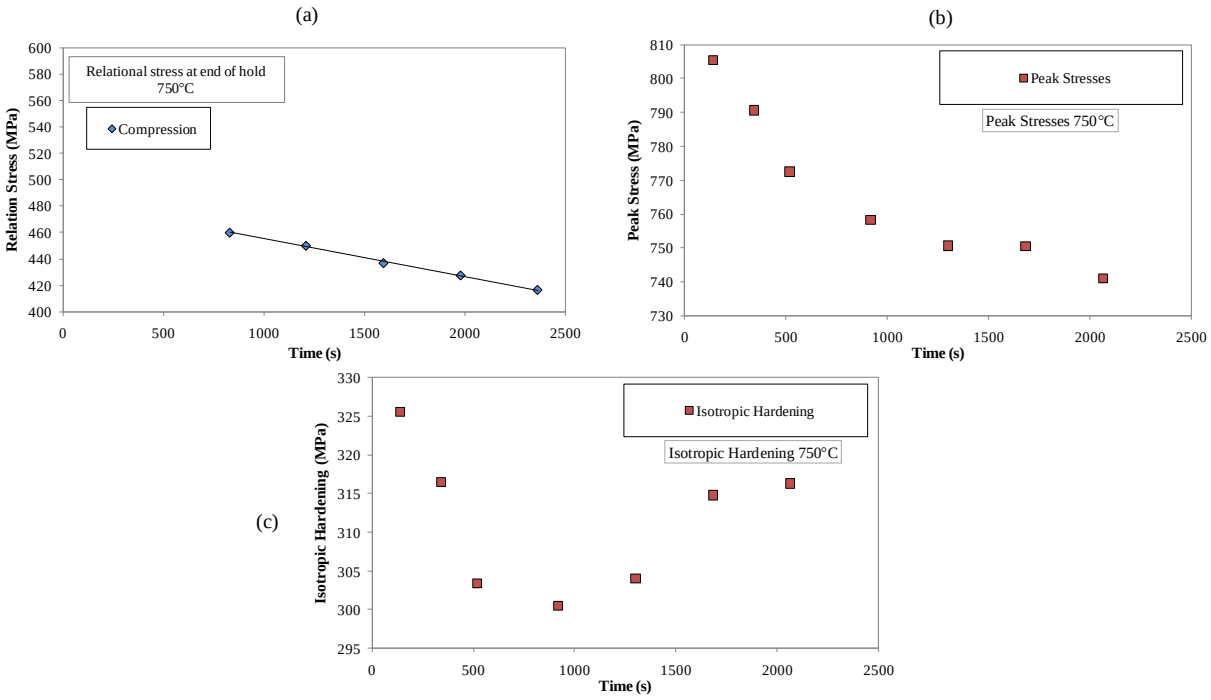

Figure 5-8. Constitutive experiment stress response results corresponding to slow rate with superimposed holds at 750°C. Shown is (a) relaxation stress at the end of each hold (b) peak stresses (c) calculated isotropic hardening.

With the exception of 750°C, isotropic hardening saturates early into cycling. The anomalous response at 750°C may be due to lacking the tensile relaxation response. Never the less, as isotropic hardening is observed to saturate quickly between 450°C and 650°C, evolution of this ISV will be treated as insignificant and neglected in the constitutive model. Instead the threshold stress inherits the effects of the saturated isotropic hardening.

5.1.3 Calibration Results

Constitutive model parameters are listen in Table 5-3. Fitted responses are shown in Fig. 5-9, Fig. 5-10, Fig. 5-11 and Fig. 5-12.

Table 5-3: IN100 unified creep-plasticity constitutive model parameters

IN100 Constitutive Model Parameters										
Temperature (°C)	α (°C^{-1})	E (GPa)	ν	Q (kJ·(mol·K)$^{-1}$)	A (s^{-1})	n	κ (MPa)	A_1 (GPa)	B_1	D (MPa)
450	1.50E-05	192.60	0.33	319	836.61	17.53	105.30	85.91	118.1	85.0
550	1.50E-05	182.73	0.33	319	836.61	13.67	26.47	279.11	522.3	36.4
650	1.50E-05	177.45	0.33	319	836.61	11.77	12.73	182.60	534.6	25.6
750	1.50E-05	149.92	0.33	319	836.61	10.09	1.50	150.00	1009.0	15.0

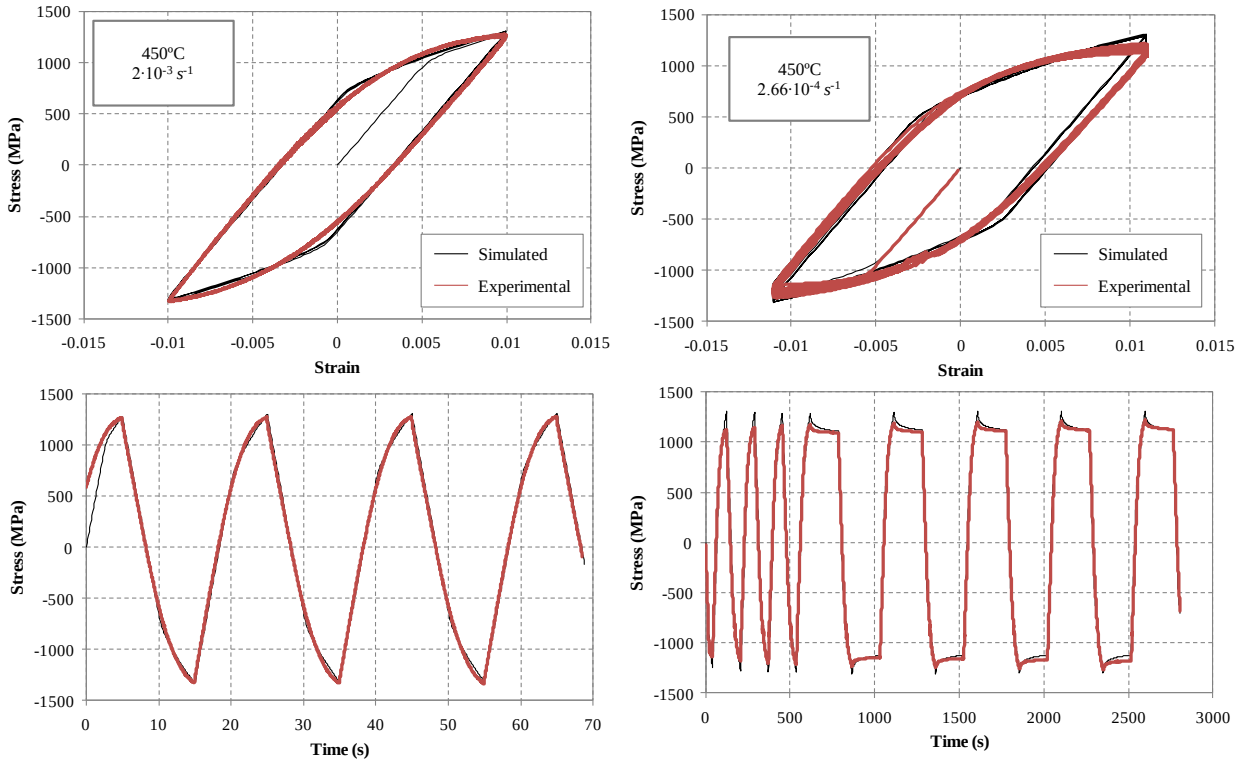

Figure 5-9. IN100 isothermal fit for two strain rates at 450°C.

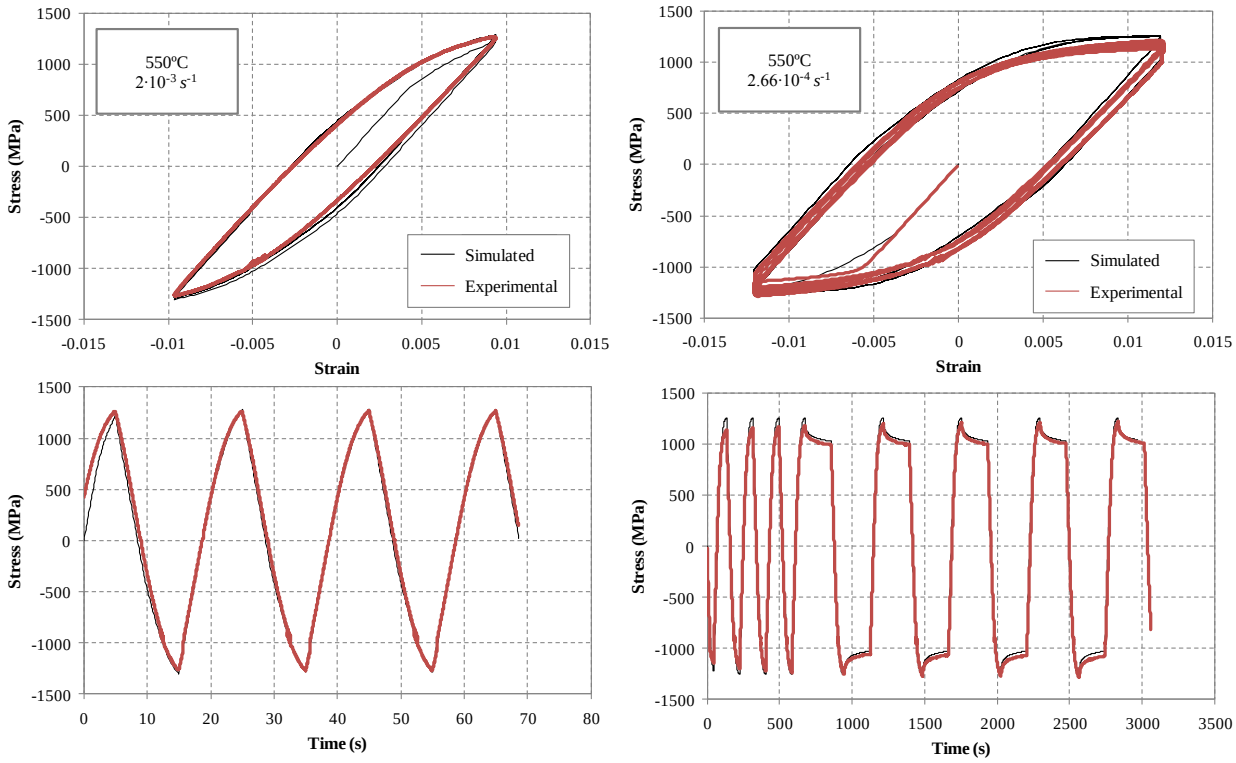

Figure 5-10. IN100 isothermal fit for two strain rates at 550°C.

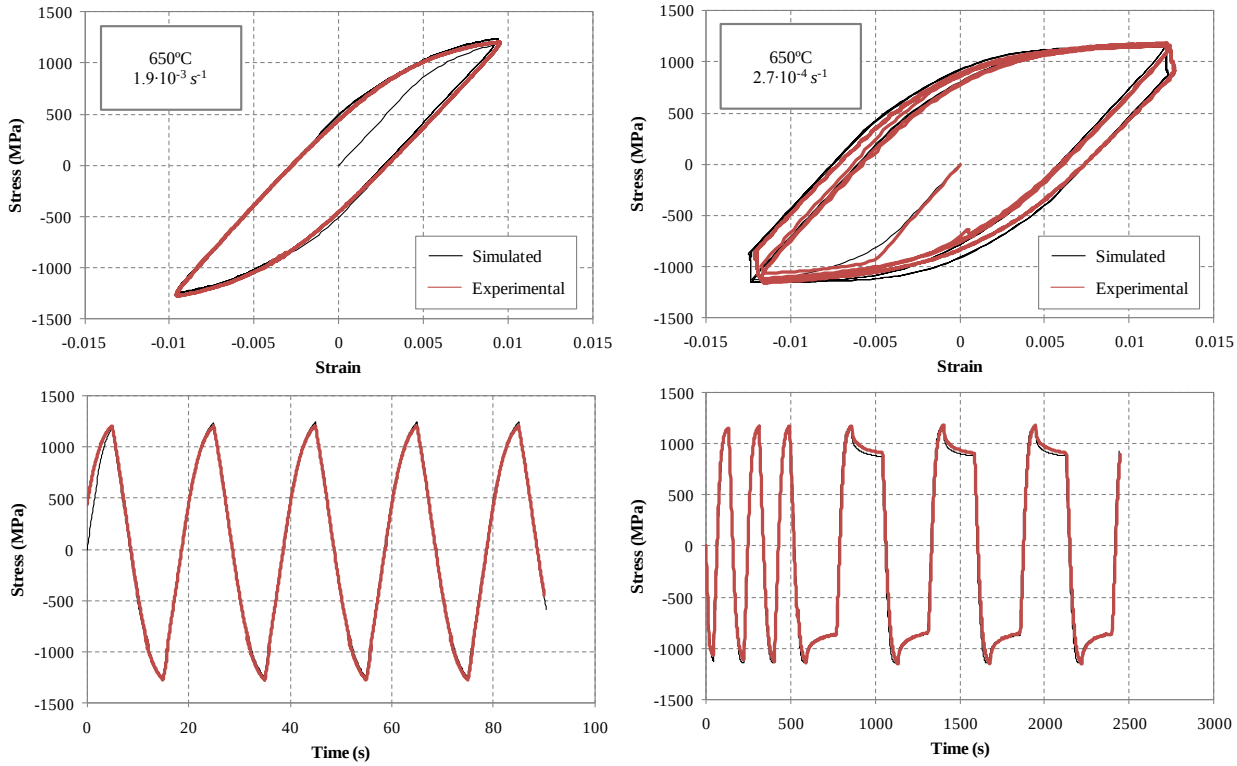

Figure 5-11. IN100 isothermal fit for two strain rates at 650°C.

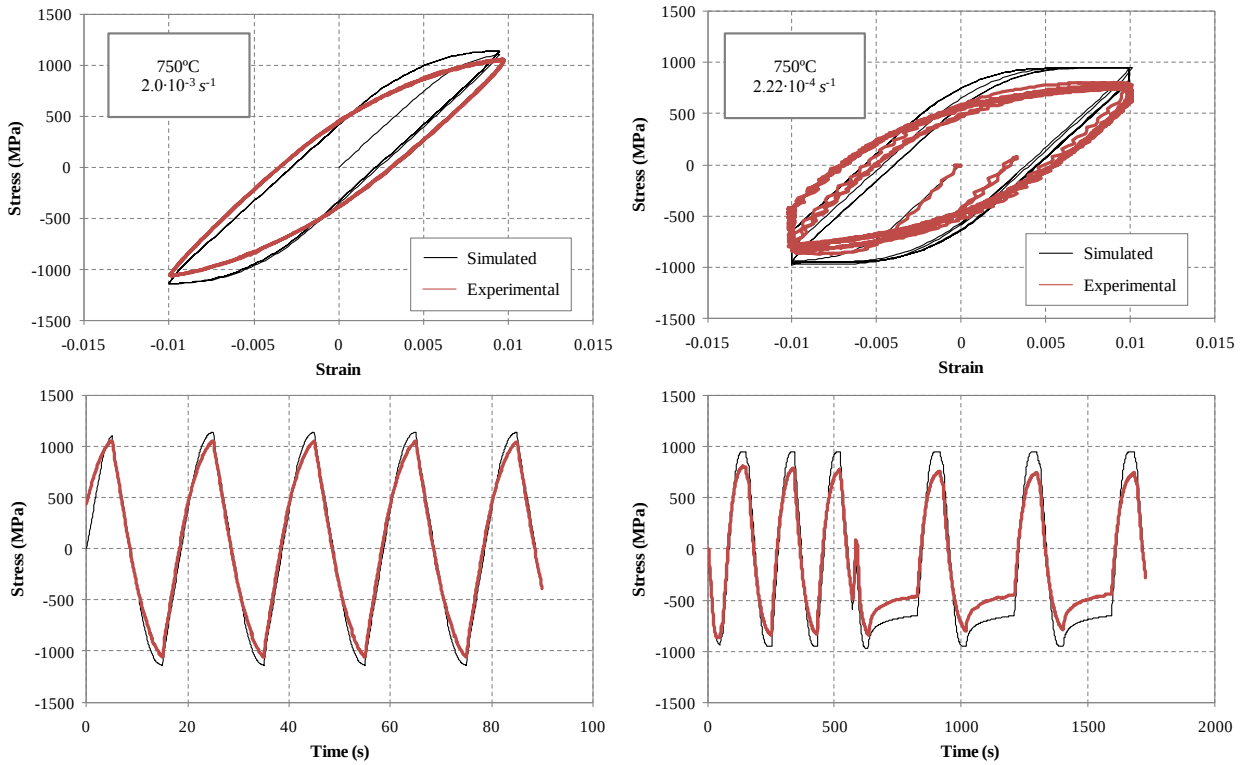

Figure 5-12. IN100 isothermal fit for two strain rates at 750°C.

A linear interpolation scheme is utilized to determine material parameters at temperatures in between 450°C, 550°C, 650°C and 750°C. Predicted TMF responses are shown in Fig. 5-13.

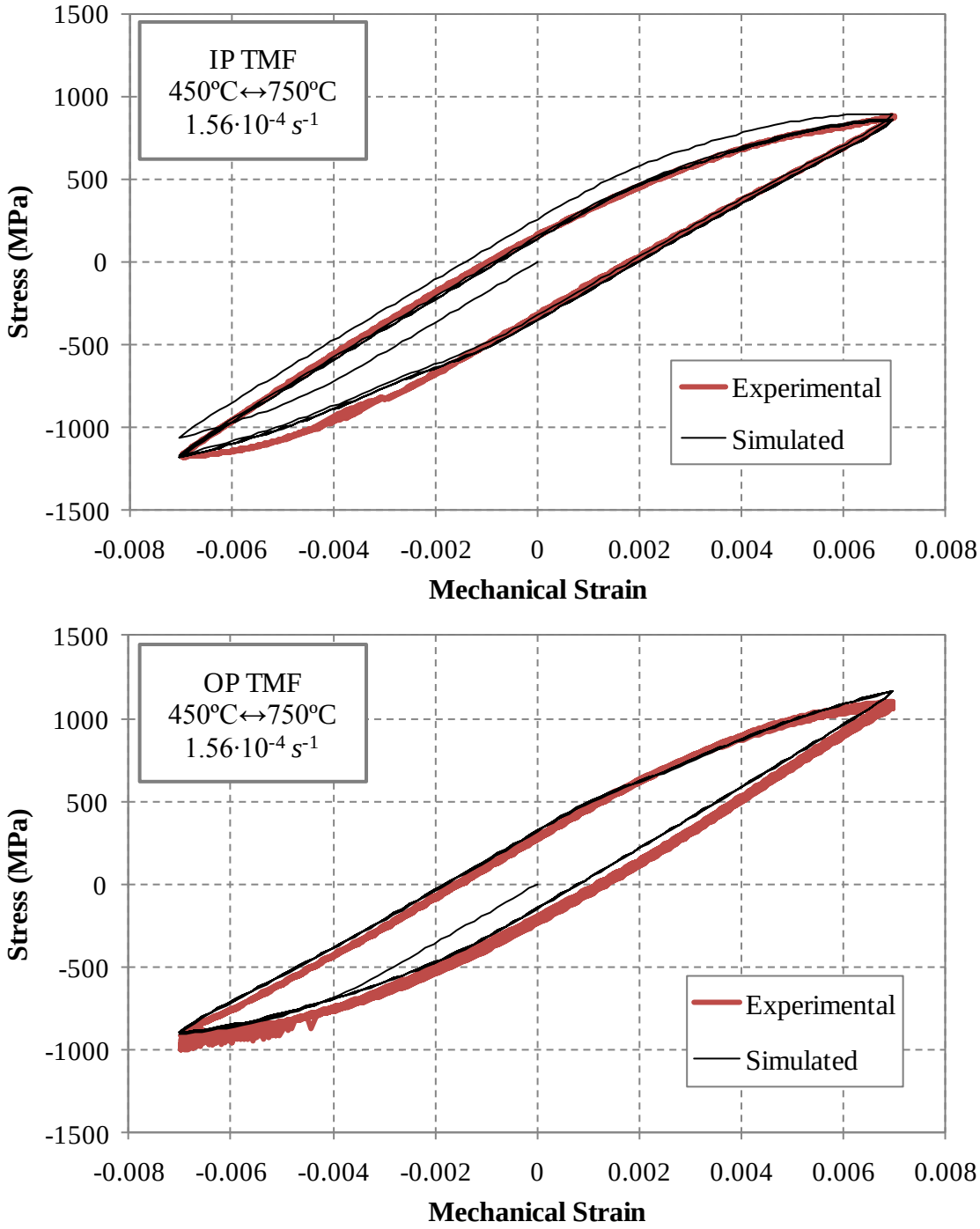

Figure 5-13. Experimental and numerical OP and IP uniaxial TMF results.

With the exception of 750°C all isothermal fits capture flow stresses at both strain rates well and also capture stress relaxation well. TMF predictions for both IP and OP TMF match the

experimental results well. As the primary objective of developing the constitutive model is to determine the localized notch response under TMF loadings, it is not critical that the isothermal 750°C results are poorly fit. The poor fit may be due to significantly increased diffusional flow that the chosen flow rule cannot correctly capture.

5.2 CM247LC DS

A computationally efficient method is necessary for studying the fatigue notch effects observed experimentally. Efficiency is critical to perform a large parametric study across several notch specimen geometries and applied loads. Additionally, sufficiently fine meshing is necessary to capture relevant spatial gradients in the component analysis.

Crystal plasticity is advantageous as the method explicitly accounts for the 3D crystal structure in determination of macroscopic scale quantities such as stress and strain. However, for modeling DS alloys, an average technique is needed to homogenize the response within the plane of isotropy. Homogenizing the response involves performing the same simulation multiple times, each time varying the secondary angle (euler angle θ) and finally averaging all responses. Additionally, axisymetric conditions cannot be utilized and as such a full 3D finite element model is necessary. For the notched components in this study fully 3D models using quarter symmetry required roughly 100 thousand elements for a sufficiently refined mesh.

The transversely isotropic model developed by Shenoy et al. [67-68] reduces the explicit considerations for deformation on individual crystallographic planes and reduces the response to the macroscopic level. In this fashion axisymetric conditions can be taken advantage of to create a reduced finite element model that requires only 5000 elements for a refined mesh. The computational advantages here are (1) using a fundamentally less expensive constitutive model

(2) no need for response homogenization or averaging (3) a factor of 20 reduction in the total number of elements in this particular implementation.

A comparison between the two alloys, CM247LC DS and GTD-111, is shown in Fig. 5-14.

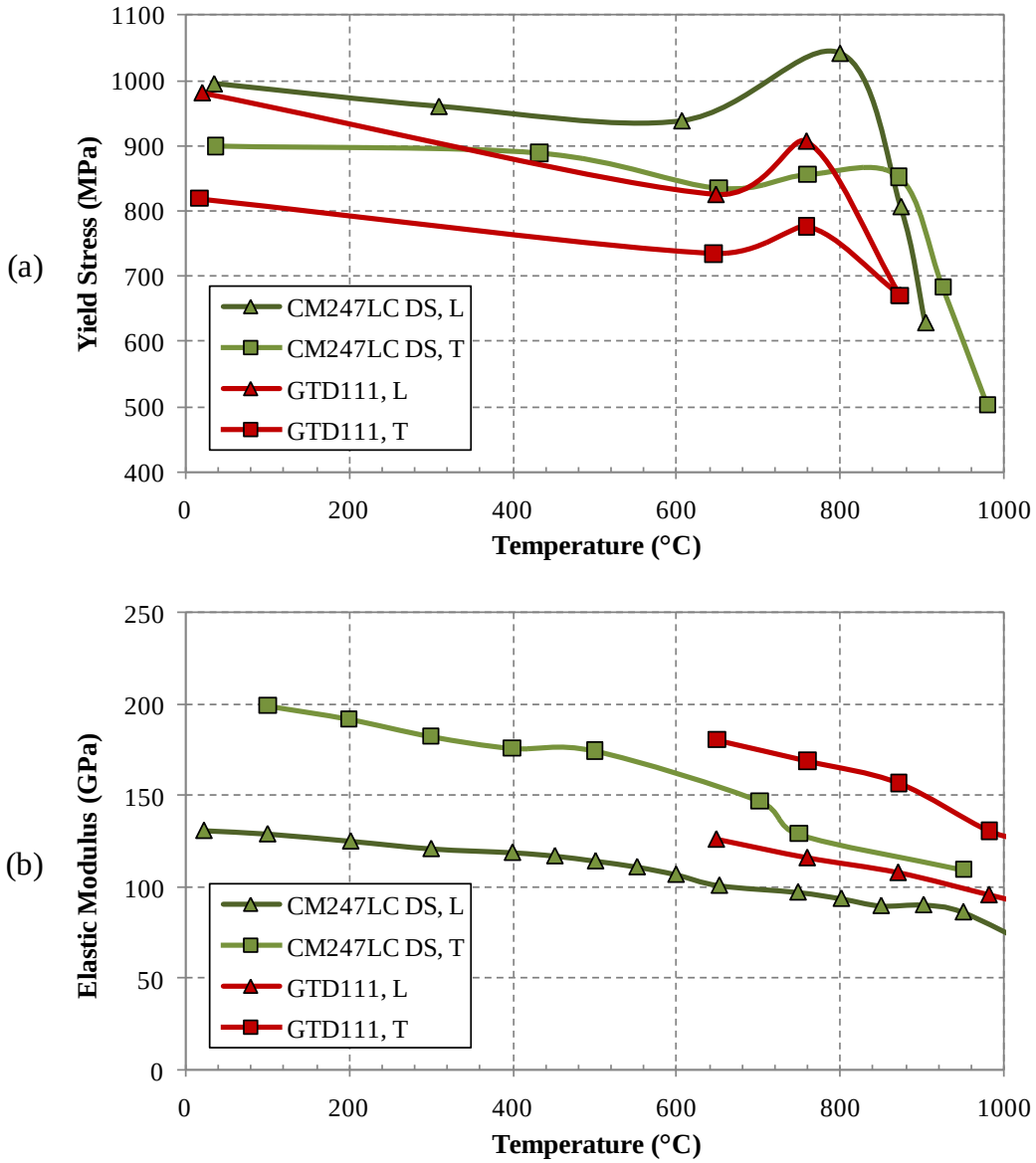

Figure 5-14. Comparison of (a) yield strength and (b) modulus between the alloys CM247LC DS [6] and GTD-111 [73] as a function of temperature.

The yield strength of CM247LC DS can be up to 100 *MPa* larger than GTD-111 at a given temperature. GTD-111 is also more stiff by about 20 *MPa*. For the same applied strain in the longitudinal direction, GTD-111 would be expected to yield larger plastic strains. Never the less, the two alloys have comparable behavior and GTD-111 simulations will be sufficient for determining trends.

5.2.1 Transversely Isotropic Viscoplasticity Continuum Model

Details of the transversely isotropic constitutive model, including integration procedure and necessary thermodynamic constraints may be found in Shenoy's works [56, 67-68]. The foundation of the continuum constitutive model can be expressed in the formulation of deformation gradient. Kinematics of thermomechanical finite elastoplastic deformation are quantified utilizing a multiplicative decomposition of the deformation gradient into thermal, plastic and elastic components.

$$\boldsymbol{F} = \boldsymbol{F}^{e} \cdot \boldsymbol{F}^{p} \cdot \boldsymbol{F}^{\theta} \tag{5.14}$$

Here $\boldsymbol{F}^{e}$ represents linearized elastic deformation and rigid body lattice rotation, $\boldsymbol{F}^{p}$ the plastic deformation and $\boldsymbol{F}^{\theta}$ expansion of the lattice due to temperature changes. An illustration of the multiplicative decomposition is shown in Fig. 5-15.

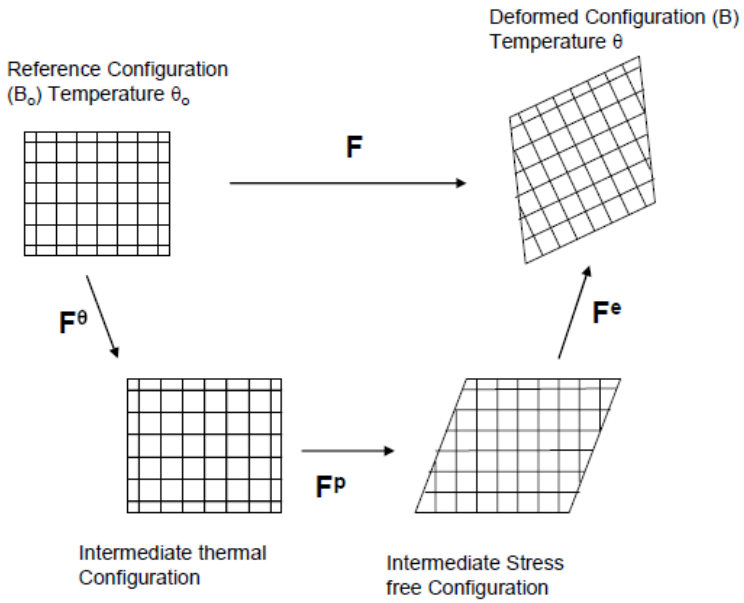

Figure 5-15. Multiplicative decomposition of the deformation gradient for finite elastic-plastic deformation under TMF conditions [68].

The second Piola-Kirchhoff stress, σ^{PK2}, is expressed as a linear relationship between the Green elastic strain and the 4th rank elasticity tensor.

$$\boldsymbol{\sigma}^{PK2} = \boldsymbol{C}_0 : \boldsymbol{E}^e \tag{5.15}$$

where the Green elastic strain tensor is expressed in terms of the elastic part of the deformation gradient.

$$\boldsymbol{E}^e = \left(\boldsymbol{F}^{eT} \cdot \boldsymbol{F}^e - \boldsymbol{I} \right) \tag{5.16}$$

The thermal expansion portion of the deformation gradient can expressed using the definition of the velocity gradient associated with thermal expansion. Assuming that thermal expansion is isotropic the velocity gradient is expressed as

$$\boldsymbol{L}_o^\theta = \dot{\boldsymbol{F}}^\theta \cdot \left(\boldsymbol{F}^\theta\right)^{-1} = \alpha_\theta \dot{\theta} \boldsymbol{I} \tag{5.17}$$

where α_θ is the coefficient of thermal expansion and $\dot{\theta}$ is the temperature time rate of change. Direct integration results in an expression for the thermal part of the deformation gradient at some time $t + \Delta t$ as a function of the previous thermal deformation gradient at time t.

$$\boldsymbol{F}_{t+\Delta t}^\theta = \exp\left(\boldsymbol{L}_o^\theta \Delta t\right) \boldsymbol{F}_t^\theta \tag{5.18}$$

The plastic part of the deformation gradient is quantified using a power-law viscoplastic flow rule that defines the symmetric part of the viscoplastic velocity gradient.

$$\boldsymbol{D}_i^p = \dot{p}\boldsymbol{N} = A \exp\left(-\frac{Q}{RT}\right) \left\langle \frac{\bar{\sigma} - K}{D_0} \right\rangle^n \boldsymbol{N} \tag{5.19}$$

Where $\bar{\sigma}$ is the effective stress, K the threshold stress, D_0 the drag stress, Q the activation energy, R the universal gas constant, T the temperature, $\boldsymbol{N}$ a unit vector in the direction of inelastic strain rate and A a constant. The threshold stress and exponent are temperature dependent material parameters. The effective stress is a function of the symmetric overstress,

$$\bar{\sigma} = f(\Sigma) \tag{5.20}$$

$$\boldsymbol{\Sigma} = \boldsymbol{\sigma}^{'PK2} - \boldsymbol{\alpha} \tag{5.21}$$

where α is the backstress which is treated as an internal state variable. The functional form of the effective stress is complicated and can be found in [67-68]. The backstress evolves according to the evolution equation,

$$\dot{\alpha} = H\left(L\boldsymbol{D}_i^p - \boldsymbol{\pi}\dot{p}\right) - R_\alpha \bar{\alpha}^m \boldsymbol{\pi} \tag{5.22}$$

where H, L, R_α and m are temperature dependent material constants. The tensor $\boldsymbol{\pi}$ is a function of the backstress and can be found in [67-68]. The first part of the backstress evolution equation provides hardening, the second term dynamic recover and the last static thermal recovery.

5.2.2 Transversely Isotropic Material Constants

Material parameters were determined by Shenoy [67] in a systematic fashion utilizing isothermal experimental cyclic and creep responses. The five independent elastic constants for defining transverse isotropy were determined directly from isothermal elastic responses across the temperature range of interest. Material constants corresponding to the viscoplastic flow rule and backstress evolution were determined from a minimization procedure implemented within the commercial optimization software Epogy. Details can be found in Shenoy's works [56, 67-68]. Optimal material parameters for GTD-111 are shown in Table 5-4.

Table 5-4: CM247 LC DS transversely isotropic viscoplasticity model parameters [67]

Material parameters

Temperature (°C)	E_L (MPa)	E_T (MPa)	ν_T	ν_L	G_L (MPa)
427	126,340	159,048	0.4	0.195	104,000
650	120,930	156,190	0.4	0.195	97,900
760	103,425	146,667	0.4	0.195	95,200
871	95,200	126,000	0.4	0.195	89,650
982	89,650	121,505	0.4	0.195	82,740
1038	82,740	121,505	0.4	0.195	75,850

Temperature (°C)	K (MPa)	n	ξ	ς	H	L (MPa)	R_α (MPa^{-3})	m
427	100	30	0.33	0.44	130	180	0	–
650	175	22	0.33	0.44	150	310	6.00E − 15	3
760	150	8	0.165	0.22	500	275	1.00E − 13	3
871	100	4	0.056	0.075	200	250	5.75E − 13	3
982	20	4	0.056	0.075	225	190	4.00E − 12	3
1038	20	4	0.056	0.075	125	190	–	–

Q (K J/mol)	R (J/mol K)	A (1/s)	D_0 (MPa)
319	8.314	3.3174E + 7	270

Initial conditions: at time $t = 0$, $\sigma = \mathbf{0}$, $\alpha = \mathbf{0}$.

Note that in the original reference the values for ν_T and ν_L are mistakenly swapped. TMF simulations were performed utilizing linear interpolation for temperatures between isothermally calibrated temperatures.

5.3 Finite Element Modeling

Reduced FEA models of the full notched specimens were utilized that modeled only the gage section of each notched specimen. The reduction greatly reduces the number of necessary elements without compromising the accuracy of the local notch response. The axisymetric model corresponding to notch geometry $k_t = 1.3$ is shown in Fig. 5-16 along with all applied boundary conditions, constraints and material orientations.

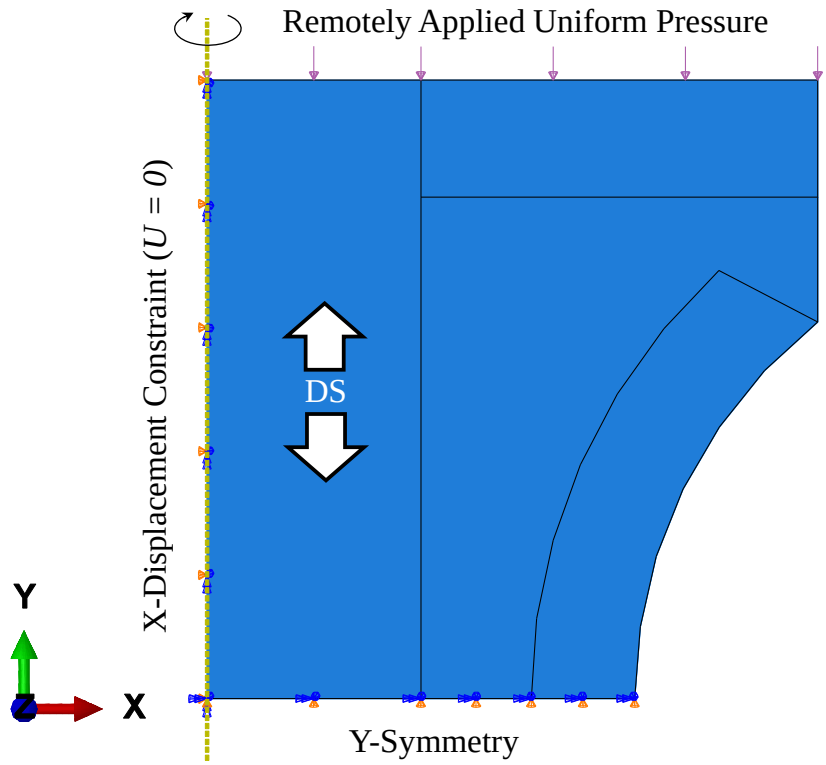

Figure 5-16. Axisymetric model of circumferentially notched specimen showing applied boundary conditions.

Y-symmetry conditions are applied at the notch root (displacement and rotation). Displacement constraints in the x-direction are set along the axis of symmetry (displacement and rotation). All other surfaces are treated as free surfaces (zero traction). The axis perpendicular to the plane of isotropy (X-Z plane) is always oriented in the direction of the remotely applied load. The uniformly applied pressure was determined based on the desired net section stress amplitude and the ratio of the net section area and applied surface area. Simulations were performed utilizing 300 *MPa,* 400 *MPa* and 500 *MPa* net section stress values. The same boundary conditions and constraints were utilized across all notch geometries.

Mesh convergence was excellent utilizing roughly 5000 quadrilateral elements for each geometry. Fine mesh refinement was utilized along the notch surface close to the notch root to accurately capture the response and relevant gradients necessary for post processing. Meshes were verified to have no heavily distorted elements; no elements had interior angles greater than 145° or less than 35°. Meshes for each specimen geometry are shown in Fig. 5-17.

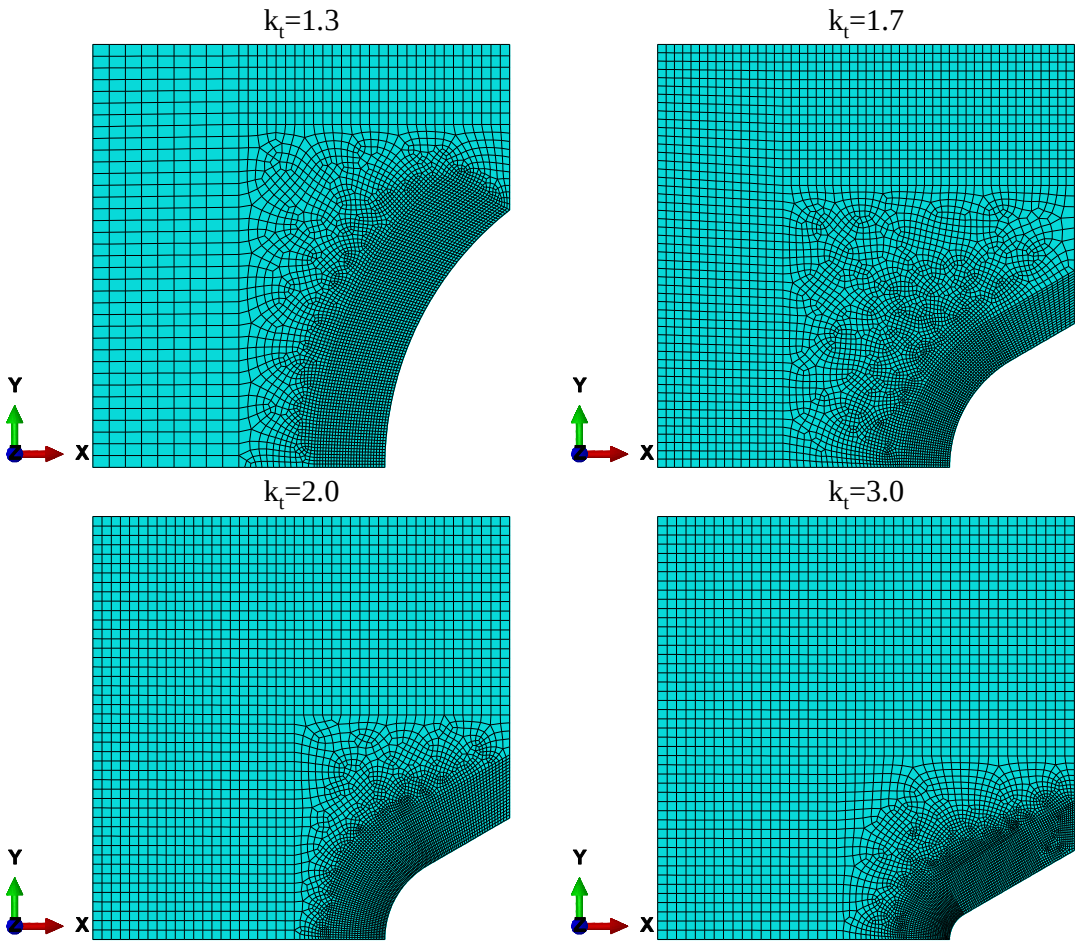

Figure 5-17. Finite element meshes for each circumferentially notch geometry.

All performed simulations utilized a 500°C↔950°C temperature range and a 180 *s* cycle time. Due to computational time required for a parametric study, only three reversals (1.5 cycles) were performed. The final cycle (final 2 reversals) were utilizing for all analyses. High temperature loading was applied first within the first reversal to guarantee two high temperature loads within 270 *s*. The first reversal behaves as a monotonically applied load on virgin material which promotes hardening and sets residual stress fields. These 270 s simulations took approximately 250 to 300 *hrs* of CPU time each.

To illustrate the evolution of material response within a notch the stress-strain response for an element along the notch root in a 500°C↔950°C OP TMF crystal viscoplasticity (CVP) simulation from Kupkovits [6] is shown in Fig. 5-18.

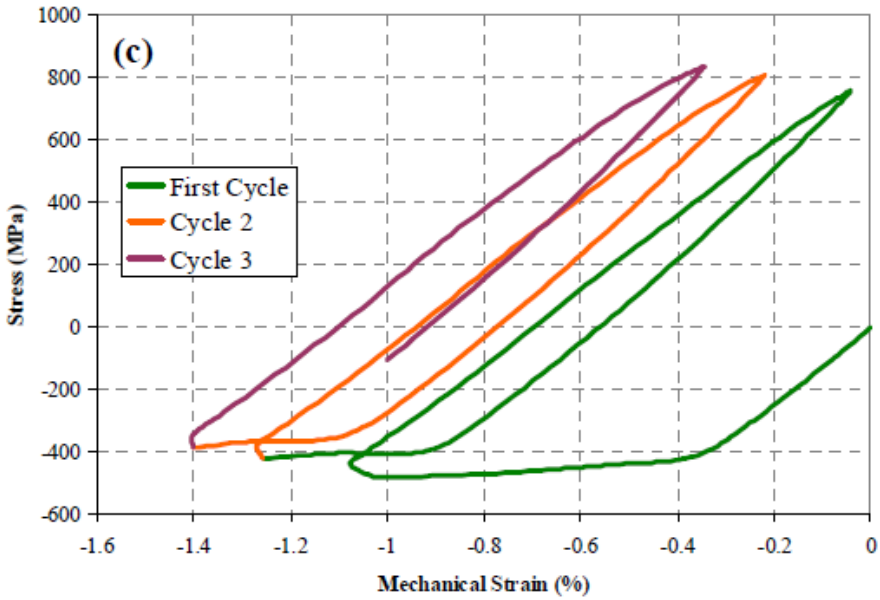

Figure 5-18. Stress-strain response of an element on the notch root in a simulation performed by Kupkovits [6].

The inelastic strain range corresponding to each hysteresis loop changes little between the 3 cycles. The stress range changes little however mean stress does increase each cycle with no clear stabilization. The ratchet strain decreases, however it is unclear if it has stabilized. As the inelastic strain range changes little within the first three cycles and there is no clear saturation in mean stress, it is sufficient to simulate three reversals rather than cycles for the purposes of comparing the influences of notch severity while minimizing computational costs. The stress-strain response at a notch root element from a transversely isotropic notch simulation is shown in Fig. 5-19.

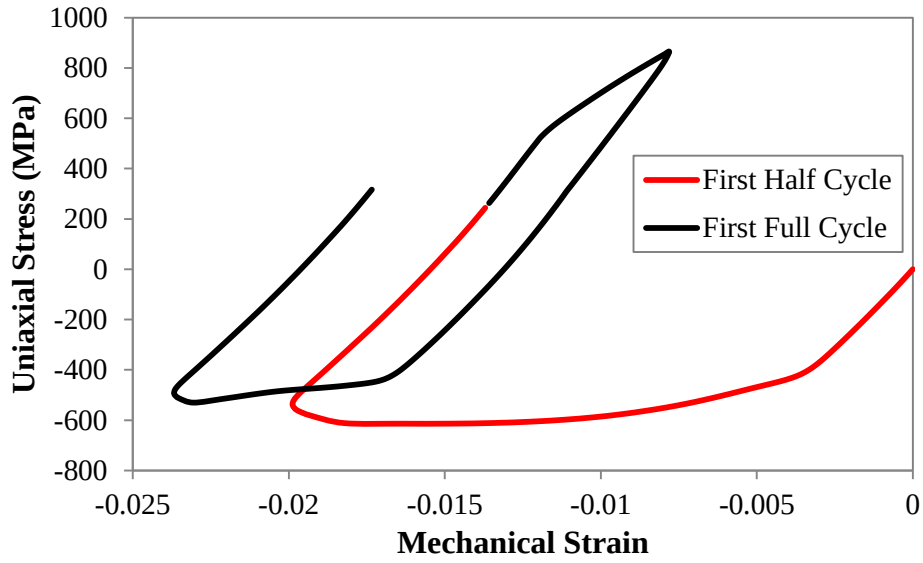

Figure 5-19. Stress-strain response from an element at the notch root under OP TMF 500°C↔950°C using the transversely isotropic GTD-111 model.

As expected the first half cycle response behaves like a monotonic loading/unloading which initiates hardening and produces residual stress fields that affect the next full cycle. All simulated results will utilize the final 2 reversals as a cycle, utilizing the first reversal to set residual stresses.

Simulated OP TMF GTD-111 transversely isotropic stress-strain histories for uniaxial conditions with alternating applied stresses in the longitudinal direction are shown in Fig. 5-20. The corresponding cyclic inelastic strain range and inelastic ratcheting increment histories are shown for uniaxial loading in Fig. 5-21.

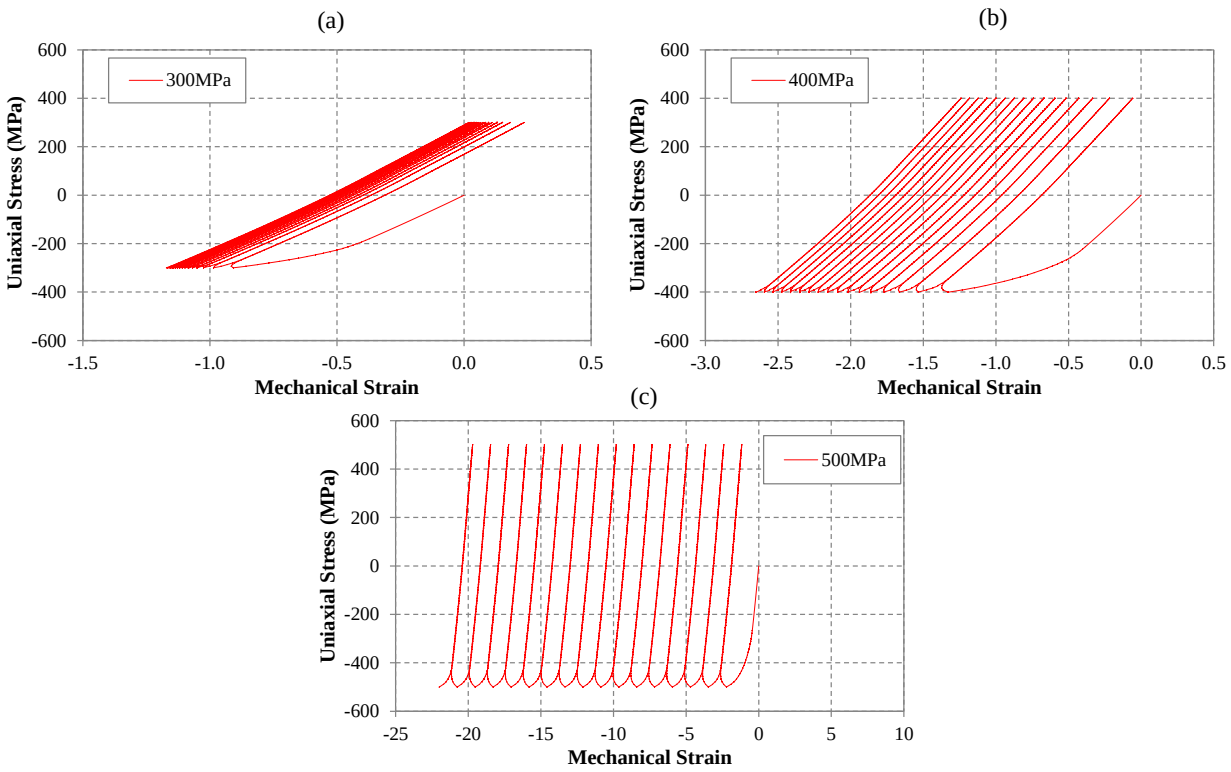

Figure 5-20. Simulated uniaxial $500°C \leftrightarrow 950°C$ OP TMF GTD-111 loaded uniaxially.

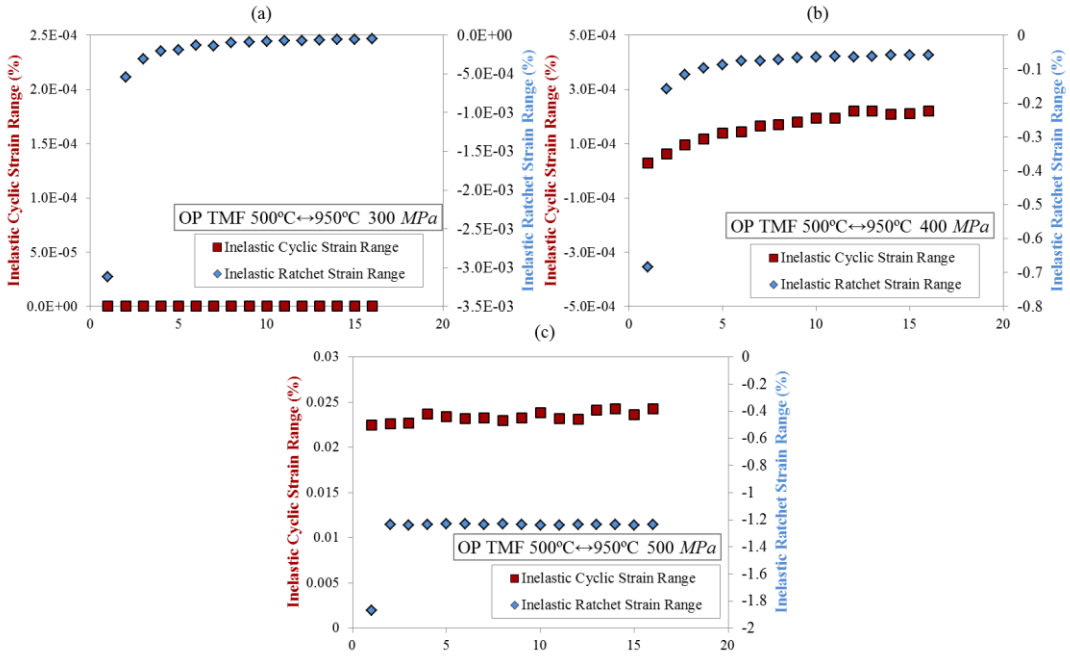

Figure 5-21. Cyclic inelastic strain range and inelastic ratcheting increment for uniaxially loaded GTD-111 under OP TMF.

Simulated results indicate that cyclic inelastic strain range under uniaxial stress conditions continues to evolve even after 15 cycles. For the case of 300 *MPa*, the cyclic inelastic strain range is negligible. At 400 *MPa* the per-cycle increase in cyclic inelastic strain range is on the same order as the cyclic inelastic strain range. At 500 *MPa* the per-cycle increase in cyclic inelastic strain range is small compared to the cyclic inelastic strain range. The response under multiaxial loading a notch will likely saturate at a faster rate due to additional constraint effects. As such it is sufficient to utilize the response over three reversals so that calculations may be made less expensive.

CHAPTER 6 THERMOMECHANICAL FATIGUE OF NOTCHED SPECIMENS: INFLUENCE OF APPLIED BOUNDARY CONDITIONS

The effects of applied boundary conditions on the thermomechanical fatigue of notched specimens are presented in the following chapter. The influence of remotely applied force or displacement boundary conditions on life to crack initiation is studied by performing IP and OP TMF experiments on circumferentially notched specimens with varying elastic stress concentrations between $k_t = 1.3$ and $k_t = 2.0$. Materials utilized in this study include a directionally-solidified Ni-based superalloy, CM247LC DS loaded longitudinally, and a polycrystalline Ni-based superalloy, IN100.

6.1 IN100 TMF Results

6.1.1 OP TMF IN100

Force control and displacement control IN100 OP TMF 450°C↔750°C life results are shown as a function of net section stress amplitude in Fig. 6-1. Mean stresses developed during cycling in displacement control are shown as well.

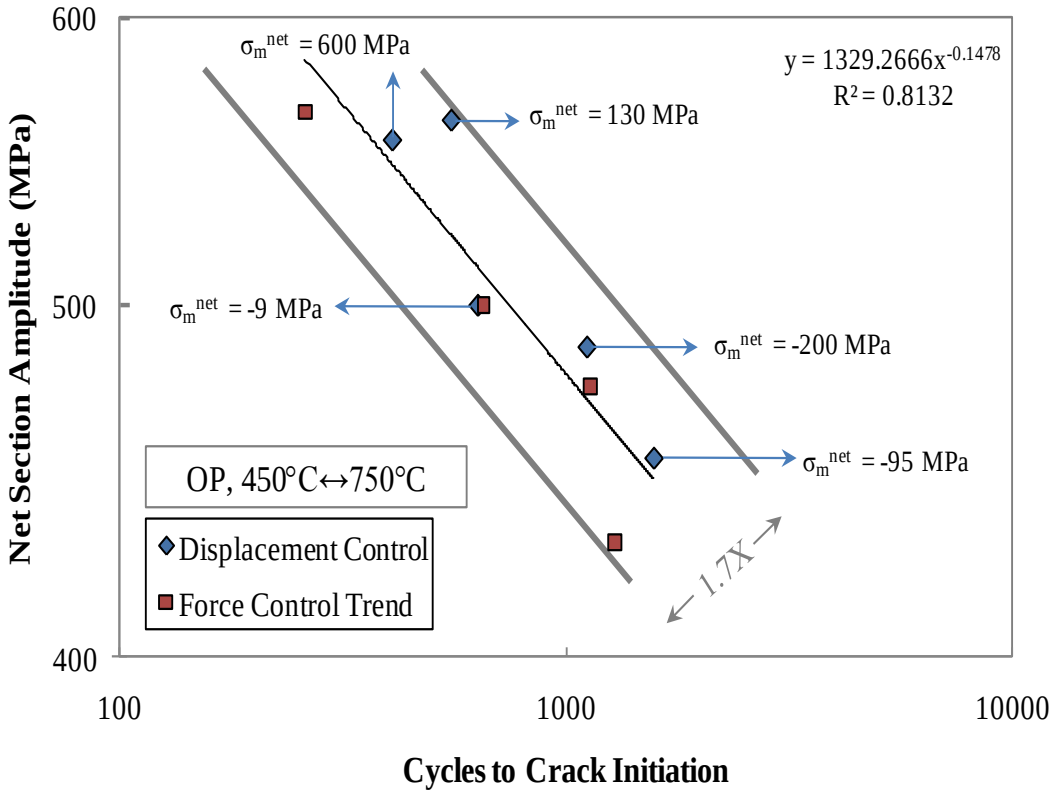

Figure 6-1. IN100 OP TMF life results based on net section stress.

Under the applied conditions and stress amplitudes, initiation lives under both control modes followed the same life trend within a factor of 1.7. Mean stresses developed under displacement control loading. This is expected for TMF tests as there is tension-compression asymmetry due to temperature cycling. Mean stresses develop even from pure elastic loading due to a continuous variation of the modulus, see Fig. 6-2.

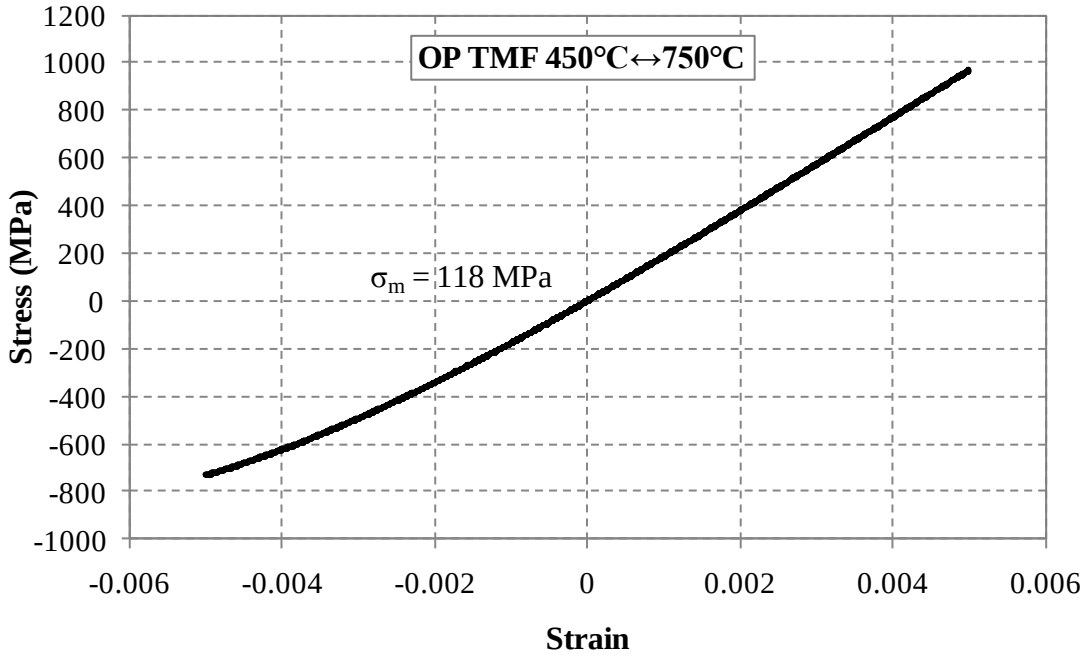

Figure 6-2. Fully reversed uniaxial elastic stresses calculated from temperature dependent elastic properties for IN100 OP TMF.

Most displacement control tests were not run fully reversed. Rather, the displacement mean and amplitudes were determined to follow force control displacement response trends which were performed first. The displacement response from force control experiments developed mean displacements due to creep and plastic ratcheting. An example for CM247LC DS is shown in Fig. 6-3.

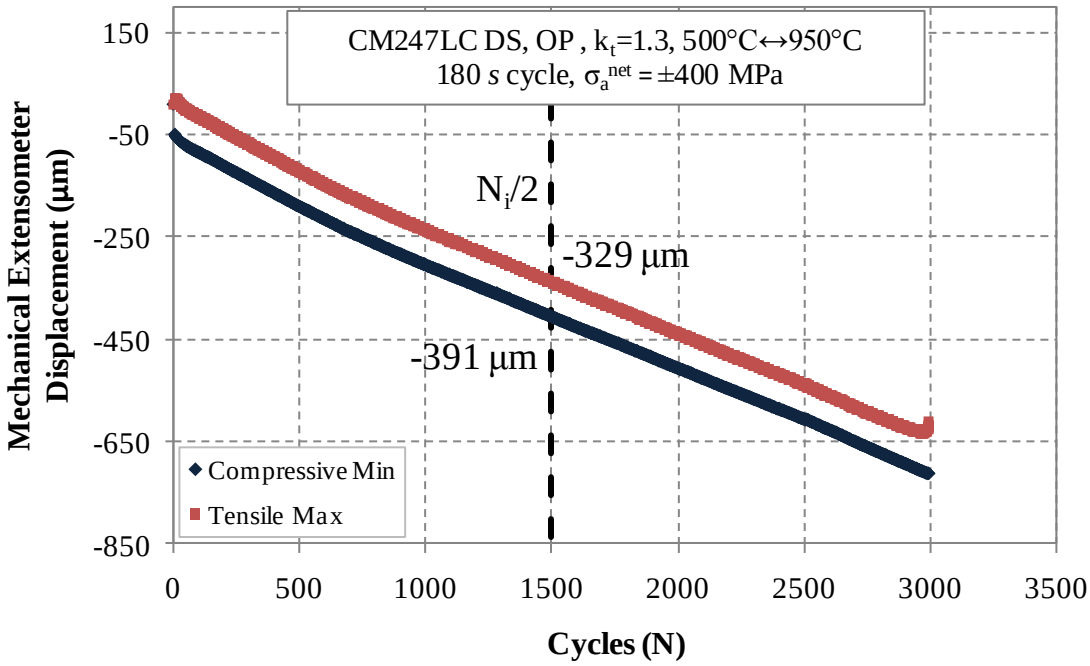

Figure 6-3. Displacement response under force control TMF.

Stress histories for displacement control tests are shown in Fig. 6-4. All OP TMF IN100 displacement control conditions and result are shown in Table 6-1. Force control results are in Table 6-2.

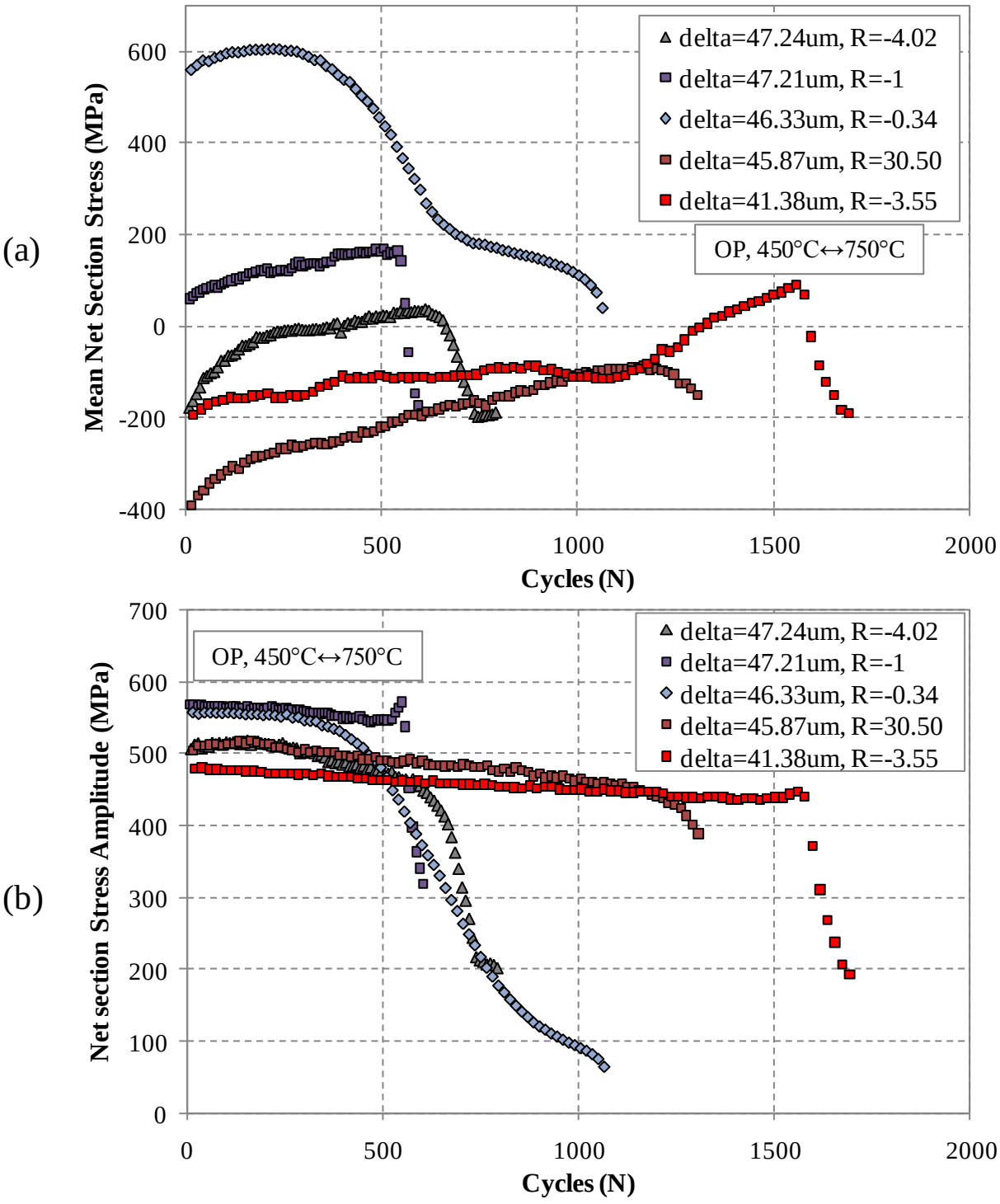

Figure 6-4. Net section mean stress and stress amplitude histories for OP TMF displacement control IN100 tests.

Table 6-1: OP TMF IN100 notch displacement control conditions and results

OP TMF IN100 Notch Displacement Control TMF Tests									
Period (s)	T_{min} (°C)	T_{max} (°C)	$\Delta\delta_m$ (μm)	Mean δ_m (μm)	R_δ	k_t	σ_a^{net} (MPa)	σ_m^{net} (MPa)	Initiation Life (cycles)
180	450	750	45.87	-24.49	30.50	2	490	-200	1114
180	450	750	47.24	-14.22	-4.02	2	500	-9	636
180	450	750	47.21	0.00	-1.00	2	562	130	555
180	450	750	46.33	11.37	-0.34	2	555	600	410
180	450	750	41.38	-11.60	-3.55	2	457	-95	1570

Table 6-2: OP TMF IN100 notch force control conditions and results

OP TMF IN100 Baseline Force Control TMF Tests									
Period (s)	T_{min} (°C)	T_{max} (°C)	σ_a^{net} (MPa)	R_σ	k_t	$\Delta\delta_m$ (μm)	Mean δ_m (μm)	R_δ	Initiation Life (cycles)
180	450	750	565	-1	2	48.35	-25.89	29.19	260
180	450	750	500	-1	2	46.15	-11.04	-2.83	653
180	450	750	475	-1	2	42.71	-11.70	-3.42	1133
180	450	750	430	-1	2	40.16	-6.98	-2.07	1287

Fracture surfaces for both force control and displacement control OP TMF tests are shown in Fig. 6-5. In all tests multiple crack initiation sites formed around the circumference of the notch root and grew inwards. Under force control cracks grew until some critical size, after which fast fracture occurred leaving a fast fracture pattern on the surface. Under displacement control circumferential cracks grew inwards until fracture, however from the fracture surfaces there is no evidence of a fast fracture occurring. Rather the crack grew in a stable fashion until no material remained.

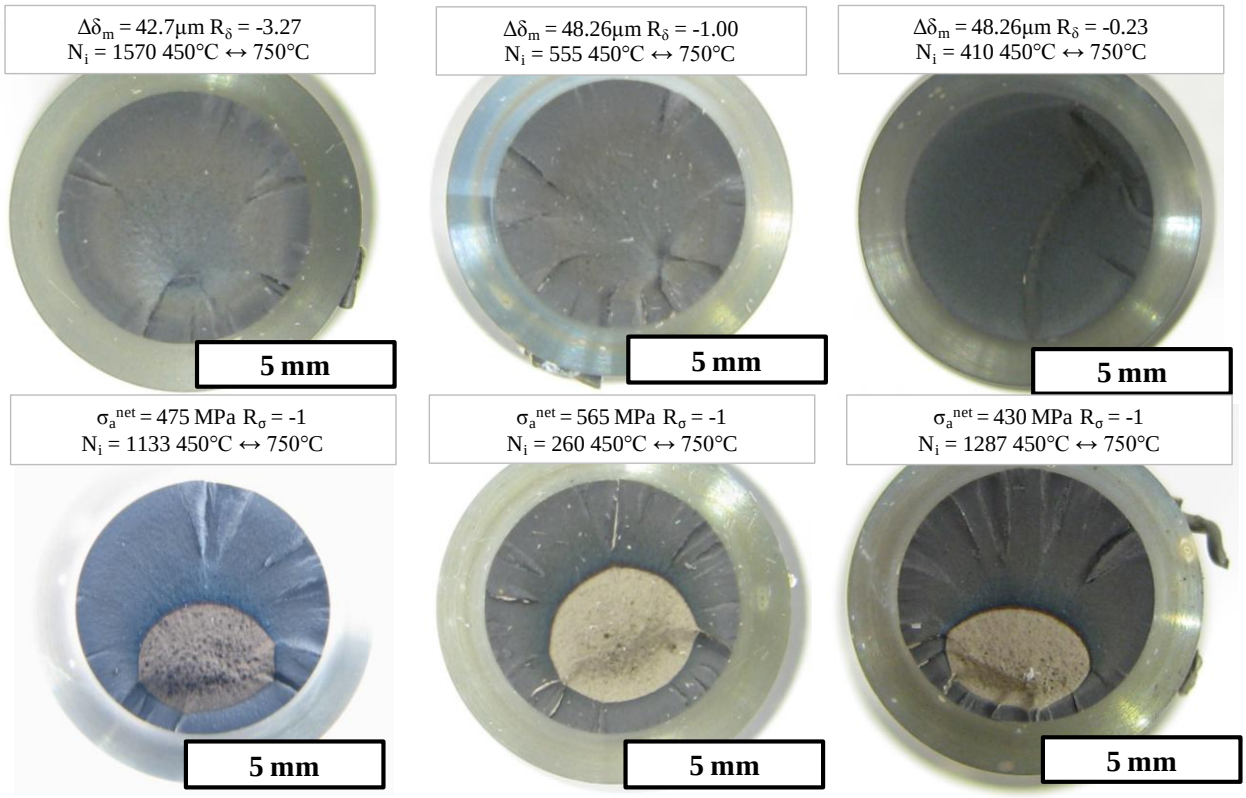

Figure 6-5. Fracture surfaces for OP TMF notch specimens. Top row are displacement control tests, bottom row are force control tests.

The area of fast fracture is on average 29% of the total net section area for the OP TMF specimens shown in Fig. 6-5. Assuming that the cracks grew concentrically this would correspond to an effective crack length of 3.42 *mm*. Using a fracture mechanics approach for a round bar with a circumferential crack under remotely applied force, fast fracture occurs at a predicted crack length of 2.13 *mm*, as shown in Fig. 6-6.

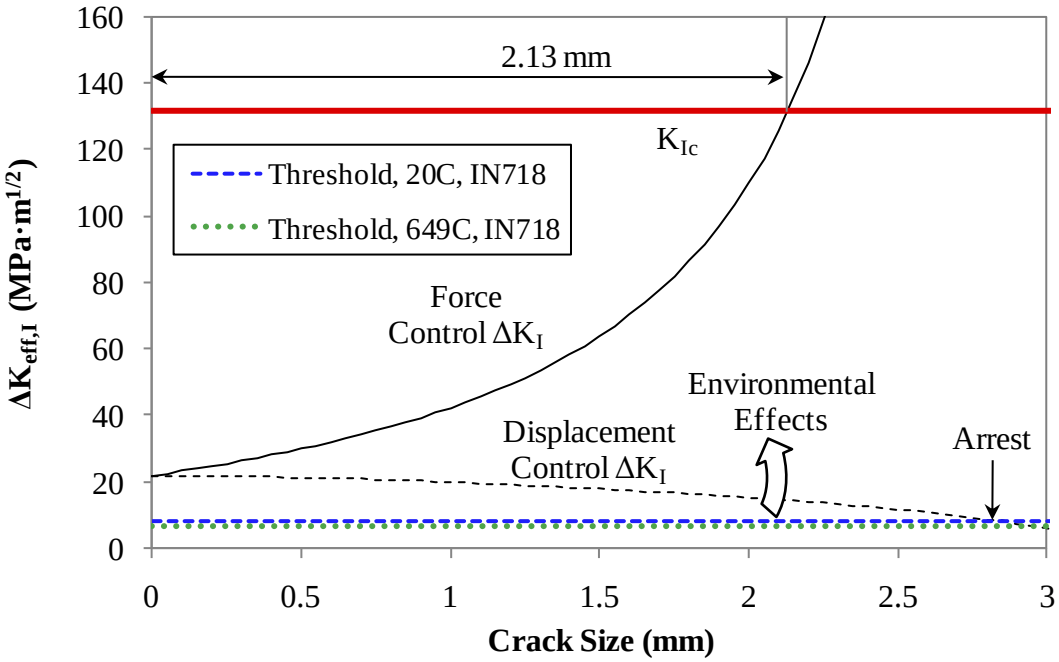

Figure 6-6. Schematic illustrating role of applied boundary conditions on physically small crack growth.

The stress intensity follows the form [26],

$$K = \frac{P}{\pi b^2}\frac{1}{2\beta^{1.5}}\left[1+\frac{1}{2}\beta+\frac{3}{8}\beta^2-0.363\beta^3+0.731\beta^4\right]\sqrt{\pi a} \tag{6.1}$$

where $\beta = \left(1-a/b\right)$, b is the radius of the un-cracked roundbar and a is the circumferential crack length. It was assumed for this analysis that the notch behaved as a crack and as such the notch root radius is initially the quantity $(b-a)$. See Fig. 6-7 for a schematic.

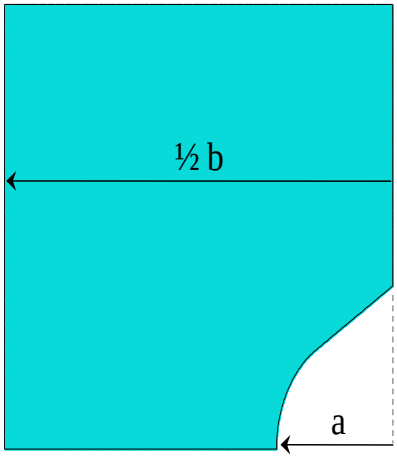

Figure 6-7. Circumferentially notched geometry for fracture mechanics analysis.

As all experiments were fully reversed, the effective stress intensity range was determined from the tensile loading only. The stress intensity threshold $\Delta K_{th} = 7.9 MPa \cdot m^{1/2}$ corresponds to IN718 at room temperature [74]. The stress intensity threshold for IN718 at 649°C, $\Delta K_{th} = 6.6 MPa \cdot m^{1/2}$, was included for considering tensile maximum temperature differences between IP and OP loading. This simple analysis agrees well with the experimentally observed behavior for notched IN100. Under force controlled conditions the circumferential crack grows in a stable fashion until a critical crack size is reached and fast fracture occurs.

For the case of displacement control the same stress intensity factor is utilized but it is assumed that the applied force decreases proportionally with the ratio of the remaining area to the initial area. This assumption predicts a decreasing stress intensity factor with increasing crack size which is possible for certain geometries and loadings [75]. Two things may occur as the crack growth driving force decreases; (1) the crack growth remains stable until fracture (2) crack arrest occurs when the stress intensity range reaches a threshold value. The load-temperature phasing is critical as environmental effects, dominant under OP loading, increase the crack

growth driving force and resulting in stable crack growth until fracture. Environmental effects are negligible under IP loading and hence the crack growth driving force is less than expected for OP TMF, leading to the experimentally observed crack arrest.

A study by Adair on TMF crack growth of IN100 showed that embrittlement of the crack tip from high temperature environmental effects directly increased the crack growth rate [76]. Experiments were performed alternating the specimen temperature between 315°C and 649°C and at each temperature isothermally performing either blocks of 1, 10 or 100 cycles at R=0.1 f = 0.33 *Hz*. For the case of 1 and 10 blocks the crack growth rates were higher than expected compared against independent isothermally predicted growth. This was due to oxide formation at elevated temperatures followed by brittle cracking of the oxide at the decreased temperature. For the case of 100 blocks the growth rate was slower because the crack outgrew the brittle oxide layer quickly. Other have also observed that environmental interactions increase crack growth rate in polycrystalline Ni-base superalloys [77-79].

The effects of boundary conditions on crack initiation for notched OP TMF IN100 were found to be negligible. Experiments performed under both control modes follow the same trend and scatter is bounded by a factor of 1.7. The lack of boundary condition sensitivity is due to crack initiation mechanisms under both control modes being dominated by environmental-fatigue mechanisms. Evidence from fracture surfaces and simple fracture mechanics arguments illustrate that crack propagation however is heavily influenced by the applied conditions.

6.1.2 IP TMF IN100

IP TMF life results are shown in Fig. 6-8. IP TMF experiments under displacement control conditions were considered run-out tests as there was no observed indication of crack

initiation after 5000 cycles. Compared to force controlled trends the IP displacement control tests benefitted greatly from additional imposed displacement constraints.

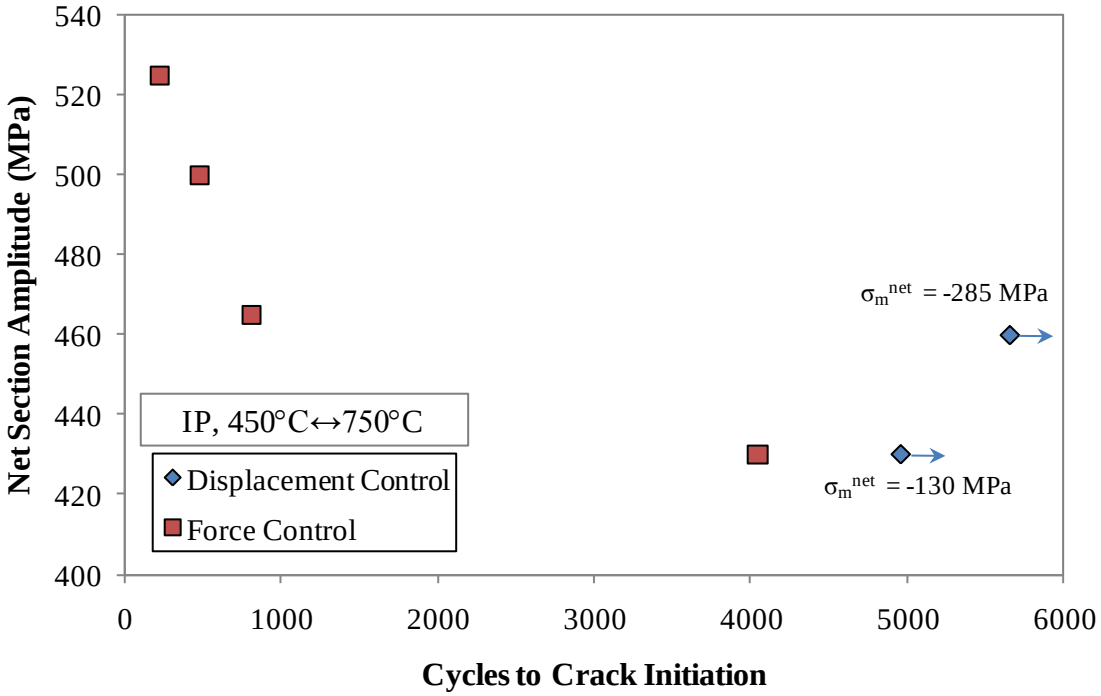

Figure 6-8. IP TMF life results based on net section stress.

A summary of all IP TMF IN100 force control experiments are shown in Table 6-3 and displacement control experiments in Table 6-4. Net section mean stress and amplitude were determined for displacement controlled tests from the half life cycle. Displacement amplitude and mean values for force control tests were also determined from the half life cycle.

Table 6-3: IP TMF IN100 notch force control conditions and results

IP TMF IN100 Baseline Force Control TMF Tests									
Period (s)	T_{min} (°C)	T_{max} (°C)	σ_a^{net} (MPa)	R_σ	k_t	$\Delta\delta_m$ (μm)	Mean δ_m (μm)	R_δ	Initiation Life (cycles)
180	450	750	525	-1	2	48.42	-0.19	-1.02	221
180	450	750	500	-1	2	42.72	-2.60	-1.28	481
180	450	750	465	-1	2	42.11	3.92	-0.69	813
180	450	750	430	-1	2	33.99	9.35	-0.29	4045

Table 6-4: IP TMF IN100 notch displacement control conditions and results

IP TMF IN100 Notch Displacement Control TMF Tests									
Period (s)	T_{min} (°C)	T_{max} (°C)	$\Delta\delta_m$ (μm)	Mean δ_m (μm)	R_δ	k_t	σ_a^{net} (MPa)	σ_m^{net} (MPa)	Initiation Life (cycles)
180	450	750	39.44	-3.45	-1.27	2	460	-285	5662*
180	450	750	38.26	4.37	-0.66	2	430	-130	4965*

** Runout after 5000 cycles*

Mean net section stresses and net section stress amplitudes for IP TMF displacement control tests are shown in Fig. 6-9. Neither test resulted in final fracture nor displayed indications of crack initiation based on force history. In both cases mean net section stresses initially increased up to 200 *cycles* and then steadily decreased towards an asymptotic compressive value.

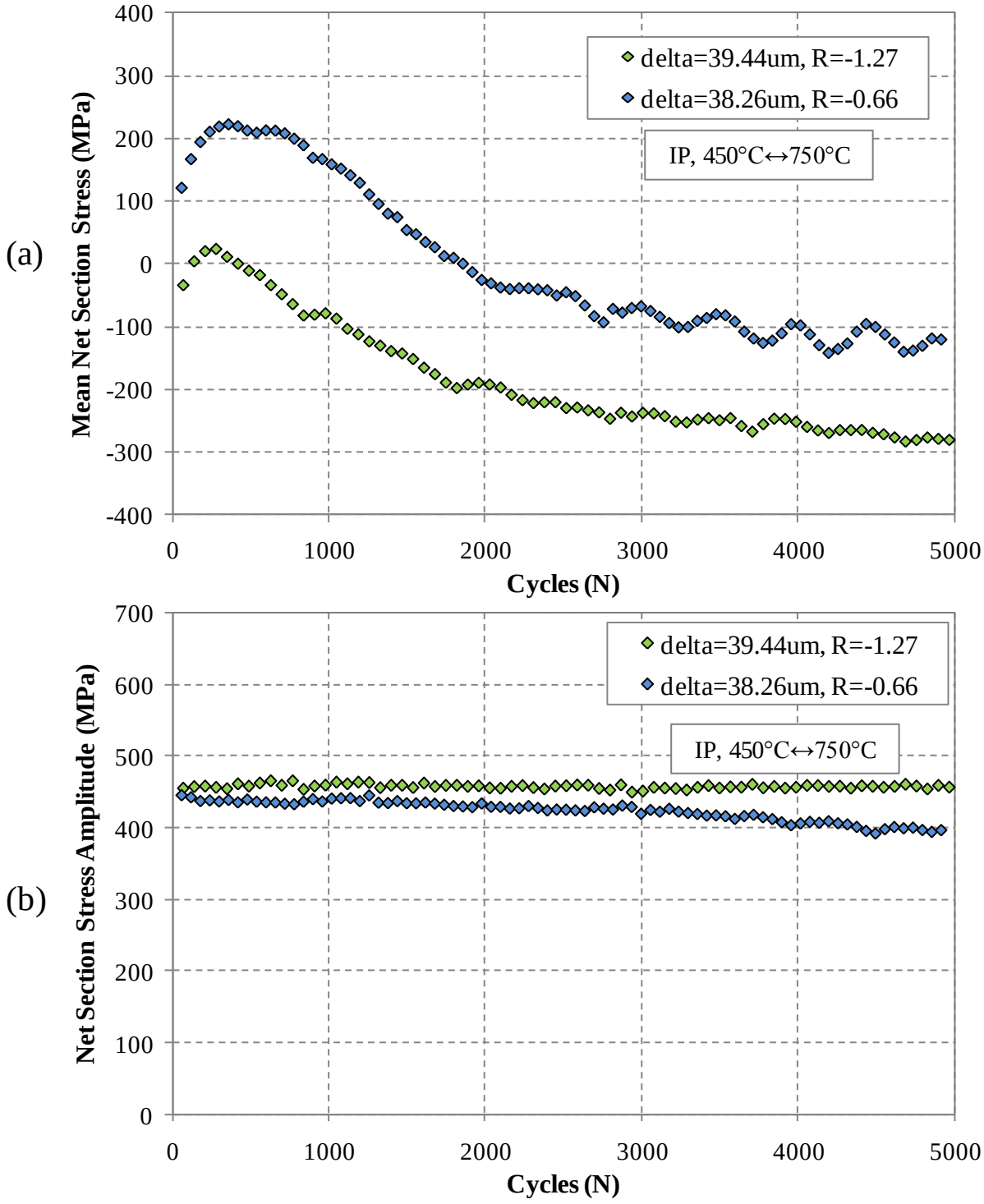

Figure 6-9. Net section mean stress and stress amplitude histories for IP TMF displacement control IN100 tests.

Stiffness histories, shown in Fig. 6-10, also lack any indication of crack initiation. Stiffness history for a force control IP TMF test is shown for comparison.

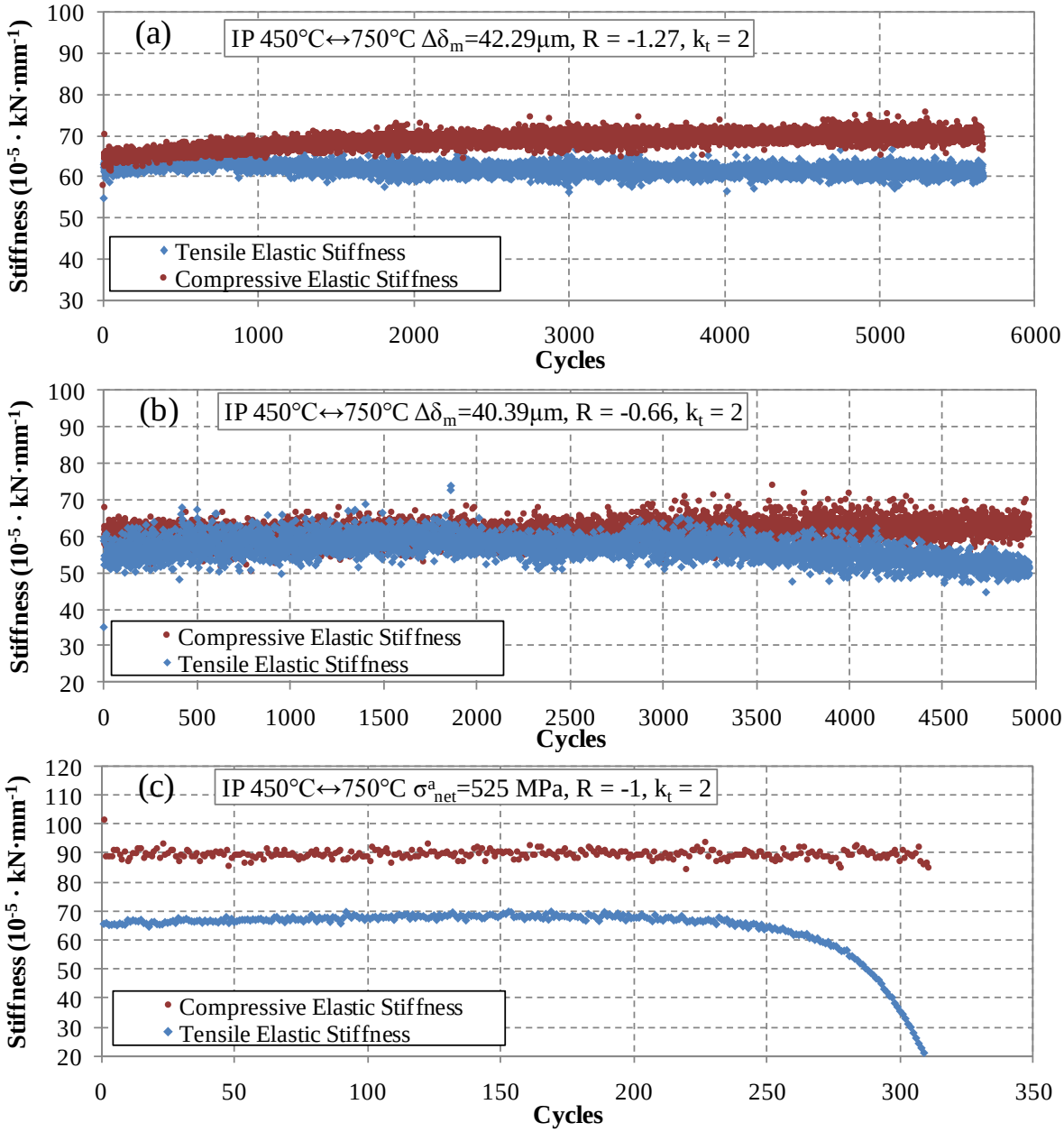

Figure 6-10. Stiffness histories for IN100 IP TMF. (a-b) Displacement control. No indication of crack initiation in either trend. (c) Force Control. Crack initiation observed by tensile stiffness reduction.

The force control stiffness history presented in Fig. 6-10 (c) has a very clearly decreasing trend in the tensile stiffness towards the end of life (prior to final fracture). This is expected as only tensile deformation is affected by the present of a crack perpendicular to the loading direction. The displacement control experiments lack any trend indicating the existence of a fatigue crack.

Following run-out each test specimens was sectioned, polished and etched for micrography. Micrographs from both tests are shown in Fig. 6-11 and Fig. 6-12. In both cases an arrested circumferential crack was found at the notch root of 450μm and 440μm average length. This corresponds to a cross sectional area reduction of 27%. Despite a macroscopically large crack being present the remote stiffness measurements failed to detect initiation. In a study on the role of control model (load versus strain) on a metal matrix composites Lerch and Halford made a similar observation where specimens under strain control never reached final fracture despite initiating a crack [58].

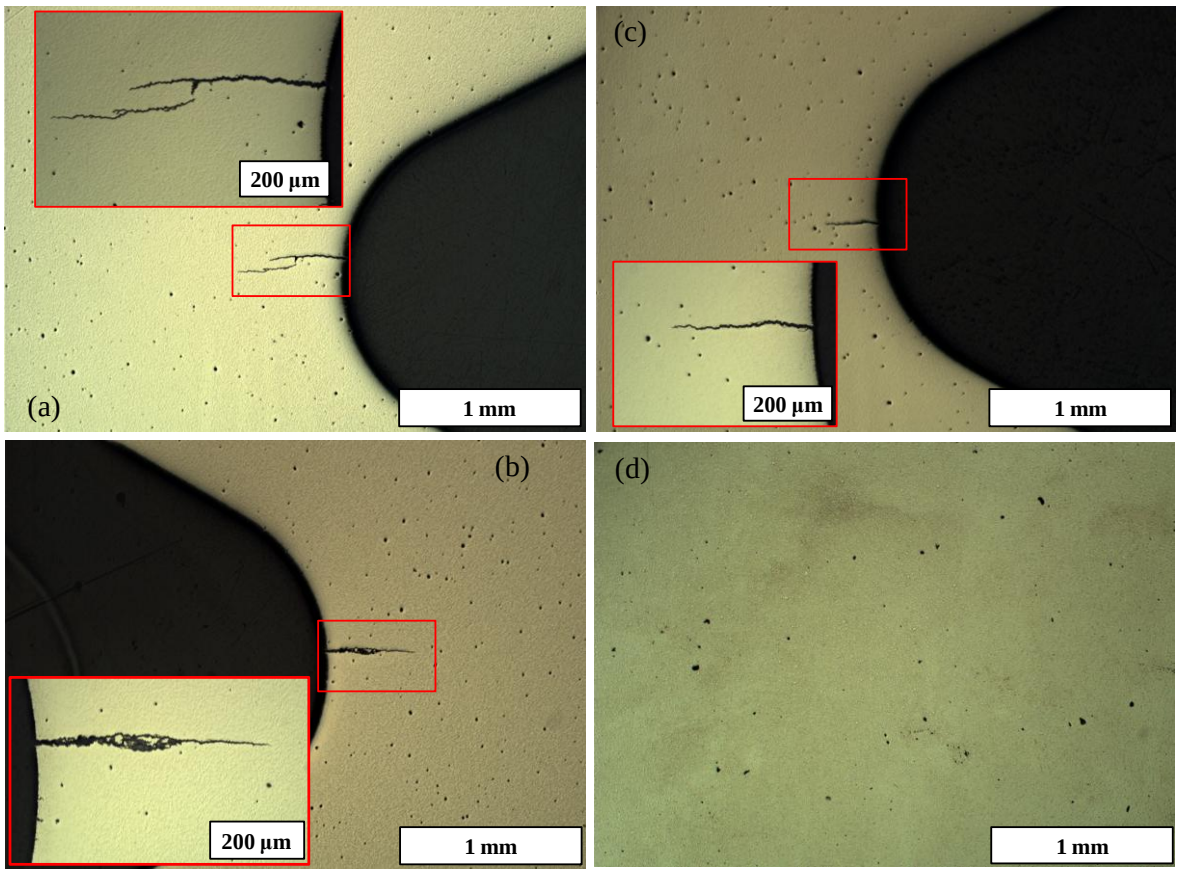

Figure 6-11. (a-c) cross sections of IP TMF 450°C-750°C $\Delta\delta_m$=39.44µm R = -1.27. (d) Pores present in virgin material prior to any applied loads. Average crack size was 450µm.

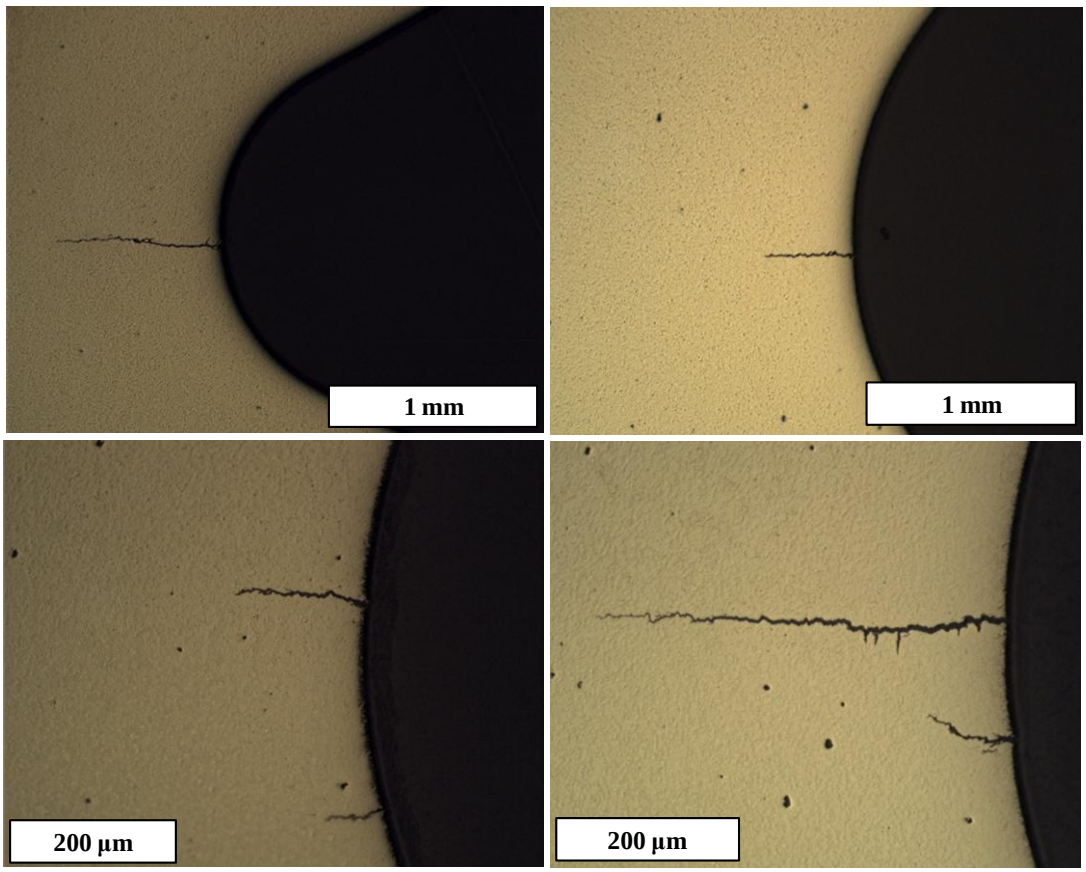

Figure 6-12. Four cross sections of IP TMF 450°C-750°C $\Delta\delta_m$=38.26 R = -0.66. Average crack size was 440µm.

Following macroscopic initiation the driving force for crack growth decreased resulting in arrest. The decreasing crack growth rate is due to the effect of remotely applied displacement boundary conditions, this agrees with the schematic presented in Fig. 6-6. Under force control the crack growth driving force remains high due to the remotely applied force conditions and as such crack initiation could easily be determined when cracks grew sufficiently larger (> 0.5 *mm*). In a study on 1CrMoV notched TMF by Mazza et al. it was observed that crack initiation was poorly captured by the remotely measured force [3]. A PD voltage drop measurement technique was suggested for accurate crack initiation detection.

Notch component simulations utilizing the calibrated IN100 unified creep-plasticity constitutive model are shown in Fig. 6-13. The equivalent cyclic inelastic strain range is highly localized at the notch root. Non-negligible inelastic strains extend over a 150μm distance away from the surface.

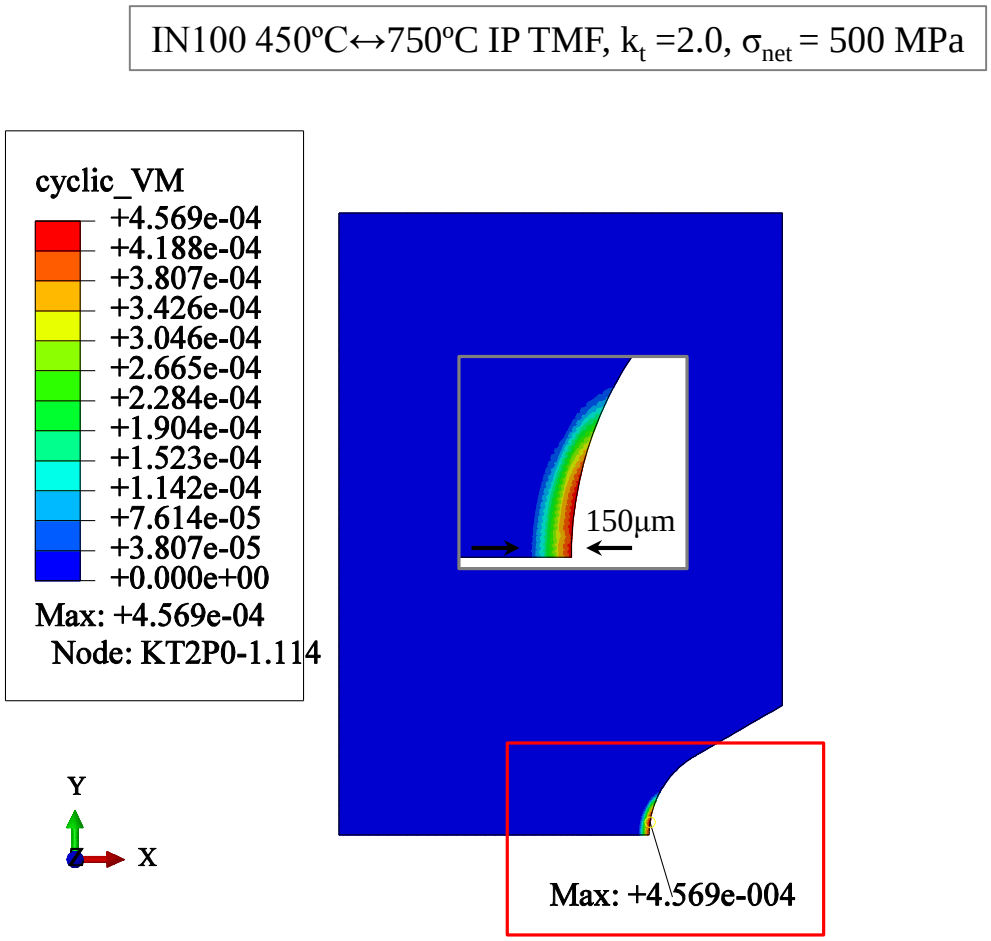

Figure 6-13. IN100 IP TMF notch component results illustrating significant inelastic deformation is highly localized at the notch root.

Axial stress at maximum applied load for three different net section stresses is shown in Fig. 6-14.

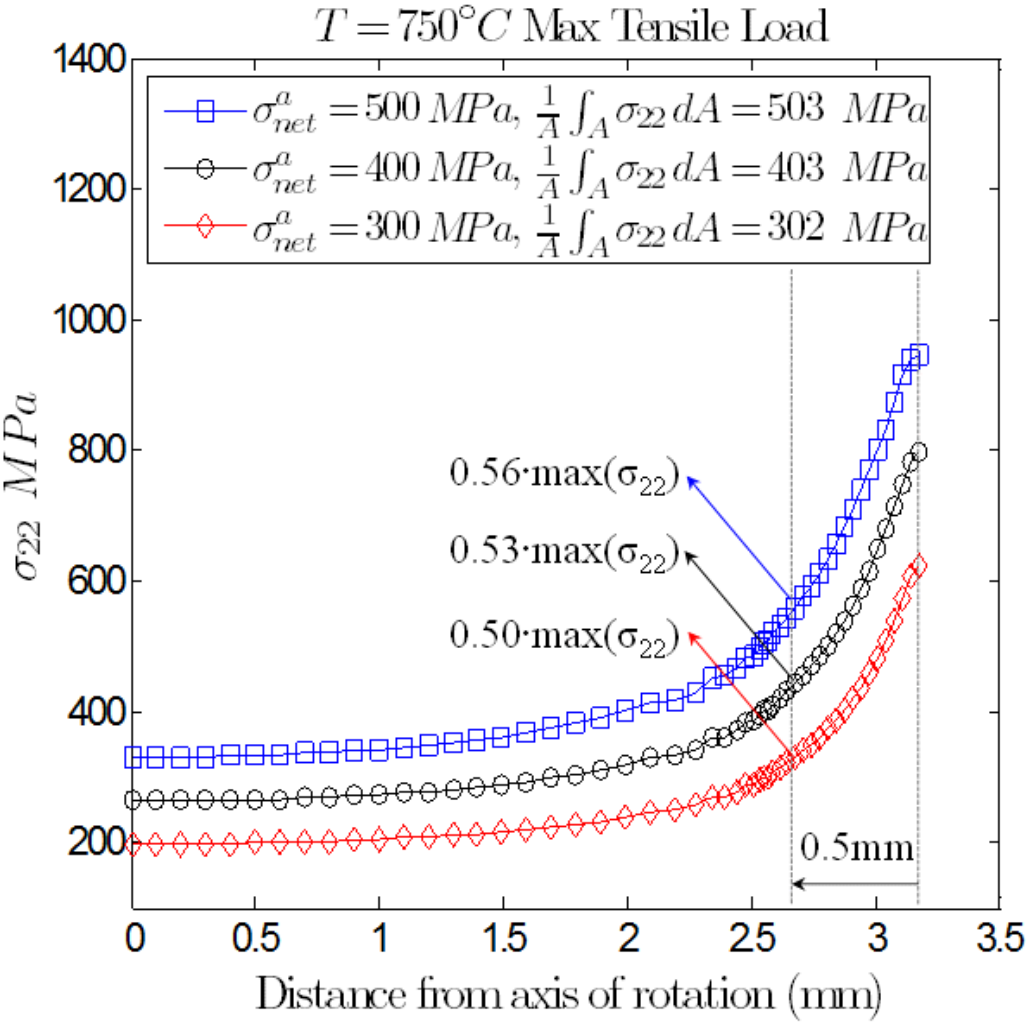

Figure 6-14. Axial stress distribution for IN100 IP TMF across the notch root for various applied next section stresses.

Results indicate that there is roughly a 50% drop in axial stress 0.5 *mm* away from the notch surface. This would clearly affect and slow crack growth. Equivalent cyclic inelastic strain range across the notch root is shown in Fig. 6-15.

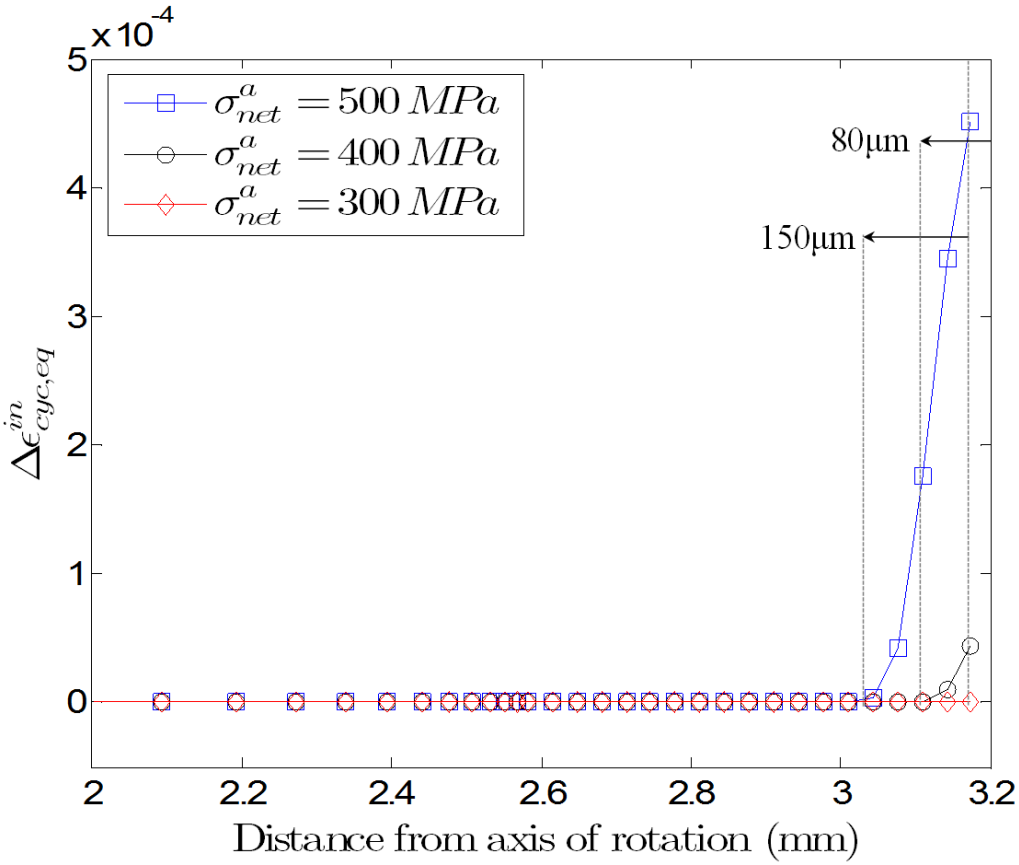

Figure 6-15. Equivalent cyclic inelastic strain range distribution for IN100 IP TMF at maximum tensile load across the notch root for various applied next section stresses.

The inelastic strain quickly decreases moving away from the notch root surface. The highly localized volume of inelastic deformation provides a small zone from which a crack may initiate. A decreasing crack propagation driving force arises from prescribing displacement boundary conditions and a quickly decreasing crack plane normal stress (axial stress). These effects result in crack arrest under the prescribed conditions in IP TMF.

Conservatively assuming that the cracks present in the IP TMF displacement control experiments grew at a constant rate throughout testing, the average crack growth rate would correspond to $9 \cdot 10^{-5}$ mm/cycles. Comparing to crack growth rates from Larson et al. [80] for

IN100, shown in Fig 6-16 (a), suggests that the stress intensity factor is low and close to the threshold value. Others have also shown that crack closure can contribute to decreasing stress intensity factors that lead to arrest [81-82]. Tanaka's results on low carbon steel are shown in Fig. 6-16 (b). Mazza et al. [3] showed that for the same temperatures and strains, the crack growth rate in a notched component is significantly slower than in a uniaxial specimen.

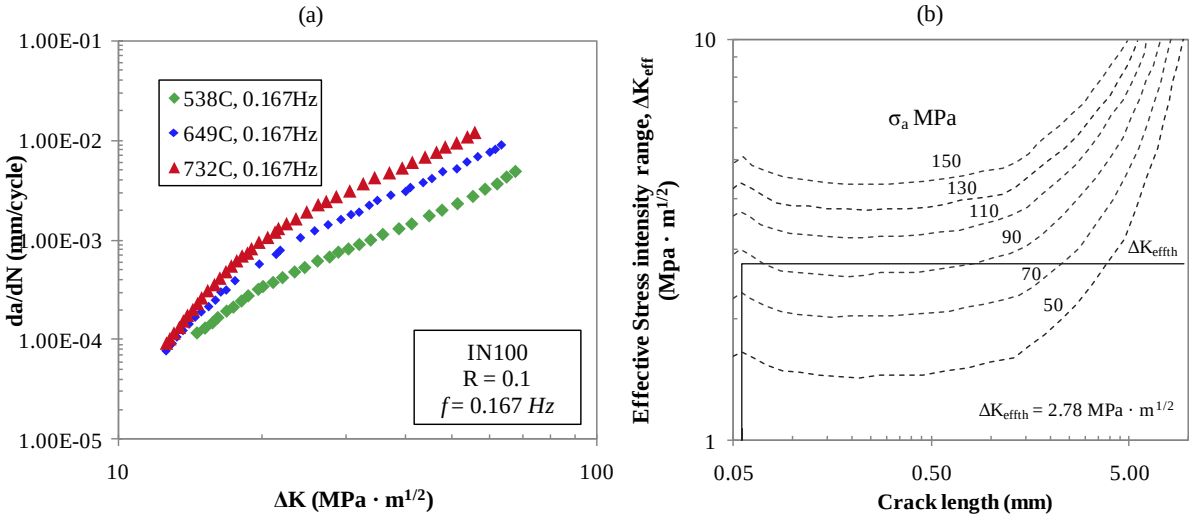

Figure 6-16. (a) Crack growth rates for IN100 at 538°C, 649°C and 732°C [80]. (b) Effects of closure on the stress intensity factor in low-carbon steel [81].

The observed crack growth arrest did not occur under OP loading due to increased oxide embrittlement from minimum temperatures occurring in tension. Under OP conditions the oxidized material at the crack front is brittle in tension which provides sufficient crack propagation driving force, even under displacement control conditions.

The effects of boundary conditions on notch specimen IN100 crack initiation life under OP TMF conditions was negligible. Lives under both force and displacement control followed the same life trend within a factor of 1.7. IP TMF results were drastically different across control modes. Crack initiation was detected in all force control experiments and all tests results in final

fracture. Under displacement control conditions no crack was detected based on force or stiffness histories, however micrographs revealed roughly a 0.5 *mm* size circumferential crack. Circumferential cracks initiated and then arrested due to a lack of sufficient driving force under IP TMF conditions.

6.2 CM247LC DS TMF Results

6.2.1 OP TMF

OP TMF life results for all geometries used under the temperature range 500°C ↔ 950°C are shown in Fig. 6-17, Fig. 6-18 and Fig. 6-19. Life is shown as a function of net section stress amplitude calculated at the notch root. Force controlled experiments were performed under fully reversed conditions. Mean net section stress values are shown for displacement controlled experiments. Several displacement control experiments utilized boundary conditions (amplitude and mean) that were taken from the stabilized or half life response corresponding to force controlled tests, shown previously in Fig. 6-3. The net section amplitude and mean stresses for displacement controlled tests were taken at the half life or stabilized cycle.

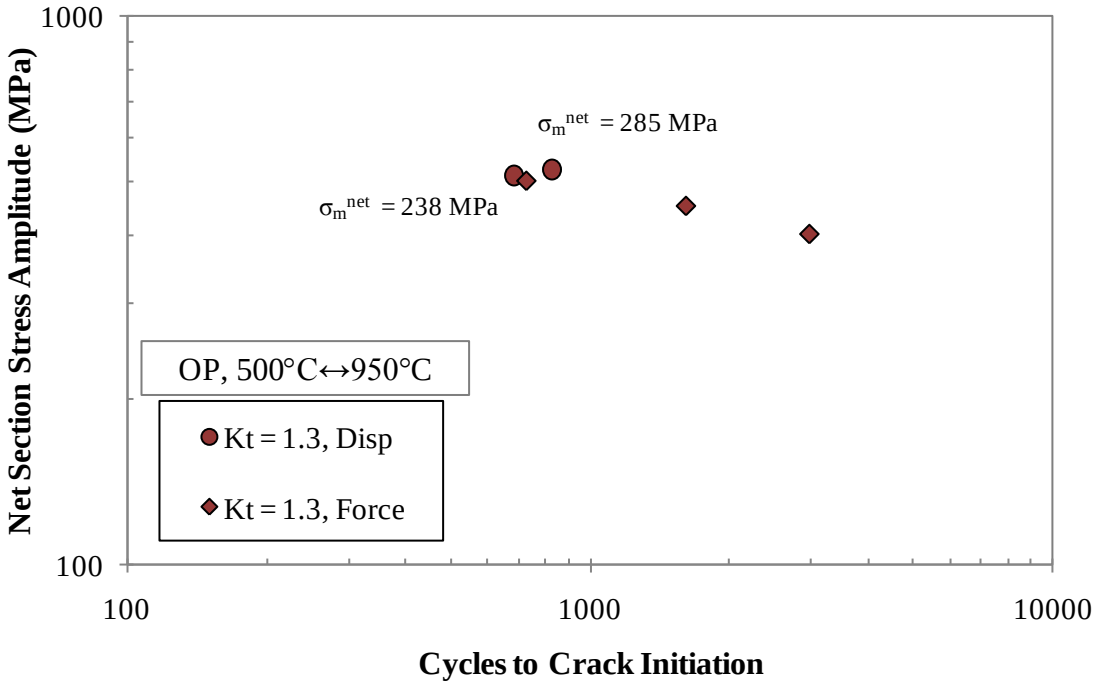

Figure 6-17. CM247LC DS OP TMF 500°C ↔ 950°C life results based on net section stress amplitude for $k_t = 1.3$.

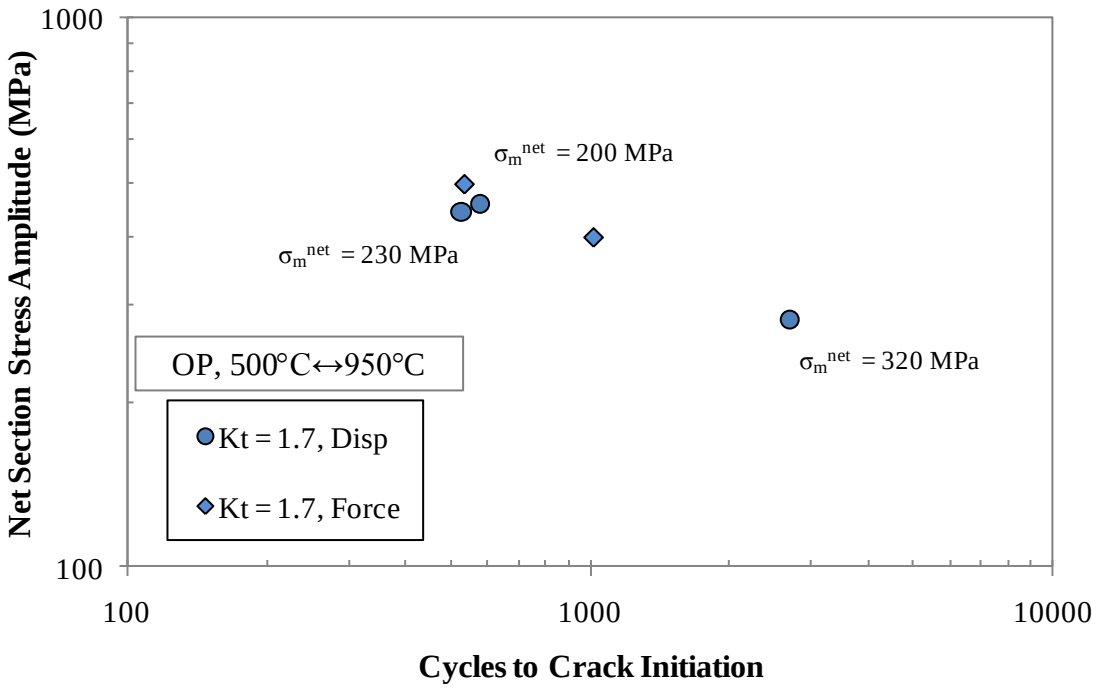

Figure 6-18. CM247LC DS OP TMF 500°C ↔ 950°C life results based on net section stress amplitude for $k_t = 1.7$.

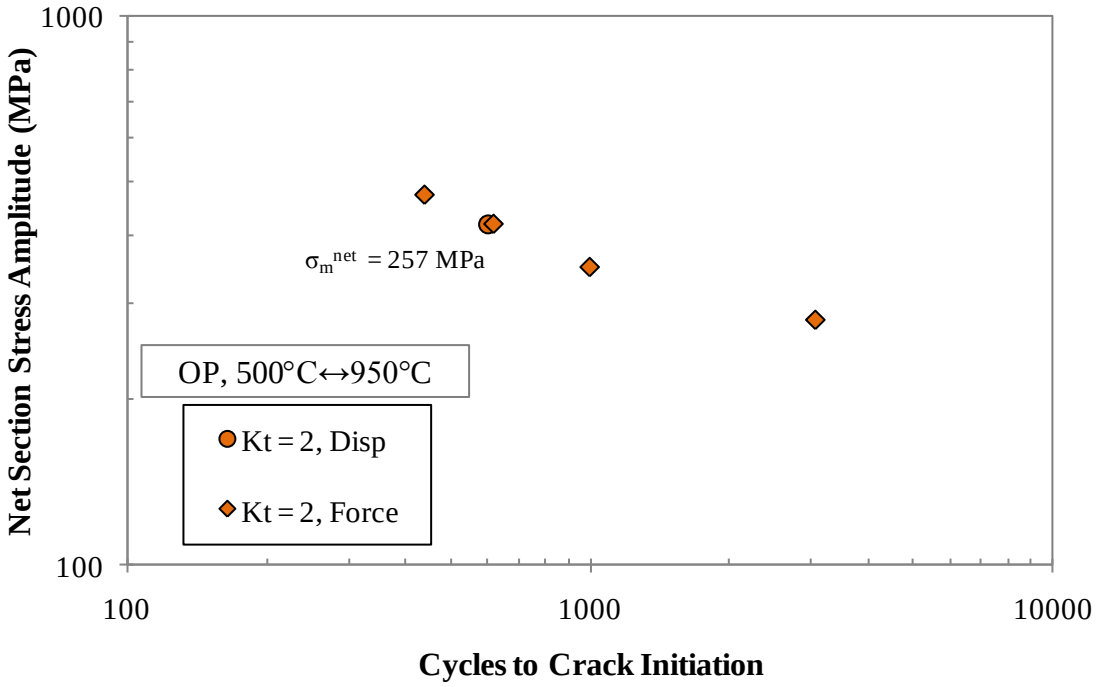

Figure 6-19. CM247LC DS OP TMF 500°C ↔ 950°C life results based on net section stress amplitude for $k_t = 2.0$.

Experimental results indicate that specimen life is independent of the remotely applied boundary conditions under OP TMF across all tested geometries. Both force control and displacement control results follow the same life trends using net section stress amplitude as the damage metric. Additionally mean stresses developed during displacement controlled testing do not significantly affect crack initiation life. Force control OP TMF 500°C↔950°C results from this study are shown in Table 6-5 and from Kupkovits in Table 6-6. Included are stabilized and half life mechanical extensometer displacement range ($\Delta\delta_m$) and mean values. Displacement control results for OP TMF 500°C↔950°C are shown in Table 6-7. The sole $k_t = 2.0$ experiment was performed by Kupkovits [6].

Table 6-5: OP TMF CM247LC DS notch force control conditions and results

OP TMF CM247LC DS Force Control Tests									
Period (s)	T_{min} (°C)	T_{max} (°C)	σ_a^{net} (MPa)	R_σ	K_t	$\Delta\delta_m$ (μm)	Mean δ_m (μm)	R_δ	Initiation Life (cycles)
180	500	950	500	-1	1.3	81.28	-165.3	1.65	728
180	500	950	450	-1	1.3	70.7	-1155.0	1.06	1614*
180	500	950	400	-1	1.3	68.41	-376.3	1.20	2987
180	500	950	500	-1	1.7	80.00	-1144.4	1.07	536*
180	500	950	400	-1	1.7	66.04	-99.1	2.00	1016
180	500	950	475	-1	2	75.81	-37.16	-100.76	440

* Heavy cyclic ratcheting caused extensometer saturation, reported values are cycles to final fracture.

Table 6-6: OP TMF CM247LC DS notch force control conditions and results from Kupkovits [6]

OP TMF CM247LC DS Force Control Tests									
Period (s)	T_{min} (°C)	T_{max} (°C)	σ_a^{net} (MPa)	R_σ	K_t	$\Delta\delta_m$ (μm)	Mean δ_m (μm)	R_δ	Initiation Life (cycles)
180	500	950	420	-1	2	70.1	-219.6	1.38	620
180	500	950	350	-1	2	52.6	-215.5	1.28	1000
180	500	950	280	-1	2	44.5	-59.68	2.19	3070

Table 6-7: OP TMF CM247LC DS notch displacement control conditions and results

OP TMF CM247LC DS Notch Mechanical Displacement Control Tests									
Period (s)	T_{min} (°C)	T_{max} (°C)	$\Delta\delta_m$ (μm)	Mean δ_m (μm)	R_δ	k_t	σ_a^{net} (MPa)	σ_m^{net} (MPa)	Initiation Life (cycles)
180	500	950	38.84	-94.11	1.52	1.7	282	320	2700
180	500	950	63.01	-93.91	2.01	1.7	443	230	527
180	500	950	34.34	-158.50	1.24	1.3	526	238	686
180	500	950	36.65	8.68	-0.36	1.3	512	285	825
180	500	950	44.90	8.16	-0.47	1.7	460	200	578
180	500	950	57.79	0.00	-1.00	2	417	257	601

Net section mean stress and stress amplitudes for all 500°C ↔ 950°C OP TMF experiments performed in displacement control are shown in Fig. 6-20.

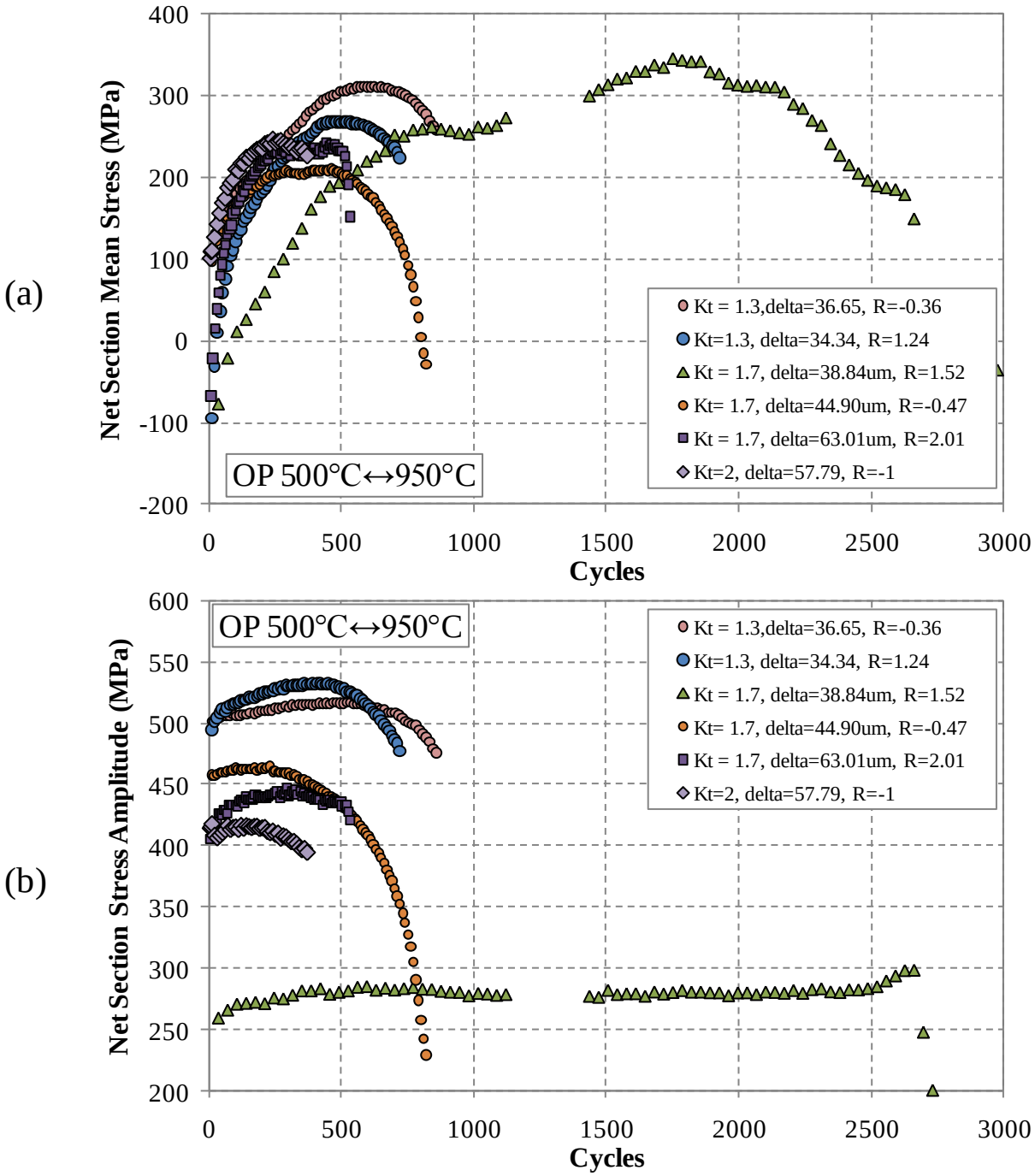

Figure 6-20. Evolution of (a) net section mean stress and (b) amplitude during displacement-control of CM247LC DS OP TMF 500°C ↔ 950°C.

Mean stresses are expected to develop during displacement controlled TMF experiments due to asymmetric tension-compression response from temperature cycling as shown in Fig. 6-21. An applied mechanical strain range of 1.0% was applied under both IP and OP conditions.

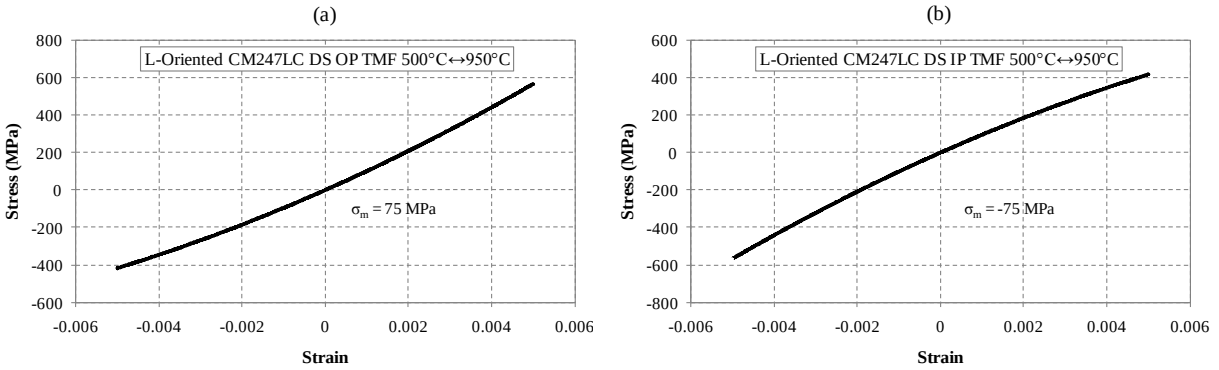

Figure 6-21. Fully reversed uniaxial elastic stresses calculated from temperature dependent elastic properties for (a) OP and (b) IP TMF.

Under purely elastic loading the evolution of mean stresses into the tensile regime is expected under displacement control OP TMF conditions. Elastic stresses are lower during compression due to a lower modulus which effectively raises the mean cyclic stress above zero. Additionally the majority of inelastic deformation occurs during the higher applied temperatures which reduces flow stresses and increases the mean cyclic stress magnitude under OP and decreases under IP TMF.

Crack initiation life results for OP TMF 500°C ↔ 750°C are shown in Fig. 6-22 and Fig. 6-23. Similar to higher temperature OP TMF tests, both force control and displacement control conditions produced the same life trends.

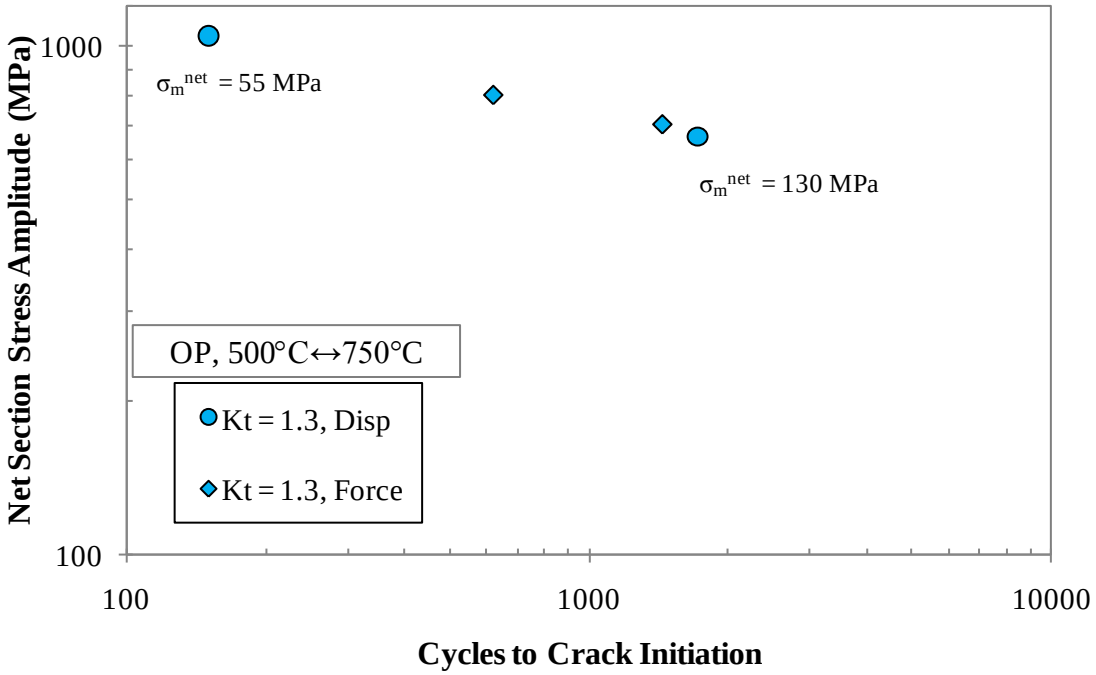

Figure 6-22. CM247LC DS OP TMF 500°C ↔ 750°C life results based on net section stress amplitude for notch geometry $k_t = 1.3$.

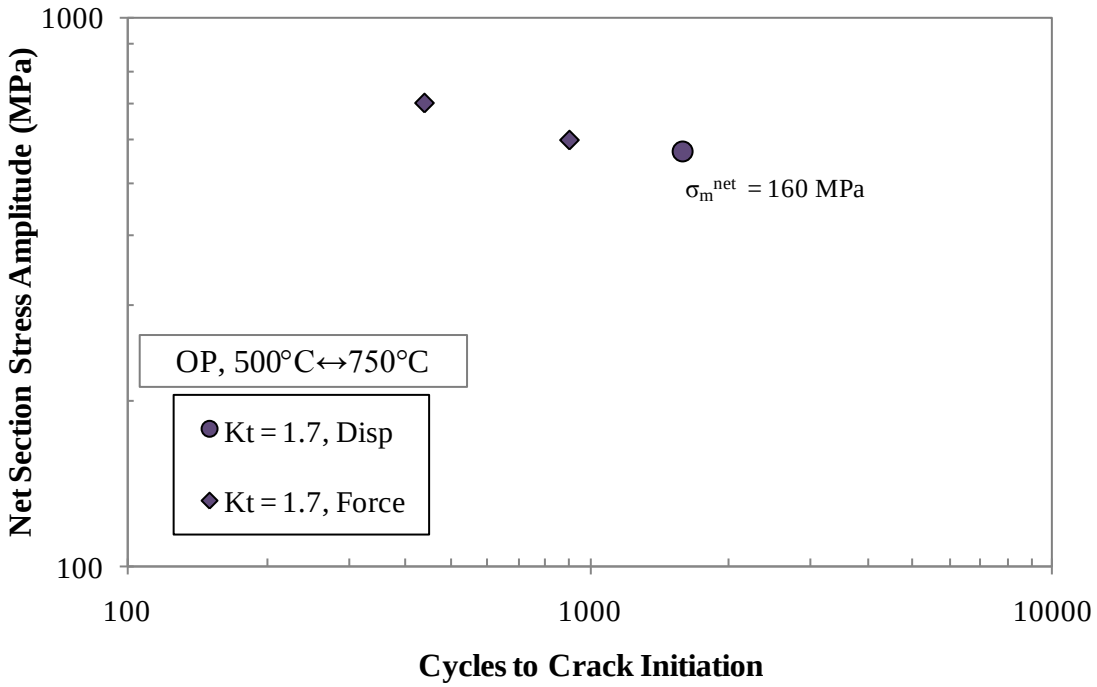

Figure 6-23. CM247LC DS OP TMF 500°C ↔ 750°C life results based on net section stress amplitude for notch geometry $k_t = 1.7$.

Displacement control lives under 500°C ↔ 750°C OP TMF followed force control life trends. Mean stress effects were negligible. Force control results are given in Table 6-8 and displacement control results in Table 6-9.

Table 6-8: OP TMF reduced T_{max} CM247LC DS notch force control conditions and results

CM247LC DS Force Control TMF Tests										
Period (s)	T_{min} (°C)	T_{max} (°C)	σ_a^{net} (MPa)	R_σ	K_t	Phasing	$\Delta\delta_m$ (μm)	Mean δ_m (μm)	R_δ	Initiation Life (cycles)
180	500	750	700	-1	1.3	OP	112.7	-95.5	3.88	1444
180	500	750	800	-1	1.3	OP	112.9	-14.6	-1.70	620
180	500	750	700	-1	1.7	OP	99.15	-14.9	-1.86	438
180	500	750	600	-1	1.7	OP	81.28	-11.4	-1.78	900

Table 6-9: OP TMF reduced T_{max} CM247LC DS notch displacement control conditions and results

CM247LC DS Notch Mechanical Displacement Control TMF Tests										
Period (s)	T_{min} (°C)	T_{max} (°C)	$\Delta\delta_m$ (μm)	Mean δ_m (μm)	R_δ	k_t	Phasing	σ_a^{net} (MPa)	σ_m^{net} (MPa)	Initiation Life (cycles)
180	500	750	161.60	-27.84	-2.05	1.3	OP	1050	55	150
180	500	750	100.30	-16.37	-1.97	1.3	OP	665	130	1717
180	500	750	77.97	-11.45	-1.83	1.7	OP	570	160	1585

Net section mean stress and stress amplitude are shown in Fig. 6-24 for all 500°C ↔ 750°C OP TMF experiments performed in displacement control. Net section stress amplitude displayed little or no hardening and remained fairly constant throughout each test prior to crack initiation.

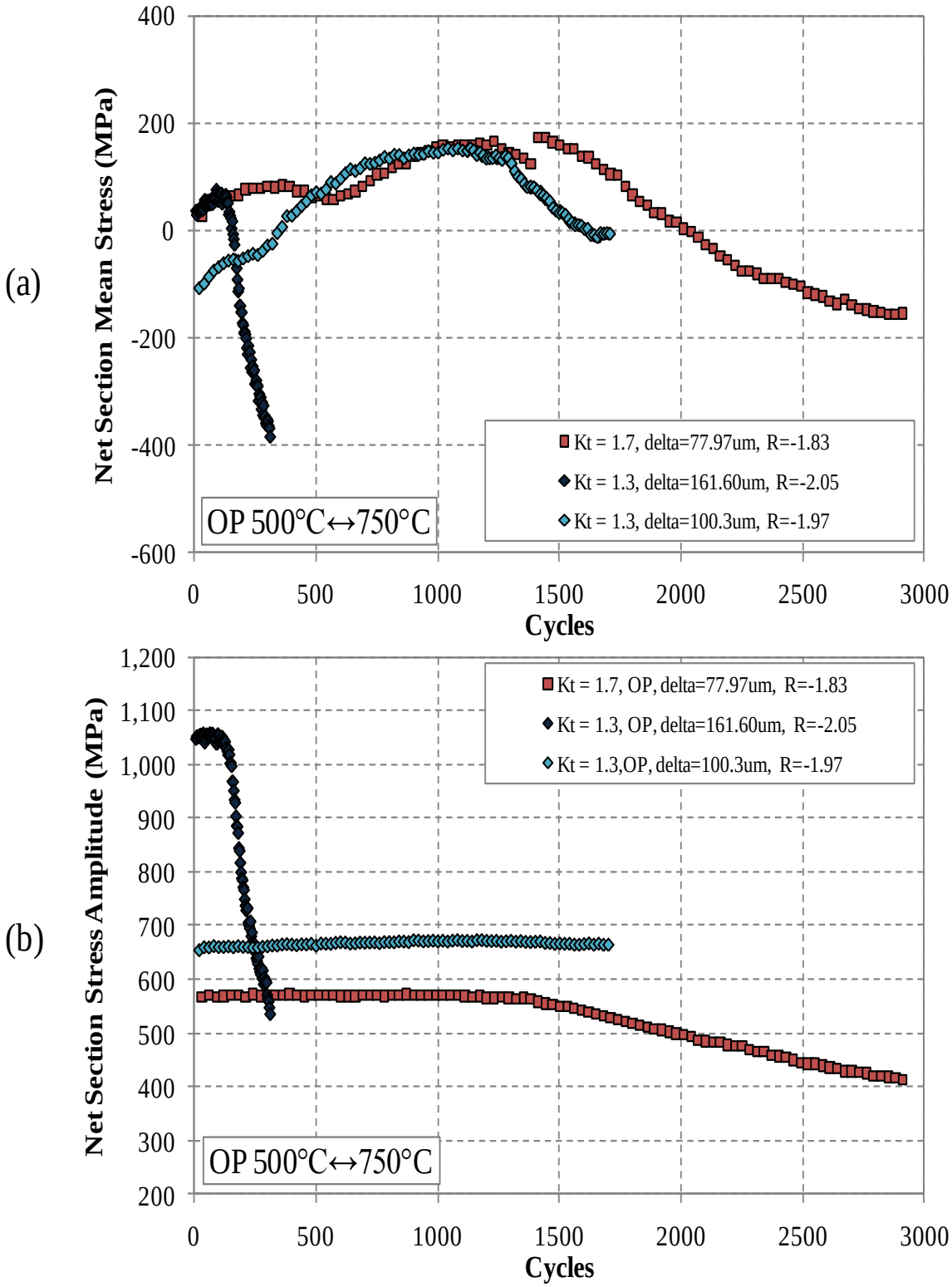

Figure 6-24. CM247LC DS OP TMF 500°C ↔ 750°C (a) net section mean stress and (b) stress amplitude history.

In a study on the effects of control mode on isothermally loaded metal matrix composites, Lerch and Halford found that under fully reversed conditions fatigue lives as a function of applied stress were insensitive to the applied control mode [58]. The authors conclude that the fatigue lives insensitivity to control mode was due to similar material responses between the two testing conditions; there was little load drop or strain ratcheting observed during testing. In a study on a titanium matrix composites Sanders and Mall made also found that fatigue lives as a function of applied strain range were insensitive to the applied control mode [59]. They attributed the results to maintaining the same damage and deformation mechanisms across the two control modes.

All CM247LC DS experiments performed under OP TMF conditions followed the same initiation life trends regardless of applied boundary conditions. At high temperature, the mechanically applied loads and temperatures are sufficient to promote environmental-fatigue damage mechanisms under both force control and displacement control. Micrographs illustrating an environmental-fatigue initiated crack from an oxide spike under displacement control is shown in Fig. 6-25.

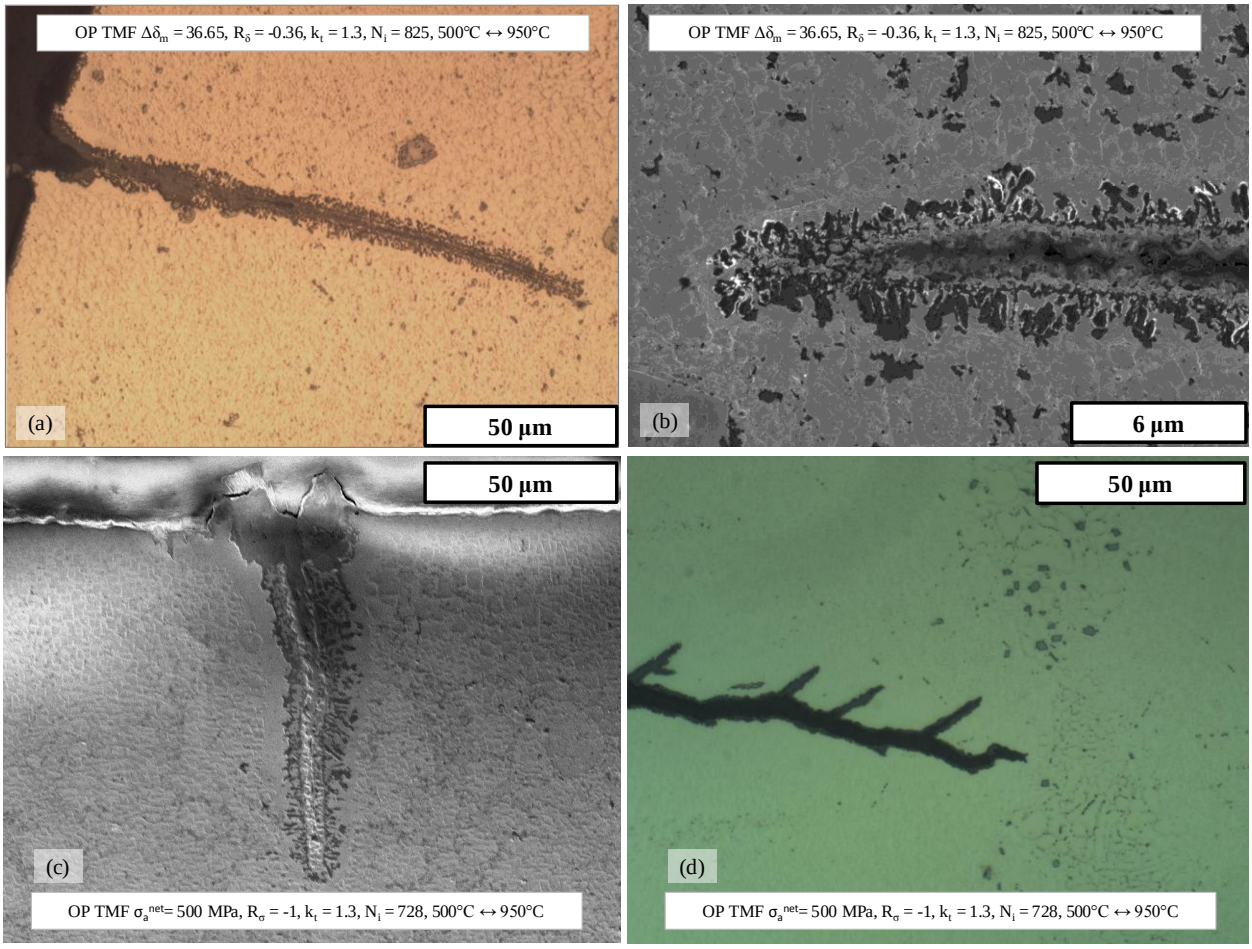

Figure 6-25. Oxide spiking and crack path oxidation of CM247LC DS OP TMF 500°C ↔ 950°C (a-b) displacement control (c-d) force control.

The experimentally observed notch deformation responses under the two control modes behave similarly as well (mean and amplitude displacements/forces). Uniaxial OP TMF results using Shenoy's crystal viscoplasticity (CVP) model calibrated for GTD-111 [56] are shown in Fig. 6- 26. Simulations were first performed utilizing strain control, then in stress control based on the previous strain control response (peak stresses). The cyclic ratchet strain is removed in Fig. 6-26 (b) so that the hysteresis curves can be compared directly.

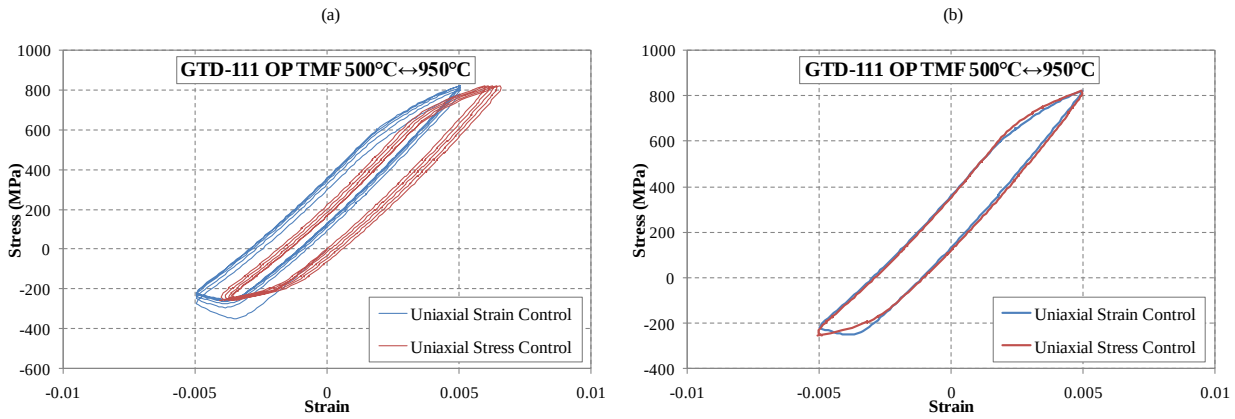

Figure 6-26. Crystal viscoplasticity uniaxial stress-strain simulation responses for DS superalloy GTD-111 at $1.11 \cdot 10^{-4}$ s^{-1} (a) Strain control and stress control responses (b) Saturated strain control response and saturated stress control response not including cyclic ratcheting.

With the exception of the compressive response, where higher temperatures increase the rate-dependency of deformation, the response is very similar and more importantly the same cyclic inelastic strain is produced. This shows that for the uniaxial deformation response under the two distinctly different control modes are similar.

6.2.2 IP TMF

IP TMF life results from Kupkovits and Neu [54] are shown in Fig. 6-27. Life results corresponding to $k_t = 1.3$ are shown for comparison. The resulting life under IP TMF based on net section stress amplitude is higher under displacement controlled conditions compared against force controlled experiments. Despite the displacement control test having a nearly identical net section stress amplitude, the resulting life was 22 higher. The experiment that failed at 121 cycles failed via a creep rupture mechanisms.

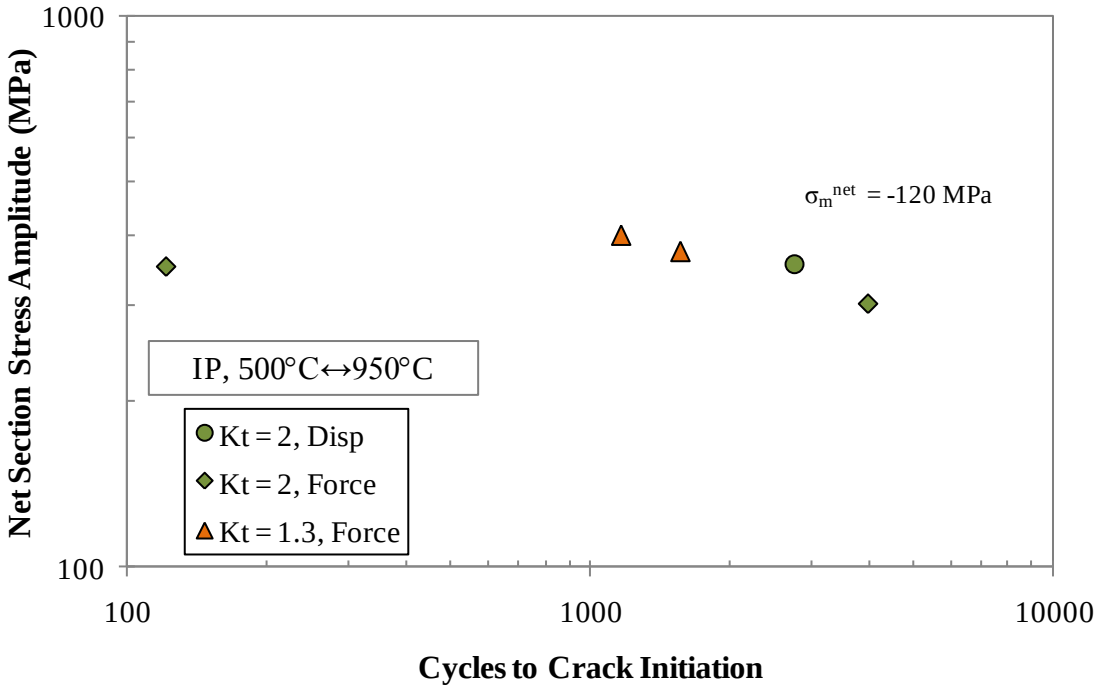

Figure 6-27. CM247LC DS IP TMF 500°C ↔ 950°C life results based on net section stress amplitude for notch geometry $k_t = 2.0$ [83].

IP TMF mean net section stress and amplitude history are shown in Fig. 6-28. A mean compressive net section stress developed during testing. This is typical for IP TMF as high temperature deformation occurs during tension and results in a decrease in both elastic and flow stresses.

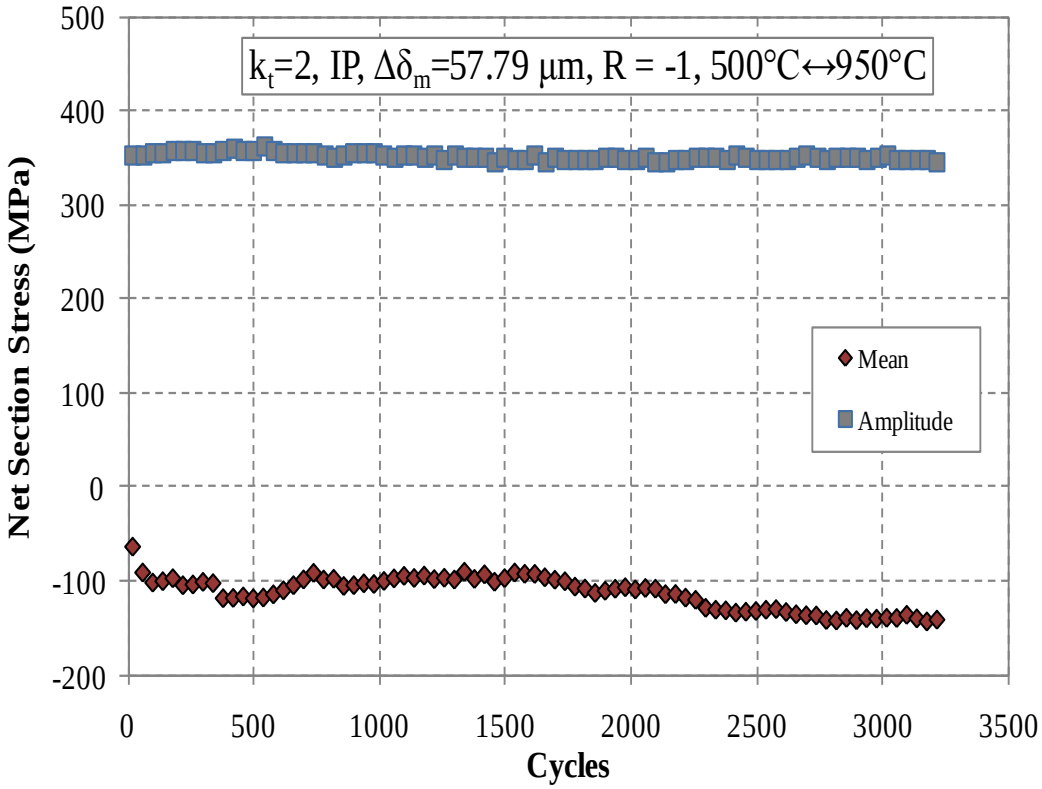

Figure 6-28. CM247LC DS IP TMF 500°C ↔ 950°C net section stress amplitude and mean stress cyclic history [83].

The resulting increase in life under displacement control IP TMF conditions is due to additional constraint that eliminates tensile creep ratcheting, prevents creep rupture and reduces cyclic creep damage. Under IP TMF creep damage accumulates during tensile loading and is indicated by the presence of microvoids or micropores. Force control IP TMF experiments performed on $k_t = 1.3$ displayed evidence of creep damage on the fracture surface of a crack initiation site as shown in Fig. 6-29(a). Fatigue striations on the fracture surface of a OP experiment under the same temperature range are shown in Fig. 6-29(b) for comparison of dominant damage mechanisms. Interdendritic microcracks found underneath the fracture surface are shown in Fig. 6-30. Test conditions and results are shown in Table 6-10.

Table 6-10: IP TMF CM247LC DS notch force control conditions and results

CM247LC DS Force Control TMF Tests										
Period (s)	T_{min} (°C)	T_{max} (°C)	σ_a^{net} (MPa)	R_σ	k_t	Phasing	$\Delta\delta_m$ (μm)	Mean δ_m (μm)	R_δ	Initiation Life (cycles)
180	500	950	400	-1	1.3	IP	65.61	128.70	0.01	1166
180	500	950	375	-1	1.3	IP	61.40	124.70	-0.01	1567

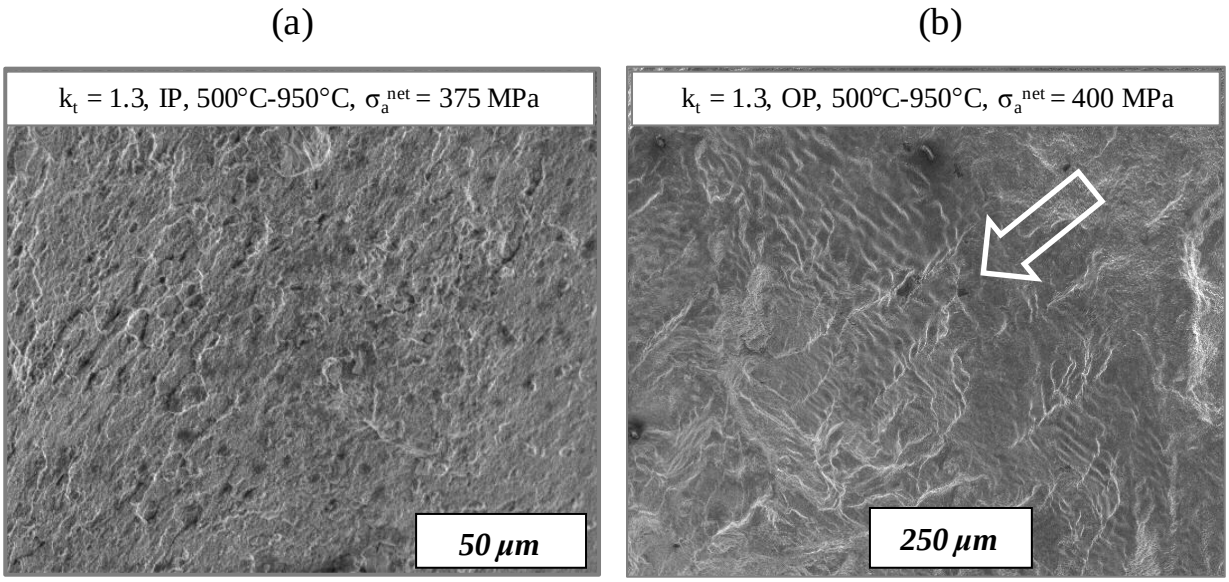

Figure 6-29. Differing damage mechanisms in IP and OP TMF 500°C ↔ 950°C (a) Creep damage observed in the form of microvoids on a crack fracture surface (b) Fatigue striations on a crack fracture surface. Arrow indicates the direction of crack propagation.

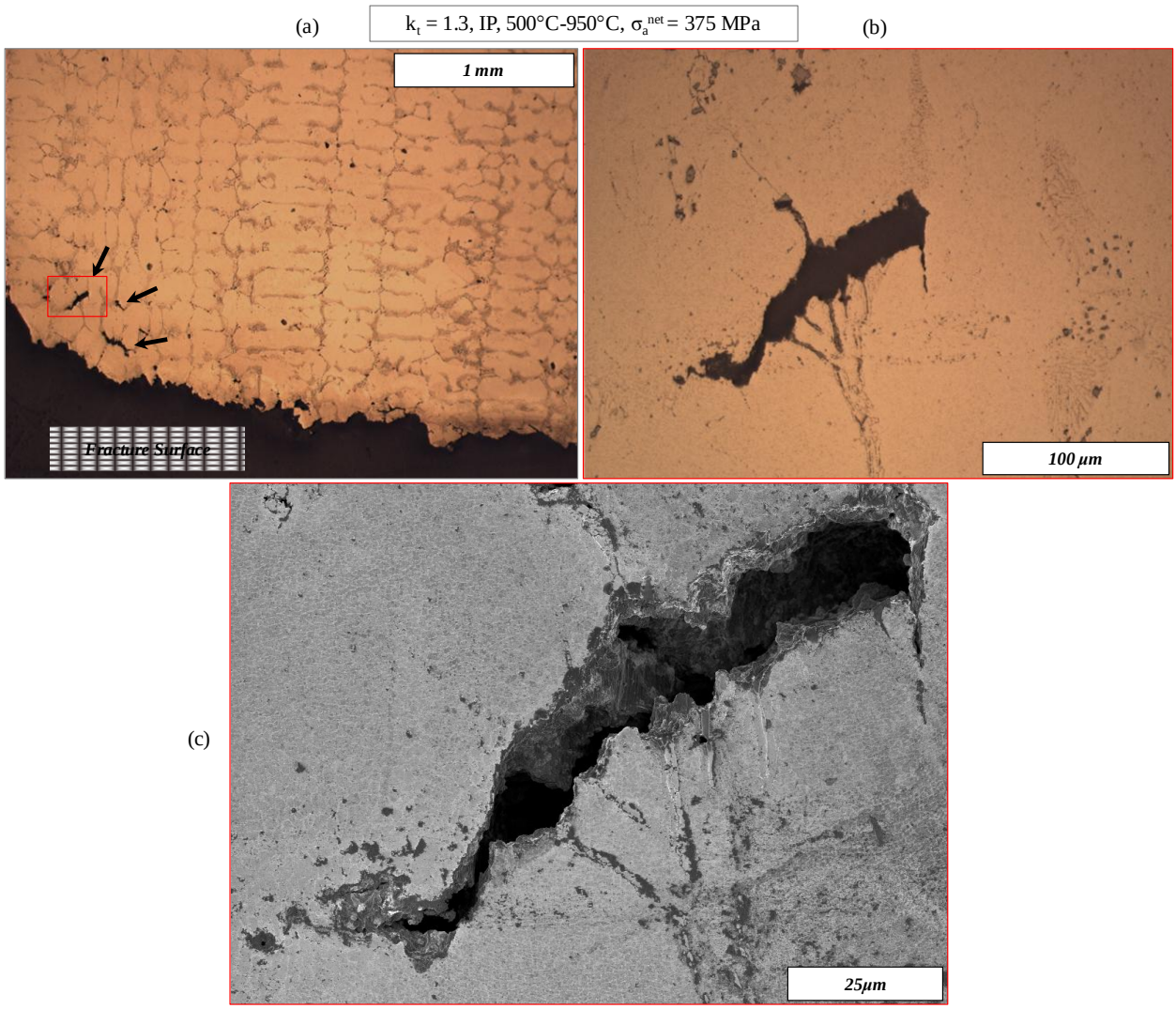

Figure 6-30. Formation of creep-assisted interdentritic microcracks under 500°C ↔ 950°C IP TMF in $k_t = 1.3$ CM247LC DS (a) Microcracks underneath the fracture surface (b) Optical image of internal microcrack (c) SEM imaging of an internal microcrack

Mechanical displacement histories measured across the notch for force control IP TMF tests are shown in Fig. 6-31. Under force control conditions there is no constraint imposed on displacement across the notch root and as such creep ratcheting and creep rupture can occur.

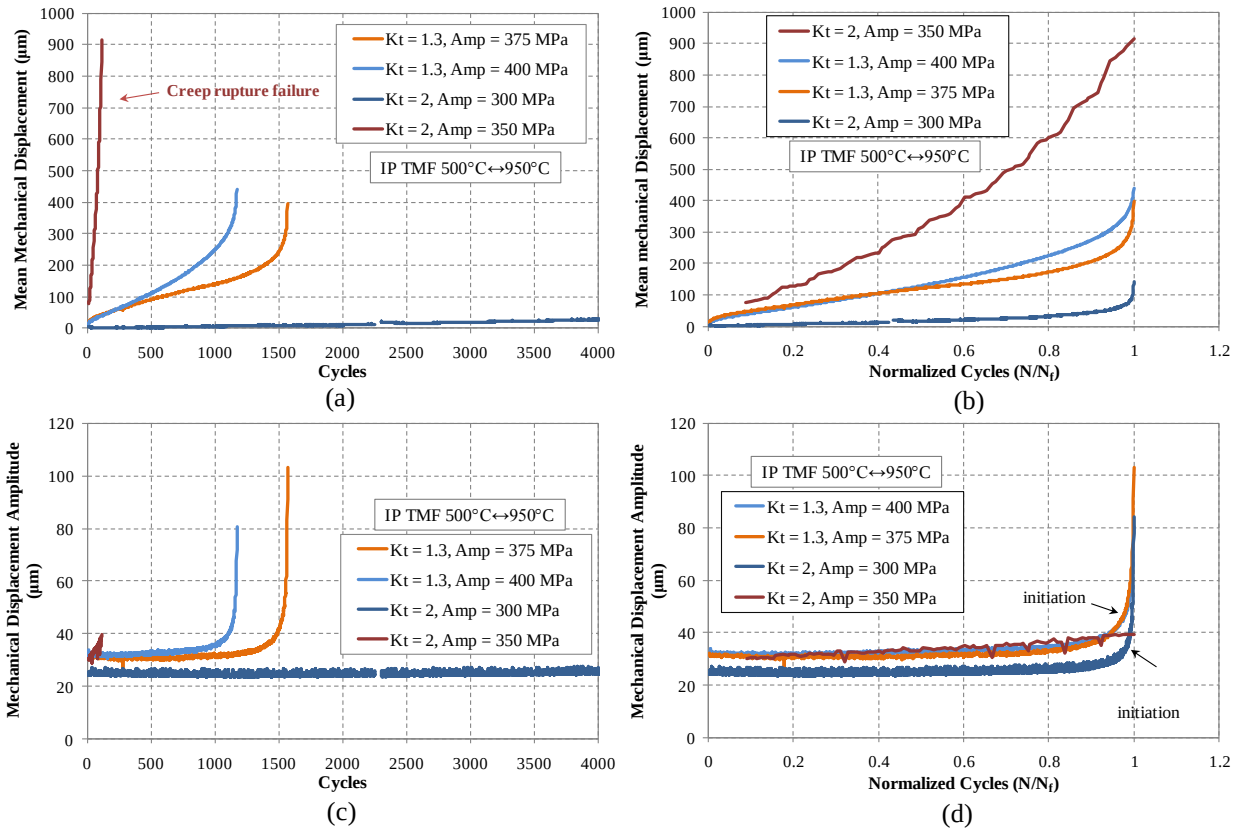

Figure 6-31. Variation in specimen ratcheting between high (creep rupture), intermediate and low ratcheting for CM247LC DS 500°C ↔ 950°C IP TMF $k_t = 1.3$ and $k_t = 2.0$. (a) Mean displacement history based on cycles (b) Mean displacement history based on % fracture life (c) Amplitude history based on cycles (d) Amplitude history based on % fracture life.

Fig. 6-31(d) illustrates that the $k_t = 2.0$ $\sigma_a^{nom} = 350MPa$ experiment displayed no trend indicative of crack initiation towards the end of life. No locations of crack initiation were displayed on the fracture surface, rather the fracture resembled rupture from bulk creep deformation. Evidence of crack initiation on fracture surfaces of the milder notch, $k_t = 1.3$, are shown in Fig. 6-32.

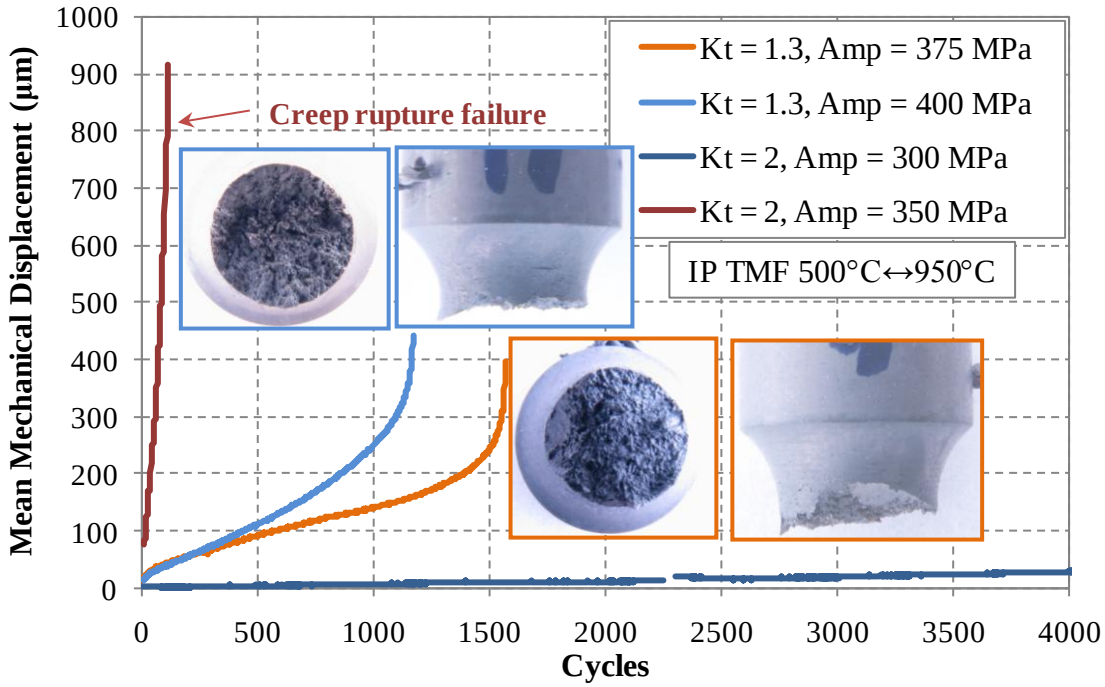

Figure 6-32. Fracture surfaces for $k_t = 1.3$ CM247LC DS 500°C ↔ 950°C IP TMF alongside the respective displacement curves indicative of creep-fatigue damage.

These results show that the level of creep ratcheting, failure mode and specimen life is highly sensitive to the applied net section stress. The $k_t = 2$ IP TMF experiment performed under displacement boundary conditions benefited from suppressed creep damage and ratcheting that resulted in a significantly longer life. Additionally displacement conditions promote stress relaxation and redistribution that may be beneficial for life. Despite having larger imposed net section stresses, notch geometry $k_t = 1.3$ did not fail from creep rupture. In both instances there is evidence of crack initiation on crystallographic planes.

Under IP TMF conditions force control conditions represent the life-limiting conditions. Displacement control conditions prevent creep rupture failure which may occur under unbounded force control conditions.

CHAPTER 7 INFLUENCE OF NOTCH SEVERITY ON TMF LIFE OF A DS NI-BASE SUPERALLOY

This chapter covers the influence notch severity on TMF life to crack initiation for the directionally solidified CM247LC DS Ni-based superalloy. Force-controlled TMF experiments were performed on specimens oriented in the longitudinal direction. Four distinct circumferentially notched geometries corresponding to elastic stress concentrations varying between $k_t = 1.3$ and $k_t = 3.0$ were utilized. Experiments were performed using both $500°C \leftrightarrow 950°C$ and $500°C \leftrightarrow 750°C$ temperature ranges to understand the impact of high temperature damage processes on TMF life. Simulated results using the GTD-111 transversely isotropic model introduced in Chapter 5 are utilized with a non-local damage approach to interpret experimentally observed trends for OP TMF $500°C \leftrightarrow 950°C$ and make life predictions.

7.1. CM247LC DS TMF 500°C↔950°C

7.1.1 OP TMF

Out-of-phase TMF life results for the temperature range $500°C \leftrightarrow 950°C$ are shown as a function of applied net section stress amplitude in Fig. 7-1. Details of experiments shown in these and subsequent figures are provided in Table 7-1, which summarize experiments conducted by Kupkovits [6], and Table 7-2, which summarizes new experiments conducted in this study.

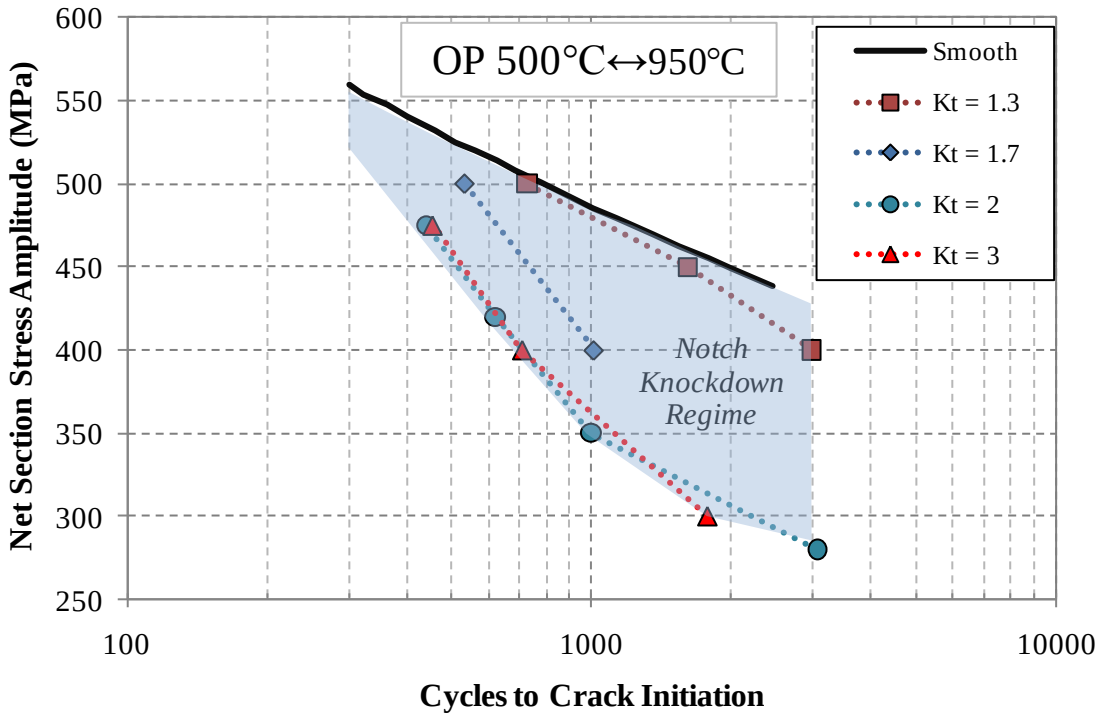

Figure 7-1. Influence of notch severity on $500°C \leftrightarrow 950°C$ OP TMF crack initiation life for CM247LC DS.

Under these conditions the least severe notch, $k_t = 1.3$, follows the smooth OP TMF life trend. This notch geometry is at the limit of fatigue notch sensitivity (notch insensitive) and does not detrimentally affect the life to crack initiation within the tested regime. Notch geometries corresponding to $k_t = 2.0$ and $k_t = 3.0$ produce the same life trend indicating the upper limit of TMF notch sensitivity. For notch geometries more severe than $k_t = 2.0$ increases in notch severity are not increasingly detrimental towards life. Notch geometry $k_t = 1.7$ produces a life trend that falls in between the lower and upper limit of notch sensitivity. Within this region OP TMF life to crack initiation is directly influenced by the notch severity and produces a notch knockdown effect that reduces life compared to the uniaxial smooth specimen.

OP TMF $500°C \leftrightarrow 950°C$ fracture surface images are shown in Fig. 7-2. Across all utilized specimen geometries multiple surface cracks initiate and propagate inwards until unstable crack growth results in final fracture. Both thumbnail and circumferential cracking is observed.

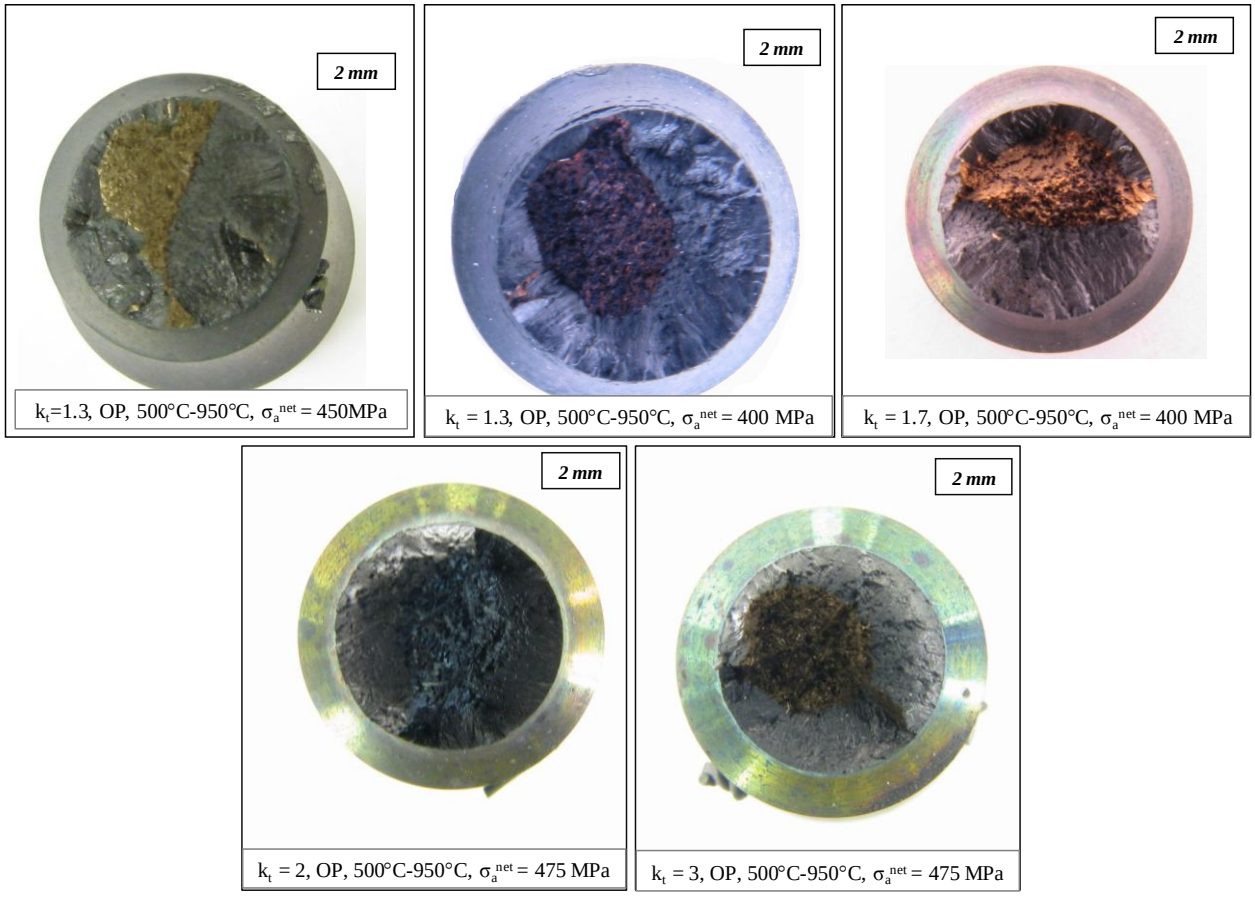

Figure 7-2. Fracture surfaces corresponding to each geometry for OP TMF $500°C \leftrightarrow 950°C$ under various applied loads.

Profile images of four $500°C \leftrightarrow 950°C$ OP TMF specimens are shown in Fig. 7-3. Images indicate that with increasing notch severity crack initiation occurs closer to the notch root.

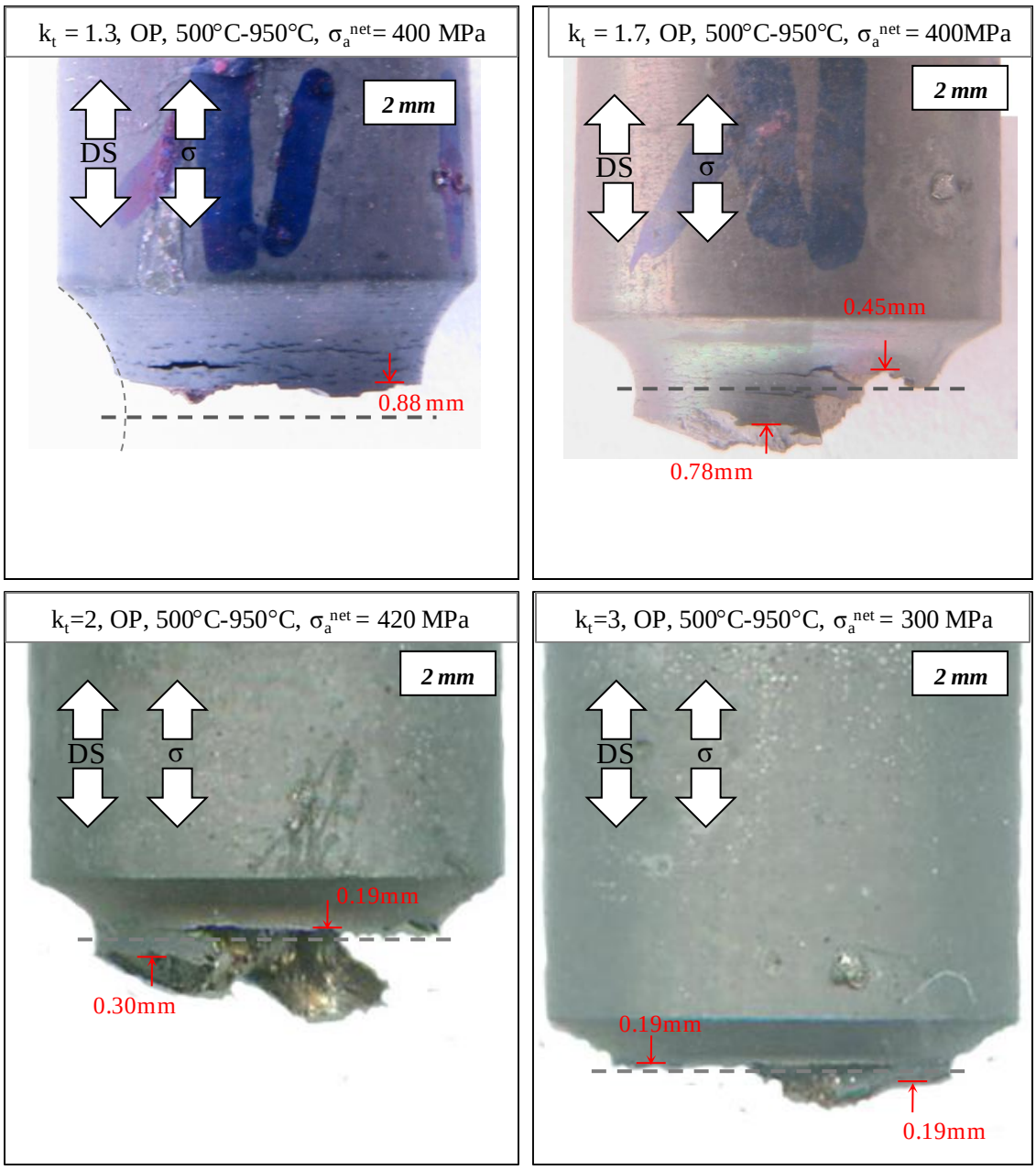

Figure 7-3. Profile images for each specimen geometry under OP TMF $500°C \leftrightarrow 950°C$ indicating the location of crack initiation relative to the notch root.

OP TMF results for each specimen geometry under an applied net section stress of 400 *MPa* are shown in Fig. 7-4. The location of maximum von Mises equivalent stress, shown by Kupkovits

[54] and Moore [57] to correspond to the location of crack initiation, occurs closer to the notch root as the stress intensity is increased.

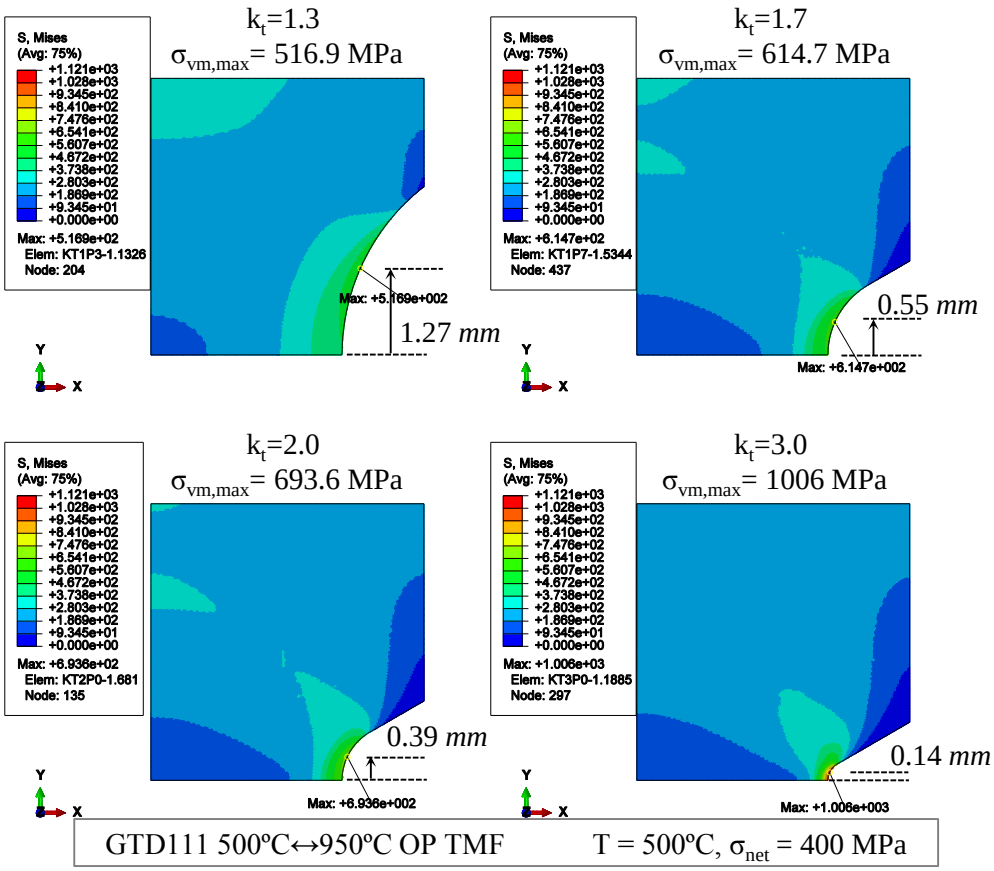

Figure 7-4. Von Mises equivalent stress distribution at minimum temperature (maximum load) under OP TMF across four tested notch geometries for $k_t = 1.3$, $k_t = 1.7$, $k_t = 2.0$ and $k_t = 3.0$.

Equivalent cyclic inelastic strain ranges across all geometries under a 400 *MPa* remotely applied net section stress are shown in Fig. 7-5.

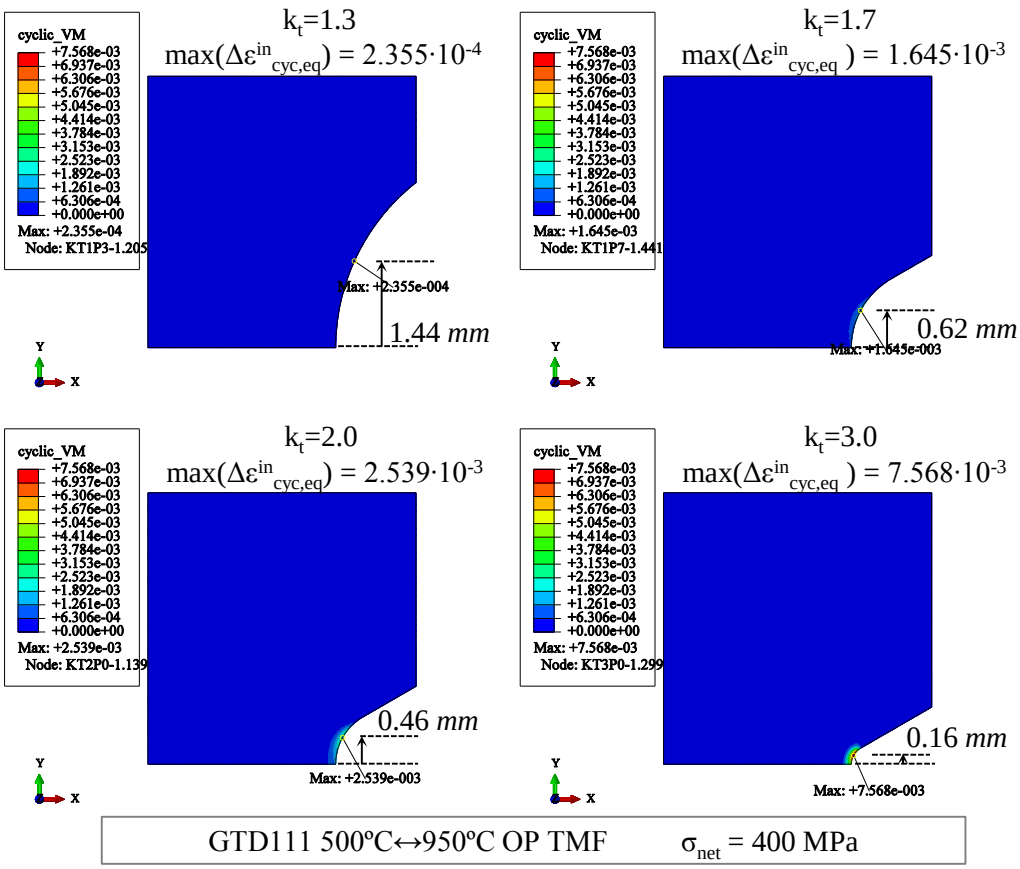

Figure 7-5. Cyclic inelastic equivalent strain range distribution under OP TMF across four tested notch geometries for $k_t = 1.3$, $k_t = 1.7$, $k_t = 2.0$ and $k_t = 3.0$.

Initiation location trends utilizing both the von Mises stress and equivalent cyclic inelastic strain range agree well experimental results that the crack initiation location approaches the notch root with increasing notch severity.

Images indicating crack initiation locations for notch geometry $k_t = 1.3$ under various applied net section stress amplitudes are shown in Fig. 7-6.

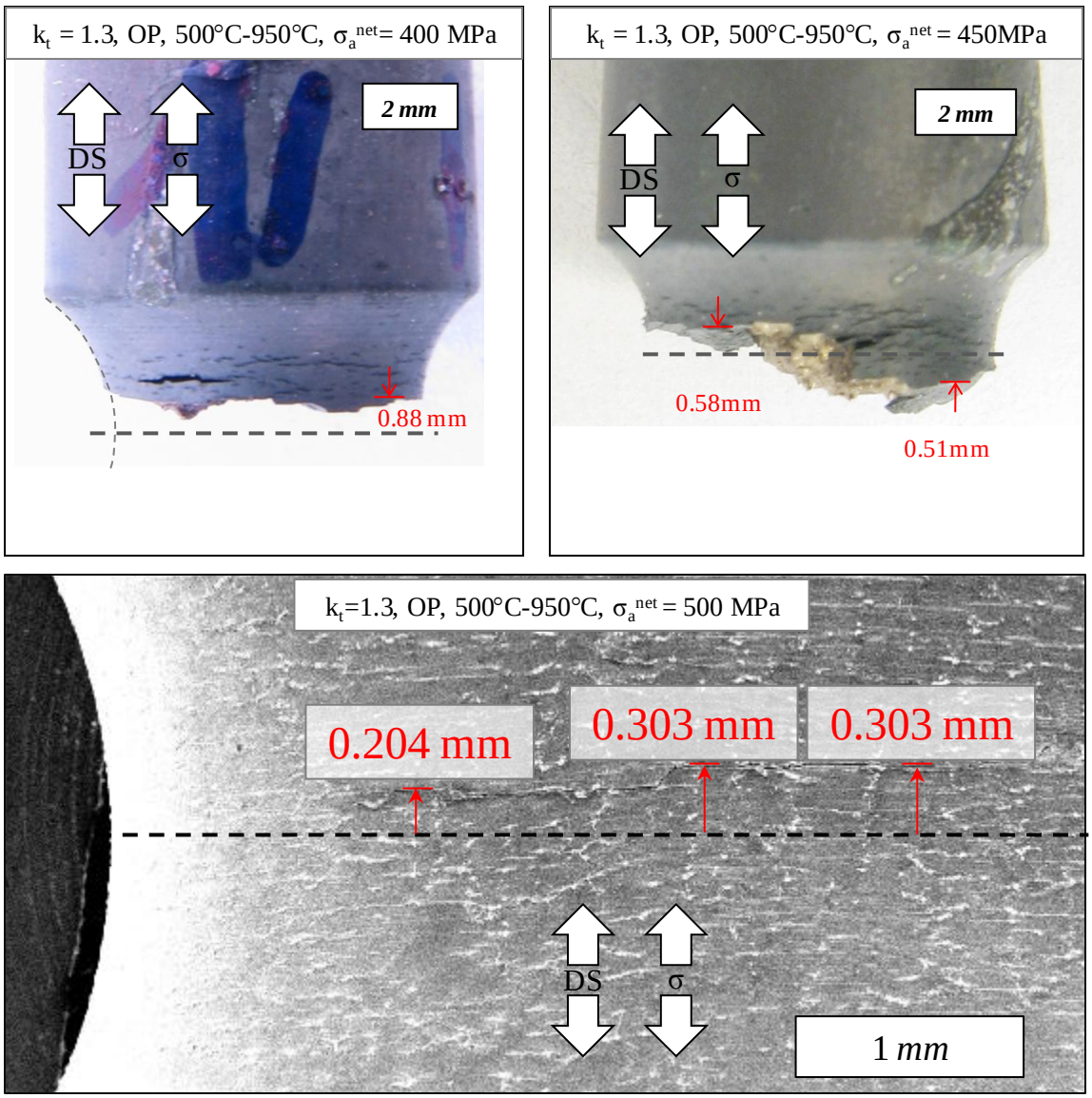

Figure 7-6. Images indicating the influence of applied net section stress on location of crack initiation for $k_t = 1.3$ under $500°C \leftrightarrow 950°C$ OP TMF.

Experimental results show that with increasing applied net section stress the location of crack initiation approaches the notch root. Notch component simulations corresponding to notch geometry $k_t = 1.3$ under applied net section stresses varying between 300 MPa and 500 MPa are shown in Fig. 7-7. Shown is the von Mises equivalent stress and the equivalent cyclic inelastic strain range.

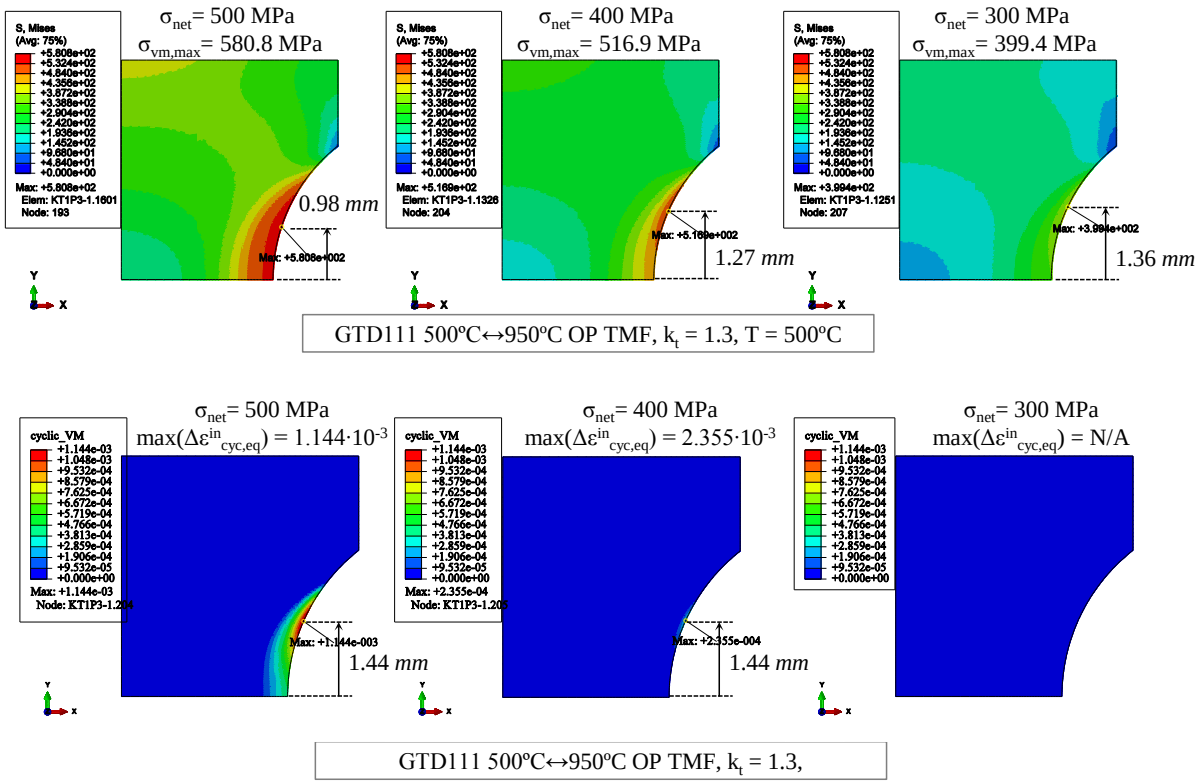

Figure 7-7. Notch geometry $k_t = 1.3$ distributions of the von Mises equivalent stress and equivalent inelastic cyclic strain range for net section stresses 300 *MPa*, 400 *MPa* and 500 *MPa*.

Simulated responses indicate that the maximum von Mises equivalent stress approaches the notch root with increasing applied net section stress. The maximum equivalent cyclic inelastic strain range however remains in the same location regardless of the applied load, with the exception of 300 *MPa* where cyclic inelastic deformation is negligible (< 1E-8). Locations of maximum von Mises stress and equivalent inelastic cyclic strain range correspond well with experimentally observed crack initiation locations. This is indicative that initiation is dependent on both the inelastic strain and stress state in the material. The location of maximum equivalent cyclic inelastic strain range is insensitive to the applied load for more severe notch geometries as well, as shown for $k_t = 2.0$ in Fig. 7-8.

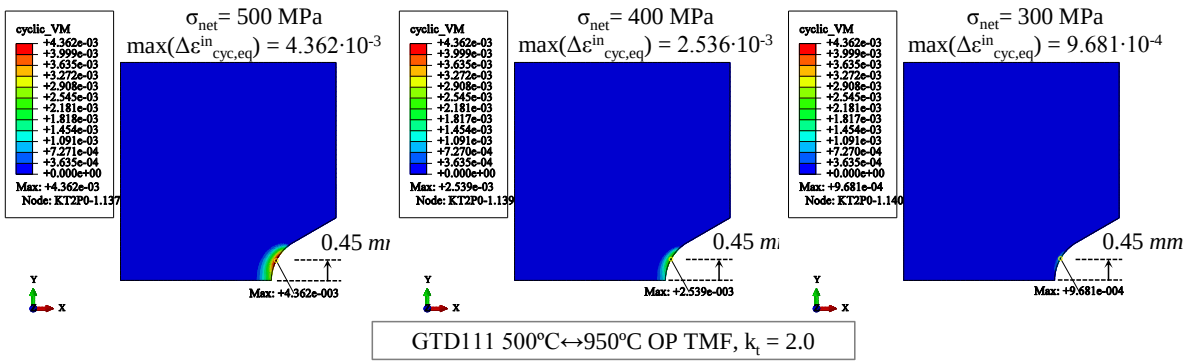

Figure 7-8. Equivalent cyclic inelastic strain range and maximum location for $k_t = 2.0$ under OP TMF.

Additional microscopy for $k_t = 1.3$ $\sigma_a^{net} = 400MPa$ is shown in Fig. 7-9. Multiple cracks initiated at the specimen surface and grew inwards circumferentially, as indicated by fatigue striations. The location of crack initiation was 0.88 *mm* away from the notch root. Environmentally degraded secondary cracks were observed around the circumference, typical of OP TMF.

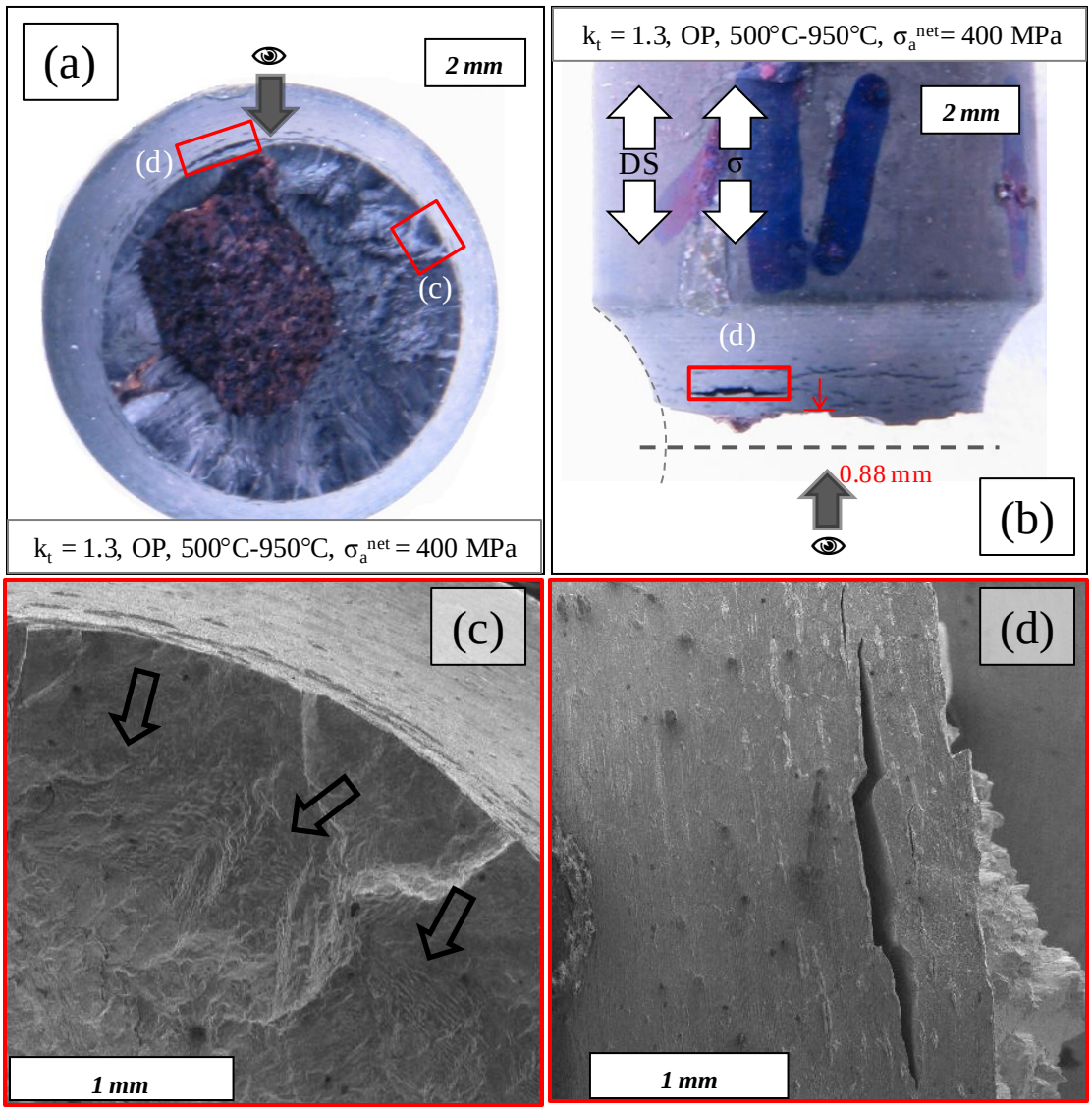

Figure 7-9. Fractured OP TMF test specimen. (a) Top view indicating multiple sources of surface crack initiation (b) side view showing initiation away from notch root and multiple secondary cracks (c) striations indicative of fatigue crack growth inward from surface initiation (d) surface initiation of secondary crack.

Micrographs of a cracked OP TMF $500°C \leftrightarrow 950°C$ specimen that failed prior to reaching final fracture are shown in Fig. 7-10. Dark field images display slip bands present in a region within the vicinity of the notch root. This corresponds to the highly stressed area within which localized inelastic deformation occurred. The slip bands form at 52.9° angles relative to the horizontal and are mirrored around the notch root. Although the exact slip trace cannot be

determined, the slip planes correspond to $(\bar{1}1\bar{1})$ and $(1\bar{1}\bar{1})$. Similar observations were made by Arakere et al. on sharp notched single crystal specimens [9, 84]. The primary crack initiated 300 μm from the notch root at an angle close to the crystallographic direction indicated by the slip bands. Crack path oxidation can be seen along the length of the crack and the crack tip. Several secondary cracks can be seen initiating at oxide spikes along the notch surface.

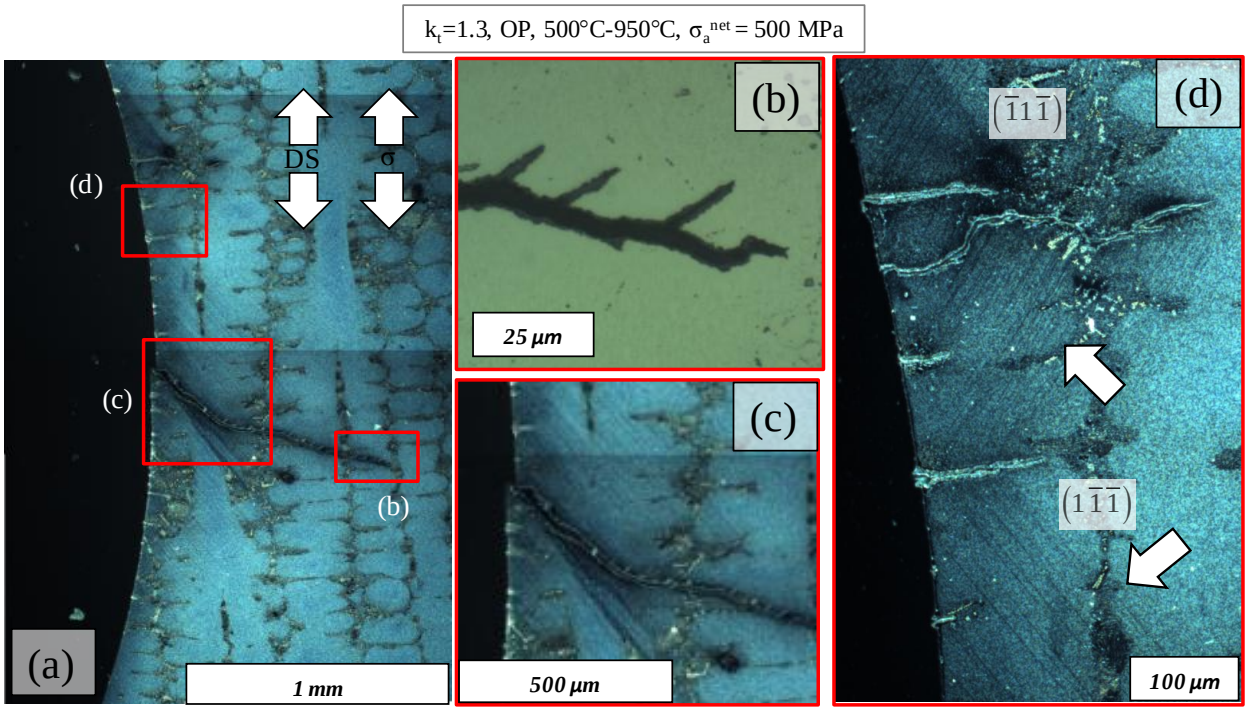

Figure 7-10. (a) Micrograph of crack initiated OP TMF specimen. (b) preferred oxidation along active slip bands (c) crack initiation at surface along slip band (d) localized inelastic deformation occurring along slip bands at the specimen surface and several oxide spikes.

Notch surface images near a primary crack are shown in Fig. 7-11. Oxide spikes and secondary environmental-fatigue cracks can be seen oriented perpendicular to the loading direction.

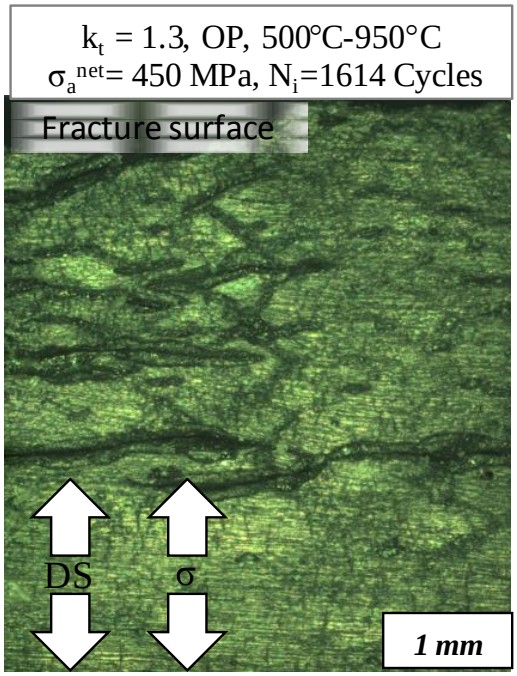

Figure 7-11. Oxide spikes and secondary environmental-fatigue cracks on the OP TMF $500°C \leftrightarrow 950°C$ specimen surface.

7.1.2 IP TMF

In-phase TMF results for $500°C \leftrightarrow 950°C$ are shown in Fig. 7-12. The OP TMF notch knockdown regime is shown for comparison.

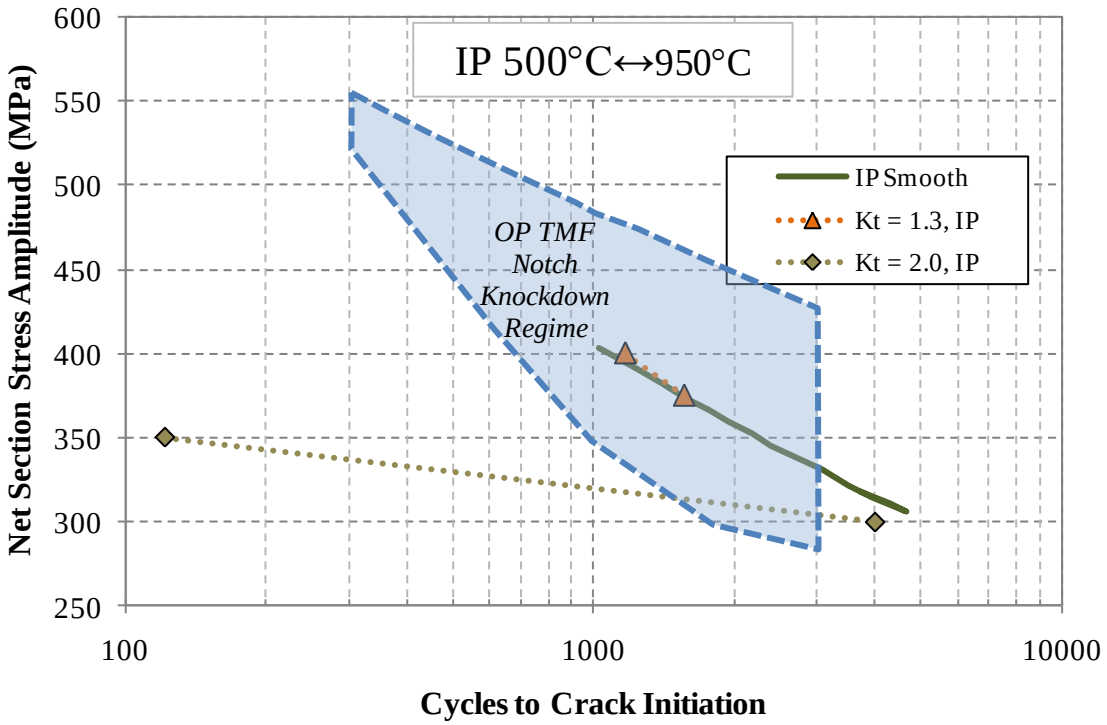

Figure 7-12. Influence of notch severity on IP TMF life for CM247LC DS $500°C \leftrightarrow 950°C$. OP TMF life trends shown for comparison.

Under the prescribed conditions the notch geometry $k_t = 1.3$ follows the same trend as a smooth specimen within the tested regime. The notch geometry corresponding to $k_t = 2.0$ produces a separate trend, but at low applied net section stresses is very close to the smooth trend. The $k_t = 2.0$ trend is also highly sensitive to the applied load level under IP TMF. A 16% increase in net section stress resulted in failure by creep rupture and decreased life by a factor of 30. There is insufficient information to determine an analogous notch knockdown regime for IP TMF, however as in the case of OP TMF, the notch $k_t = 1.3$ was not detrimental for life under the applied net section stress amplitudes.

The influence of notch geometries $k_t = 1.3$ and $k_t = 2$ on the stress response for IP TMF is shown in Fig. 7-13. The von Mises stress response is shown at minimum and maximum applied temperatures.

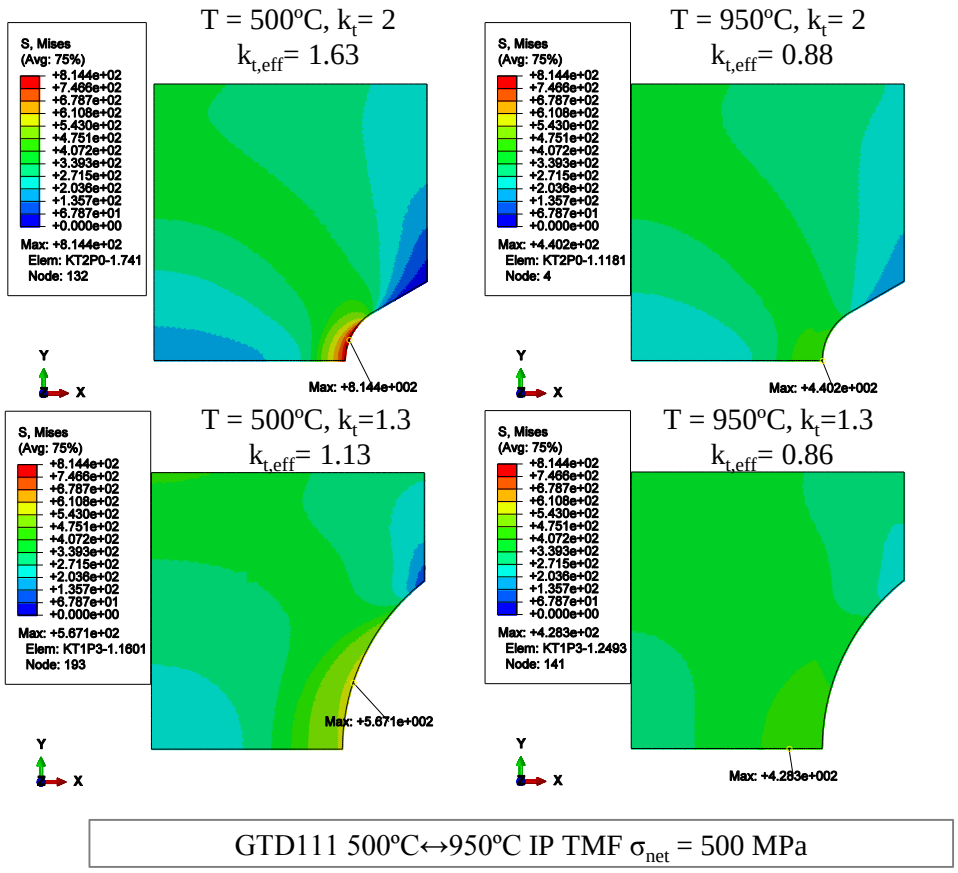

Figure 7-13. Von Mises equivalent stress distributions for IP TMF for $k_t = 1.3$ and $k_t = 2$ geometries at maximum and minimum applied force.

The reduction of flow stress coupled with stress relaxation at maximum temperature reduces the maximum von Mises stress and generates residual stresses that reduce the effective stress concentration factor. This can explain the observed stress-based life trends for $k_t = 1.3$ and $k_t = 2.0$ for low net section stress. The equivalent inelastic cyclic strains are shown for notch geometries $k_t = 1.3$ and $k_t = 2.0$ under IP TMF in Fig. 7-14.

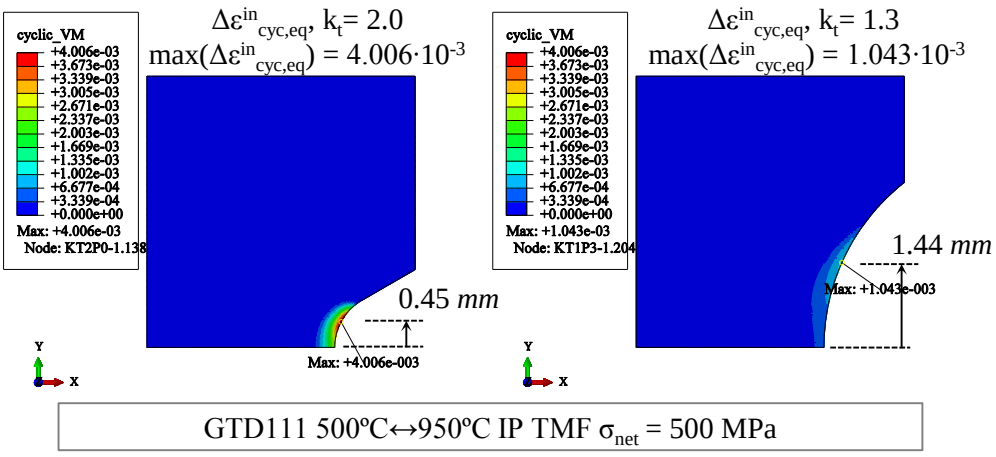

Figure 7-14. Equivalent cyclic inelastic strain range for $k_t = 1.3$ and $k_t = 2.0$ under IP TMF.

Similar to OP TMF conditions, the cyclic inelastic strain response is highly localized to the area away from the notch root and on the free surface. Locations of maximum strain range in both geometries occur away from the notch root.

Fracture surfaces corresponding to two IP TMF $500°C \leftrightarrow 950°C$ experiments for $k_t = 1.3$ are shown in Fig. 7-15 and Fig. 7-16.

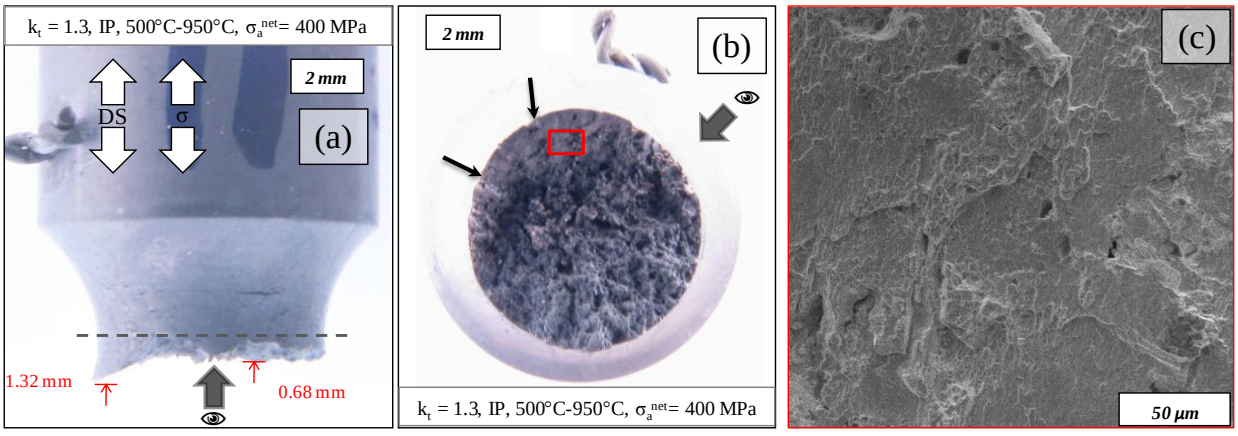

Figure 7-15. (a-b) Fractured IP TMF specimen. Crack initiated and grew on crystallographic plane. (c) Micro voids seen on the fracture surface. Black arrows display location of crack initiation.

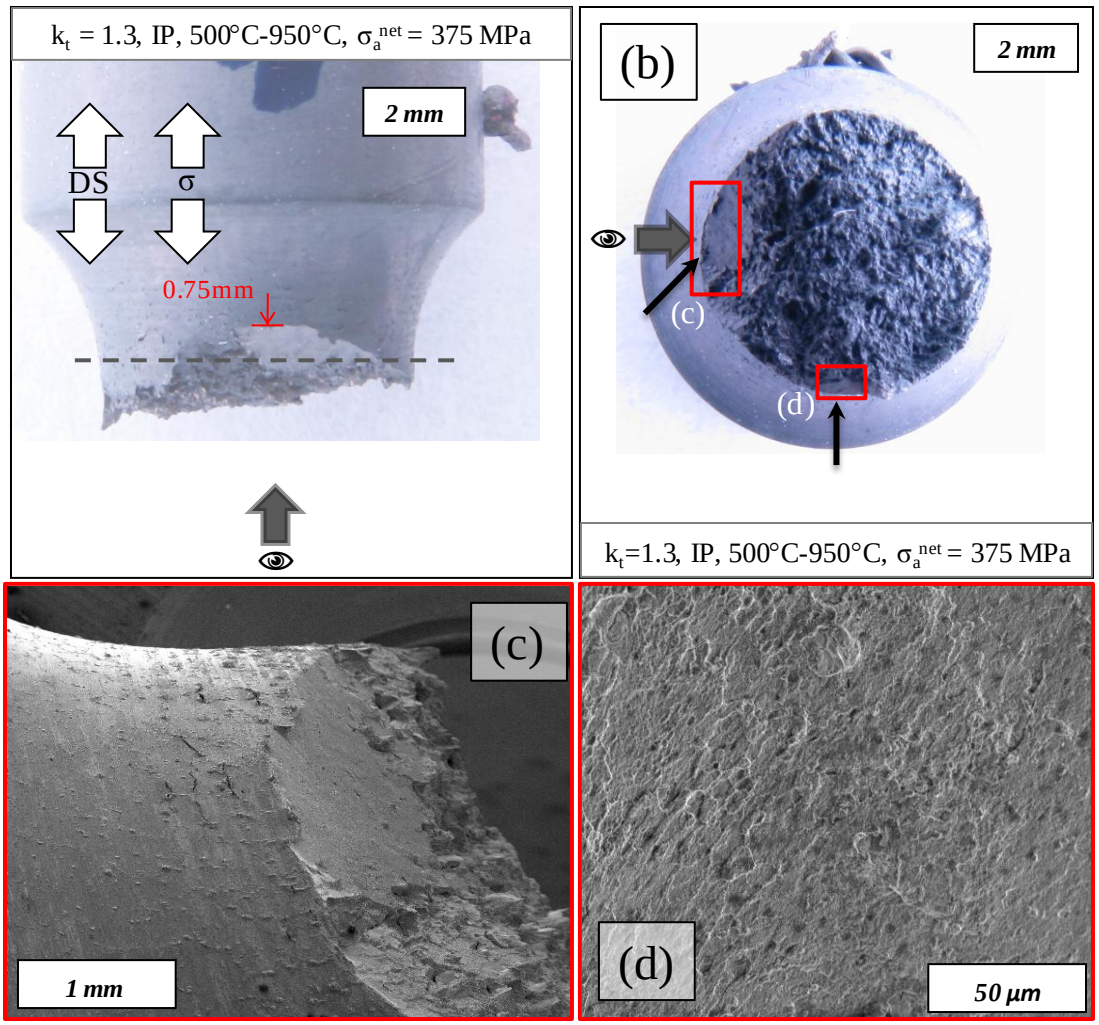

Figure 7-16. Fractured IP TMF specimen.(a) Location of crack initiation away from notch root (b) Black arrows display location of crack initiation.(c) Oxide spallation visible near primary crack. (d) Micro voids observed in a secondary crack.

Initiation occurred 1.32 *mm* and 0.75 *mm* away from the notch root on crystallographic planes. Evidence of internal microvoids were observed on the surface of the primary crack path in Fig. 7-15(c) and on a secondary crack shown in Fig. 7-16(d). This is indicative of high temperature tensile creep damage expected under IP TMF conditions.

Notch surface images near the primary crack fracture surface are shown in Fig. 7-17. Evidence of oxide spallation, typical for IP TMF, was not observed in notched specimens. A

micrograph from Kupkovits [54] on a smooth specimen under the same TMF conditions is shown for comparison.

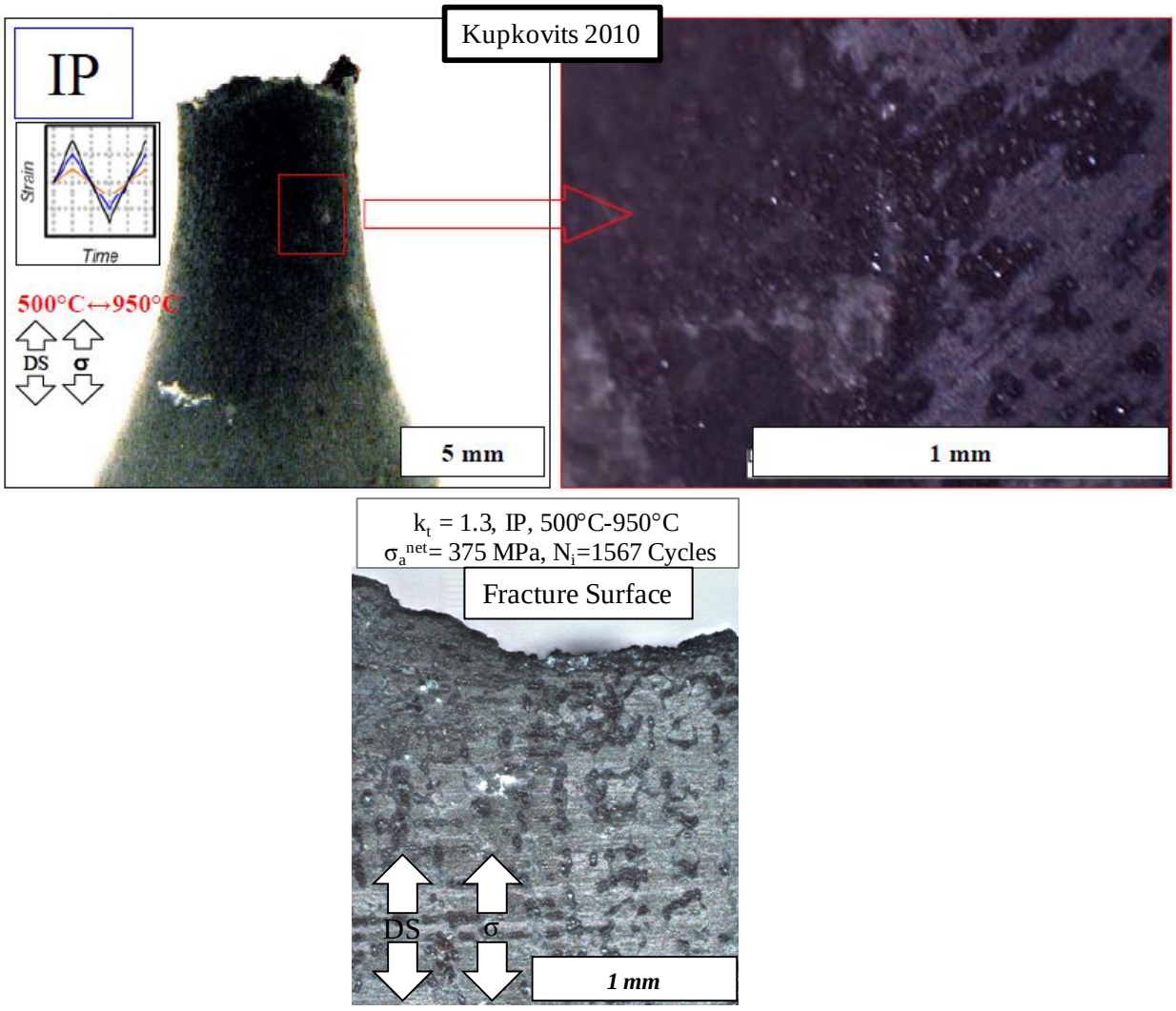

Figure 7-17. IP TMF $500°C \leftrightarrow 950°C$ specimen surface. Kupkovits results for smooth IP TMF displaying spallation is shown for comparison [54].

7.1.3 Notch Displacement Evolution

As tests were performed under prescribed force conditions, the displacement across the notch was unconstrained and evolved with time. OP TMF mechanical extensometer displacement versus net section stress is shown in Fig. 7-18. Mechanical extensometer

displacement is defined as the displacement measured across the notch excluding displacements due to thermal expansion.

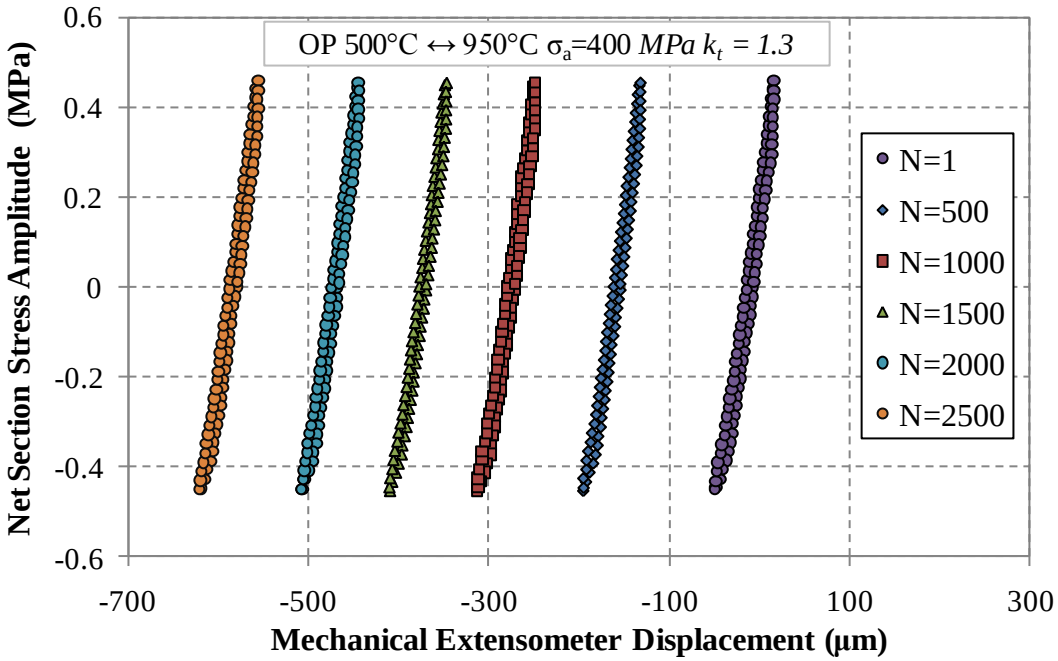

Figure 7-18. Mechanical extensometer versus net section stress amplitude shown in 500 cycle increments for an OP TMF CM247LC DS experiment. Significant compressive deformation at high temperature produces cyclic ratcheting.

Contours of equivalent inelastic ratcheting strain increment under OP TMF conditions are shown in Fig. 7-19.

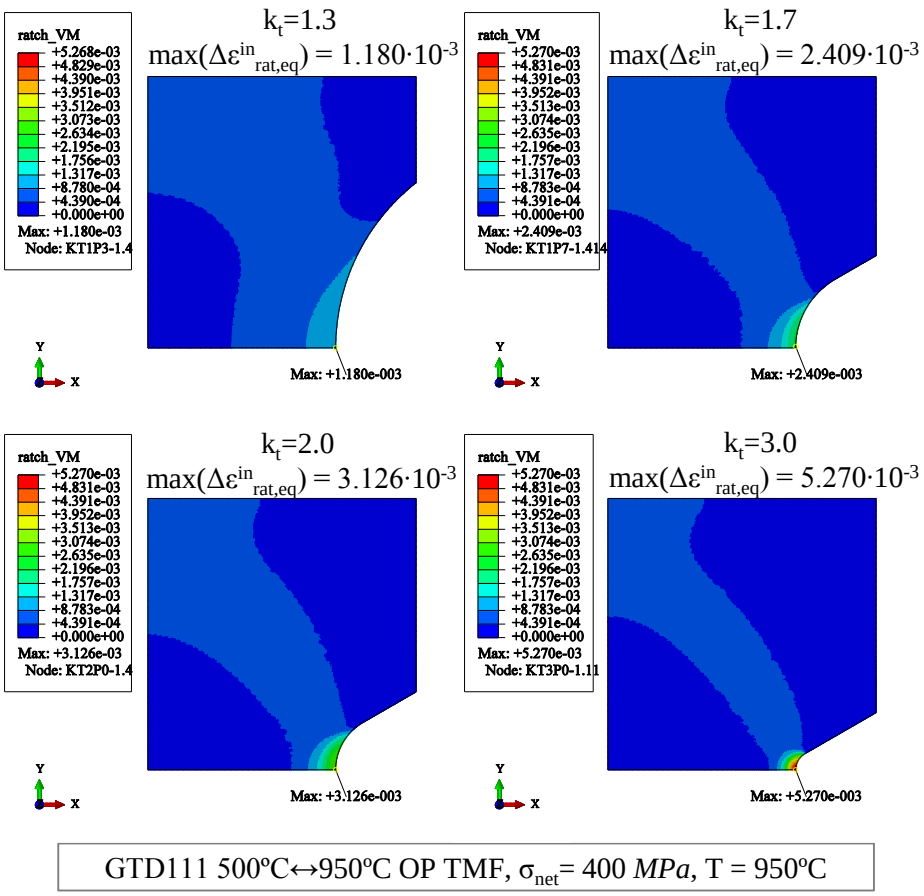

Figure 7-19. Localization of equivalent inelastic ratcheting strain increment under OP TMF conditions across each notch geometry under a 400 *MPa* applied net section stress.

The inelastic ratcheting strains are less localized compared to the highly localized cyclic inelastic strain range response. As the measured ratcheting displacements are measured remotely, they capture an averaged global deformation within the notched region. A majority of inelastic deformation occurs in high temperature loading creating a tension-compression asymmetry in inelastic deformation. This phenomena is what causes compressive ratcheting under OP loading and tensile ratcheting under IP loading.

Ratcheting result for geometries $k_t = 1.3$, $k_t = 1.7$ and $k_t = 3$ under an applied remote net section stress of 400 *MPa* are shown in Fig. 7-20. Notch geometry $k_t = 2$ is not included as no experiments were performed utilizing exactly a 400 *MPa* net section stress.

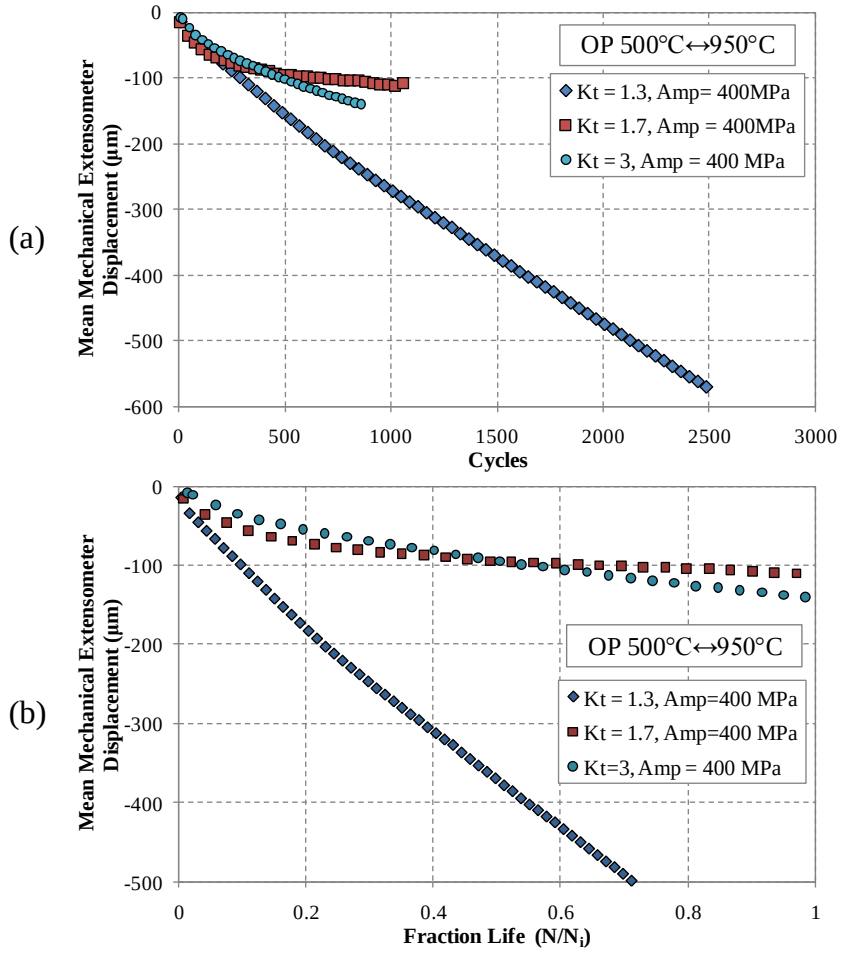

Figure 7-20. CM247LC $500°C \leftrightarrow 950°C$ OP TMF mean displacement history for $k_t = 1.3$, $k_t = 1.7$ and $k_t = 2$ shown utilizing (a) cycles and (b) fraction of fracture life.

Continuous ratcheting throughout the history of the test can be attributed to creep deformation at maximum temperature. The greatest degree of creep ratcheting was found experimentally to occur in the bluntest notch specimen, $k_t = 1.3$. Simulated results from notch root nodes

displaying the axial inelastic ratcheting increment $\left(\Delta\varepsilon_{22,rat}^{in}\right)$ are shown in Fig. 7-21 . This quantity is comparable to the axial component of creep strain rate used by Lukas et al. as a metric to quantify creep rupture time in notched CMSX-4 [85].

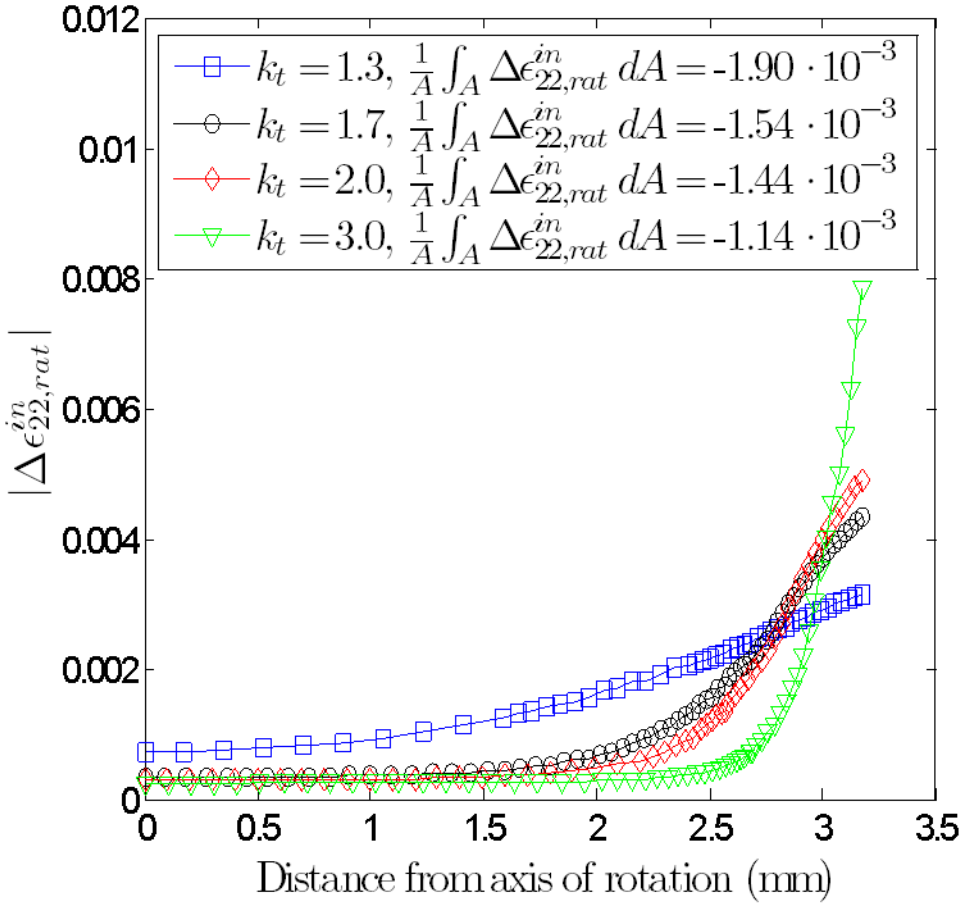

Figure 7-21. Equivalent inelastic ratcheting increment in the axial direction $\left(\Delta\varepsilon_{22,rat}^{in}\right)$ across the notch root for 500 *MPa* net section stress under OP TMF.

Simulated results indicate that the local maximum ratcheting strain increases with increasing notch severity, however the area average over the net section decreases. As experimental measurements were taken remotely far from the notch root the area averaged quantity is a better metric for quantifying far field ratcheting. The averaged strain ratcheting metric agrees well with

experimentally observed behavior. The bluntest notch was experimentally observed to experience the highest degree of cyclic ratcheting which was confirmed by simulated results. Although the ratcheting response for $k_t = 1.7$ and $k_t = 3.0$ is similar, initially the $k_t = 1.7$ notch displays more ratcheting which is captured by the simulated results. The ratio of maximum equivalent inelastic strain increment to maximum total equivalent inelastic strain increment is shown as a contour map in Fig. 7-22. This map represents the relative amount of ratcheting strain to total inelastic strain.

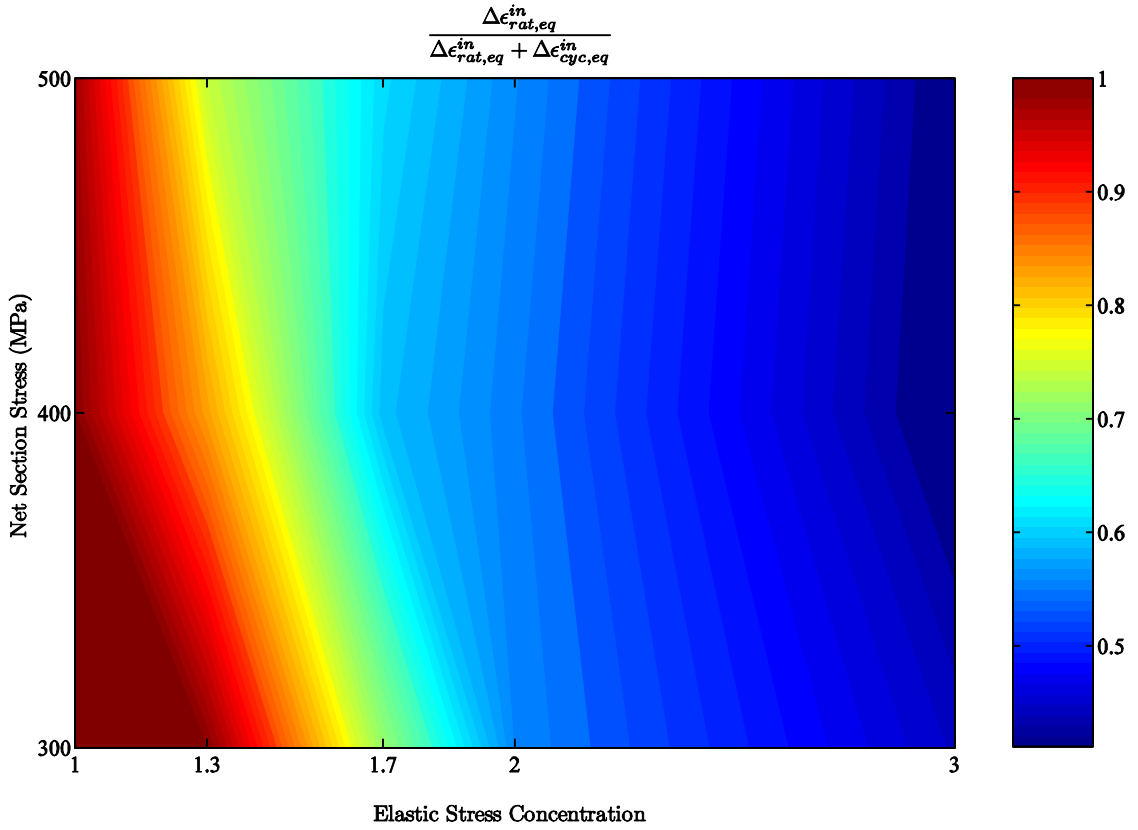

Figure 7-22. Contour map of the ratio of equivalent inelastic strain increment to total equivalent inelastic strain increment over one cycle for GTD-111 OP TMF $500°C \leftrightarrow 950°C$.

As stress intensity increases, the ratio decreases indicating that maximum cyclic inelastic strain becomes increasingly significant relative to the maximum ratcheting strain. Additionally, the

ratio decreases slightly for a constant stress concentration with increasing net section stress. Fig. 7-23 shows contours of the equivalent inelastic ratcheting strain increment. Smooth specimens in force control resulted in ratchet strains an order of magnitude larger and hence are not shown so that a sufficient amount of contours can be captured for notched specimens.

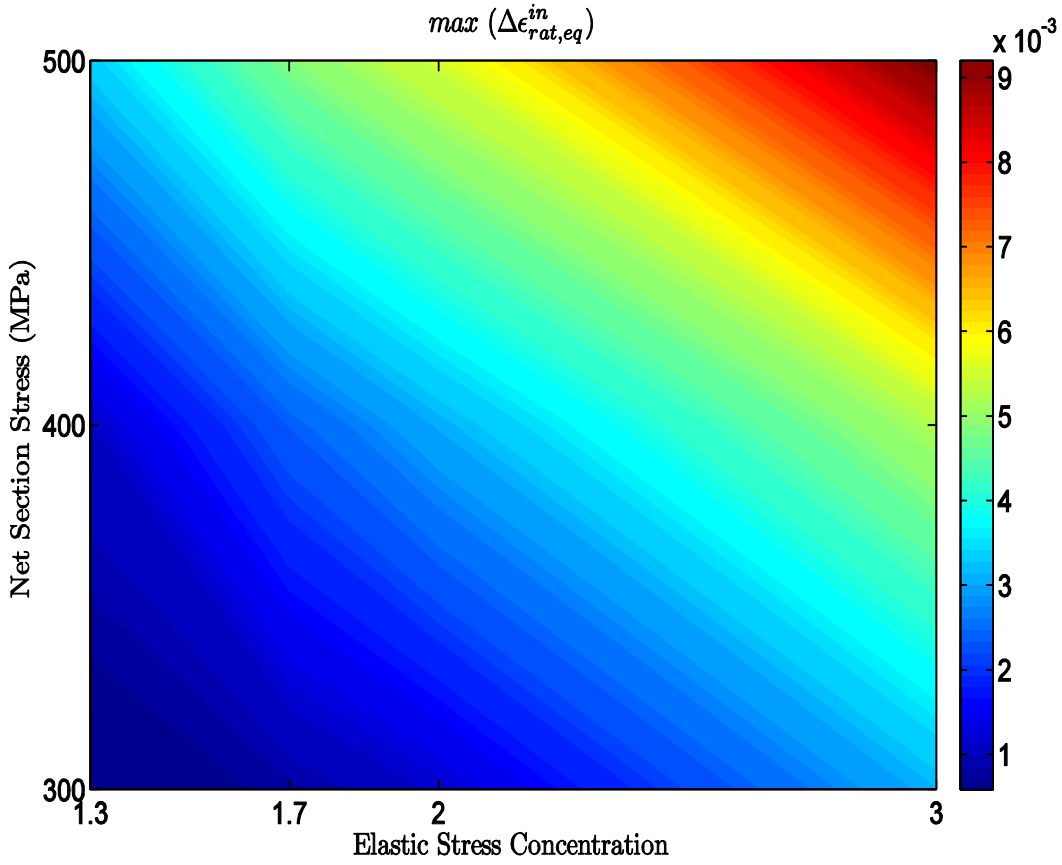

Fig. 7-23. Contour map of equivalent inelastic strain over one cycle for GTD-111 OP TMF $500°C \leftrightarrow 950°C$.

The maximum inelastic strain increment increases with increasing stress intensity and applied net section stress. Thus the observed trend that ratcheting strain decreases relative to total inelastic strain with increasing net section stress is due to the competition between ratcheting and cyclic

inelastic strain; the cyclic inelastic strain increases at a faster rate with increasing net section stress.

Notch specimen simulation results showing the equivalent inelastic ratcheting strain increment are shown in Fig. 7-24. Both the maximum and area averaged strain ratcheting increase with increasing applied net section stress for $k_t = 1.7$.

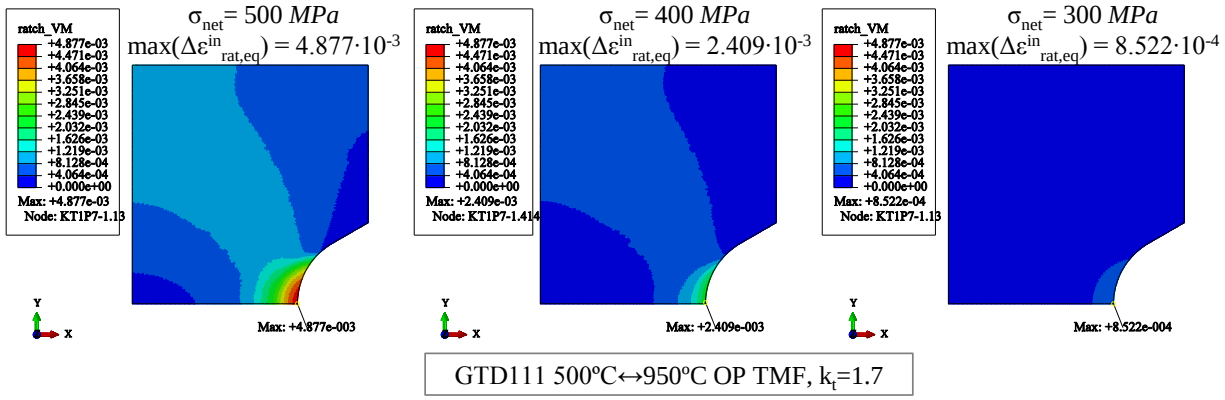

Figure 7-24. Equivalent inelastic ratcheting strain increment under OP TMF conditions for $k_t = 1.7$ with applied net section stresses 500 *MPa*, 400 *MPa* and 300 *MPa*.

During IP TMF high temperature tensile deformation contributes to tensile ratcheting. The mean mechanical extensometer displacements under IP TMF loadings are shown in Fig. 7-25.

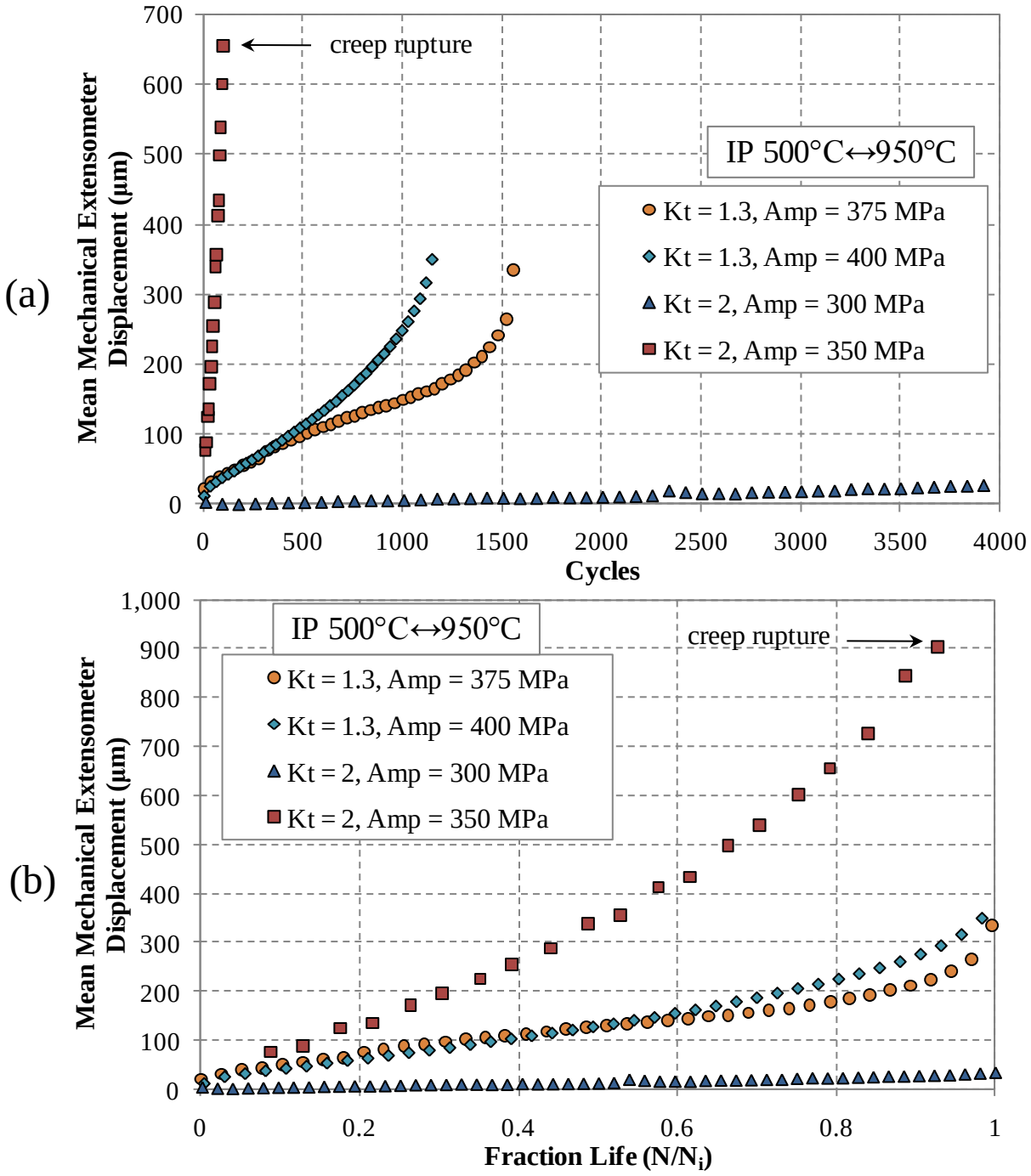

Figure 7-25. Mean mechanical extensometer displacement histories for (a) IP TMF (b) Displacement history as a function of fraction to crack initiation.

Creep rupture was the observed failure mechanism in the $k_t = 2 \quad \sigma_{net}^{a} = 350MPa$ experiment performed by Kupkovits [54]. This mode of failure occurs only under force control IP TMF, is

characterized by a high level of creep ratcheting and results in a fracture surface lacking any indication of crack initiation. Neither $k_t = 1.3$ IP TMF experiments failed due to creep rupture as crack initiation was observed on fracture surfaces, see Fig. 7-26.

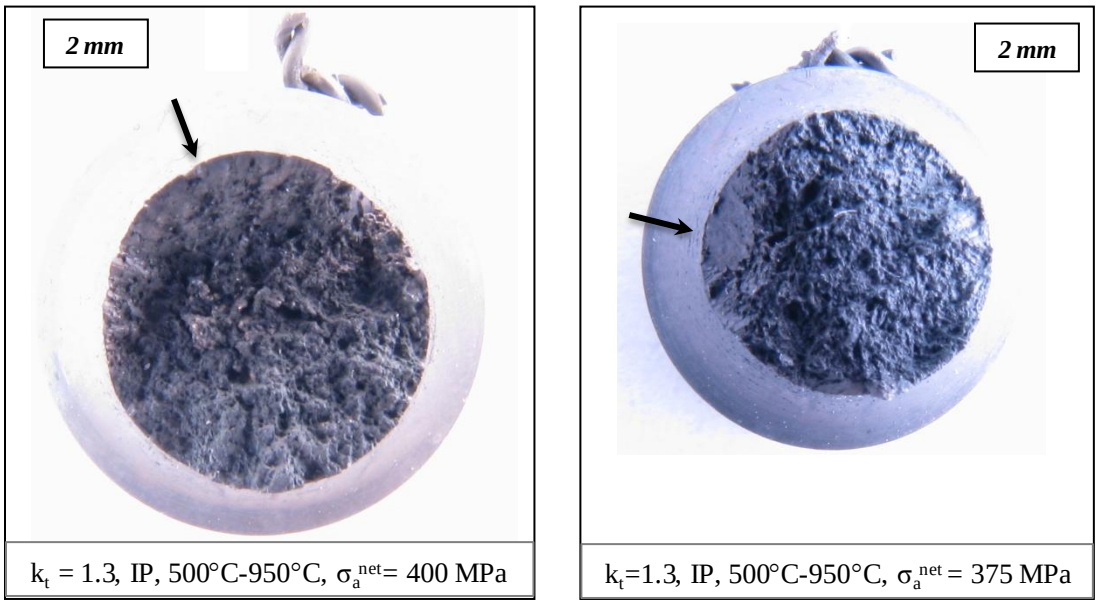

Figure 7-26. Evidence of crystallographic crack initiation in $k_t = 1.3$ notch specimen under IP TMF conditions.

The dominant failure mode is highly sensitive to the applied net section stress; for $k_t = 2$ a decrease in 50 *MPa* of net section stress resulted in completely eliminating significant creep ratcheting and a change of failure mode from failure by creep rupture to failure by creep-fatigue interactions.

Table 7-1: CM247LC DS TMF force control conditions and results

CM247LC DS Force Control TMF Tests							
Period (s)	T_{min} (°C)	T_{max} (°C)	σ_a^{net} (MPa)	R_σ	K_t	Phasing	Initiation Life (cycles)
180	500	950	280	-1	2	OP	3070
180	500	950	350	-1	2	OP	1000
180	500	950	420	-1	2	OP	620
180	500	950	350	-1	2	IP	121
180	500	950	300	-1	2	IP	3998
180	500	950	300	-1	3	OP	1771
180	500	950	400	-1	3	OP	709
180	500	750	600	-1	2	OP	729
180	500	750	530	-1	2	OP	1189
180	500	750	550	-1	3	OP	999
180	500	750	470	-1	3	OP	1671

Table 7-2: CM247LC DS TMF displacement control conditions and results

CM247LC DS Force Control TMF Tests							
Period (s)	T_{min} (°C)	T_{max} (°C)	σ_a^{net} (MPa)	R_σ	K_t	Phasing	Initiation Life (cycles)
180	500	950	500	-1	1.7	OP	536*
180	500	950	500	-1	1.3	OP	728
180	500	950	450	-1	1.3	OP	1614*
180	500	950	400	-1	1.7	OP	1016
180	500	950	400	-1	1.3	IP	1166
180	500	950	375	-1	1.3	IP	1567
180	500	950	400	-1	1.3	OP	2987
180	500	750	700	-1	1.3	OP	1444
180	500	750	800	-1	1.3	OP	620
180	500	750	700	-1	1.7	OP	438
180	500	750	600	-1	1.7	OP	900
180	500	950	475	-1	2	OP	440
180	500	950	475	-1	3	OP	455
180	500	750	745	-0.67	1	OP	1202†
180	500	750	825	-0.84	1	OP	823†

* Heavy cyclic ratcheting caused extensometer saturation, values are cycles to final fracture

†Fully reversed strain controlled experiments. Mechanical strain range 0.8% and 1.0%.

7.2 CM247LC DS TMF 500°C↔750°C

Experiments were performed with a reduced maximum temperature to study the effect of high temperature damage processes on notch sensitivity. Results for OP TMF $500°C \leftrightarrow 750°C$ on each of the four studied notched specimen geometries and smooth specimens are shown in Fig. 7-27. Smooth results are included for quantifying the effects of notches on crack initiation life. Smooth tests were performed in mechanical strain control and the net section stress amplitude reported is the measured stabilized engineering stress. The amplitudes remained stable throughout life and as such the half life stresses and stabilized cycle stresses are equivalent.

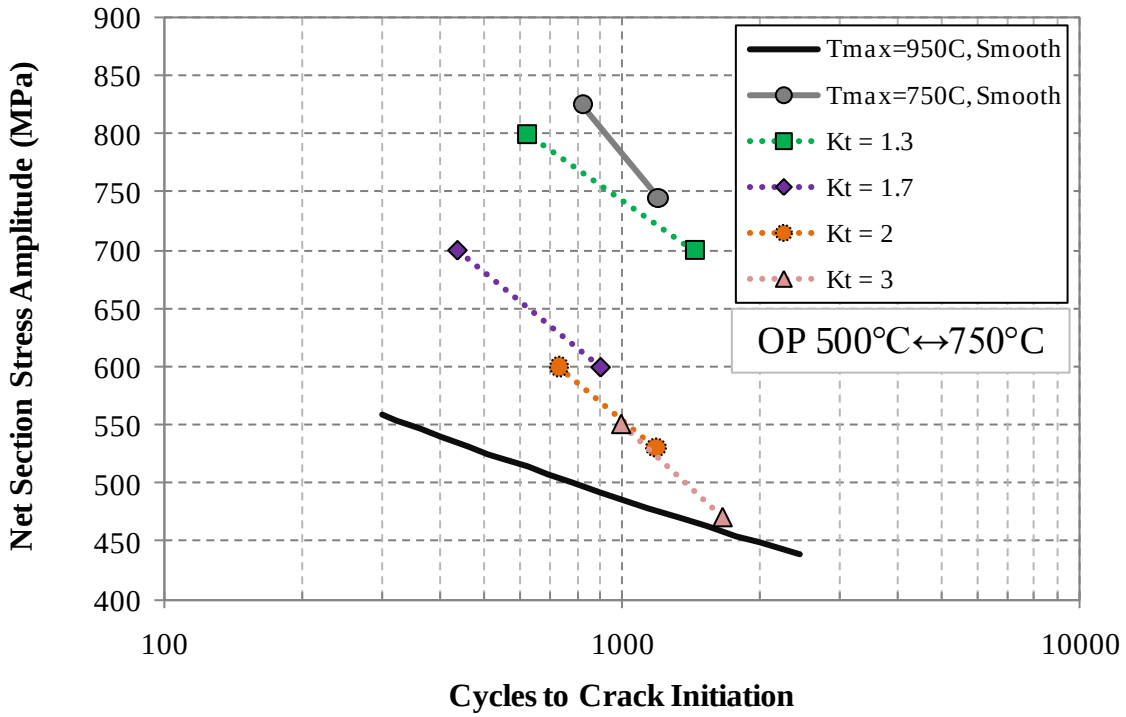

Figure 7-27. Influence of notch severity on OP TMF life for CM247 LC DS $500°C \leftrightarrow 750°C$.

Notch specimens $k_t = 2$ and $k_t = 3$ follow the same life trend over the tested range. The bluntest notch, $k_t = 1.3$, results in a small knockdown effect relative to the smooth specimen life curve.

At $T_{max} = 950°C$ the blunt notch experiences negligible life reduction relative to the smooth specimen whereas at $T_{max} = 750°C$ there is a small knockdown effect, particularly at higher stresses. The reduction in maximum applied temperature has an effect on the fatigue notch sensitivity observed in this alloy under the prescribed conditions. All four notch life trends follow the same slope within the tested regime indicating similar damage mechanisms in each. Mechanical extensometer displacement histories for these notched experiments are shown in Fig. 7-28.

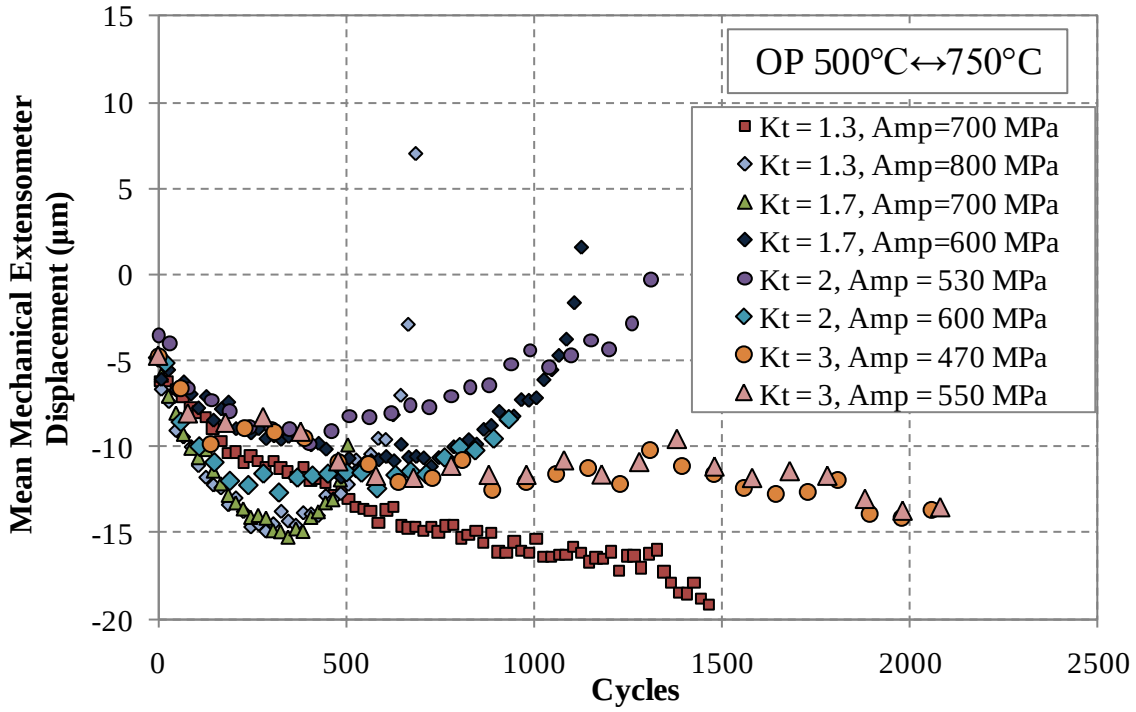

Figure 7-28. Mean mechanical extensometer displacement for all notch specimen geometries with reduced maximum temperature.

Displacements were reduced by an order of magnitude across all notch geometries. This is expected as lower maximum temperature significantly reduces creep deformation which occurs under both OP and IP loading (compression and tension, respectively).

Post failure micrographs of notched surfaces corresponding to OP TMF $T_{max} = 750°C$, OP TMF $T_{max} = 950°C$ and IP TMF $T_{max} = 950°C$ are shown in Fig. 7-29.

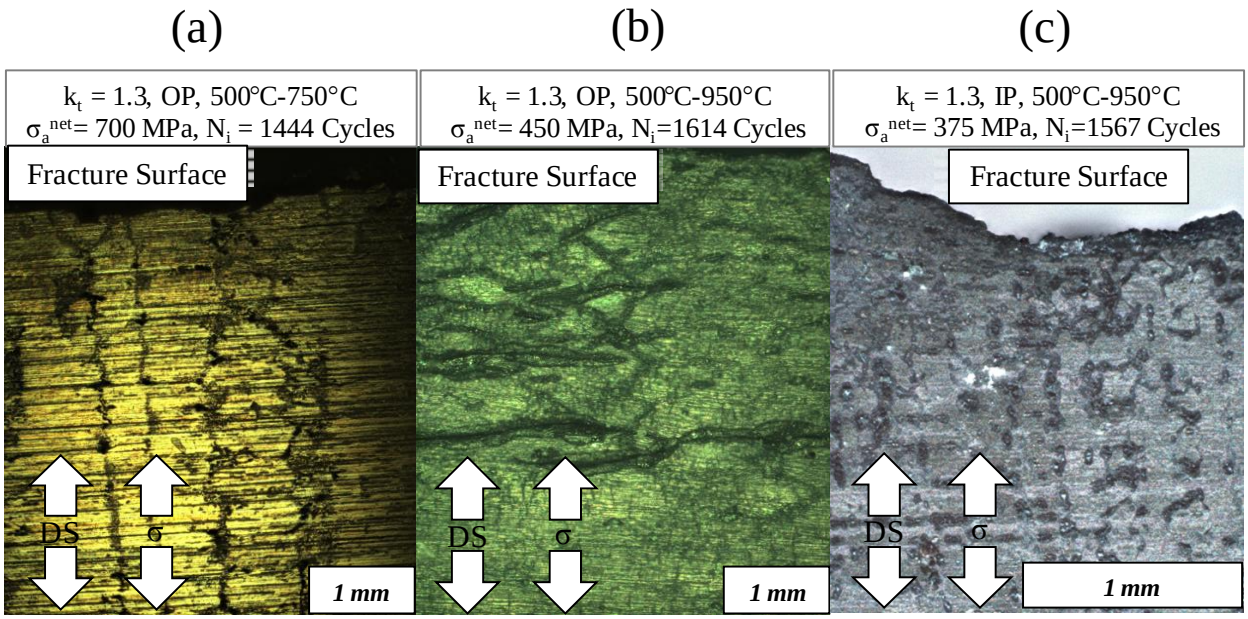

Figure 7-29. TMF notch surfaces near primary crack fracture surface for (a) OP $T_{max} = 750°C$ after 72 *hrs*, (b) OP $T_{max} = 950°C$ after 80 *hrs* and (c) IP $T_{max} = 950°C$ after 78 *hrs*.

For low applied maximum temperature, Fig. 7-29(a), some oxidation is present along grain boundaries and interdendritic regions but the effects are small; machining marks are still discernable. OP TMF at $T_{max} = 950°C$, Fig. 7-29(b), displays several secondary fatigue-environmental cracks oriented perpendicularly to the applied load. Machining marks seen at lower temperatures are no longer present due to extensive surface oxidation. Oxidation along grain boundaries and interdendritic regions is observed in Fig. 7-29(c) under IP TMF but no evidence of spallation was found.

Similar to high temperature experiments, the location of crack initiation under reduced maximum temperature conditions is also offset from the notch root, as shown in Fig. 7-30.

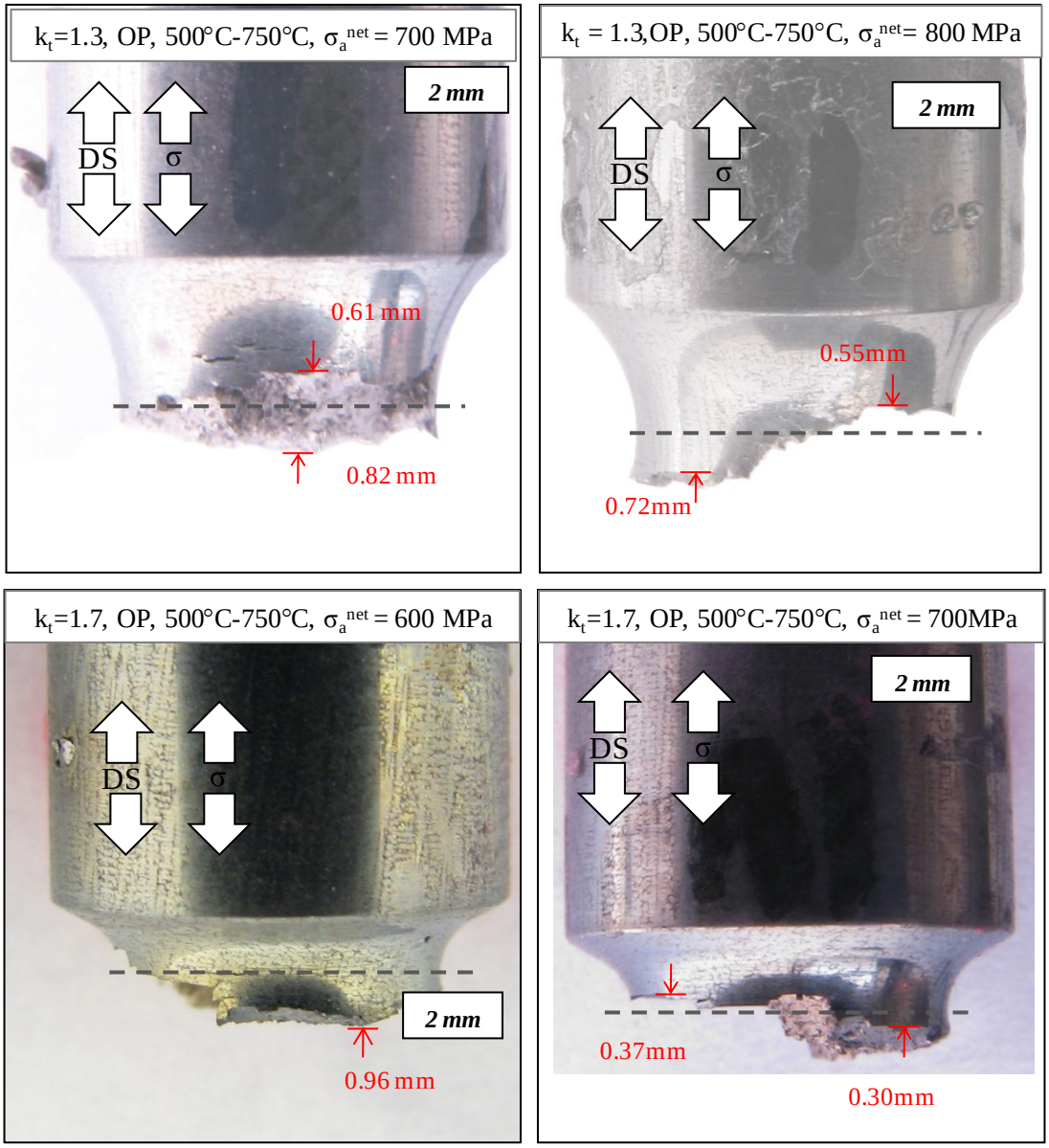

Figure 7-30. Crack initiation locations for $k_t = 1.3$ and $k_t = 1.7$ under OP TMF $500°C \leftrightarrow 750°C$

.

Crack initiation away from the notch root is expected as previous computational results show that the maximum von Mises stress in OP TMF at low temperature (500°C) occurs away from the notch root.

The fracture surface shown in Fig. 7-31 illustrates that at reduced T_{max} there are multiple locations of crack initiation in both $k_t = 1.3$ and $k_t = 1.7$ geometries. For $k_t = 1.3$ both specimens developed one dominant thumbnail shaped crack. Notch geometry $k_t = 1.7$ formed several circumferential cracks which were equally dominant.

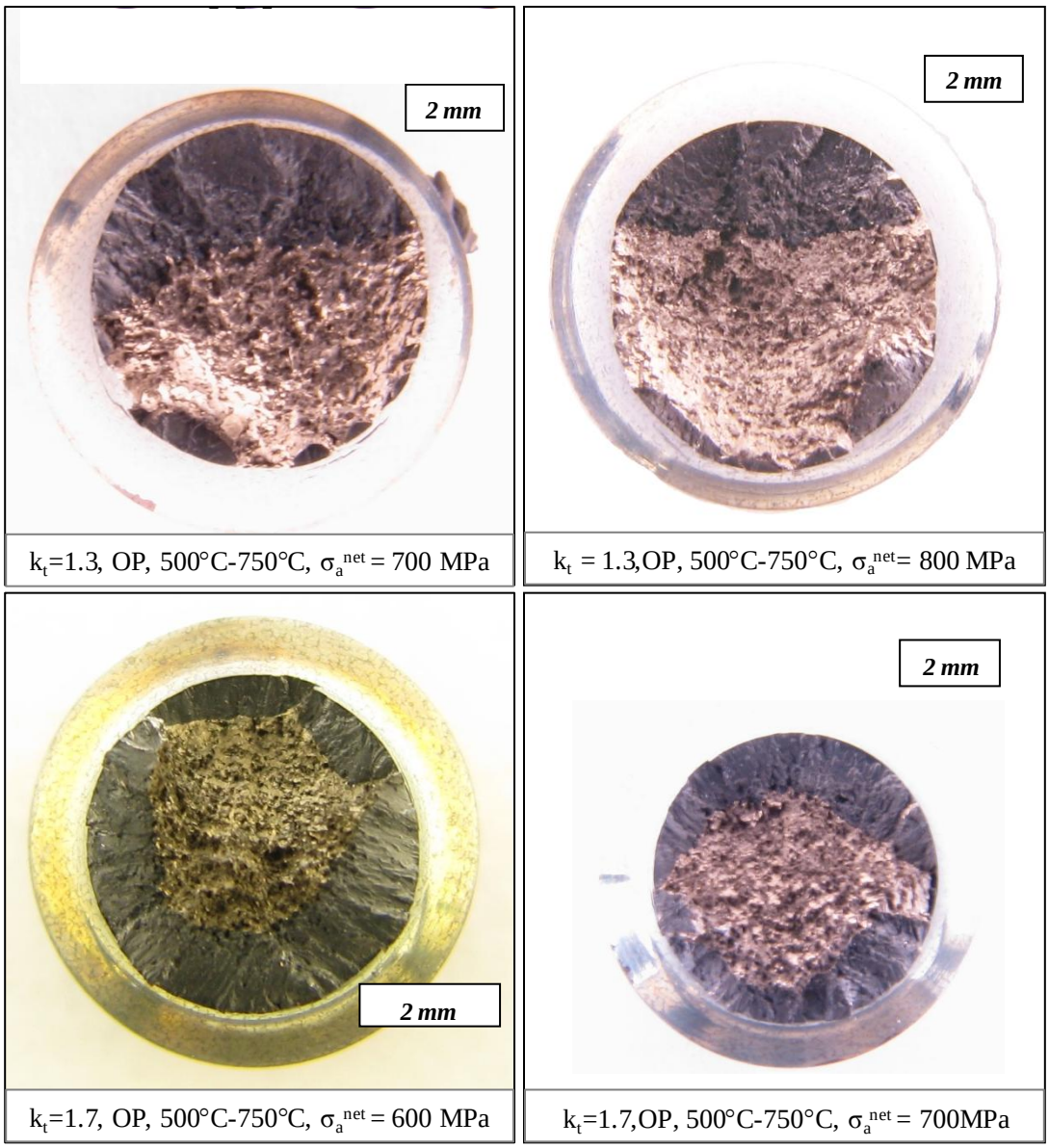

k_t=1.3, OP, 500°C-750°C, σ_a^{net} = 700 MPa | k_t = 1.3,OP, 500°C-750°C, σ_a^{net}= 800 MPa

k_t=1.7, OP, 500°C-750°C, σ_a^{net} = 600 MPa | k_t=1.7,OP, 500°C-750°C, σ_a^{net} = 700MPa

Figure 7-31. Fracture surface patterns for $k_t = 1.3$ and $k_t = 1.7$ under OP TMF $500°C \leftrightarrow 750°C$.

7.3 CM247LC DS OP TMF Life Prediction

The Smith-Watson-Topper (SWT) [44] damage metric is defined as,

$$SWT = \varepsilon_a \sigma_{\max} \tag{7.1}$$

where ε_a is the strain amplitude and $\sigma_{\max}$ is the maximum stress. This is a commonly used damage quantity used for capturing mean stress effects. This parameter was utilized by Moore [39] on a study of high temperature LCF of notched CM247LC DS specimens with reasonable success. Susmel and Taylor [33] utilized a SWT parameter to take into account mean stress effects present locally in circumferentially notched aluminum and low-carbon steel specimens.

For this study the SWT parameter was defined utilizing the equivalent cyclic inelastic strain range, as inelastic deformation drives fatigue crack initiation under OP TMF, and the maximum von Mises stress. Equivalent strain and von Mises stress were utilized to account for the multiaxial response. As the formulation for von Mises stress captures shear occurring on an octahedral plane, the SWT parameter implemented in this fashion consists of a shear strain type quantity and shear stress quantity. For OP TMF experiments ratcheting strains occur in compression and are assumed to contribute negligibly to damage. As such the cyclic inelastic strain range was utilized for the strain component of the SWT parameter. Multiaxial effects were taken into account using the equivalent cyclic inelastic strain range and the von Mises equivalent stress. The SWT damage metric takes the form

$$SWT = \Delta\varepsilon^{in}_{cyc,eq}\,\sigma_{vm}\big|^{\max}_{cyclic} \tag{7.2}$$

where $\Delta\varepsilon^{in}_{cyc,eq}$ is the equivalent inelastic strain range, introduced in Chapter 2, which is a calculated scalar produced for a given cycle. $\sigma_{vm}\big|^{\max}_{cyclic}$ is the maximum value of the von Mises stress over one cycle. Simulated results using the GTD-111 transversely isotropic constitutive model are used for determining the local notch material response. Response variables calculated at integration points are extrapolated to nodes to simplify analysis. The SWT parameter is

determined at all nodes in the FEA model. The SWT parameter quantity is determined at each node from the finite element results producing a scalar value field defined at FEA model nodes. Simulations were performed utilizing three net section stresses that span the experimentally applied net section stresses; 300 *MPa*, 400 *MPa* and 500 *MPa*.

7.3.1 Local SWT

The maximum SWT parameter for each notch geometry and three applied net section stresses is shown in Fig. 7-32.

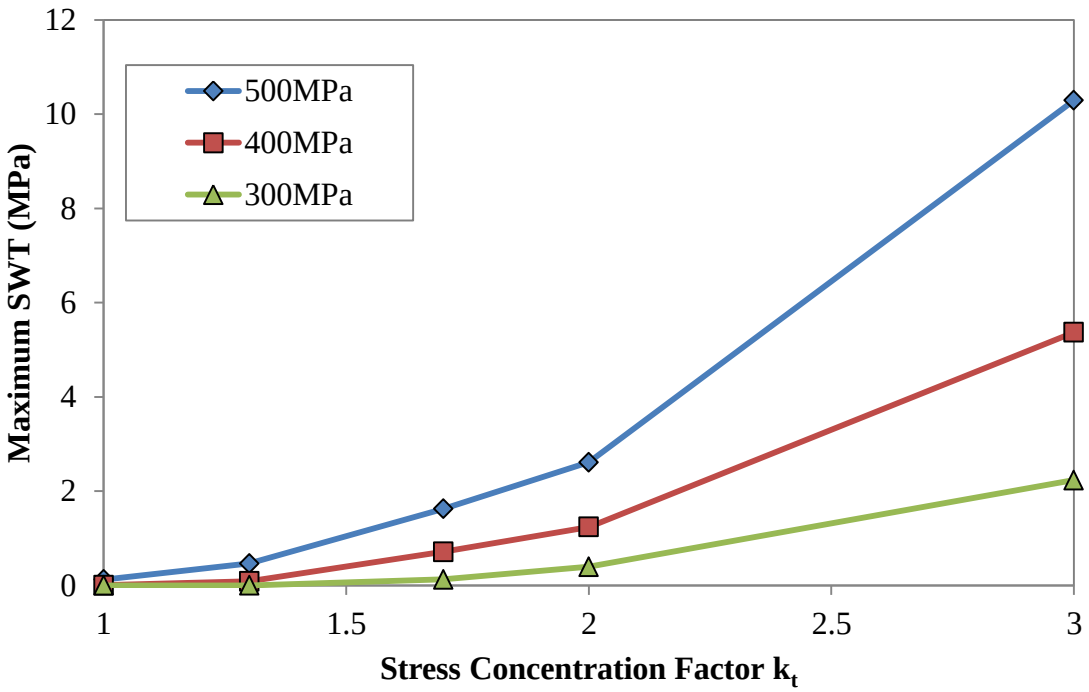

Figure 7-32. SWT parameter for each geometry and applied net section stress for $500°C \leftrightarrow 950°C$ OP TMF.

The simulated results utilizing a local method for quantifying damage do not follow experimental results; notches always appear to have a detrimental affect based on the chosen

damage parameter. Utilizing all OP TMF crack initiation results, including results from Kupkovits [6], the local SWT damage parameter for each test was estimated from the performed simulations. For experiments with applied net section stresses not equal to 300 *MPa*, 400 *MPa* or 500 *MPa*, linear interpolation was utilized to estimate the SWT values under the corresponding experimental net section stress loads. Simulated SWT parameters for all experiments are shown against experimentally determined crack initiation lives in Fig. 7-33.

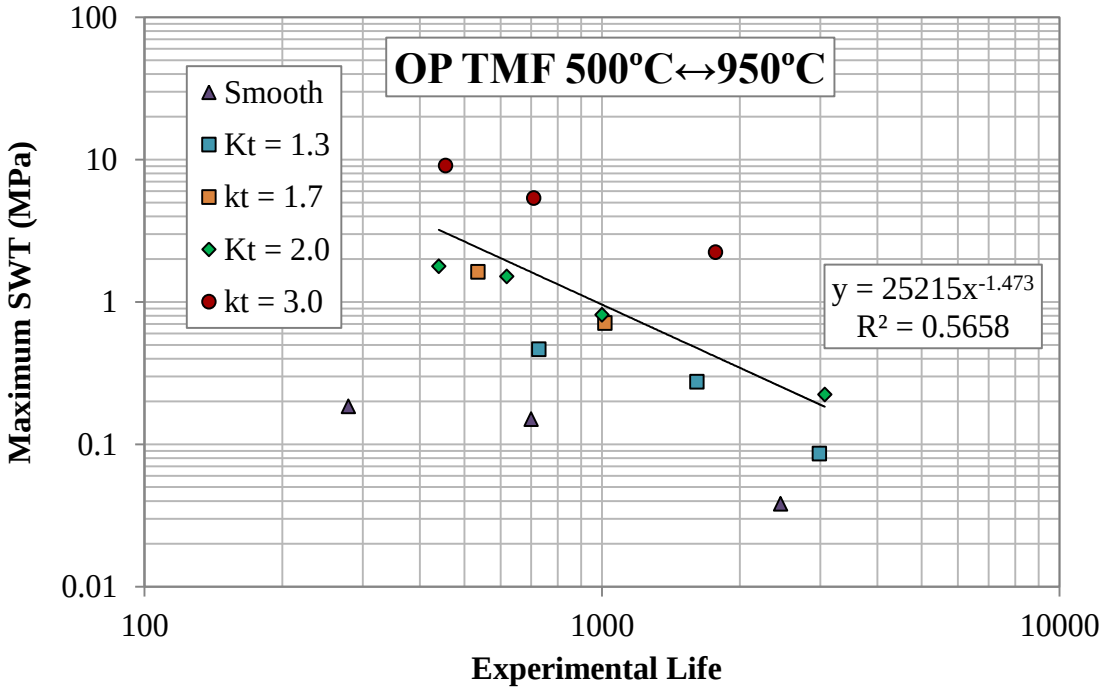

Figure 7-33. Maximum SWT parameter for all OP TMF experiments.

The resulting trend is very sparse and the power law fit is poor. A comparison between the predicted life utilizing the power law expression and experimentally determined crack initiation results is shown in Fig. 7-34.

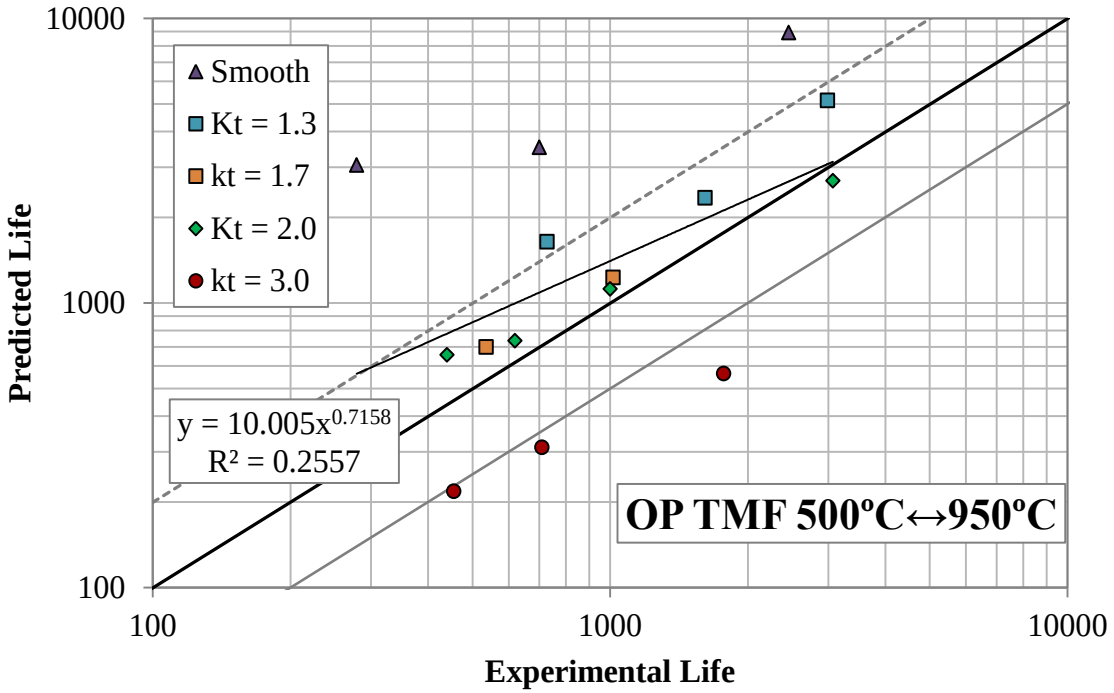

Figure 7-34. Comparison between the experimentally measured notch lives and predicted lives using the maximum SWT parameter.

Life results using the local maximum SWT value are poor. This is expected as spatial gradients present in multiaxial responses around notches plays a critical role in determining fatigue damage.

7.3.2 Nonlocal SWT

A nonlocal parameter is needed to improve predictive capabilities. An area method (AM) nonlocal approach was used based on the SWT parameter.

$$\overline{SWT} = \frac{1}{A}\int_{A} SWT\big|_{cyclic}\, dA \tag{7.3}$$

Where A is the a domain defined over the notch model area. Nonlocal approaches for isotropic materials are usually performed using a line or point methods as the response is centered about the notch root. CM247LC DS however exhibits a transversely isotropic response when loaded

longitudinally. The locations of maximum equivalent inelastic strain range and maximum von Mises stress always occur away from the notch root. Additionally the location of maximum von Mises stress changes during loading, with temperature, applied loads and with specimen geometry. The directions of maximum or minimum descent for relevant spatial gradients do not always follow the same directions and do not coincide with the surface normal or with crystallographic directions. As such an area method is better suited for capturing the complex response at the notch.

A critical area approach can be utilized to determine the integration domain. This method identifies the domain within which the damage quantity is at least a certain percentage of the maximum value. For the case of a SWT damage quantity,

$$A_{crit} = A\left(SWT \geq P \cdot \max\left\{SWT\right\}\right) \tag{7.4}$$

where A is the total component area, A_{crit} is the critical area and P is a value between 0 and 1. The SWT 95-percentile critical area for all notch geometries under a 500 *MPa* applied net section stress is shown in Fig. 7-35.

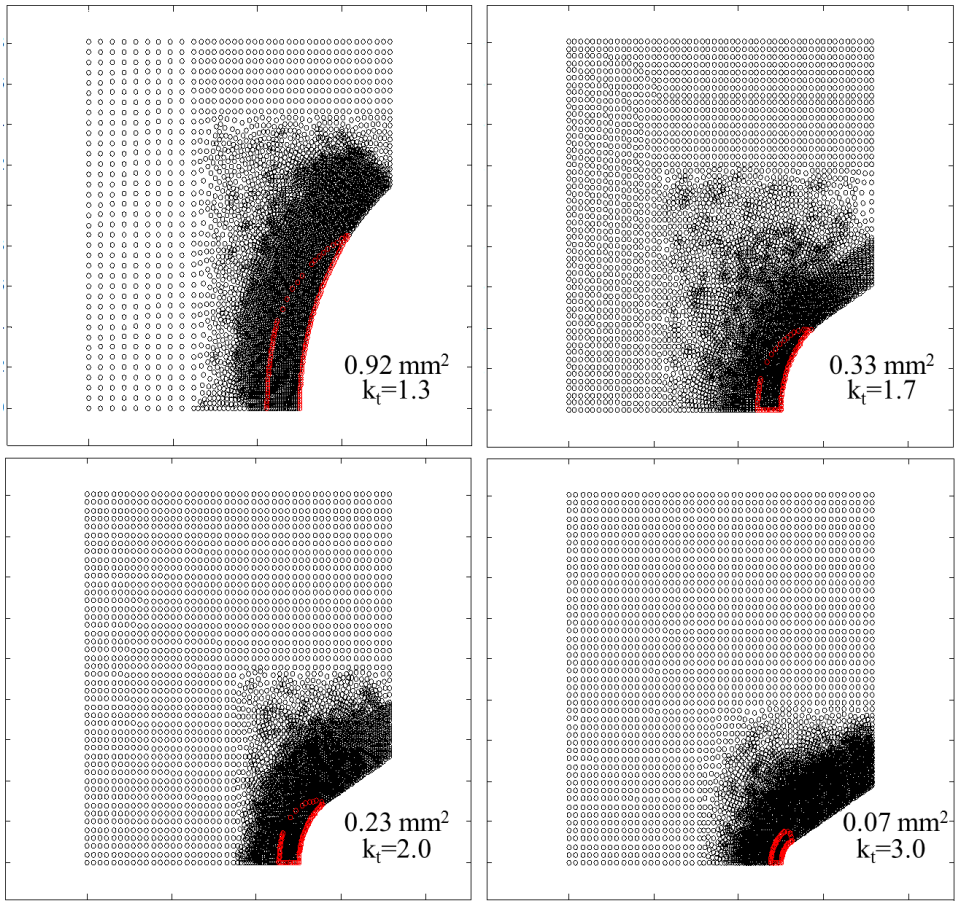

Figure 7-35. OP TMF $500°C \leftrightarrow 950°C$ 95-percentile critical areas based on SWT parameter.

As notch severity increases the size of the critical 95-percentil area decreases due to increasing spatial gradients. In the case of $k_t = 3.0$ the critical area is much smaller than all other notches because spatial gradients are significantly larger and the SWT scalar value field decreases rapidly away from the location of maximum SWT. The area averaged SWT parameter using a 95-percentile area domain is shown in Fig. 7-36 for each notch geometry and three applied net section stresses.

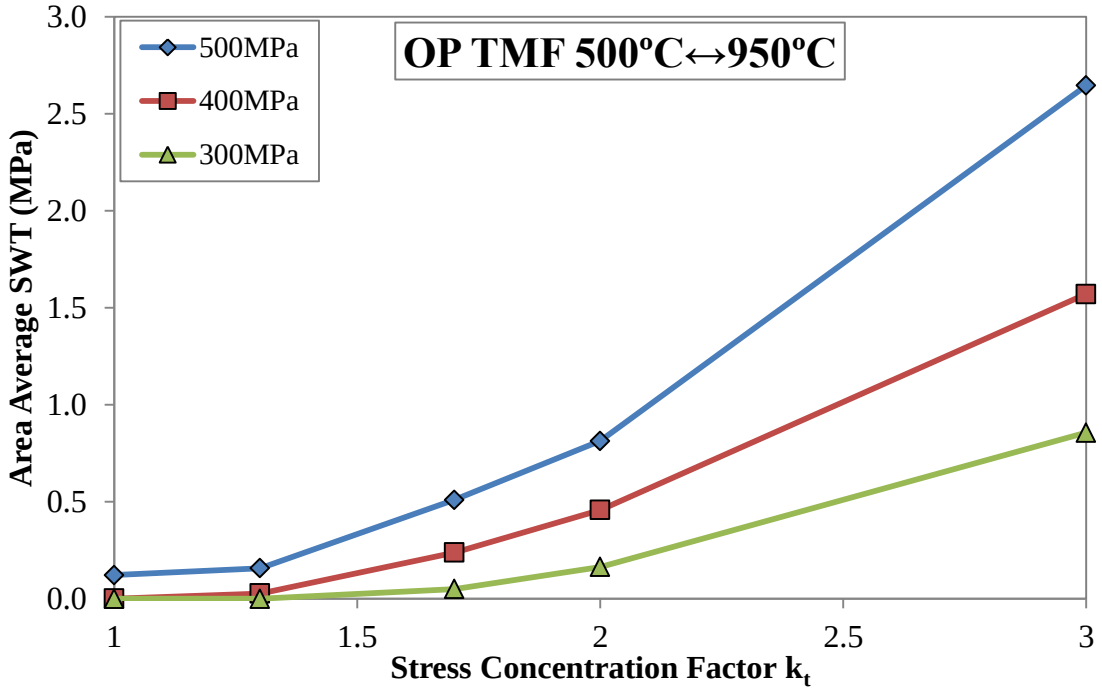

Figure 7-36. Nonlocal 95-percentile critical area $\overline{SWT}$ as a function of applied load and stress concentration.

The 95-percentile $\overline{SWT}$ parameter increases with increasing notch severity over all applied net section stresses. This method does not correctly capture any experimentally observed behavior and provides no additional benefits compared to the maximum SWT parameter. The 99-percentile, 90-percentile and 85-percentile $\overline{SWT}$ values produce the same qualitative trends.

In a study on notch life prediction using elastic-plastic analysis, Susmel and Taylor [33] chose an invariant length scale for line integration along the notch root for each geometry and loading. Here an invariant relevant area scale is necessary. Two methods were utilized for determining the area integration domain (1) a surface-sweep of the notch surface into the component as in Fig 7-37(a) and (2) a circular-sweep within the component centered about the location of maximum SWT parameter as in Fig. 7-37(b).

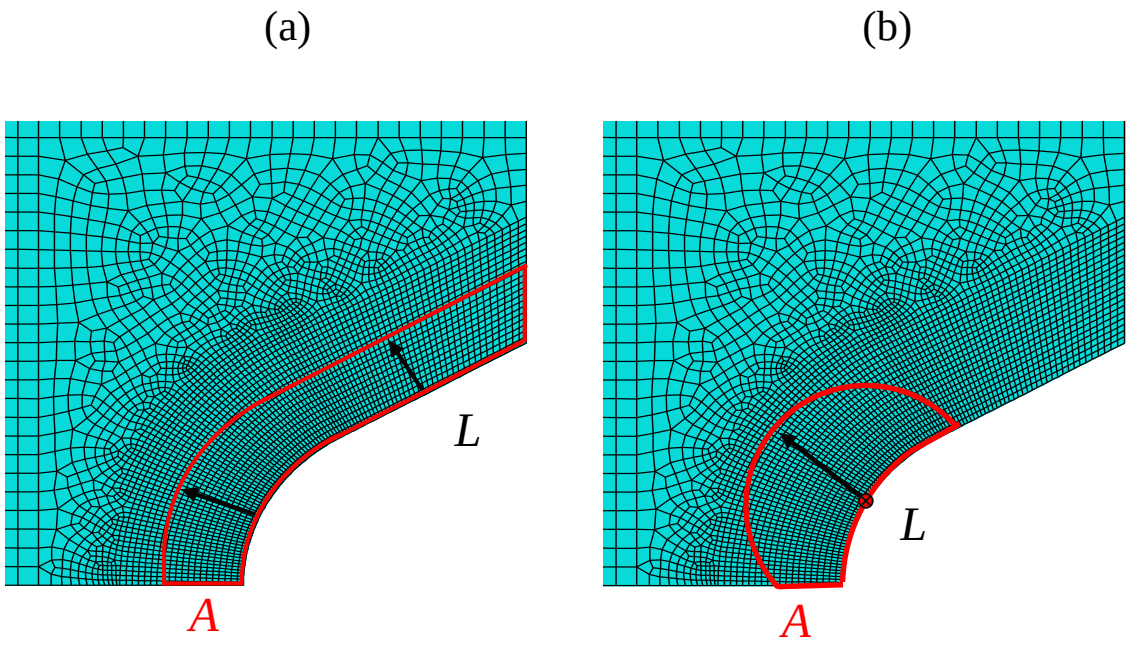

Figure 7-37. Domain for area averaging in notch geometry $k_t = 2.0$ (a) surface sweep method (b) circular sweep method.

As the area domain is irregular, an iterative method was devised where the sweeping variable, *L*, was varied until the desired area, *A*, was achieved. That domain would then define the integration domain for averaging the SWT parameters.

Using the surface-sweep method an area of 0.90 mm^2 produced the best sensitivity and life results. Sensitivity results showing the relationship between the non-local SWT value, stress concentration factor and applied net section stress is shown in Fig. 7-38.

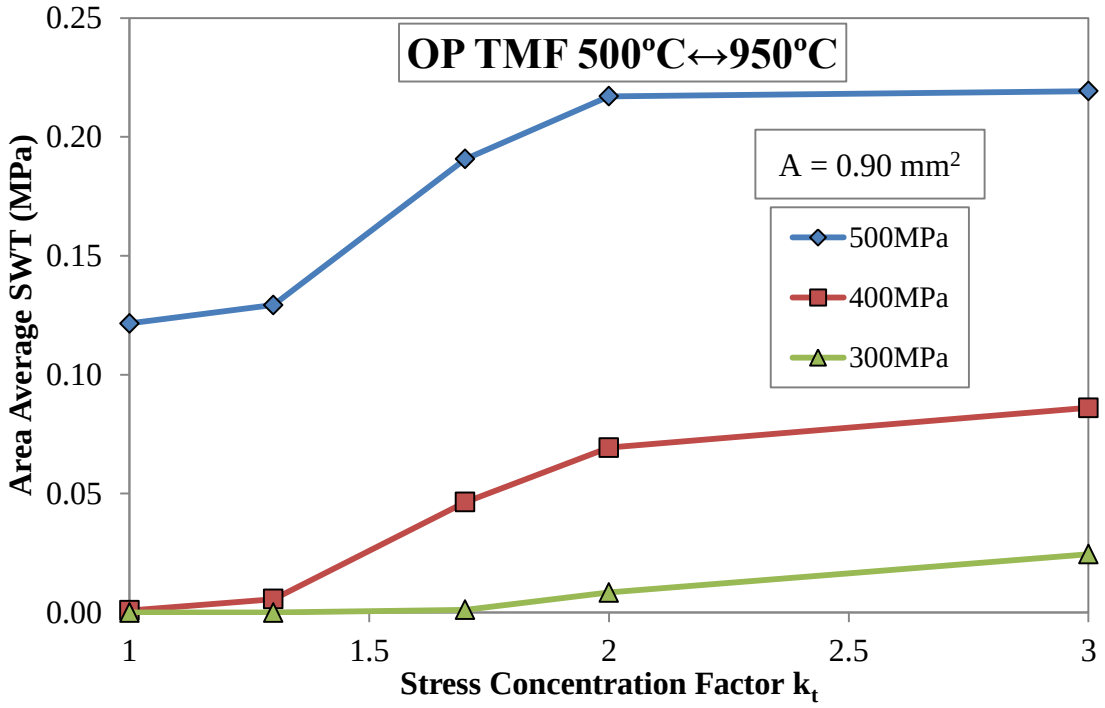

Figure 7-38. Nonlocal surface-sweep $\overline{SWT}$ as a function of applied load and stress concentration.

At 400 *MPa* and 500 *MPa* the simulated responses produces very similar $\overline{SWT}$ parameters for stress concentrations $k_t = 1$ and $k_t = 1.3$. This agrees well with the experiment observation that stress concentration $k_t = 1.3$ is not detrimental towards life. At 500 *MPa* applied net section stress, the $\overline{SWT}$ parameter between $k_t = 2.0$ and $k_t = 3.0$ increases negligibly. At 400 *MPa* applied net section stress the $\overline{SWT}$ parameter between $k_t = 2.0$ and $k_t = 3.0$ begins to decelerate. This qualitatively agrees well with experimental observations that $k_t = 2.0$ and $k_t = 3.0$ follow the same life trend and represent some notch life limit under the applied conditions.

The area scale is determined by parametrically varying the value of *A* until observed notch sensitivity trends are achieved, see Fig. 7-39. The methodology is justifiable as both experimentally observed notch life sensitivity trends at low and high stress severity values are captured with this single parametric variation.

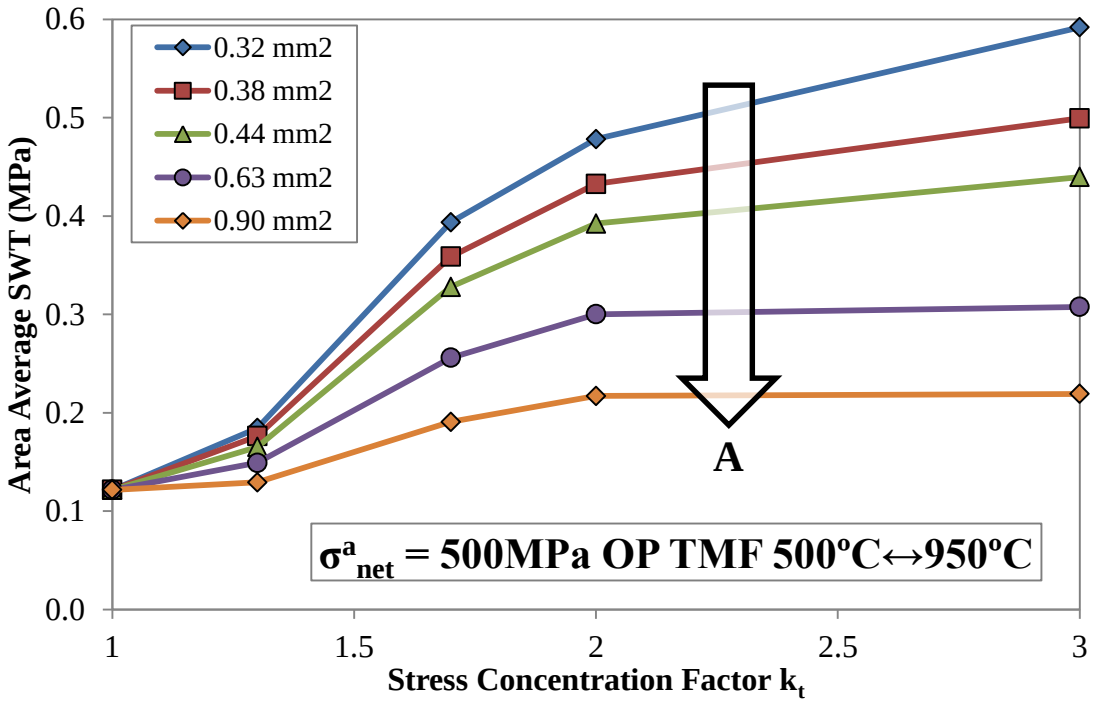

Figure 7-39. Surface-sweep nonlocal average $\overline{SWT}$ parameter for OP TMF under 500 *MPa* net section stress for increasing area domain.

Non-local $\overline{SWT}$ values were determined for each corresponding $500°C \leftrightarrow 950°C$ OP TMF experiment. Linear interpolation of simulated results at 300 *MPa*, 400 *MPa* and 500 *MPa* were used to determine the $\overline{SWT}$ parameter corresponding to each notched experiment, see Fig. 7-40.

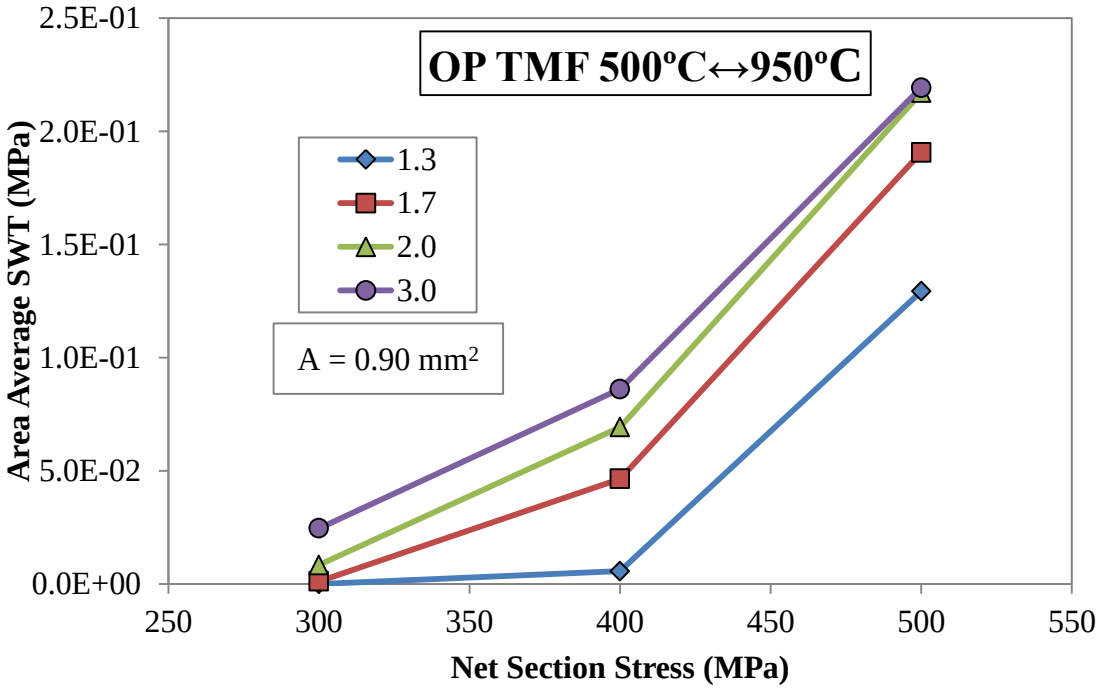

Figure 7-40. Nonlocal $\overline{SWT}$ parameter as a function of net section stress across each notch geometry.

As uniaxial simulations are computationally inexpensive linear interpolation of uniaxial $\overline{SWT}$ was not utilized. Rather, uniaxial simulations were performed using the GTD-111 transversely isotropic constitutive model to match net section stresses in each of the smooth experiments. Under uniaxial conditions the local and nonlocal SWT parameter is the same as it is idealized that there are no spatial gradients and hence the SWT remains constant throughout the material.

Nonlocal SWT parameters for each experiment performed, smooth and notched, are shown in Fig. 7-41.

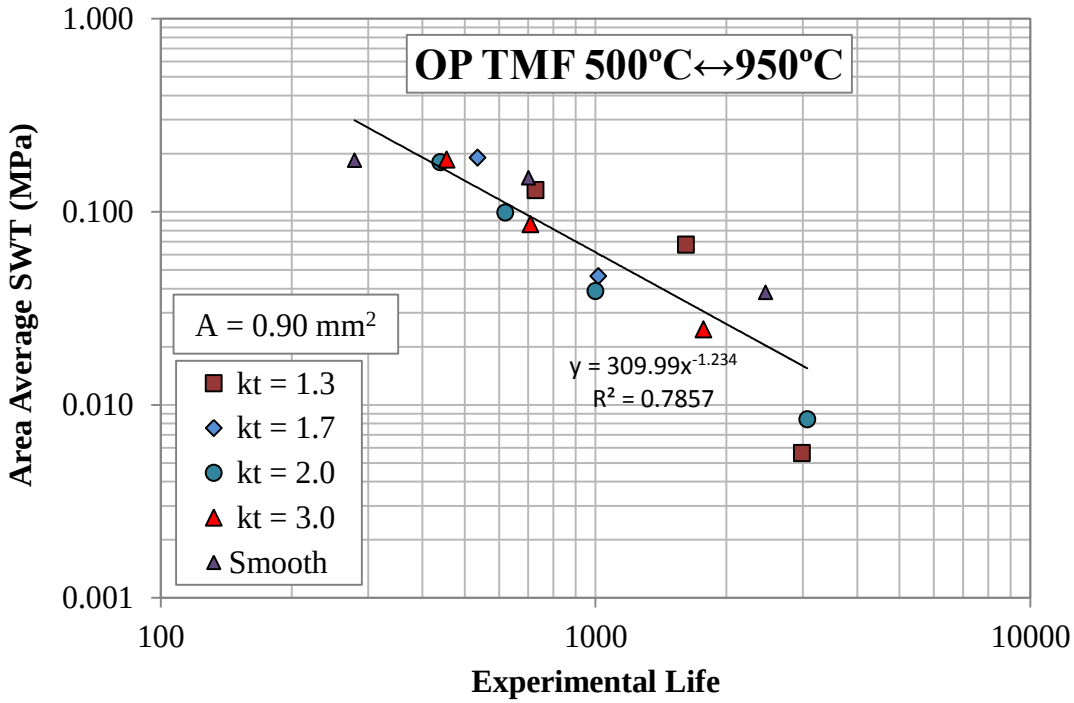

Figure 7-41. Simulated nonlocal $\overline{SWT}$ for each $500°C \leftrightarrow 950°C$ OP TMF experiment using the surface-sweep domain.

The trend collapses all the results fairly well for all specimens. Using the power law generated from this relationship, predicted lives are compared against experimental lives in Fig. 7-42.

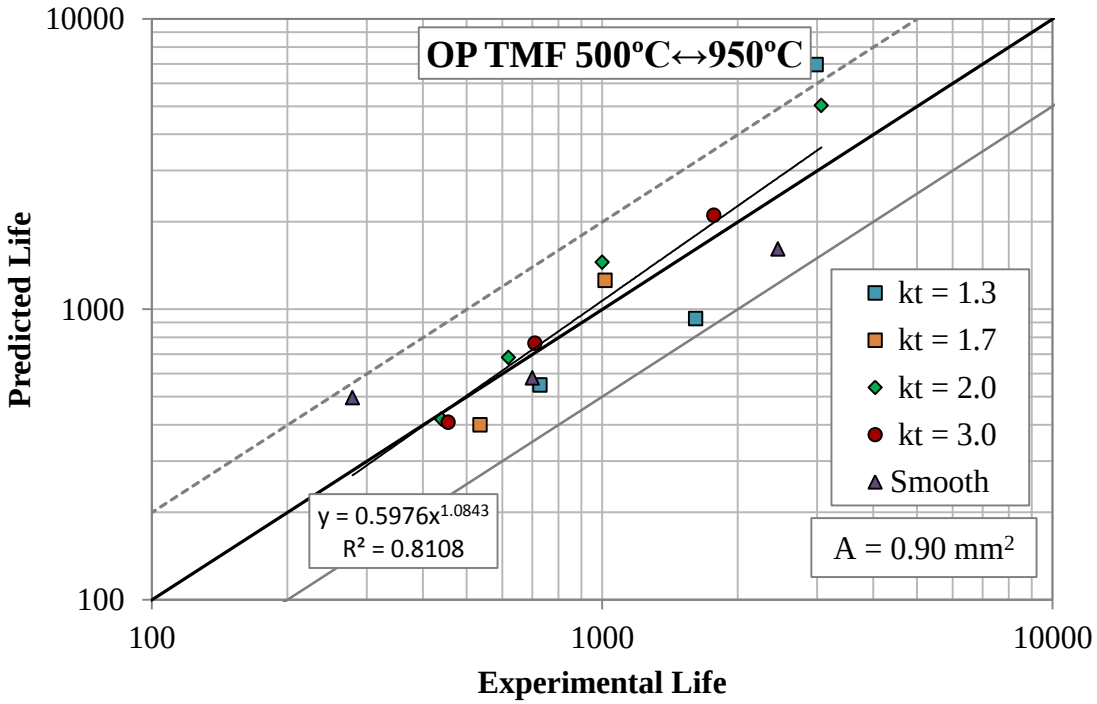

Figure 7-42. Life prediction results using the surface-sweep $\overline{SWT}$ with a power law life model.

Predicted life values are all within a factor of 2 relative to the experimentally determined lives with the exception of long life $k_t = 1.3$. Tabulated results for all OP TMF experiments and the corresponding predicted surface-sweep $\overline{SWT}$ values are shown in Table 7-3.

Table 7-3. Nonlocal area average SWT results using a surface sweep domain

A = 0.90 mm^2 Surface Sweep Results							
T_{min} (°C)	T_{max} (°C)	σ^a_{net} (MPa)	k_t	Phasing	Cycles To Init.	Predicted SWT	Predicted Life
500	950	553	1	OP	279	1.86E-01	496
500	950	524	1	OP	700	1.51E-01	580
500	950	431	1	OP	2460	3.83E-02	1611
500	950	500	1.7	OP	536	1.91E-01	400
500	950	500	1.3	OP	728	1.29E-01	548
500	950	450	1.3	OP	1614	6.75E-02	929
500	950	400	1.7	OP	1016	4.64E-02	1257
500	950	400	1.3	OP	2987	5.63E-03	6949
500	950	280	2	OP	3070	8.39E-03	5026
500	950	350	2	OP	1000	3.89E-02	1452
500	950	420	2	OP	620	9.89E-02	681
500	950	300	3	OP	1771	2.46E-02	2105
500	950	400	3	OP	709	8.61E-02	762
500	950	475	2	OP	440	1.80E-01	419
500	950	475	3	OP	455	1.86E-01	408

The identical analysis was performed utilizing the circular-sweep integration method and produced similar results. The $\overline{SWT}$ parameter at 500 *MPa* across all notch geometries for various area domains is shown in Fig. 7-43. The area domain that produced the best sensitivity trends and life predictions in this case was 0.77 mm^2. Notch sensitivity results are shown in Fig. 7-44.

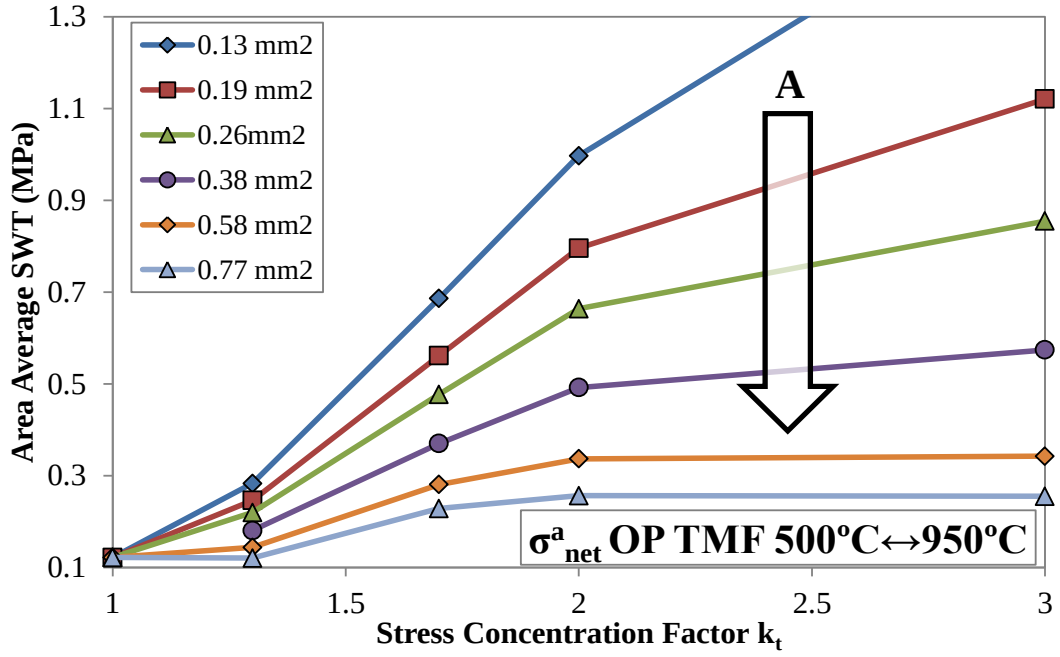

Figure 7-43. Circular-sweep nonlocal average $\overline{SWT}$ parameter for OP TMF under 500 *MPa* net section stress for increasing area domain.

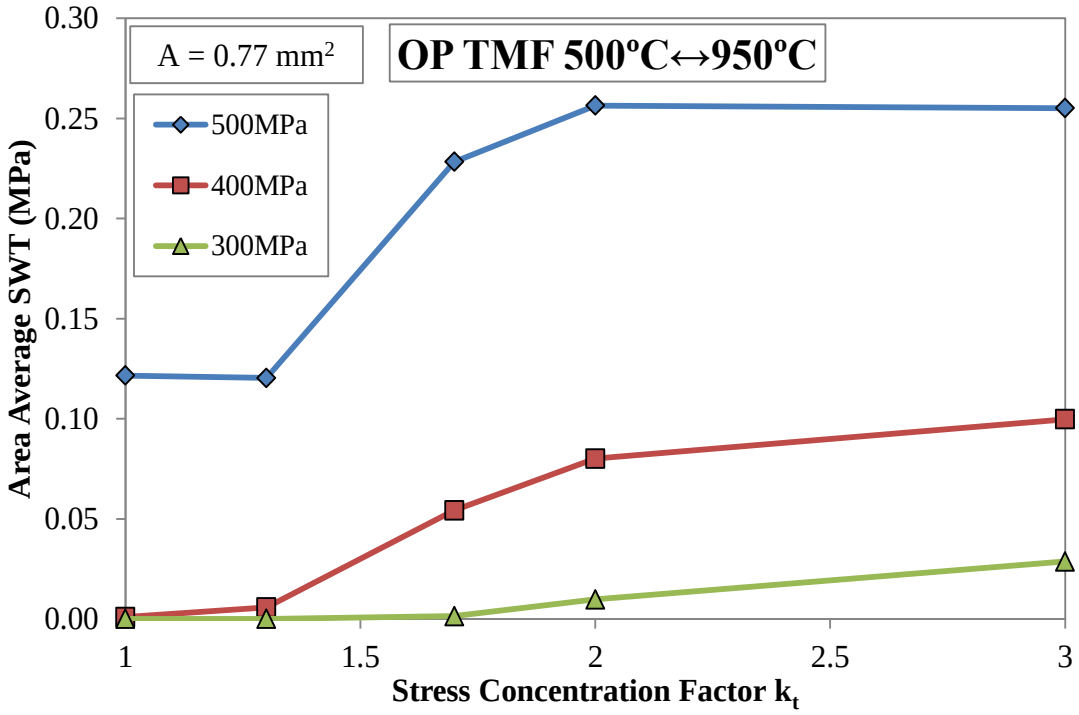

Figure 7-44. Nonlocal $\overline{SWT}$ using the circular-sweep domain as a function of applied load and stress concentration.

Compared to experimentally observed notch life sensitivity trends utilizing the circular-sweep area domain are good. At 500 *MPa* this implementation predicts relative damage in smooth and $k_t = 1.3$ exactly, as well as relative damage in $k_t = 2$ and $k_t = 3$. The circular-sweep $\overline{SWT}$ parameter is shown against experimental crack initiation lives in Fig. 7-45.

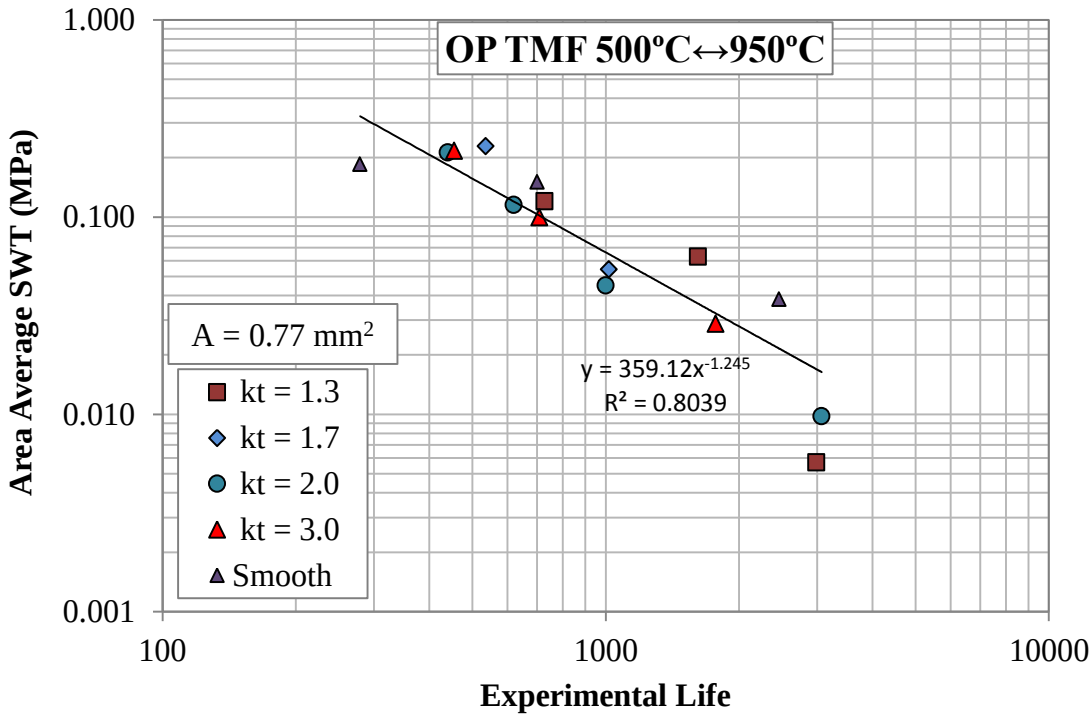

Figure 7-45. Simulated nonlocal $\overline{SWT}$ for each $500°C \leftrightarrow 950°C$ OP TMF experiment using the circular-sweep domain.

Experimental lives correlate better with the $\overline{SWT}$ parameter generated utilizing a circular-sweep area domain. Life prediction results are shown in Fig. 7-46 for the circular sweep area average method.

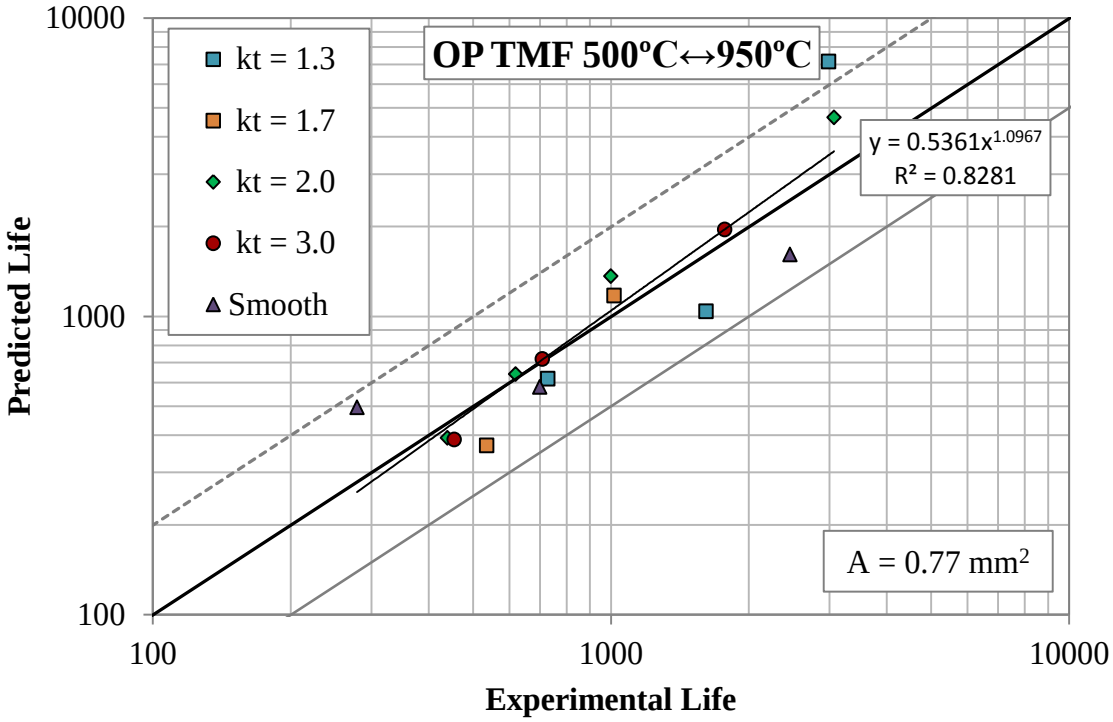

Figure 7-46. Life prediction results using the circular-sweep $\overline{SWT}$ with a power law life model.

Life results are good, all but one point are within a factor of 2. The point outside of a factor of two is again $k_t = 1.3$ at high life. It is possible that at longer lives, environmental-fatigue interactions become more influential and hence a power-law life model becomes less reliable.

It is important to note that the nonlocal method is somewhat invariant to the domain shape (surface-sweep or circular-sweep) which shows that the method is robust. The tabulated results for all OP TMF experiments and the corresponding predicted circular-sweep $\overline{SWT}$ values are shown in Table 7-4.

Table 7-4: Nonlocal area average SWT results using a circular sweep domain

A = 0.77 mm^2 Surface Sweep Results							
T_{min} (°C)	T_{max} (°C)	σ^a_{net} (MPa)	k_t	Phasing	Cycles To Init.	Predicted SWT	Predicted Life
500	950	553	1	OP	279	1.86E-01	496
500	950	524	1	OP	700	1.51E-01	580
500	950	431	1	OP	2460	3.83E-02	1611
500	950	500	1.7	OP	536	2.28E-01	369
500	950	500	1.3	OP	728	1.20E-01	618
500	950	450	1.3	OP	1614	6.30E-02	1039
500	950	400	1.7	OP	1016	5.42E-02	1173
500	950	400	1.3	OP	2987	5.70E-03	7155
500	950	280	2	OP	3070	9.77E-03	4643
500	950	350	2	OP	1000	4.49E-02	1364
500	950	420	2	OP	620	1.15E-01	640
500	950	300	3	OP	1771	2.87E-02	1953
500	950	400	3	OP	709	9.97E-02	719
500	950	475	2	OP	440	2.12E-01	392
500	950	475	3	OP	455	2.16E-01	386

The sweeping length scale, *L*, is shown for each notch geometry and both averaging schemes in Table 7-5. The surface-sweep scale is smaller as the sweeping area is performed over the entire notch surface length. The length scale changes to preserve the same size area for averaging the SWT response in each notch geometry.

Table 7-5: Sweeping Length Scales for Optimized Area Domains

Circular-Sweep		Surface-Sweep	
k_t	L (μm)	k_t	L (μm)
1.3	686	1.3	276
1.7	670	1.7	386
2	678	2	413
3	735	3	476

The relevant length scales are larger than the 200 μm length scale for point and line methods utilized by Moore [39]. Naik et al. found the line average domain to be between 20 μm and 100 μm for notched Ti-6Al-4V with stress concentrations varying between 2 and 4 [40]. For notched aluminum Susmel and Taylor utilized a 244 μm length scale for implementing a point method approach and a 154 μm length scale for a line method approach [33]. In the same study on notched low-carbon steel 492 μm and 396 μm scales were utilized for point and line methods, respectively.

OP TMF notch specimen life prediction trends expressed in terms of the applied net section stress are shown in Fig. 7-47. The circular-sweep method was used as it produced better notch sensitivity trends and a slightly tighter power law from life prediction.

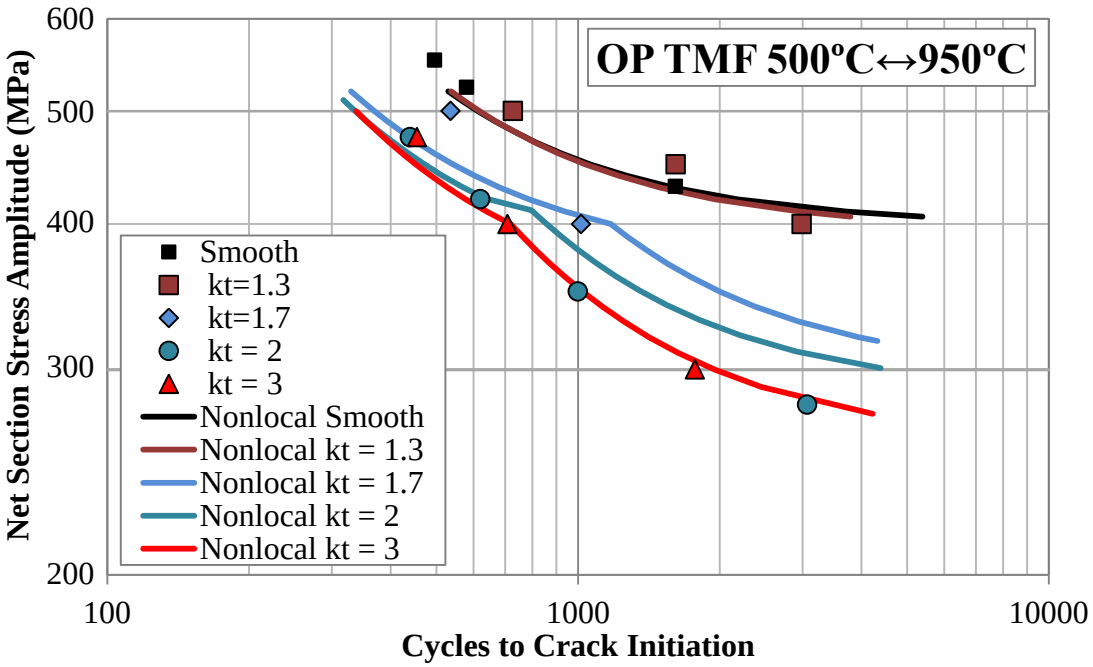

Figure 7-47. Circular-sweep nonlocal $\overline{SWT}$ predicted life trends for each notch geometry under OP TMF $500°C \leftrightarrow 950°C$.

Prediction of life trends is excellent at high stresses but becomes less accurate with decreasing net section stress, particularly for $k_t = 2.0$ and $k_t = 3.0$ trends. Observed "bumps" at 400 *MPa* occur due to linear interpolation of the $\overline{SWT}$ parameter. Ideally additional simulations with finer applied net section stress steps would alleviate this and improve predictions. Improvements could be made by utilizing a calibrated CM247LC DS constitutive model. Predicted lives for 300 *MPa*, 400 *MPa* and 500 *MPa* net section stresses as a function of notch severity is shown in Fig. 7-48.

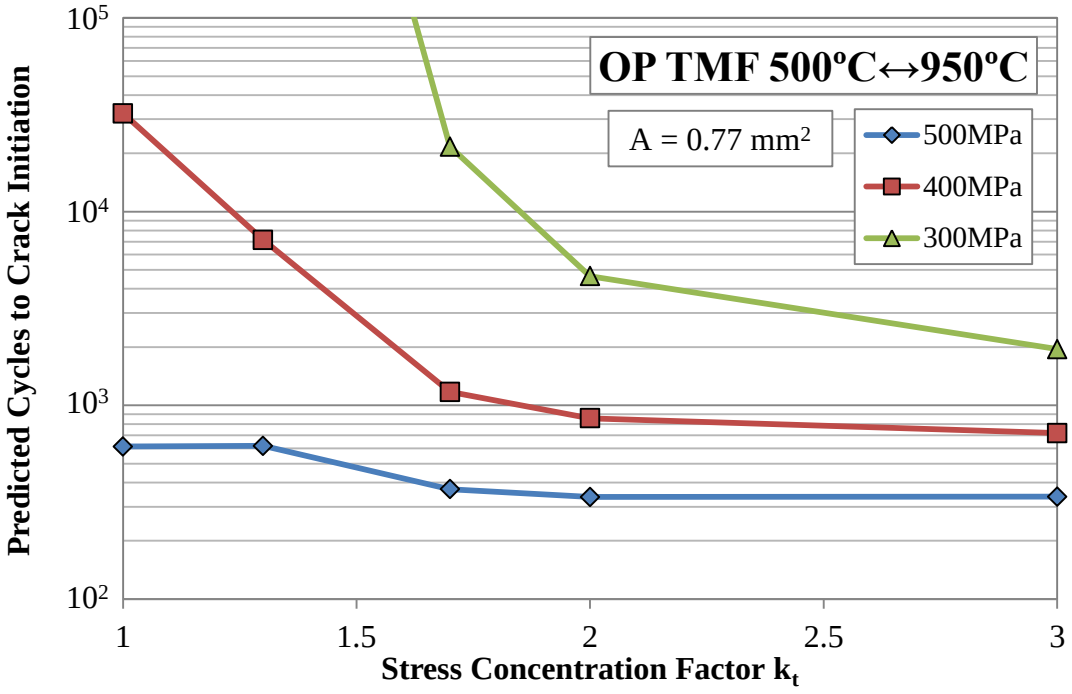

Figure 7-48. Predicted lives utilizing a circular-sweep $\overline{SWT}$ parameter across all notch specimen geometries.

The observed notch sensitivity trends are represented exactly by the 500 *MPa* net section stress simulations; $k_t = 1.3$ is notch insensitive, $k_t = 1.7$ falls in between $k_t = 2$ and $k_t = 3$ lives, and $k_t = 2$ and $k_t = 3$ represent the upper limit of the notch knockdown regime. At 400 *MPa*

notch sensitivity predictions are good with the exception of missing the insensitivity of $k_t = 1.3$. Under all applied net section stresses, the predicted lives appear to by asymptotically approaching some bound which qualitatively agrees with experimental observations. The rate of approach and the bound itself are heavily dependent on the material response and hence the constitutive model. Clearly predictive improvements could be made utilizing a CM247LC DS constitutive model that more accurately represents the tested material.

Shown in Fig. 7-49 is a contour of the equivalent inelastic strain increment for notched specimens. Smooth specimens in force control resulted in ratchet strains an order of magnitude larger and hence are not shown so that there is sufficient resolution.

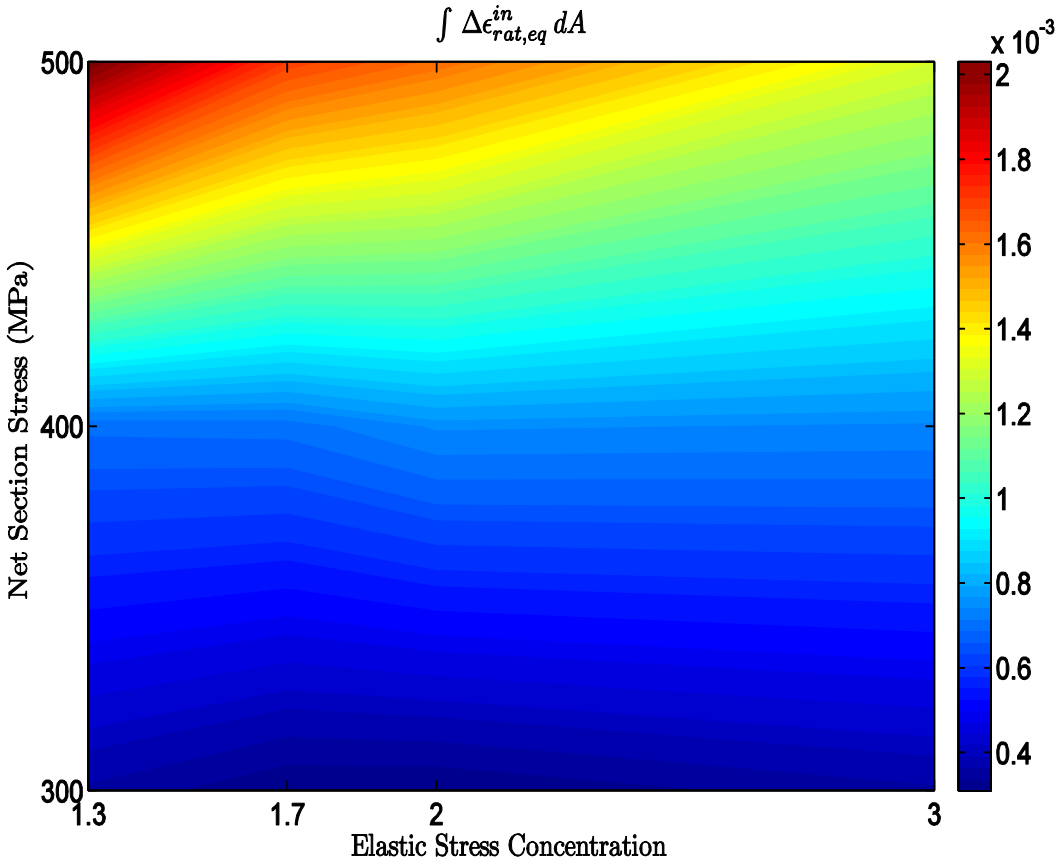

Figure 7-49. Contour map of averaged equivalent inelastic strain increment over the notch root for one cycle for GTD-111 OP TMF $500°C \leftrightarrow 950°C$.

Results indicate that global ratcheting increases with increasing applied net section stress and decreases with increasing notch severity at high net section stresses; the latter is due to multiaxiality constraint. These results show that the results presented in Fig. 7-49 are due to a competition where the inelastic strain dominates with increasing net section stress and increasing notch severity.

CHAPTER 8 INFLUENCE OF TEMPERATURE EFFECTS ON CRACK INITIATION OF A NOTCHED NI-BASE SUPERALLOY UNDER THERMOMECHANICAL FATIGUE

8.1 IN100 Phasing Effects

In phase and out of phase fully reversed force control life results are shown in Fig. 8-1. The net section stress amplitude is used as a damage metric for quantifying initiation life.

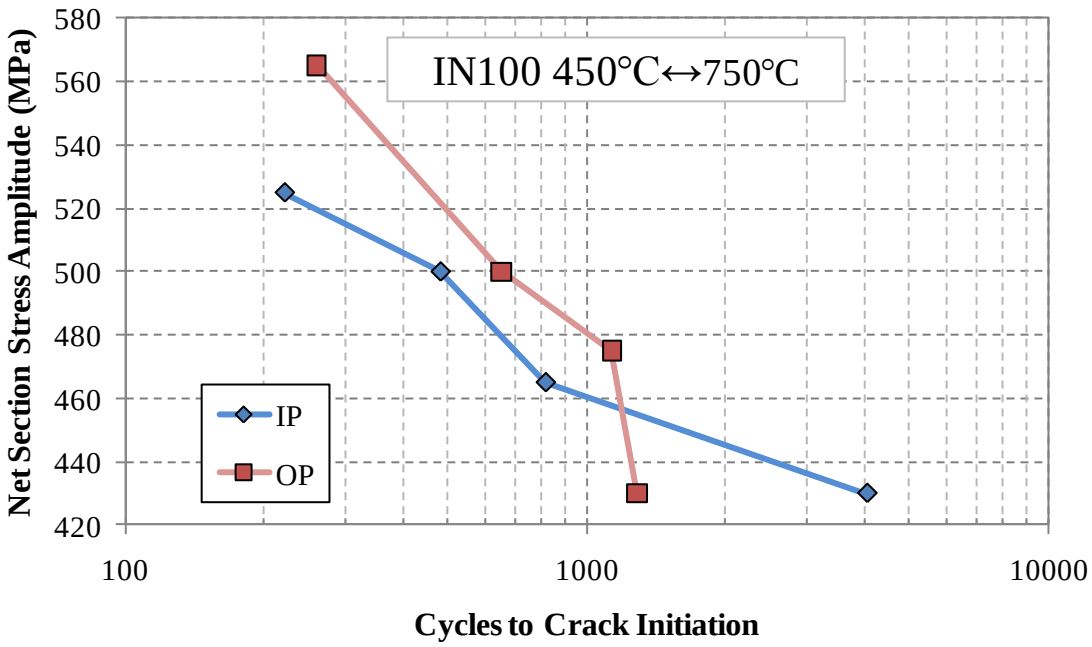

Figure 8-1. IN100 force control TMF crack initiation.

Trends for OP and IP intersect at a specific threshold net section stress value of 455 *MPa*. Below this threshold value OP lives are longer than corresponding IP lives; above which IP lives are longer. Similar trends have been observed by other authors using mechanical strain or inelastic strain range as damage metrics [54, 56, 86-88].

Damage during OP TMF tests is typically dominated by fatigue and high temperature oxidation interactions [56, 86-87, 89]. Figures 8-2 and 8-3 display multiple locations of surface cracks initiated at the specimen surface typical of fatigue-environmental damage.

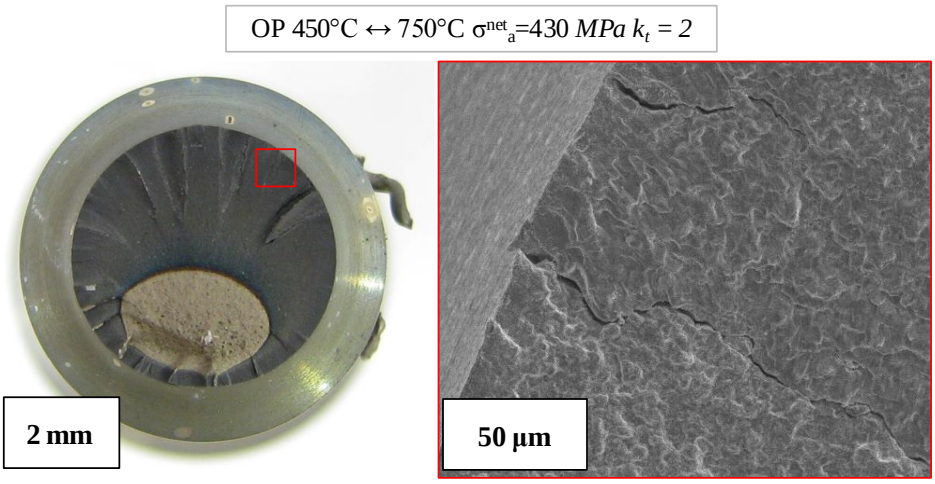

Figure 8-2. OP TMF fracture surface indicating an oxidized crack path and multiple sources of crack initiation at the notch root surface.

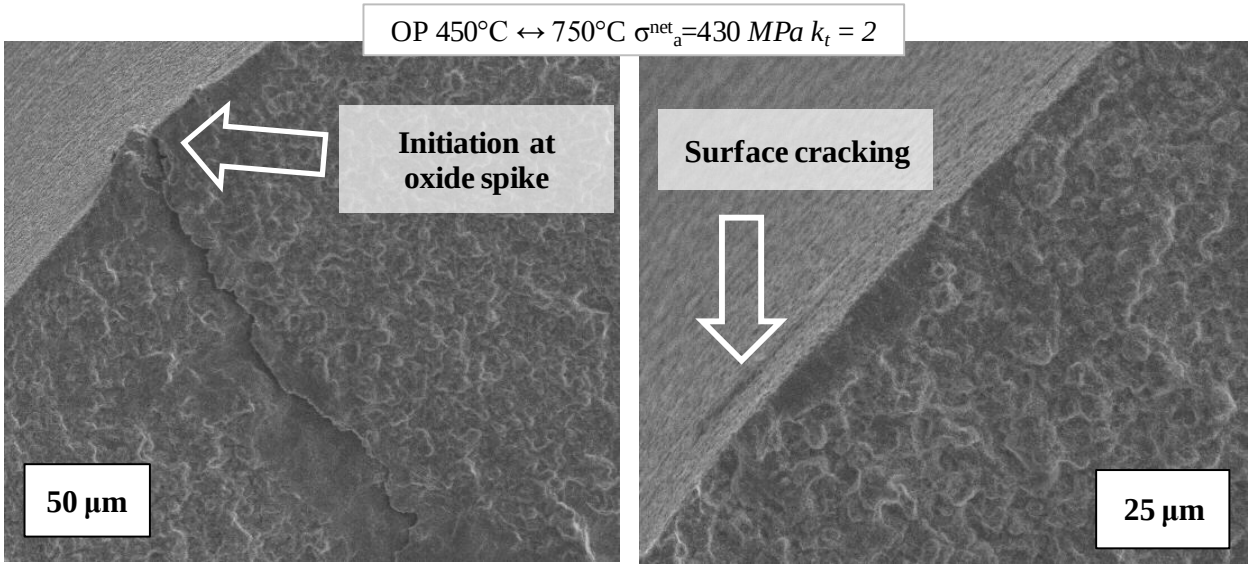

Figure 8-3. IN100 450°C-750°C, σ_a = 430 MPa, k_t = 2, OP TMF fracture surface showing crack initiation at a oxide spike and secondary surface cracking.

IP TMF tests at sufficiently high temperatures and loads are dominated by fatigue and creep interactions [20, 86-87]. Fracture surfaces for the IP TMF test with largest applied net section stress are shown in Figures 8-4 and 8-5.

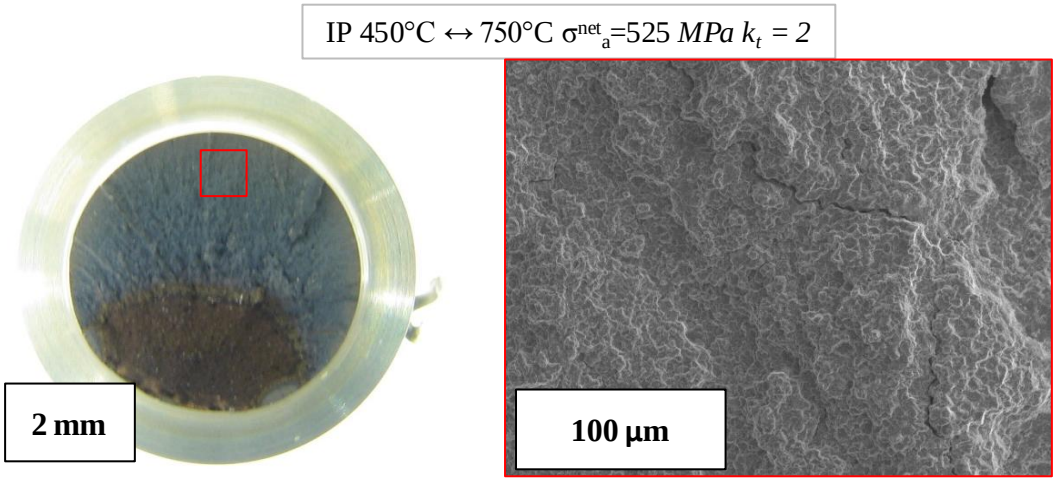

Figure 8-4. IP TMF fracture surface with evidence of internal intergranular microcracking.

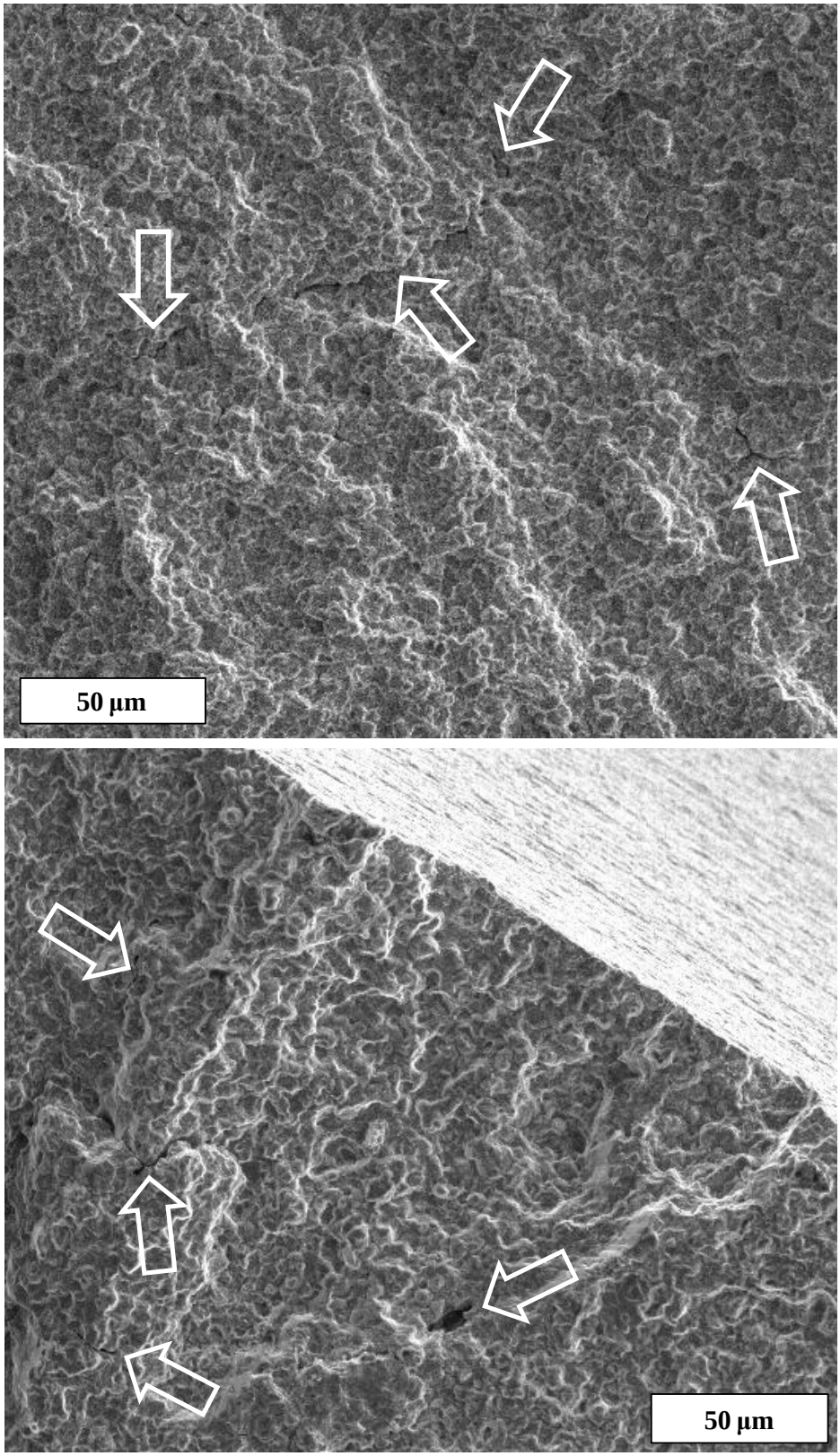

Figure 8-5. IN100 450°C-750°C, σ_a = 525 MPa, k_t = 2, IP TMF fracture surface showing intergranular micro cracking along the crack path.

Evidence of internal intergranular cracking on the crack propagation fracture surface indicates sufficient thermal and mechanical energy were applied to induce short-circuit diffusion along grain boundaries during tensile deformation. In an alloy with such high grain boundary density ($d_g \approx 5\mu m$) the damage from creep is significant.

Both IP and OP waveforms result in similar levels of fatigue damage. As such the observed trends can best be described by considering the degree of contribution from oxidation and creep damage under OP and IP conditions respectively. Below the cross over stress creep damage was significantly diminished in IP tests due to reduced applied stresses and overall damage was dominated by fatigue. Although applied stresses provide supplemental mechanical energy to promote thermally activated oxidation, oxidation processes are less sensitive to the applied stresses than creep mechanisms. As such both oxidation and fatigue damage are present below the cross over stress resulting in lower OP lives. Above the cross over stress both creep and fatigue damage are present in IP tests. In this case the creep-fatigue interactions are more damaging than the corresponding environmental-fatigue interactions.

8.2 Effect of OP TMF T_{max} on IN100

OP TMF experiments were performed on IN100 with applied temperature ranges 650°C ↔ 950°C and 650°C ↔ 800°C to study the effects of applied temperature on TMF life. Experimental details are shown in Table 8-1. All specimens experienced heavy ratcheting and were stopped prior to final fracture. Even at extremely low applied net section stresses the displacement across the notch ratcheted heavily and produced significant geometric distortion, as seen in Fig. 8-6. Such heavy ratcheting and distortion in a component would be considered a failure due to high machining tolerances necessary for component operation.

Table 8-1: IN100 elevated temperature range OP TMF conditions and results

IN100 Elevated T_{max} Force Control TMF Tests							
Period (s)	T_{min} (°C)	T_{max} (°C)	σ_a^{net} (MPa)	R_σ	k_t	Phasing	Initiation Life (cycles)
180	650	950	200	-1	2	OP	-
180	650	950	125	-1	2	OP	-
180	650	800	200	-1	2	OP	-

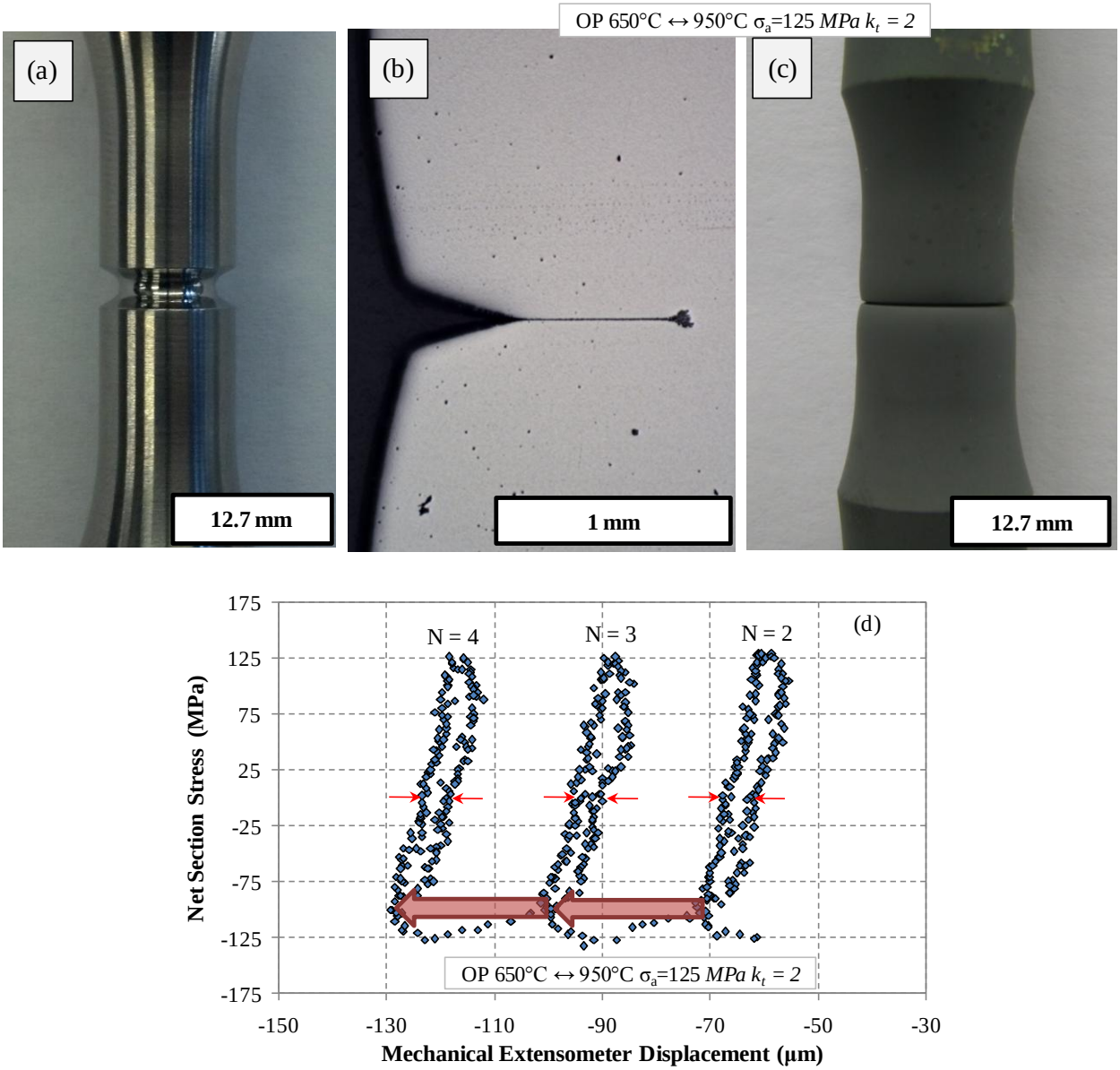

Figure 8-6. (a) as-received notched specimen (b) Cross section micrograph of severe notch geometry deformation (c) Image of severely deformed sample (d) heavy notch displacement ratcheting.

The increase of maximum temperature during TMF cycling promoted bulk creep deformation. The OP experiments performed experienced large scale creep ratcheting that distorted the specimen geometry shortly into cycling. At such high temperatures it is expected that IP TMF tests would have failed by creep rupture. Turbine disks manufactured from IN100 typically do not encounter temperatures as high as 800°C and if so would be damaged greatly from geometric distortion and creep damage.

CHAPTER 9 CONCLUSIONS

The results of this research are as follows:

1. **Influence of notch severity on TMF crack initiation life of CM247LC DS.**
   - Out-of-phase thermomechanical experiments were performed on longitudinally oriented smooth specimens and notched geometries $k_t = 1.3$, $k_t = 1.7$, $k_t = 2.0$ and $k_t = 3.0$ for temperature ranges $500°C \leftrightarrow 750°C$ and $500°C \leftrightarrow 950°C$.
   - Notch geometry $k_t = 1.3$ shows negligible effect on fatigue life compared against smooth specimens under $500°C \leftrightarrow 950°C$ OP TMF. $500°C \leftrightarrow 750°C$ OP TMF $k_t = 1.3$ has a small knockdown effect relative to the smooth specimen life trend.
   - Notch geometry $k_t = 1.7$ displays a knock-down affect in life compared against smooth specimens under $500°C \leftrightarrow 950°C$ OP TMF. The life trend for $k_t = 1.7$ falls between $k_t = 2.0 / k_t = 3.0$ and smooth/$k_t = 1.3$. The same knockdown effect is observed under $500°C \leftrightarrow 750°C$ OP TMF.
   - In-phase experiments were performed on longitudinally oriented notched geometry $k_t = 1.3$ over the temperature range $500°C \leftrightarrow 950°C$.
   - Notch geometry $k_t = 1.3$ followed smooth specimen life trends under $500°C \leftrightarrow 950°C$ IP TMF. Failure occurred by crack initiation and propagation. Creep rupture was not observed.
   - Global creep ratcheting was significant for all $500°C \leftrightarrow 950°C$ TMF experiments. Under $500°C \leftrightarrow 750°C$ global creep ratcheting was negligible.

2. **Influence of applied boundary conditions on TMF crack initiation life of CM247LC DS and IN100.**
   - CM247LC DS force and displacement control experiments under OP TMF $500°C \leftrightarrow 950°C$ produced identical life trends for $k_t = 1.3$, $k_t = 1.7$ and $k_t = 2.0$. Under OP TMF $500°C \leftrightarrow 750°C$ force and displacement control modes produce identical life trends for $k_t = 1.3$ and $k_t = 1.7$ Lives are similar across control modes as local notch deformation and initiation mechanisms are similar across the two control models.
   - IN100 force and displacement control experiments under OP TMF $450°C \leftrightarrow 750°C$ produced identical life trends for $k_t = 2.0$.
   - IN100 displacement control experiments under IP TMF initiated circumferential cracks (0.5 *mm*) that arrested. In this case force control represents the life-limiting conditions.
3. **Determine the local notch response in both CM247LC DS and IN100 using finite element analysis under TMF conditions.**
   - A transversely isotropic GTD-111 constitutive model was utilized for notch specimen finite element analysis to predict CM247LC DS local notch responses under $500°C \leftrightarrow 950°C$ OP and IP TMF loadings.
   - A unified creep-plasticity constitutive model was implemented for IN100, calibrated for various isothermal temperatures and verified for OP and IP $450°C \leftrightarrow 750°C$ TMF. Finite element analysis for $k_t = 2.0$ was performed to determine the local response for interpreting experimental observations.

- Cyclic response parameters were coupled with finite element analysis to decouple the inelastic strain response into ratcheting strains and cyclic strains.
- Both von Mises stress and equivalent cyclic inelastic strain range parameters qualitatively capture the location of crack initiation observed across all notch geometries in CM247LC DS under $500°C \leftrightarrow 950°C$ OP TMF.
- The equivalent cyclic inelastic strain range is maximum away from the notch root. Inelastic ratcheting strain increment is maximum at the notch root.
- An average of the axial inelastic ratcheting strain increment over the notch root best describes the experimental ratcheting response which is measured remotely away from the notch in CM247LC DS under $500°C \leftrightarrow 950°C$ OP TMF
- The IN100 inelastic cyclic strain response under IP TMF $450°C \leftrightarrow 750°C$ loading is highly localized to within a 150 μm region at the notch root. Uniaxial stresses decrease by 50% 0.5 *mm* away from the notch surface. This response partially explains observed crack arrest under displacement control IP TMF.

4. **Determine the role of thermomechanical fatigue loading parameters on crack initiation and deformation of notched IN100.**
   - Force controlled IN100 experiments were performed on $k_t = 2.0$ under $450°C \leftrightarrow 750°C$ IP and OP TMF.
   - A 455 *MPa* cross-over stress was determined for $450°C \leftrightarrow 750°C$ TMF below which IP lives are longer than OP and above which IP lives are shorter than OP.
   - OP TMF experiments were performed with elevated temperatures $650°C \leftrightarrow 950°C$ and $650°C \leftrightarrow 800°C$ to study the effects of temperature range on OP TMF.

- Even at low remotely applied loads, creep ratcheting was dominant under elevated temperature TMF experiments. Global ratcheting was so significant that notched components experienced heavy geometric distortion.

5. **Investigate life prediction methods to capture observed effects of notch severity.**
   - A Smith-Watson-Topper (SWT) parameter was utilized for life prediction. The equivalent inelastic cyclic strain range and von Mises stress were used. Analysis was performed on CM247LC DS OP TMF $500°C \leftrightarrow 950°C$.
   - The local maximum SWT criteria incorrectly predicts damage increasing with increasing notch severity.
   - A percentile based nonlocal area method was implemented where the domain boundary is defined by a percentile of the maximum SWT value. This method implicitly accounts for gradients yet produced the same values as the maximum local SWT method.
   - Nonlocal area method formulations were implemented where the size of the averaging domain was held constant across geometries and loads. Both the circular-sweep and surface-sweep methods produced satisfactory notch life sensitivity trends within experimental error. The circular-sweep method performed slightly better.
   - Both area-methods produced similar results indicating that the method is robust.
   - The circular-sweep method can be a useful tool for designers as it accounts for location of maximum SWT (initiation location) and automatically includes some small process volume where small crack growth occurs.

CHAPTER 10 RECOMMENDATIONS

There are several additional research opportunities that could add value and broaden the findings presented in this study. Listed below are several potential research areas that could add to the knowledge-base of thermomechanical fatigue crack formation in Ni-base superalloys in the presence of stress elevators.

Determine Notch Severity Effects in Disk Alloy IN100

Only notched IN100 specimens were utilized in this study. Experiments on smooth specimens and additional notched geometries could be used to determine TMF notch life sensitivity for IN100. This complimentary research on IN100 would produce an analogous methodology for predicting equiaxed notched TMF lives.

Implementation of a elastic-plastic fracture mechanics coupled with constitutive model response could be utilized to explain experimentally observed crack arrest under displacement control IP TMF. Coupling traditional fatigue methods with a fracture mechanics approach could better quantify IN100 TMF displacement control results. This could lead to a powerful design tool useful in a damage-tolerance type approach to disk component fatigue.

Incorporating a PD voltage drop methodology for better capturing initiation could experimentally address the role of small crack formation in IN100 TMF lives.

Numerically Investigate Notch Severity Effects at Low Temperatures in CM247LC DS

The parametric study on across all notch geometries was performed under OP TMF for the temperature range $500°C \leftrightarrow 950°C$. Analogous notch life sensitivity behavior was also observed experimentally at the lower temperature range, $500°C \leftrightarrow 750°C$. Additional numerical

simulations at the lower temperature range, $500°C \leftrightarrow 750°C$, could be perform similar predictions and built upon the methodology put in place here.

Develop an Analogous Life Prediction Mythology to Predict IP TMF

IP TMF was studied in this work however the large focus of the modeling effort was on OP TMF. Additional notched experiments on $500°C \leftrightarrow 950°C$ IP TMF could be performed coupled with analogous numerical simulations to develop a life prediction method for IP TMF. Developing a life prediction method for IP TMF, coupled with the work presented in this study, would bolster the predictive capabilities of notched components under TMF loads.

Assess Influence of Fatigue in Notch Life Sensitivity from Low Cycle Fatigue Testing

Little evidence of environmental interactions were observed under $500°C \leftrightarrow 750°C$ OP TMF, yet analogous notch life sensitivity results were observed at these lower temperatures. It is possible that the notch life sensitivity is controlled by fatigue damage alone and is not influenced heavily by TMF conditions. Isothermal low cycle fatigue tests of notched specimens ($k_t = 1.3$, $k_t = 1.7$, $k_t = 2.0$, $k_t = 3.0$) at sufficiently low temperatures (500°C) could be used to evaluate this hypothesis. Experimental results could be coupled with numerical nonlocal component analysis.

Development of A Mechanistic Damage Life Model

A simple power-law type expression was utilized in this study for nonlocal life prediction. Although this is adequate for low cycle lives where fatigue damage is dominant, longer lives would have a greater contribution from environment-fatigue damage processes which cannot be captured in a simple power-law fashion. A modular type damage model based

on the work of Neu and Sehitoglu [86] and Boismier and Sehitoglu [21] could be implemented. The work by Amaro [10] on environmental-fatigue of SX PWA1484 could be extended to include nonlocal methodologies. However coupling these models with FEA results is not trivial as environmental effects are localized at the material surface. It may be possible to couple the nonlocal area-method for quantifying fatigue damage with a nonlocal line-method along the free surface for capturing environmental effects. Or it may be the case that environmental damage can be captured using an area-method approach over very thin area at the material surface. This would account for the physical process in which oxidation at the surface results in a weakened γ'-depleted scale growing inwards. If this is feasible it may be physically realistic to define the area-integration domain as a function of cycles, somehow related to the γ' kinetics. Some authors have successfully used similar approaches for defining the nonlocal domain as a function of life [27, 40]. This approach would require an iterative approach for determining life predictions.

Determination of Local Notch Response Utilizing Crystal Plasticity Theory

Crystal plasticity models for CM247LC DS could be used to perform OP TMF simulations over the temperature range $500°C \leftrightarrow 950°C$. Numerical results would capture a more physically accurate response in the notch. Explicit knowledge of slip on octahedral and cubic planes could be utilized to verify experimentally observed slip traces near the notch surface. Additionally, explicit knowledge of slip characteristics in the notch could be used to effectively implement a life model based on the Cottrell-Hull mechanism [90].

Determining the Role of Notch Severity and Maximum Temperature on Ratcheting Response

It was observed that under sufficiently high temperature IN100 notches deformed significantly and creep ratcheting was the dominant deformation mechanism. Under force control

IP TMF conditions one CM247LC DS notched specimen experienced failure by creep rupture following significant creep ratcheting. It is critical that designers and analyst have the capability of predicting the degree of ratcheting as a function of applied temperatures, loads and notch severity. A numerical parametric study on CM247LC DS could provide valuable insight into developing methods for predicting the degree of ratcheting deformation in notched components. Numerical simulations could be performed varying notch geometries, loads, temperature ranges and TMF phasing. This database could be coupled with some quantitative criteria and potentially experimental creep results to inform designers and analyst when ratcheting is expected to be significant or negligible.

REFERENCES

1. Mazur, Z., et al., *Failure analysis of a gas turbine blade made of Inconel 738LC alloy.* Engineering Failure Analysis, 2005. **12**(3): p. 474-486.
2. Gordon, A.P., *Crack Initiation Modeling of a Directionally-Solidified Nickel-Base Superalloy*, in *Mechanical Engineering*. 2006, Georgia Institute of Technology: Atlanta. p. 440.
3. Mazza, E., Hollenstein, M., Holdsworth, S., Skelton, R.P., *Notched specimens thermo-mechanical fatigue of a 1CrMoV turbine steel.* Nuclear Engineering and Design, 2004. **234**(1-3): p. 11-24.
4. Malpertu, J.L. and L. Remy, *Influence of test parameters on the thermal mechanical fatigue behavior of a superalloy.* Journal Name: Metallurgical Transactions, A (Physical Metallurgy and Materials Science); (USA); Journal Volume: 21:2, 1990: p. Medium: X; Size: Pages: 389-400.
5. Reed, R., C., *The Superalloys Fundamentals and Applications*. 2006. Cambridge. 372.
6. Kupkovits, R.A., *Thermomechanical Fatigue Behavior of the Directionally-Solidified Nickel-Base Superalloy CM247LC*, in *Mechanical Engineering*. 2008, Georgia Institute of Technology: Atlanta. p. 252.
7. Xianfeng Ma, J.G., Huiji Shi,Guofeng Chen, Xiaodong Xu, *Investigation of Low Cycle Fatigue (LCF) Behavior for Anisotropic Materials*. 2008, Tsinghua University, CT China: Tsinghua. p. 112.
8. Suresh, S., *Fatigue of Materials*. 2nd ed. 1998, Cambridge, UK: Cambridge University Press. 679.
9. Ebrahimi, F., et al., *Effect of notch orientation on the evolution of plasticity in superalloy single crystals.* Materials Science and Engineering: A, 2006. **426**(1-2): p. 214-220.
10. Amaro, R.L., *Thermomechanical Fatigue Crack Formation in a Single Crystal Ni-Base Superalloy*, in *Mechanical Engineering*. 2010, Georgia Institute of Technology: Atlanta. p. 328.
11. Bao-Tong, M. and C. Laird, *Overview of fatigue behavior in copper single crystals—I. Surface morphology and stage I crack initiation sites for tests at constant strain amplitude.* Acta Metallurgica, 1989. **37**(2): p. 325-336.
12. Pollock, T.M. and A.S. Argon, *Creep resistance of CMSX-3 nickel base superalloy single crystals.* Acta Metallurgica et Materialia, 1992. **40**(1): p. 1-30.
13. Engler-Pinto, C.C., Jr., C. Noseda, Nazmy M.Y., Rezai-Aria, F., *Interaction between creep and thermo-mechanical fatigue of CM247LC-DS.* TMS, 1996.
14. Erickson, G.L. and K. Harris., *DS and SX Superalloys for Industrial Gas Turbines*. 1994, Liège, Belgium: Kluwer Academic Publishers Group.
15. Kear, B.H., Piearcey, B.J., *Tensile and creep properties of single crystals of the nickel-base superalloy Mar-M200.* Transactions of the Metallurgical Society of AIME, 1967. **239**: p. 1209-1218.
16. Liu, L.R., et al., *Formation of carbides and their effects on stress rupture of a Ni-base single crystal superalloy.* Materials Science and Engineering: A, 2003. **361**(1–2): p. 191-197.

17. Kim, W.H. and C. Laird, *Crack nucleation and stage I propagation in high strain fatigue—II. mechanism.* Acta Metallurgica, 1978. **26**(5): p. 789-799.
18. Oshida, Y., Liu, H.W., *Oxidation and Low Cycle Fatigue Life Prediction.* Proc Third Annual Workshop on Turbine Hot Section Technology, 1984. **321**.
19. Romanoski, G.R., Antolovich, Stephen D., Pelloux, Regis M., Remy, L., Sims, C. T., Ilschner, B., *A model for life predictions of nickel-base superalloys in high-temperature low cycle fatigue. Discussion*. 1988, Philadelphia, PA, ETATS-UNIS: American Society for Testing and Materials. 14.
20. Beck, T., et al., *Lifetime, cyclic deformation and damage behaviour of MAR-M-247 CC Under in-Phase, out-of-Phase and phase-Shift TMF-Loadings*, in *European Structural Integrity Society*, L. Rémy and J. Petit, Editors. 2002, Elsevier. p. 115-124.
21. Boismier, D.A., Sehitoglu, Huseyin, *Thermo-Mechanical Fatigue of Mar-M247: Part 2—Life Prediction.* Transactions of the ASME, 1990. **112**: p. 80-89.
22. Boismier, D.A., Sehitoglu, Huseyin, *Thermo-Mechanical Fatigue of Mar-M247: Part 1—Experiments.* Transactions of the ASME, 1990. **112**: p. 68-79.
23. Antolovich, S.D., Baur, R., Liu, S., ed. *A Mechanistically Based Model for High-Temperature LCF of Nickel-Base Superalloys* Superalloys 1980, ed. Champion. Vol. 21-25. 1980, Champion: Pa. 605-613.
24. Boyd-Lee, A.D., *Fatigue crack growth resistant microstructures in polycrystalline Ni-base superalloys for aeroengines.* International Journal of Fatigue, 1999. **21**(4): p. 393-405.
25. Manonukul, A., F.P.E. Dunne, and D. Knowles, *Physically-based model for creep in nickel-base superalloy C263 both above and below the gamma solvus.* Acta Materialia, 2002. **50**(11): p. 2917-2931.
26. Dowling, N.E., *Mechanical Behavior of Metals*. 3rd ed, ed. H. Stark. 2006, Upper Saddle River, NJ: Prentice Hall. 936
27. Susmel, L. and D. Taylor, *A novel formulation of the theory of critical distances to estimate lifetime of notched components in the medium-cycle fatigue regime.* Fatigue & Fracture of Engineering Materials & Structures, 2007. **30**(7): p. 567-581.
28. Bannantine, J.A., Comer, J.J., Handrock, J.L., *Fundamentals of Metal Fatigue Analysis*. 1990: Prentice Hall.
29. Kuhn, P., Hardrath, H.F., *Engineering method for estimating notch-size effect in fatigue tests on steel*, in *National Advisory Committee for Aeronautics*. 1952: Washington, DC.
30. Pilkey, W.D., *Peterson's Stress Concentration Factors*. 2nd ed, ed. I. John Wiley & Sons. 1997, New York.
31. Neuber, H., *Theory of Stress Concentration for Shear-Strained Prismatical Bodies With Arbitrary Nonlinear Stress-Strain Law.* Journal of Applied Mechanics of Materials, 1961. **4**: p. 550-554.
32. Taylor, D., *The theory of critical distances.* Engineering Fracture Mechanics, 2008. **75**(7): p. 1696-1705.
33. Susmel, L. and D. Taylor, *An Elasto-Plastic Reformulation of the Theory of Critical Distances to Estimate Lifetime of Notched Components Failing in the Low/Medium-Cycle Fatigue Regime.* Journal of Engineering Materials and Technology, 2010. **132**(2): p. 021002-8.

34. Mucke, R., Kiewel, Holger, *Nonlocal Cyclic Life Prediction for Gas Turbine Components With Sharply Notched Geometries.* Journal of Engineering for Gas Turbines and Power, 2008. **130**(1): p. 012506-8.
35. Ambrico, J.M. and M.R. Begley, *Plasticity in fretting contact.* Journal of the Mechanics and Physics of Solids, 2000. **48**(11): p. 2391-2417.
36. Socie, D.F., Dowling, N.E., Kurath, P., *Fatigue Life Estimation of Notched Members.* Fracture Mechanics: Fifteenth Symposium, 1984: p. 284-299.
37. Varvani-Farahani, A., Kodric, T., Ghahramani, A., *A method of fatigue life prediction in notched and un-notched components.* Journal of Materials Processing Technology, 2005. **169**(1): p. 94-102.
38. Fatemi, A. and D.F. Socie, *A Critical Plane Approach to Multiaxial Fatigue Damage Including Out-of-Phase Loading.* Fatigue & Fracture of Engineering Materials & Structures, 1988. **11**(3): p. 149-165.
39. Moore, Z.J., *Life Modeling of Notched CM247LC DS Nickel-Base Superalloy*, in *Mechanical Engineering*. 2008, Georgia Institute of Technology: Atlanta. p. 146.
40. Naik, R.A., Lanning, David B., Nicholas, Theodore, Kallmeyer, Alan R., *A critical plane gradient approach for the prediction of notched HCF life.* International Journal of Fatigue, 2005. **27**(5): p. 481-492.
41. Findley, W.N., *Fatigue of metals under combinations of stresses.* Trans ASME, 1957(79): p. 1337-1348.
42. Das, D.K., Singh, Vakil, Joshi, S. V., *High temperature oxidation behaviour of directionally solidified nickel base superalloy CM–247LC.* Materials Science & Technology, 2003. **19**(6): p. 695-708.
43. Okada, M., et al., *Initiation and Growth of Small Cracks in Directionally Solidified Mar-M247 Under Creep-Fatigue. Part I: Effect of Microstructure.* Fatigue & Fracture of Engineering Materials & Structures, 1998. **21**(6): p. 741-750.
44. Smith, K.N., Watson, P., Topper, T.H., *A Stress-Strain Function for the Fatigue of Metal.* J. Mater., 1970. **5**: p. 767-778.
45. Reger, M. and L. Remy, *High temperature, low cycle fatigue of IN-100 superalloy II: Influence of frequency and environment at high temperatures.* Materials Science and Engineering: A, 1988. **101**(0): p. 55-63.
46. Li, M.H., et al., *Oxidation behavior of a single-crystal Ni-base superalloy in air. I: At 800 and 900C.* Oxidation of Metals, 2003. **59**(Compendex): p. 591-605.
47. Li, M.H., et al., *Oxidation Behavior of a Single-Crystal Ni-Base Superalloy in Air—II: At 1000, 1100, and 1150°C.* Oxidation of Metals, 2003. **60**(1): p. 195-210.
48. Zhao, L.G., O'Dowd, N. P., Busso, E. P., *A coupled kinetic-constitutive approach to the study of high temperature crack initiation in single crystal nickel-base superalloys.* Journal of the Mechanics and Physics of Solids, 2006. **54**(2): p. 288-309.
49. Giggins, C.S. and F.S. Pettit, *Oxidation of Ni-Cr-Al Alloys Between 1000[degree] and 1200[degree]C.* Journal of The Electrochemical Society, 1971. **118**(11): p. 1782-1790.
50. Li, M.H., et al., *Oxidation Behavior of a Single-Crystal Ni-Base Superalloy in Air. I: At 800 and 900°C.* Oxidation of Metals, 2003. **59**(5): p. 591-605.
51. Akhtar, A., S. Hegde, and R. Reed, *The oxidation of single-crystal nickel-based superalloys.* JOM Journal of the Minerals, Metals and Materials Society, 2006. **58**(1): p. 37-42.

52. Evans, H.E. and M.P. Taylor, *Creep relaxation and the spallation of oxide layers.* Surface and Coatings Technology, 1997. **94–95**(0): p. 27-33.
53. Wang, J.S. and A.G. Evans, *Measurement and analysis of buckling and buckle propagation in compressed oxide layers on superalloy substrates.* Acta Materialia, 1998. **46**(14): p. 4993-5005.
54. Kupkovits, R.A., Neu, Richard W., *Thermomechanical fatigue of a directionally-solidified Ni-base superalloy:*
Smooth and cylindrically-notched specimens. International Journal of Fatigue, 2010. **32**: p. 12.
55. Huang, Z.W., et al., *Thermomechanical fatigue behavior and life prediction of a cast nickel-based superalloy.* Materials Science and Engineering: A, 2006. **432**(1–2): p. 308-316.
56. Shenoy, M.M., et al., *Thermomechanical Fatigue Behavior of a Directionally Solidified Ni-Base Superalloy.* Journal of Engineering Materials and Technology, 2005. **127**(3): p. 325-336.
57. Moore, Z.J., Neu, R. W., *Creep-Fatigue of a Directionally-Solidified Ni-base Superalloy – Smooth and Cylindrically Notched Specimens.* Fatigue & Fracture of Engineering Materials & Structures, 2010. **32**(8).
58. Lerch, B. and G. Halford, *Effects of control mode and R-ratio on the fatigue behaviour of a metal matrix composite.* Materials Science and Engineering A, 1995. **200**(1-2): p. 47-54.
59. Sanders, B. and S. Mall, *Isothermal fatigue behavior of a titanium matrix composite under a hybrid strain-controlled loading condition.* Materials Science and Engineering: A, 1995. **200**(1–2): p. 130-139.
60. Sonsino, C.M., *Influence of load and deformation-controlled multiaxial tests on fatigue life to crack initiation.* International Journal of Fatigue, 2001. **23**(2): p. 159-167.
61. Jackson, M.P. and R.C. Reed, *Heat treatment of UDIMET 720Li: the effect of microstructure on properties.* Materials Science and Engineering: A, 1999. **259**(1): p. 85-97.
62. Davis, J.R., *Heat-resistant materials*, ed. A. International. 1997.
63. Chaboche, J.L., *Constitutive equations for cyclic plasticity and cyclic viscoplasticity.* International Journal of Plasticity, 1989. **5**(3): p. 247-302.
64. Freed, A.D., Walker, K.P., *Refinements in a Viscoplastic model*. 1989: NASA Tech. Memo. p. pp 16.
65. Ohno, N. and J.D. Wang, *Kinematic hardening rules with critical state of dynamic recovery, part I: formulation and basic features for ratchetting behavior.* International Journal of Plasticity, 1993. **9**(3): p. 375-390.
66. ABAQUS, ABAQUS v6.9. 2009, Dassault Systèmes: Providence, RI.
67. Shenoy, M.M., D.L. McDowell, and R.W. Neu, *Transversely isotropic viscoplasticity model for a directionally solidified Ni-base superalloy.* International Journal of Plasticity, 2006. **22**(12): p. 2301-2326.
68. Shenoy, M.M., *Constitutive Modeling and Life Prediction in Ni-Base Superalloys*, in *Mechanical Engineering*. 2006, Georgia Institute of Technology: Atlanta. p. 298.
69. Lemaitre, J., Chaboche, J.-L., *Mechanics of Solid Materials*. illustrated ed. 1990, Cambridge: Cambridge University Press.
70. Armstrong, P.J., Frederick, C.O., *A mathematical representation of the multiaxial Bauschinger effect*, in *CEGB Report*. 1966, Berkeley Nuclear Laboratories.

71. McGinty, R.D., *Multiscale Representation of Polycrystalline Inelasticity*, in *Mechanical Engineering*. 2001, Georgia Institute of Technology: Atlanta. p. 407.
72. Marin, E.B., *A Critical Study of Finite Strain Porous Inelasticity*, in *Mechanical Engineering*. 1993, Georgia Institute of Technology: Atlanta. p. 249.
73. Ibanez, A.R., *Modeling Creep Behavior in a Directionally Solidified Nickel Base Superalloy*, in *Mechanical Engineering*. 2003, Georgia Institute of Technology: Atlanta.
74. King, J.E., *Fatigue crack propagation in nickel-base superalloys: effects of microstructure, load ratio, and temperature*. Vol. 3. 1987, London, ROYAUME-UNI: Maney.
75. Anderson, T.L., *Fracture Mechanics Fundamentals and Applications*. 3rd ed. 2005, Boca Raton, FL: CRC Press.
76. Adair, B., *Thermo-Mechanical Fatigue Crack Growth of A Polycrystalline Superalloy*, in *Mechanical Engineering*. 2010, Georgia Institute of Technology: Atlanta.
77. Leo Prakash, D.G., et al., *Crack growth micro-mechanisms in the IN718 alloy under the combined influence of fatigue, creep and oxidation.* International Journal of Fatigue. **31**(11-12): p. 1966-1977.
78. Liu, H.W. and Y. Oshida, *Grain boundary oxidation and fatigue crack growth at elevated temperatures.* Theoretical and Applied Fracture Mechanics, 1986. **6**(2): p. 85-94.
79. Osinkolu, G.A., G. Onofrio, and M. Marchionni, *Fatigue crack growth in polycrystalline IN 718 superalloy.* Materials Science and Engineering: A, 2003. **356**(1–2): p. 425-433.
80. Larson, J.M., Rosenberger, Andrew H., Hartman, George A., Russ, Stephan M., John, Reji, *The Role of Spectrum Loading in Damage-Tolerance Life-Management of Fracture Critical Turbine Engine Components.* 2001.
81. Tanaka, K. and Y. Akiniwa, *Resistance-curve method for predicting propagation threshold of short fatigue cracks at notches.* Engineering Fracture Mechanics, 1988. **30**(6): p. 863-876.
82. Tanaka, K., *Modeling of Propagation and Non-Propagation of Small Fatigue Cracks* Small Fatigue Cracks, 1986: p. 20.
83. Kupkovits, R.A., D.J. Smith, and R.W. Neu, *Influence of minimum temperature on the thermomechanical fatigue of a directionally-solidified Ni-base superalloy.* Procedia Engineering, 2010. **2**(1): p. 687-696.
84. Arakere, N.K., Siddiqui, Shadab, Magnan, Shannon, Ebrahimi, Fereshteh, Forero, Luis E., *Investigation of Three-Dimensional Stress Fields and Slip Systems for fcc Single-Crystal Superalloy Notched Specimens.* Journal of Engineering for Gas Turbines and Power, 2005. **127**(3): p. 629-637.
85. Lukás, P., Preclík, P., Cadek, J., *Notch effects on creep behaviour of CMSX-4 superalloy single crystals.* Materials Science and Engineering A, 2001. **298**(1-2): p. 84-89.
86. Neu, R. and H. Sehitoglu, *Thermomechanical fatigue, oxidation, and Creep: Part II. Life prediction.* Metallurgical and Materials Transactions A, 1989. **20**(9): p. 1769-1783.
87. Neu, R. and H. Sehitoglu, *Thermomechanical fatigue, oxidation, and creep: Part i. Damage mechanisms.* Metallurgical and Materials Transactions A, 1989. **20**(9): p. 1755-1767.
88. Sehitoglu, H., *Thermal and Thermomechanical Fatigue of Structural Alloys*. ASM Handbook. Vol. 19. 1996. 20.

89. Esmaeili, S., Engler-Pinto Jr., C.C., Ilschner, B., Rezai-Aria, F. , *Interaction between oxidation and thermo-mechanical fatigue in IN738LC superalloy. I.* Scripts Metallurgica et Materialia, 1995. **32**(11): p. 1777-1781.
90. Cottrell, A.H. and D. Hull, *Extrusion and Intrusion by Cyclic Slip in Copper*. Proceedings of the Royal Society of London. Series A. Mathematical and Physical Sciences, 1957. **242**(1229): p. 211-213.